

A NEUTRAL MATTER WAVE MICROSCOPE  
(NEMI): DESIGN AND SETUP

SABRINA DANIELA EDER



Dissertation

submitted to the Department of Physics and Technology in  
partial fulfillment of the requirements for the degree of

Philosophiae Doctor (PhD)

at the University of Bergen

December 2011

Sabrina Daniela Eder: *A neutral matter wave microscope (NEMI): design and setup*,  
Dissertation, December 2011

SUPERVISOR:

Prof. Bodil Holst, University of Bergen

CO-SUPERVISOR:

Dr. William Allison, University of Cambridge, Cavendish Laboratory

LOCATION:

University of Bergen

## ABSTRACT

---

Matter wave microscopes such as electron microscopes or helium ion microscopes are vital tools in numerous fields of sciences. This thesis presents the design of a new matter wave microscope using neutral helium atoms as imaging probe. In contrast to the already well established helium atom scattering techniques where information about the surface is obtained through diffraction and spectroscopy analysis, **Nemi** (short for NNeutral helium MMicroscopy) uses a focused beam of neutral ground-state helium atoms to image the surface of a sample. The main advantages which set this technique aside from already existing scanning probe techniques is that the helium probe has a much lower energy (less than 100 meV) for a de Broglie wavelength of less than 0.1 nm and that the helium atoms are uncharged and chemically inert. This means that the NEMI technique is in principle equally suitable for insulators, semiconductors, metals and organic samples provided they are vacuum compatible. The new NEMI technique is also particularly suited for the investigation of fragile samples.

The focusing of the neutral helium beam is realized with a so called Fresnel zone plate. As a part of this thesis it is shown, for the first time, that sub-micron focusing with this type of diffraction grating is possible.

A complete design concept for the microscope including a detailed evaluation of the expected helium flow rates in the probe beam as well as of the background gas between the vacuum chambers is presented. The functionality and technical design for the different components are discussed.

First test results characterizing the probe beam of the assembled beam column are presented.



## ACKNOWLEDGMENTS

---

There have been many people accompanying me during this PhD project in one way or another and I am grateful for all their help and support. I can just try to express my gratitude to each of them within these next lines but words will never be enough.

First of all I would like to thank Prof. Bodil Holst for being a great supervisor throughout these last four years and for giving me the opportunity to work on this project. Thank you for all the encouragement and guidance, for providing motivational words when needed and never letting me lose interest in scientific work. I am very grateful to have been part of this research group.

I would also like to thank Prof. William Allison for being my co-supervisor on this project. Thank you for the interesting discussions during your visit.

I am also very thankful for all the support and help from Bjørn Samelin. This work could not have been done without all the exciting discussions and his tips and tricks in the lab. Thank you for being there for all my questions.

Another huge thank goes to Gianangelo Bracco who was of great help throughout the *Nemi* project.

Special thanks I would like to express to Thomas Reisinger. During the time here in Norway he has not just been a great office mate answering all my sometimes quite curious questions, but he also became a close friend. Thank you for that and especially also for all your patience and help at work. Next there is Katrin Fladischer who I would like to thank for the great time when she was visiting our group. And of course also all the other members of our group.

The design of a new instrument is in my opinion not possible without experienced technicians and therefore I would like to thank Kurt Ansperger from Graz who with his technical knowledge and experience contributed a lot to this work. I'd also like to thank his team. Further, I want to acknowledge the professional support of the workshop here at the physics department in Bergen, in particular Roald Langøen and his team.

Moving to another country is not only exiting but also always combined with being anxious about how it will be. For me it became one of the best experiences in my life and that is to the most part due to the people who warmly welcomed me here in Bergen. In this regard I have to specially thank Sigrid Meyer and Andreas Samnøy for always letting me feel home here in Bergen and of course also Jenny Luneng, Hege Erdal and Beate Krøvel Humberstet who became close friends during this years. Also Martin Greve for being my best buddy and always being up for testing some new weird sport. And all the others who I cannot mention here.

Here is also the place to say thank you to Marisa Loitfelder, Markus Koini, Gernot Trattnig, Barbara Salzburger, Evelin Fissltahler, Stefan Sax, Carmen Tomaschitz, Melanie Ostermann, Karin Schrettlinger, Martina Steurer, and Miriam Capelli who even though I moved away about 2500km from Austria always let me know that they did not forget about me. Thank you for all the video calls, for a place to stay on the several short visits to Graz and Vorarlberg, for knowing that a package of tea is exactly what is needed, for the visits in Bergen and for letting me know that I am missed by them.

And finally I am deeply grateful to my family. My mother Anita, my two sisters Astrid and Petra and my niece Michelle. And of course also to my stepfather Siegi and my brother in law Heinrich. Thank you for your endless support, for your encouragement and for reassuring me that I always have a family to count on. I could not have gotten here without you.

# CONTENTS

---

0	INTRODUCTION	1
0.1	Background	1
0.2	Motivation	2
0.3	Previous work	6
0.4	Overview of the thesis	10
1	NEMI	11
1.1	General design considerations	11
1.2	Main components and conceptual limitations	13
1.2.1	Beam source	13
1.2.2	Skimmer	13
1.2.3	Atom optical element	14
1.2.4	Detection system	16
1.3	Final design parameters	16
2	HELIUM FLOW CALCULATION	19
2.1	He-beam flow rate calculation	19
2.1.1	Particle flow $\dot{N}_0(x)$ at a position $x$ along the beam direction	20
2.1.2	Particle flow at the ZONE PLATE position	21
2.1.3	Losses due to diffraction process at the ZP ( $T_{ZP}$ )	28
2.1.4	Reflection at the sample	28
2.1.5	Comparison of determined helium flow values $\dot{N}_R$ entering the detection system	31
2.1.6	Pressure increase in the PITOT TUBE detector	31
2.2	Lay-out of the pumping system	34
2.2.1	Some vacuum technology and flow basics	35
2.2.2	System setup	36
2.2.3	Partial helium pressure increase in the UHV system	39
2.2.4	Partial pressure increase due to the helium diffusion process from the source chamber $p_{diff}$	42
2.2.5	Partial pressure increase due to the helium beam $p_{beam}$	45
2.2.6	Total partial pressure increase due to the helium beam and diffusion	49

2.3	Lay-out of the prevacuum System	51
2.3.1	Prevacuum-line source chamber (SC)	53
2.3.2	Prevacuum-line pumping stage/ zone plate /sample detector chamber (PST/ZPC/SDC)	56
2.4	Ultimate Parameters and Settings	58
3	SOURCE	61
3.1	Theoretical Background for a Free Jet Expansion	61
3.2	Effusive Beams	61
3.3	Free Jet Expansion	62
3.4	Final average speed of a monoatomic gas	63
3.5	Virtual source	64
3.6	Velocity distribution and Speed Ratio	67
4	FOCUSING ELEMENT	69
4.1	Background	69
4.2	Zone plate aberrations and resolution	72
4.3	Atom optical parameters	75
4.4	Focused spot size	78
4.5	Zone plate fabrication	79
5	DETECTION	83
5.1	Theoretical background detection system	83
5.2	Working principle PITOT TUBE	83
5.3	Cold cathode pressure measurement gauge	84
6	TECHNICAL REALIZATION	87
6.1	Source Chamber	87
6.1.1	Nozzle / Source	88
6.1.2	Nozzle mounting	92
6.1.3	Skimmer	94
6.1.4	Complete source chamber	95
6.2	Pumping Stage Chamber and Zone Plate Chamber	111
6.2.1	Pumping stage chamber (PST)	111
6.2.2	Zone plate chamber (ZPC)	112
6.3	Sample and Detector Chamber	126
6.3.1	Sample implementation	126
6.3.2	Detection	136
6.3.3	Sample chamber	152
6.4	Instrument placing	162



7	BEAM ALIGNMENT	165
7.1	Beam alignment	165
7.1.1	Skimmer nozzle adjustment	165
7.1.2	Zone plate adjustment	166
7.1.3	Reflection detector adjustment	168
7.1.4	Sample holder adjustment	171
7.1.5	Sample-reflection detector alignment	172
8	FIRST SUB-MICRON HELIUM FOCAL SPOT	173
8.1	Sub-micron focusing of neutral helium beam (Paper A)	173
8.2	Experimental Speed Ratio determination	174
8.2.1	Experimental setup for Speed Ratio determination	174
8.2.2	Speed ratio evaluation	177
8.2.3	Example for the new correction method for a room temperature beam	182
9	NEMI MEASUREMENTS	187
9.1	Characterization of the 5 $\mu\text{m}$ free-jet expansion beam	187
9.1.1	Measured source chamber pressures	189
9.1.2	Measured pumping stage chamber pressures	191
9.1.3	Measured ZONE PLATE chamber pressure	193
9.1.4	Measured “ <i>in-line</i> ” PITOT tube detector pressure rise	196
9.1.5	Summary and discussion of the measurement results	198
10	OUTLOOK	199
10.1	Conclusion and outlook	199
I	APPENDIX	201
A	APPENDIX PAPER A	203
B	APPENDIX TECHNICAL DRAWINGS	215
B.1	Design drawings and component specifications	215
B.1.1	UHV Design XYZT64-50-H XYZ stage	215
B.1.2	Sample holder	217
B.1.3	Piezo-tablet	221
B.1.4	Alio XYZR stage	223
B.1.5	Sample chamber	229
C	APPENDIX PRESSURE GAUGES	235

C.1	Appendix Specifications pressure measurement gauges	235
C.1.1	Prevacuum gauges	235
C.1.2	Ultra high vacuum gauges	236
D	APPENDIX PREVACUUM	239
D.1	Types of flow regimes	239
D.2	Intermediate - Knudsen Flow	240
D.2.1	Knudsen's Equation	240
D.2.2	Minimum conductance	241
D.2.3	Transition pressure	242
D.2.4	Limits of the intermediate range	243
D.2.5	The molecular-viscous intersection point	244
D.3	General equation Knudsen flow	245
D.4	Conductance $C_m$ Molecular Flow for different Components	246
D.4.1	Molecular flow conductance of an aperture	246
D.4.2	Molecular flow conductance of a tube of constant cross section	247
D.4.3	Molecular flow conductance of a short tube of constant cross section	247
D.4.4	Molecular flow conductance - elbows	247
D.5	Conductance $C$ intermediate (KNUDSEN) flow regime	248
D.6	Total conductance $C_{total}$ of an intermediate flow regime vacuum system	249
D.7	Conductance prevacuum line source chamber (SC)	249
D.8	Conductance prevacuum line PST/ ZPC /SDC	254
E	APPENDIX FLIGHT TIME CALIBRATION TOF MEASUREMENTS	259
E.1	Flight time $t_f$ calibration TOF-measrements	259
	List of Figures	261
	List of Tables	278
	BIBLIOGRAPHY	283

## ACRONYMS

---

AFM	Atomic force microscope
CAD	Computer aided design
ESEM	Environmental scanning electron microscopy
FWHM	Full width at half maximum
HAS	Helium atom scattering
He	Helium
HeIM	Helium-ion microscopy
HV	High vacuum
HVEM	High voltage electron microscopy
LED	Light emitting diode
LiF	Lithium fluoride
LN	Liquide nitrogen
MaGiE	Makroskopische Gitter Experimente
NEMI	Neutral microscope
PST	Pumping stage chamber
PTFE	Polytetrafluoroethylene (Teflon)
RT	Room temperature
SC	Source chamber
SDC	Sample detector chamber
SEBL	Scanning electron-beam-lithography
SEM	Scanning electron microscope

SHeM Scanning helium microscope

SK Skimmer

SNOM Near-field scanning optical microscopy

SPM Scanning probe microscopy

STED Stimulated emission depletion microscopy

STM Scanning tunneling microscope

TEM Transmission electron microscope

TOF Time of flight

TP Turbomolecular pump

UHV Ultra high vacuum

UIB Universitetet i Bergen

ZP Zone plate

ZPC Zone plate chamber



## INTRODUCTION

---

### 0.1 BACKGROUND

When Dünnoyer in 1911 established a directed beam of neutral atoms, he opened the window to a promising new field of science and technology. By generating for the first time a so called “molecular beam” he found an ideal tool for further experiments providing the possibility to answer questions in several fields of science and research, reaching from basic studies of gas kinetics over chemical reactions to surface science assignments [1]. Soon after Otto Stern gave this new technology a starting ground by building the first molecular beam laboratory in the world. He proved the versatility of molecular beams for investigating the interaction of single atoms/molecules with photons, external fields, other atoms or molecules and most importantly for the work presented in this thesis, with surfaces.

In the special case of surface science Estermann et al. (1931) [2] were the first to show atom beam diffraction from freshly cleaved LiF crystals and thereby proved the wave nature of atoms [1]. Estermann and his colleagues worked with a beam of neutral *helium* atoms.

A next major development were molecular beams produced by gas dynamic expansion through a small nozzle by Kantrowitz and Grey in 1951 [3]. For the first time they presented a source which was not effusive and which had a significantly narrower velocity distribution and higher intensity [1].

The progress in vacuum techniques during the following years provided new possibilities and in the early 1970s the development of *supersonic beams* and ultra-high vacuum based universal detection schemes marked a next big step in molecular beam scattering [4]. Since the end of the 1970s “*helium atom scattering*” (*HAS*) has been an important technique for the investigation of structural and dynamic properties of surfaces [5]. The size and orientation of surface unit cells (with or without adsorbates) [5, 6] can be determined from *HAS* diffraction spectra and with applying *time-of-flight (TOF)* it is possible

to obtain high resolution information on low energy surface phonons [7, 8]. One of the biggest advantages of the neutral helium atom beam is the low beam energy (less than 0.1 eV) and the fact that the beam is neutral. For example a room temperature beam has a *de Broglie* wavelength of around  $\sim 0.1$  nm which corresponds to a beam energy of less than 0.1 eV. This means that the helium probe beam has a lower energy for a given wavelength than most other “particle” probes. For example about a factor 1000 compared to electrons. The energy is so low that there is no penetration into the sample. Furthermore due to the neutrality of the helium atoms there is no charging of the investigated samples. A neutral helium beam can therefore be applied to metals, insulators and semiconductors equally. Even extreme fragile structures can be investigated without any damage, and since helium is a very nonreactive element also no chemical reactions with the substrate or surface adsorbates will occur. A further advantage of using neutral helium atoms for sample investigations is the possibility to image magnetic or highly charged materials without any interference effects.

## 0.2 MOTIVATION

The aim of this work is to create a new surface science tool, exploiting the advantages of low energy, neutral helium beams in a new NEutral MIcroscope NEMI.

The motivation behind all microscopy technologies is the same, namely to build an instrument that provides the opportunity to observe features smaller than what we can see with our naked eye.

The first optical microscope was developed around 1595 [9]. Early microscopes were based on optical lens systems using light to investigate objects. From then on microscopes have become an important tool in natural science, and many improvements in the field of microscopy have been made with regard to magnification, resolution limits and image contrast ever since. Especially the last century provided immense improvements in the field of optical microscopy as well as in the development of completely new microscopy techniques using matter waves (electron and helium ion beams) or most recently scanning probe microscopes where a solid probe scans the sample surface [10, 11]. The motivation for the new techniques have been to overcome the resolution limit of classical light microscopy. The theoretical resolution limit of

classical optical microscopes (far-field) has been shown by E. K. Abbe to be approximately  $\lambda/2$  for imaging in air where  $\lambda$  represents the wavelength of light [12]. Abbe was one of the founders of Zeiss instruments and already at the end of the 19th century microscopes reached this limitation. Since visible light has a minimum wavelength located in the area around 0.4 micron (violet light) the absolute theoretically resolution limit for a classical optical microscope is in the range about 0.2 micron. In practice the value is considerably higher. Good imaging is rarely possible with a resolution of less than 1 micron.

One way to achieve higher resolutions is to work with shorter wavelengths which is done by X-ray microscopy [13, 14]. This technique has its advantage in the ability of observing thick specimens even in selected environments like gases or liquids, but this technology suffers, among others, from sample damage due to the high energies of the beam (12 keV for a wavelength of 0.1 nm).

A new technique to overcome Abbe's limitation is *Stimulated emission depletion microscopy (STED)* in combination with fluorescence. Fluorescence of a material is induced by an excitation laser focused to a small spot. A second laser shaped in a doughnut form, the so called *STED-laser* is used to quench the fluorescent emission in a localized area. When the two lasers overlap, only the center of the doughnut (area without *STED* laser) still emits fluorescent light. The new resolution limit is defined by the inner diameter of the doughnut and the intensity of the *STED-laser* [15, 16, 17]. A disadvantage of *STED* microscopy is that the investigated materials need to exhibit fluorescence and the energies are quite high.

Another way to overcome Abbe's limit is to exploit the behavior of evanescent waves. This is done in *scanning near-field optical microscopy (SNOM)* [18]. A fiber optic tip placed within a few nanometers distance to the sample is collecting light which is emitted from the sample surface. In that way the resolution is only limited by the size of the tip-opening and no longer by the wavelength of the light. With this approach resolutions of a few tens of nanometers are possible [19, 20]. The very small distance between the tip and the sample restricts the method to smooth surfaces and the data can be difficult to interpret.

An obvious way to improve the resolution of standard optical microscopes while decreasing the damage caused by the energy of the beam is to use particle beam probes which have a lower energy for a given wavelength than a photon. Ernst Ruska and Max Knoll published the first images based on electrons

utilized as a probe beam in 1932 [21, 22, 23]. The wavelength of electrons can be determined by the de Broglie relation  $\lambda = h/p$  which relates the wavelength  $\lambda$  of a particle to its momentum  $p$  ( $h$  is the Planck's constant) [24]. The momentum of an object is related to its kinetic energy  $E = p^2/2m$  (ignoring relativistic effects). There are two different types of electron microscopes. In *scanning electron microscopes (SEM)* electron beams with a typically energy in the range between 0.1 – 30 keV are scanned over a sample [25]. The image information is gained from the backscattered electrons or, more frequently, from the so called secondary electrons which are generated by inelastic excitation of the sample. A special type of scanning electron microscopes is the *environmental scanning electron microscope (ESEM)* [26]. With an ESEM tool it is possible to overcome the restriction of a high vacuum requirement for standard SEM microscopes. Samples which are either fundamentally incompatible with the vacuum environment or would contaminate the vacuum system of the instrument (for example biological tissues, liquids, colloids, damp or dirty samples) can be observed with an ESEM [25]. Furthermore ESEM can to some extent be used to image insulating samples. In *transmission electron microscopes (TEM)* a beam of electrons is transmitted through very thin samples and the transmitted electron intensity distribution is detected. Such instruments typically work with electron beam energies between 40 keV-500 keV (high voltage electron microscopy HVEM 500 keV-3 MeV) [27]. For all electron microscopes the final resolution is limited not by the wavelength but by the electron-optical system which is consisting of electromagnetic lenses. Significant improvements have been made in the recent years so that presently the resolution for SEM tools lies in the nm range and TEM instruments can provide resolutions even in the sub-Ångström area [28]. The high resolution comes at some price. Samples normally have to be conductive since otherwise charging of the substrate will occur which influences the image quality. There can be specimen heating due to the probe beam which might lead to a thermally induced sample damage or there can be radiation damages as a consequence of ionization. This kind of damage is especially an issue for TEM microscopy where the applied beam voltages lie in the keV range and the specimens have to be very thin but it is also a serious limitation for SEM [27]. A fairly new technique working with charged particles as a probe beam is *helium-ion microscopy (HeIM)*. The high source brightness and the low wavelength of the helium ions is utilized to achieve high resolutions. The excitation volume of the He-ion beam with the



sample is smaller than with the SEM technique and therefore HeIM is more surface sensitive [29, 30]. Still sample charging and to some amount sample damage will also be an issue in HeIM.

A completely different way to overcome Abbe's limit of resolution is presented by *scanning probe microscopy (SPM)*. This alternative field of imaging techniques started out with the invention of the *scanning tunneling microscope (STM)* in 1982 [31]. A tunneling current between the sample and a sharp tip is utilized to gain information about the sample surface [11]. The measured current originates in quantum tunneling. To generate this tunneling current a bias voltage is applied between the tip and the sample. In the commonly used constant current operation mode the bias voltage is kept constant by a change in the spacing between the tip and the sample surface. An image of the topography of the surface is then formed by logging this distance change during the scanning process. Beside this constant current mode there also exists a constant height mode where the change in the bias voltage is recorded as well as spectroscopic and manipulation modes [10]. While these instruments provide atomic resolution, they also require that the tip as well as the sample are good conductors which limits the range of samples that can be investigated. *Atomic force microscopy (AFM)* represents a SPM technique which is not limited by requirements of conductivity. Similar to STM, the AFM technology is also based on the interaction of a sharp tip with the sample surface [32]. AFM images are recorded by measuring the interatomic forces between the tip and the sample surface while scanning across the sample. The resolution limit of AFM currently lies in the range of  $\sim 10 - 15 \text{ nm}$ . In special cases with the tapping mode even in the  $2 \text{ nm}$  range [33].

Both SPM methods suffer from drawbacks. For example they are very sensitive to inappropriately selected operating parameters which can cause imaging artifacts. Rough and soft samples might require very slow scanning speeds and high aspect ratio samples cannot easily be investigated. Also sample- or tip-damages by tip-interaction with the surface are quite common [10].

To summarize: while all existing microscopy techniques are very useful, there is no technique presently available which can image fragile, insulating samples, in particular samples with high aspect ratios in a fast, reliable manner. Neutral helium atom microscopy (NEMI) offers a new microscopy technique to fill

this niche. We foresee that it will prove particularly useful in the imaging of polymeric nanostructures (nanoimprint, biochips etc.), but there will no doubt be many other applications.

### 0.3 PREVIOUS WORK

The idea of building a microscope based on neutral atom/molecular beam scattering is not new, but the technical realization has proven to be rather challenging. The main problem has been to focus the neutral helium atom beam. Focusing of the neutral helium atoms with magnetic or electric lenses, used for example in SEM and TEM instruments, is not possible. Furthermore neutral, ground state helium does not have any internal degrees of freedom and hence cannot be manipulated with the "classical" atom optics techniques used for example in Bose-Einstein condensation experiments [35, 36]. This restricts the possible approaches to techniques which manipulate the atoms via their de Broglie wavelength in analogy to classical optics. Low energy neutral helium atoms do not penetrate into solid material, which narrows the possibilities even further down. Thus the two possible techniques are limited to either focusing using *Fresnel zone plates* with free standing zones or using *mirrors*.

The idea of focusing neutral helium atoms with a mirror has been investigated by several groups. In 1997 B. Holst and W. Allison used an atom mirror created from a single 50  $\mu\text{m}$  thick silicon crystal cut along the (111) plane to focus a helium beam into a  $250 \pm 50 \mu\text{m}$  diameter spot [37]. The crystal surface was hydrogen passivated to make it inert and a parabolic profile for focusing was achieved by electrostatically deforming the crystal in a parallel plate capacitor setup. Further work on this silicon crystal setup was published [38] and in 2010 a focal spot diameter of  $26.8 \pm 0.5 \mu\text{m} \times 31.4 \pm 0.8 \mu\text{m}$  was presented [39]. A major drawback of the Si(111)-H(1x1) mirror is the poor reflectivity of less than 1%. To overcome this limitation a novel Si(111) coating of quantum stabilized Pb of "magic" height (certain thicknesses are more energetically favored than others) was introduced by D. Farias, R. Miranda and co-workers [40]. In this way a reflectivity of ca. 15% could be achieved. Further improvements solved the problem of temperature stability of the surfaces which initially was limited up to only 250 K. Currently these Pb coated atom-optical mirrors give a stable

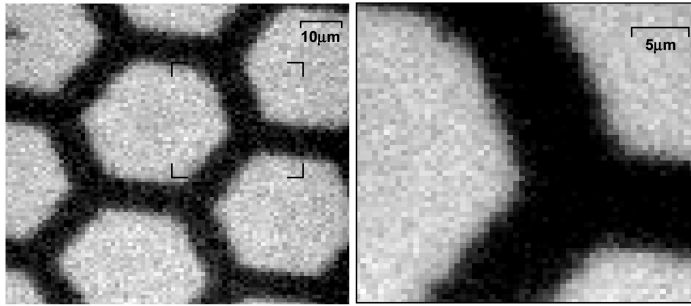


Figure 0.1: First 2D images obtained using a neutral helium atom beam to image a hexagonal copper grating. This pictures were obtained with a (top)  $3\ \mu\text{m}$  diameter and (bottom)  $2\ \mu\text{m}$  focused helium beam spot in a transmission imaging setup [34].

reflectivity over several weeks up to surface temperatures of 450 K (under UHV conditions) [41]. The initial mirrors were all made by coating Si(111) surfaces. The idea was that Si(111) wafers can be made very thin (down to 50 microns) so that the macroscopical mirror shape can be created with electrostatic bending. Performing the electrostatic bending with sufficient accuracy has proven a big obstacle and for the time being limits mirror focusing to the order of 20-30 microns. A new and even better approach has been presented very recently by Farias and coworkers. In a new paper they use graphene to coat a surface and a stable helium reflectivity of 20% is achieved [42, 43]. The monolayer surfaces proved to be stable up to 1150 K. This year saw a final major improvement when Farias and co-workers showed that the graphene monolayer can be grown also on a sapphire substrate which opens the possibility of creating a preshaped mirror by grinding a surface in advance and then simply coat it with graphene, thus avoiding electrostatic bending completely. This could be the crucial point favoring mirror focusing instead of zone plates. However, for the time being it is still not clear if it can be realized technically and so for this work a zone plate approach has been considered the most feasible and the one we used. The drawback of the zone plates is that they suffer chromatic aberrations. A discussion on the theoretical limitations is presented in [44].

Another mirror focusing approach which has to be mentioned here is the utilization of quantum reflection from concave microscopically rough quartz surfaces. One dimensional focal widths of below  $2\ \mu\text{m}$  were presented with such quantum reflection mirrors [45].

Focusing of a neutral helium beam with a zone plate approach was carried out for the first time in 1991 by Mlynek and co-workers [46]. The achieved focus had a FWHM of  $18 \pm 1 \mu\text{m}$ . Before this, atom diffraction had successfully been performed on freestanding microstructures [47, 48].

An experiment from 1999 presented by Grisenti and co-workers [49] obtained a diameter  $d \leq 2 \mu\text{m}$  focal spot. This major improvement was achieved utilizing a so called microskimmer (conical shaped aperture, see section 1.2.2) as the imaged object.

Several *Fresnel zone plate* focusing experiments were performed in our group during the last years and in 2008 our group was able to present the first microscopy images (in transmission mode) taken with neutral helium atoms [34]. The pictures are presented in figure 0.1. A  $540 \mu\text{m}$  diameter *Fresnel zone plate* [50, 51] was applied to focus a *helium* beam to a  $2 - 3 \mu\text{m}$  diameter probe beam spot. The focused probe beam was then scanned across a hexagonal copper grating with a period of  $36 \mu\text{m}$  and a rod thickness of  $8 \mu\text{m}$ . The recorded images were taken in transmission.

The most recent and very encouraging result for neutral atom microscopy was published earlier this year by Philip Witham and Erik Sánchez [52]. They presented the first He scattering reflection images obtained with a neutral atom microscope working by a principle analogous to pin hole optics. One of their images is presented in figure 0.2. With a simple setup consisting of a *free-jet source*, a *collimating* aperture, a mechanically scan-able sample setup and a *residual gas analyzer* implemented as a detector they managed to achieve images with resolutions of up to  $1.5 \mu\text{m}$ . However flow calculations show that this resolution is also close to the limit of the setup ( for a spot diameter smaller than  $500 \text{ nm}$  the intensity in the spot is at least an order of magnitude less than for our instrument). Hence a major improvement in resolution is not possible for this method without significant improvement in helium detection efficiency. Another problem is that the distance between source and sample needs to be very small (less than  $150 \text{ micron}$  ). But the results demonstrates beautifully the potential power of He-microscopy as a surface imaging technique.

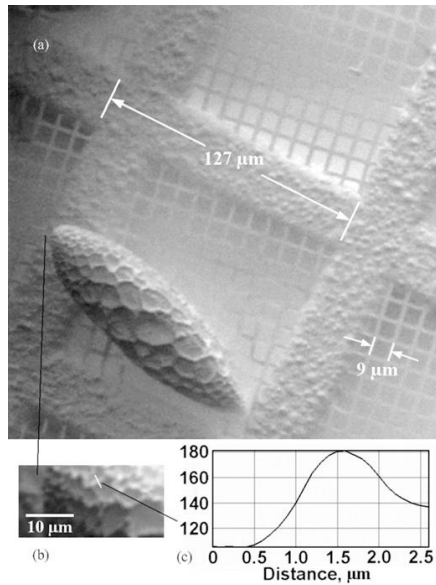


Figure 0.2: (a) He scattering image of an uncoated pollen grain on a Quantifoil™ TEM grid, back side. (b) Magnified area. (c) Line profile taken across linear features in (b), vertical units are gray-scale units, where 255 = white (max. He partial pressure) and 0 = black (min. pressure) published by Philip Witham and Erik Sànches earlier this year [52].

## 0.4 OVERVIEW OF THE THESIS

The aim of the work presented in this thesis has been the design of a *reflection neutral helium atom beam scanning microscope* with sub-micrometer resolution. A complete technical design is presented together with characterization measurements of *zone plates* demonstrating sub-micrometer focusing of a neutral helium beam for the first time.

The thesis is organized in the following way:

- Chapter 1 - NEMI

*Introducing "NEMI" presenting basic requirements, design considerations and parameters for building a "NEutral matter wave MIcroscope" as a new surface investigation tool.*

- Chapter 2 - Chapter 5

*Presents the detailed calculations determining the technical design parameters and physical limitations.*

- Chapter 6 - Chapter 7

*Presents the technical approach for designing, manufacturing and assembling of NEMI.*

- Chapter 8 - FIRST SUB-MICRON HELIUM FOCAL SPOT

*Presents the first experimental realization of a sub-micrometer neutral helium focal spot using zone plates. The results are presented in Paper A (Appendix A).*

- Chapter 9 - NEMI MEASUREMENTS

*Presents the first beam characterizing measurement results gained with the new microscope setup.*

- Chapter 10 - OUTLOOK

*Gives an outlook on the next assembling steps and future possibilities and applications for systems like NEMI.*

- Section B.1 - Section C.1

*The appendix includes Paper A, additional technical design drawings of some components, the specifications for the pressure measurement gauges as well as the detailed prevacuum calculations and a detailed explanation for the determination of the actual particle flight time  $t_f$  from TOF-measurements.*

## NEMI

---

### 1.1 GENERAL DESIGN CONSIDERATIONS

The idea, as presented in the introduction, is to build a *NEutral helium scattering Microscope (NEMI)* which provides the possibility to gain highly localized information about a sample surface. Since presently no 2D helium detectors exists, the basic setup was chosen to be similar to that of a SEM, creating an image by scanning a *focused beam of neutral helium atoms* across the sample.

The main components required to build a *neutral helium beam microscope* are

- *BEAM SOURCE (Nozzle)*
- *BEAM SHAPING ELEMENT ( Skimmer)*
- *OPTICAL ELEMENT (Zone Plate)*
- *DETECTION SYSTEM*

A sketch of the *Nemi* microscope presenting these main components is shown in figure 1.1. The optical element focuses the image of the beam shaping element (skimmer) onto the sample. The resolution is given by the size of the image, determined by the diameter of the skimmer and the demagnification factor  $b/g$ .

The final central issue to consider is the physical dimensions of NEMI. They were determined as follows: To enable enough space for the handling of the sample-detector arrangement, a minimum working distance of  $b = 205$  mm between the sample and the zone plate was defined. The diameter of the beam shaping element, the *skimmer (microskimmer)* is another predefined value. It is limited to  $d_{sk} = 1 - 3$   $\mu\text{m}$ . The smallest skimmers that have so far been tested and known to function are 1 micron in diameter, so this is taken as one parameter. In addition, to ensure higher intensity, a skimmer of 3 micron is picked. Giving the two parameters  $b$  and  $d_{sk}$ , the final distance  $g$  from skimmer to sample is now chosen so that we are sure to get an instrument which works

significantly better than an optical microscope. With this considerations a distance between *skimmer* and *zone plate* of  $g = 935\text{ mm}$  was chosen. The demagnification factor is  $M = 0.219$ .

The following sub-chapters present a short description of the components listed in the beginning. Further details and explanations can be found in the corresponding main chapters.

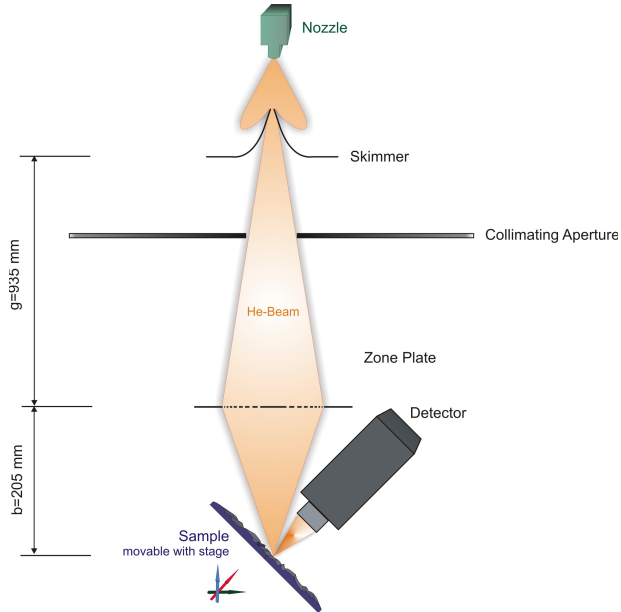


Figure 1.1: Schematic of the working principle illustrating the main components of the new *NEutral helium scattering MICROscope* named *Nemi*. The instrument is based on a *Nozzle* for the beam generation, a *Skimmer* for selecting the central part of the beam, a *Zone Plate* as an optical element for beam focusing, and a *Detection System* for detecting the helium beam atoms which are back-scattered from the sample surface.

Since *Nemi* is working with an uncharged helium atom probe beam, the possible techniques for manipulating the beam are limited. Therefore the image is generated by scanning the sample across the beam rather than the beam across the sample (fixed beam, moving stage setup).



## 1.2 MAIN COMPONENTS AND CONCEPTUAL LIMITATIONS

### 1.2.1 *Beam source*

The *source* principle is the same as used in any modern *helium atom scattering* (HAS) apparatus. To generate a probe beam consisting of *neutral helium atoms*, high pressure helium gas is expanded through a small nozzle aperture into a chamber with low-pressure ambient background conditions. The properties defining the source are the nozzle diameter  $d_N$ , the helium gas pressure  $p_o$  (further on also referred to as “source/beam pressure”), the nozzle temperature  $T_o$  and as a consequence of the last parameter the resulting final average velocity  $v_{He}$  of the helium atoms within the generated beam. Provided the right choice for these values, a so called “*free-jet expansion*” (often also referred to as *supersonic expansion* ) can be achieved, yielding a high intensity *free-jet* helium beam with a nearly monochromatic velocity distribution. As a boundary condition for such a *free-jet expansion* the nozzle pressure and the nozzle diameter have to be chosen so that the mean free path of the atoms in the helium gas becomes smaller than the nozzle pinhole diameter. Here are some technical limitations:

Commercially available helium gas bottles have a pressure of  $p_o = 200$  bar. A compressor can be used to reach higher pressures, but this can lead to clustering in the beam even at room temperatures. A long term stable pressure value of  $p_o = 180$  bar is a suitable value, which can be maintained for a long time using a standard helium bottle.

The smallest commercially available diameters for the implemented nozzle plate holes are  $5\ \mu\text{m}$  which is sufficiently small for this first approach of the microscope.

Details regarding the *free-jet expansions* and the helium flow parameters defining the probe beam are presented in chapters 2 and 3 respectively.

### 1.2.2 *Skimmer*

As beam shaping element a so called “*skimmer*” is implemented. From experience and calculations it is known that an about 10 to 15 mm *skimmer-nozzle* distance is an optimum value. At this point the helium atoms propagate on

straight trajectories without any further collisions. From the skimmer onwards the helium atoms are assumed to be subject to molecular flow conditions.

A *skimmer* is a conical shaped aperture with a small orifice diameter at its source facing side. It is also the separating element between the source chamber and its neighboring ultra high vacuum chamber (see figure 2.16) and therefore the system is working as a differential pumping stage. Hence it provides a first reduction of the helium background in the beam line, which is originating from the high helium flow within the source chamber. An additional function of this element is the fact that it confines the helium beam. All the atoms with trajectories strongly deviating from the central beam line will not pass through the small skimmer orifice but rather be diverted by the conical skimmer shape. Subsequently they are pumped out of the source chamber without further interference with the beam. The size of the skimmer orifice diameter will have an influence on the final focus size, since the skimmer is restricting the spatial intensity distribution of the free-jet expansion source. In reality the free-jet expansion is not a point source. Its spatial intensity distribution (also called virtual source) depends on the nozzle diameter, the source pressure and the source temperature. In the case of small skimmer diameters (compared to the nozzle diameter and consequently also to the virtual source size) the skimmer orifice restricts the spatial distribution of the free-jet expansion. This is a necessary requirement to achieve small focal spot diameters of the helium beam since the skimmer diameter in that case represents the object size which is imaged by the focusing zone plate. Therefore *microskimmers* [53] are utilized in *Nemi*. This is discussed in more detail in chapter 4.

### 1.2.3 Atom optical element

When it comes to focusing a beam of neutral atoms or molecules, there are just classical optical elements to accomplish this task as discussed in the introduction. Since the particles are uncharged, magnetic or electric field manipulation is not possible. The atom beam has to be manipulated via its de Broglie wavelength. These atom optical focusing elements are based on the principle of atom (molecule) diffraction/reflection on elements structured with nanometer precision. This high precision is necessary since the wavelength of the matter waves lies in or even below the Ångström regime. As discussed in the introduction, there are still several technical limitations with the mirrors,

and therefor we use a Fresnel zone plate.

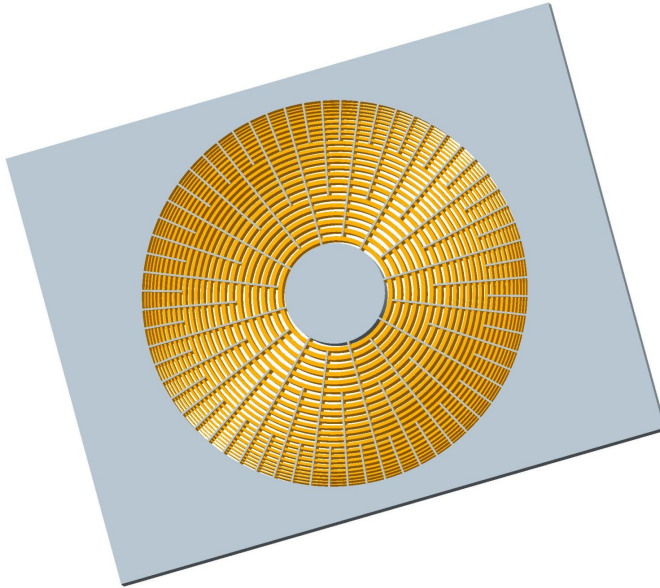


Figure 1.2: Sketch of a FRESNEL *zone plate* element similar to the ones used in NEMI. The orange highlighted ring system structure represents the FRESNEL zones, whereas the gray disc in the middle and the gray rod structures orientated in radial direction represents the so called middle stop disc and the supporting grid structure for holding the ring system in place. The middle stop disc acts as a blocking element for the main part of the zero order fraction (not diffracted) of the beam. A more detailed description of these functions can be found in chapter 4.

A FRESNEL *zone plate* (ZP) is a circular diffraction grating consisting of a system of free standing rings, so called "*Fresnel zones*", with decreasing lattice constant for increasing radii (see figure 1.2). The structure of this pattern will vary for a given focal length depending on the de BROGLIE wavelength of the helium atom probe beam. In the measurements presented in section 8, we could show that they deliver very stable focus spot sizes below  $1\ \mu\text{m}$  diameter and at the same time still provide a reasonable, high enough beam intensity within the focal spot close to what would be expected from theory [54]. The theoretical limitation for the minimal focal spot diameter achievable with this elements is primarily determined by the chromatic aberration effects [44].

#### 1.2.4 Detection system

There are basically three main techniques for detecting neutral helium atoms, (1) ionization detectors [55], (2) laser-based detectors [56] and (3) accommodation and accumulation detectors [57]. The first one is based on ionizing the neutral helium atoms and subsequently mass selecting the helium-ions and counting them in an ion-detector (channeltron) [58, 55]. The second type is applied for spectroscopic detection of atomic and molecular species (state selective detection). If there is no need to do time-resolved analysis, *time of flight* (TOF) measurements, it is possible to simply utilize an accumulation based detection system. This can be done by using a sensitive pressure measurement gauge to deduce the helium intensity from a pressure increase  $\Delta p$  in a small accumulation volume (a so called PITOT TUBE). The PITOT TUBE approach has been chosen for NEMI, because it is simple and easy to implement. This tube has a small (ca. 0.5 – 1 mm ) entrance pinhole aperture (low-conductivity channel). When the entering beam flow is equal to the effusive flow back out of the small pinhole aperture an equilibrium pressure can be measured. The pressure rise in this equilibrium pressure can be taken as a measure for the reflected beam intensity. For more details see chapter 5.

This method has the disadvantage that there is the need of a very low background pressure surrounding the sample (low  $\times 10^{-9}$  mbar range), to gain enough sensitivity for the pressure measurement with the *cold-cathode ionization* gauge. On the other hand it has the big advantage that it can be easily implemented into the system.

### 1.3 FINAL DESIGN PARAMETERS

Table 1.1 contains the final design parameters for NEMI. A principle diagram of the instrument with the main components can be found in figure 1.1, and 1.3. The decisions for choosing these parameters, is outlined above and discussed in details in the chapters 2, 3, 4, 5 and 6. The best expected resolution that can be achieved with these parameters is 380 nm.

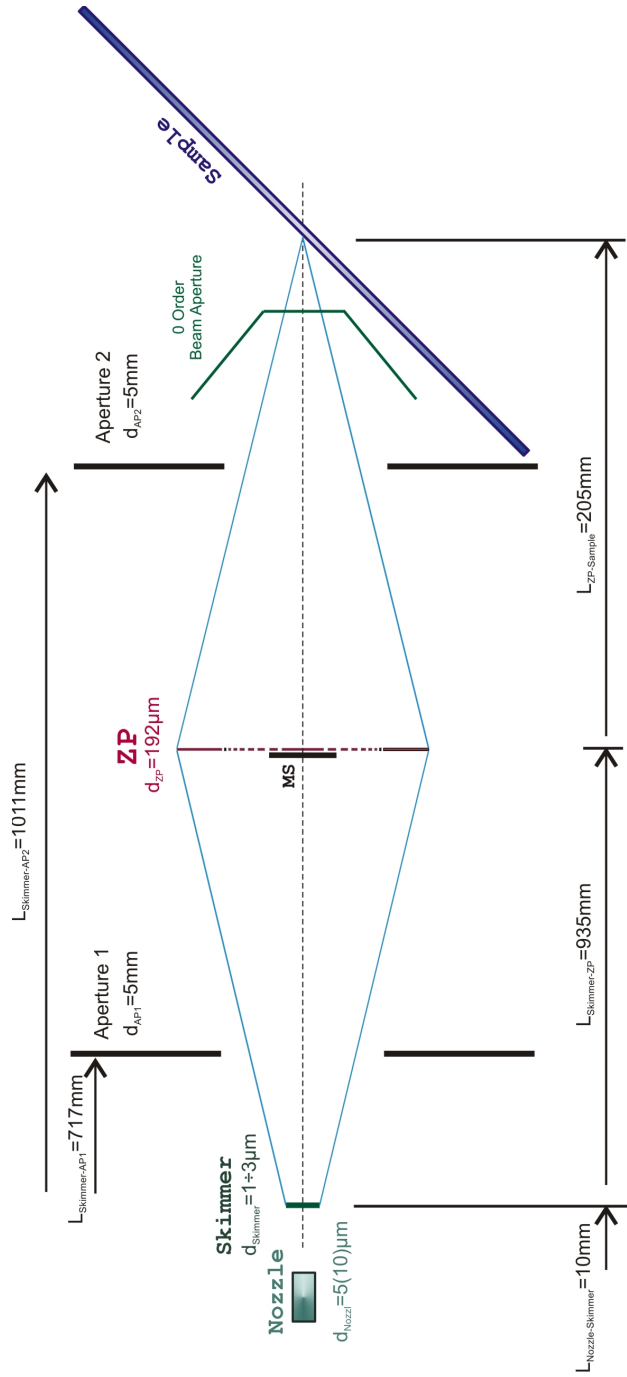


Figure 1.3: Diagram of the helium microscope with the main distances and dimensions.

ATOM OPTICAL PARAMETERS OF NEMI	
$v_{He} = 1823$ [m/s] ( $T_N = 320$ K)	$v_{He} = 1019$ [m/s] ( $T_N = 100$ K)
$\lambda_{He_{RT}} = 0.5469$ [Å]	$\lambda_{He_{LN}} = 0.9782$ [Å]
$d_{ZP} = 192$ [μm]	
$f = 168.14$ [mm]	
$g = 935$ [mm]	
$b = 205$ [mm]	
$M = 0,219$	
$d_{Sk} = 1$ [μm]/3 [μm]	
$d_N = 5(10)$ [μm]	
$d_{AP1} = 5$ [mm]	$d_{AP2} = 5$ [mm]
$d_{th} = 1.43$ [μm]/1.56 [μm]	$d_{th} = 0.38$ [μm]/0.73 [μm]

Table 1.1: Atom optical parameters and dimensions for the *neutral helium atom scattering microscope* NEMI based on the considerations in the chapters 2, 3, 4, 5 and 6.  $v_{He}$  final average He-atom velocity,  $\lambda_{He}$  mean He-beam de Broglie wavelength,  $d_{ZP}$  zone plate diameter,  $f$  zone plate focal length,  $g$  object distance (skimmer-ZP),  $b$  image distance (ZP-sample),  $M$  demagnification factor,  $d_{Sk}$  microskimmer orifice diameter,  $d_N$  nozzle diameter,  $d_{AP1}$  &  $d_{AP2}$  aperture diameter at the PST/ZPC connection and the ZPC/SDC connection and  $d_{th}$  theoretically expected focus spot diameter (limited by the chromatic aberration of the ZPs) for the two different nozzle temperatures  $T_N$ . The best expected resolution for the present setup is 380 nm.

## HELIUM FLOW CALCULATION

---

*One of the first issues in this project was the calculation of the helium-atom-flow rate within the system. In other words: “is it possible at all to build an instrument with the desired resolution, and still get enough signal at the detector?” Based on the parameters of the new instrument: nozzle and skimmer diameter of the source, the zone plate characteristics defining the focusing of the beam and the efficiency of the detection system, an evaluation of the expected helium count rate was made.*

*Furthermore the partial pressure increase in the Ultra High Vacuum (UHV) chambers and the backing vacuum system due to the helium flow has to be considered for the design of the pumping system layout. All the considerations and evaluations in respect to these points will be presented in this chapter. For simplicity the final design is presented in the calculations and it is shown that it fulfills the requirements.*

### 2.1 HE-BEAM FLOW RATE CALCULATION

The following evaluation of the particle flow within the HELIUM microscope, and the corresponding expected helium count-rates, is based on the work of DAVID R. MILLER [59] and BJØRN SAMELIN [58], as well as the literature presented in [60, 61, 62]. All calculations are made with the assumption that there is a *free-jet helium* beam created by a *free-jet expansion*. This means a neutral beam of helium atoms, extracted from a high-pressure gas source expands into a low-pressure ambient background. A more detailed principle description of this *free-jet expansion* is presented in chapter 3. For simplification, collisions of the beam atoms with the background gas are ignored. This assumption is reasonable since the mean free path for helium atoms in the *ultra high vacuum (UHV)* range ( $p < 1 \cdot 10^{-7}$  mbar) is around  $\sim 1.8$  km (see section D.1). Hence the probability for any particle collisions between the beam particles and background gas in the chamber is very low.

In general the particle flow  $\dot{N}$  which enters the detection system can be described as follows:

$$\dot{N} = \dot{N}_o(x) \cdot T_{ZP} \cdot R_{sample} \quad (2.1)$$

It is composed of three components. The first component  $\dot{N}_o(x)$  describes the particle flow in the *helium beam* at the position ( $x$ ) where the transmissive focusing element, the *zone plate (ZP)* is located (i.e. impinging flow onto the ZP). The second factor  $T_{ZP}$  gives the transmissivity of the zone plate, and the last factor  $R_{sample}$  provides a measure for the final amount of particles entering the detector. It combines an estimate for the reflectivity of the investigated sample surface with the expected entrance probability into the detector tube. In the following these three shares, which are building up the final particle amount entering the detection system, will be considered independently.

### 2.1.1 Particle flow $\dot{N}_o(x)$ at a position $x$ along the beam direction

MILLER [59] states that the ideal free-jet center-line intensity per steradian  $I_{str}$  can be described by the nozzle flow rate  $\dot{N}$  and a peaking factor  $\kappa$ . This leads to the following three equations.

$$I_{str} = \kappa \cdot \dot{N} \cdot \pi^{-1} \text{ [molecules/s} \cdot \text{sr]} \quad (2.2)$$

$$\dot{N} = F(\gamma) \cdot n_o \cdot \sqrt{\frac{2kT_o}{m}} \cdot \left(\frac{\pi d_N^2}{4}\right) \quad (2.3)$$

$$F(\gamma) = \left(\frac{\gamma}{\gamma+1}\right)^{1/2} \cdot \left(\frac{2}{\gamma+1}\right)^{\frac{1}{\gamma-1}} \quad (2.4)$$

with  $n_o$  the particle density before the nozzle expansion,  $k$  the BOLTZMANN constant,  $T_o$  the nozzle temperature [K],  $m$  the mass of the expanding gas (atoms),  $d_N$  the nozzle diameter,  $\kappa$  the peaking factor  $\kappa = 1.98$  (see [59]) and  $\gamma$  the heat capacity ratio or adiabatic index <sup>1</sup>.

The variable  $n(x)$  defines the particle density at the given distance  $x$  from the nozzle along the beam central line, and  $\dot{N}_o(x)$  is the corresponding particle

<sup>1</sup>  $\gamma = \frac{c_p}{c_v} = \frac{f+2}{f}$ , with  $f$  the ideal gas related degrees of freedom  $\Rightarrow \gamma_{He} = \frac{5}{3}$



flow. For simplification just the center-line intensities are considered for the beam flow. This intensity close to the center-line is:

$$I_{str} = \frac{\partial \dot{N}_o}{\partial \Omega} \Big|_{\Omega=0}, \quad \dot{N}_o = \Delta \Omega \cdot \frac{\partial \dot{N}_o}{\partial \Omega} \quad (2.5)$$

with the solid angle  $\Delta \Omega$  defined by the opening surface  $A$  at the distance  $x$ .

$$\Delta \Omega = \frac{A}{x^2} \quad (2.6)$$

Combining equations 2.2 - 2.6, the particle flow at the position  $x$  can be written as

$$\dot{N}_o = \Delta \Omega \cdot I_{str} = \frac{A}{x^2} \cdot \kappa \cdot \frac{1}{4} \cdot F(\gamma) \cdot n_o \cdot \sqrt{\frac{2kT_o}{m}} \cdot d_N^2 \quad (2.7)$$

Since the velocity spread of a free-jet beam is sufficiently small, the particle flow density  $j(x)$  can be described as the product of the density  $n(x)$  times the beam particles average velocity  $v$ .

$$j(x) = \frac{\dot{N}_o}{A} = n(x) \cdot v \Rightarrow n(x) = \frac{\dot{N}_o}{A \cdot v} \quad (2.8)$$

With the beam velocity (final average velocity) for *helium* given by  $v_{He} = \sqrt{\frac{5 \cdot k \cdot T_o}{m_{He}}}$  (see chapter 3.4), and equation 2.7,  $n(x)$  is found to be

$$n(x) = \frac{1}{4} \cdot \left( \frac{d_N}{x} \right)^2 \cdot \kappa \cdot F(\gamma) \cdot n_o \cdot \sqrt{\frac{2}{5}} = 0.16075 \cdot n_o \cdot \left( \frac{d_N}{x} \right)^2 \quad (2.9)$$

Hence the particle flow for a *helium* beam at the distance  $x$  along the beam center-line is given by:

$$\dot{N}_o(x) = n(x) \cdot v_{He} \cdot A \quad (2.10)$$

### 2.1.2 Particle flow at the ZONE PLATE position

With the above stated equation 2.10 one can determine the particle flow of He atoms impinging on the focusing ZONE PLATE. A sketch of the main microscope parameters is shown in figure 1.3.

To calculate  $\dot{N}_o(x)$  at the *zone plate*, the three parameters representing the right side of equation 2.10 have to be determined.

$$A_{ZP} = r_{zp}^2 \cdot \pi = \frac{d_{zp}^2 \pi}{4} \quad (2.11)$$

$$v_{He} = \sqrt{\frac{5kT_o}{m_{he}}} \quad (2.12)$$

$$n(x) = 0.16 \cdot n_o \cdot \left(\frac{d_N}{x}\right)^2 \quad (2.13)$$

#### 2.1.2.1 Penetrable surface at the ZONE PLATE

$$A_{ZP} = r_{zp}^2 \cdot \pi = \frac{d_{zp}^2 \pi}{4} \quad (2.14)$$

A detailed description of the *zone plates* used for NEMI can be found in chapter 4. The outer ring diameter of this ZPs is given by  $d_{zp} = 192 \mu\text{m}$ . As figure 1.3 indicates, a beam blocking *middle-stop* disc is placed in the center of this ZPs. The batch of ZPs fabricated for NEMI have two different possible central blocking disc diameters,  $d_{MS20\mu\text{m}} = 20 \mu\text{m}$  and  $d_{MS50\mu\text{m}} = 50 \mu\text{m}$  respectively. The corresponding numbers for the penetrable-surfaces  $A_{ZP}$  of the two different kinds of NEMI ZPs are presented in table 2.1.

MIDDLE-STOP DIAMETER $d_{MS}$ [ $\mu\text{m}$ ]	PENETRABLE SURFACE $A_{ZP}$ [ $\text{m}^2$ ]
20	$2,864 \cdot 10^{-8}$
50	$2,699 \cdot 10^{-8}$

Table 2.1: Beam penetrable surface on the *zone plates*. All of them have an outer diameter of  $d_{zp} = 192 \mu\text{m}$ .

#### 2.1.2.2 He-particle velocity $v_{he}$

$$v_{He} = \sqrt{\frac{5kT_o}{m_{he}}} \quad (2.15)$$

As equation 2.15 indicates, the final average velocity of the *helium* atoms depends on the atoms thermal energy defined by the temperature of the nozzle (see section 3.4). For this evaluation two different cases are of interest, a room temperature beam  $T_{RT} = 300 \text{ K}$ , and a liquid nitrogen cooled beam with a temperature of approximately  $T_{LN} = 100 \text{ K}$ . The calculated numbers for these two cases, as well as the parameters needed to calculate them, are shown in

table 2.2. A graph representing the helium atom speed characteristic versus the nozzle temperature is shown in figure 2.1.

FINAL AVERAGE BEAM VELOCITY $v_{He}$
Boltzmann constant $k = 1,38065 \cdot 10^{-23} \text{ J/K}$
mass helium $m_{He} = 6,646 \cdot 10^{-27} \text{ kg}$
mean velocity RT $v_{He_{RT}} = 1765 \text{ m/s}$ ( $\hat{=} \lambda \approx 0,565 \text{ \AA}$ )
mean velocity LN $v_{He_{LN}} = 1019 \text{ m/s}$ ( $\hat{=} \lambda \approx 0,978 \text{ \AA}$ )

Table 2.2: Final average velocity  $v_{He}$  for the two different cases of a room temperature (RT), and a liquid nitrogen cooled beam (LN) respectively. Also presented here are the required constants to calculate these values.  $\lambda$  hereby states the corresponding *de Broglie* wavelength for the helium atom beam (see section 4.3)

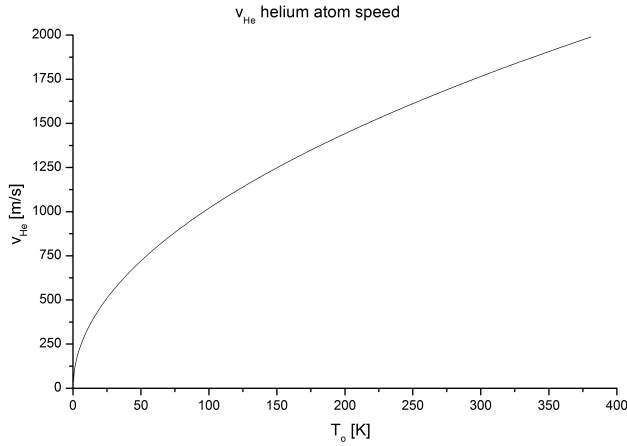


Figure 2.1:  $v_{He}$  final average speed of the helium atoms depending on the nozzle temperature  $T_0$ .

### 2.1.2.3 Beam particle density $n(x)$ at the ZP

To calculate the beam particle density at the ZP (e.q. 2.13), first a determination of the particle flow quitting at the nozzle has to be made. This value is gained by the help of the ideal gas law:

$$n_0 = \frac{N_0}{V_0} = \frac{p_0}{k \cdot T_0} \quad (2.16)$$

The parameters used for the particle density determination are stated in table 2.3. The geometrical dimensions of the setup can be seen in figure 1.3. The characteristics of the particle density at the *nozzle* as well as of the particle density impinging on the *zone plate* are presented in figures 2.2, 2.3, 2.4 and 2.5. The source (nozzle) pressure for all these evaluations was set to  $p_0 = 180$  bar, except for the graph presented in figure 2.3, where this parameter is varied.

PARTICLE DENSITY $n(x)$ AT THE ZP (POSITION $x$ )				
[m <sup>3</sup> ]				
	$n_0$	$d_{N_1} = 3 \mu\text{m}$	$d_{N_2} = 5 \mu\text{m}$	$d_{N_3} = 10 \mu\text{m}$
$T_0 = 300$ K	$4,345 \cdot 10^{27}$	$7,0075 \cdot 10^{15}$	$1,9465 \cdot 10^{16}$	$7,7861 \cdot 10^{16}$
$T_0 = 100$ K	$1,303 \cdot 10^{28}$	$2,1022 \cdot 10^{16}$	$5,8396 \cdot 10^{16}$	$23,358 \cdot 10^{16}$

Table 2.3: Particle density of the He-beam at the nozzle ( $n_0$ ) as well as at the ZP ( $n(x)$ ) placed at the distance  $x = L_{\text{Nozz-ZP}} = 0,945$  m from the nozzle along the beam line. The numbers are calculated for a source pressure of  $p_0 = 180$  bar, and the different nozzle diameters of  $d_{N_1} = 3 \mu\text{m}$ ,  $d_{N_2} = 5 \mu\text{m}$  and  $d_{N_3} = 10 \mu\text{m}$  respectively.

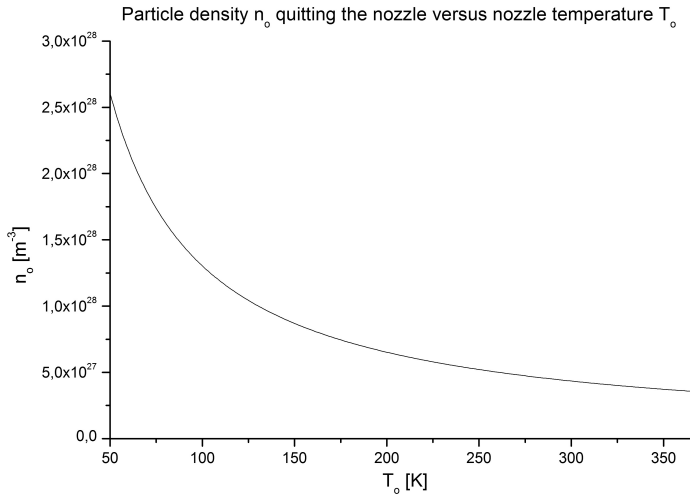


Figure 2.2: Particle density  $n_0$  entering the source chamber (SC) directly at the nozzle versus the nozzle temperature  $T_0$  for a nozzle pressure of  $p_0 = 180$  [bar].

As figure 2.3 indicates, a decrease of the nozzle temperature  $T_0$  and hence a decrease of the kinetic energy assigned to the atoms, will lead to a higher

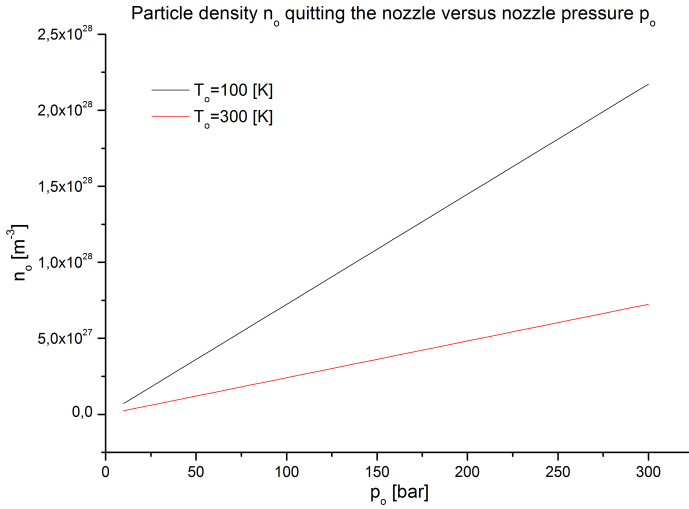


Figure 2.3: Particle density  $n_o$  entering the source chamber (SC) directly at the nozzle versus the nozzle pressure  $p_o$  for a nozzle temperature of  $T_o = 100$  [K] and  $T_o = 300$  [K] respectively.

particle density  $n_o$  leaving the source. Consequently a nozzle temperature as low as possible would be desired. On the other hand the helium atoms will start to cluster if the temperature falls below a certain limit [63]. Also technical and financial effort makes it currently unreasonable to implement a complex cooling system. Therefore it was decided to design the system to work either with a roughly room temperature beam or cooled down to approx. 100 K.

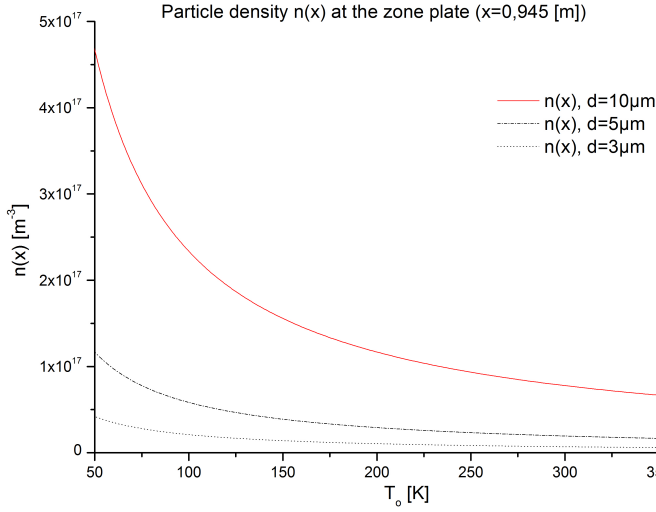


Figure 2.4: Particle density  $n(x)$  at the *zone plate* position  $x = 0.945$  [m] over the nozzle temperature  $T_o$  at a nozzle pressure  $p_o = 180$  [bar] for varying nozzle diameters.

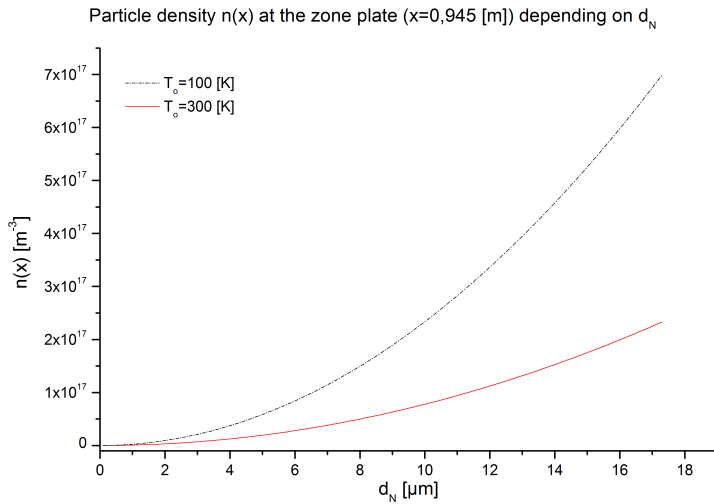


Figure 2.5: Particle density  $n(x)$  at the *zone plate* position  $x = 0.945$  [m] over the nozzle diameter  $d_N$  for the two different nozzle temperatures  $T_o = 300$  K and  $T_o = 100$  K at a pressure of  $p_o = 180$  [bar].

## 2.1.2.4 Particle flow hitting the ZP

Finally together with equation 2.10 the theoretical *particle flow*  $\dot{N}_o(x)$  *impacting onto the ZP* can be determined. The calculated values for different sets of setup parameters are presented in the tables 2.4, 2.5 and in figure 2.6 for the two different ZPs with the beam blocking disc diameters of 20  $\mu\text{m}$  and 50  $\mu\text{m}$  respectively.

PARTICLE FLOW $\dot{N}_o(x)$ IMPACTING ONTO THE ZONE PLATE WITH $d_{MS} = 20 \mu\text{m}$			
[s <sup>-1</sup> ]			
	$d_{N_1} = 3 \mu\text{m}$	$d_{N_2} = 5 \mu\text{m}$	$d_{N_3} = 10 \mu\text{m}$
$T_o = 300 \text{ K}$	$3,5423 \cdot 10^{11}$	$9,8399 \cdot 10^{11}$	$3,9359 \cdot 10^{12}$
$T_o = 100 \text{ K}$	$6,1355 \cdot 10^{11}$	$1,7043 \cdot 10^{12}$	$6,8173 \cdot 10^{12}$

Table 2.4: Calculated He-particle flow  $\dot{N}_o(x)$  impacting on the ZP with a *middle-stop* diameter of  $d_{MS} = 20 \mu\text{m}$ . The corresponding penetrable zone plate surface is  $A_{zP_{MS}(20\mu\text{m})} = 2,864 \cdot 10^{-8} \text{ m}^2$ , and the nozzle pressure is set to  $p_o = 180 \text{ bar}$ . Values for the three different nozzle diameters of  $d_{N_1} = 3 \mu\text{m}$ ,  $d_{N_2} = 5 \mu\text{m}$  and  $d_{N_3} = 10 \mu\text{m}$  are presented at the two different nozzle temperature conditions of  $T_o = 300 \text{ K}$  and  $T_o = 100 \text{ K}$  respectively.

PARTICLE FLOW $\dot{N}_o(x)$ IMPACTING ONTO THE ZONE PLATE $d_{MS} = 50 \mu\text{m}$			
[s <sup>-1</sup> ]			
	$d_{N_1} = 3 \mu\text{m}$	$d_{N_2} = 5 \mu\text{m}$	$d_{N_3} = 10 \mu\text{m}$
$T_o = 300 \text{ K}$	$3,3383 \cdot 10^{11}$	$9,2732 \cdot 10^{11}$	$3,7093 \cdot 10^{12}$
$T_o = 100 \text{ K}$	$5,7822 \cdot 10^{11}$	$1,6061 \cdot 10^{12}$	$6,4247 \cdot 10^{12}$

Table 2.5: Calculated He-particle flow  $\dot{N}_o(x)$  impacting on the ZP with a *middle-stop* diameter of  $d_{MS} = 50 \mu\text{m}$ . The corresponding penetrable zone plate surface is  $A_{zP_{MS}(50\mu\text{m})} = 2,699 \cdot 10^{-8} \text{ m}^2$ , and the nozzle pressure is set to  $p_o = 180 \text{ bar}$ . Values for the three different nozzle diameters of  $d_{N_1} = 3 \mu\text{m}$ ,  $d_{N_2} = 5 \mu\text{m}$  and  $d_{N_3} = 10 \mu\text{m}$  are presented at the two different nozzle temperature conditions of  $T_o = 300 \text{ K}$  and  $T_o = 100 \text{ K}$  respectively.

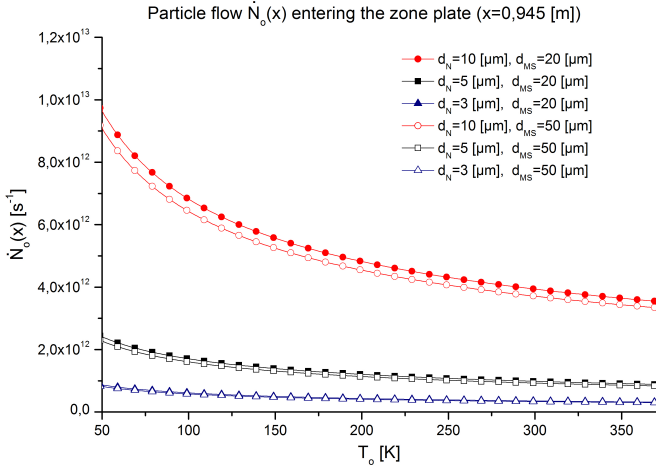


Figure 2.6: Particle flow  $\dot{N}_o(x)$  impinging on the zone plate surface  $A_{zp}$  over the nozzle temperature  $T_o$  with the three different nozzle diameters of  $d_N = 3$   $\mu\text{m}$ ,  $d_N = 5$   $\mu\text{m}$  and  $d_N = 10$   $\mu\text{m}$  presented for the two different zone plates with the middle stop diameters (blocking disc) of  $d_{MS} = 20$   $\mu\text{m}$  and  $d_{MS} = 50$   $\mu\text{m}$  respectively

### 2.1.3 Losses due to diffraction process at the ZP ( $T_{ZP}$ )

As a next step the *transmissivity* of the *zone plates* has to be taken into account. Theoretically it is expected that 10.1% of the beam enter into the first order focus [64] but the area of the support rods has to be subtracted.

Preliminary investigation on the transmissivity of similar ZPs [54, 65] show that the actual transmissivity is  $T_{ZP} = 0.08$ . This is slightly less than expected.

### 2.1.4 Reflection at the sample

The last factor influencing  $\dot{N}$  in equation 2.1,  $R_{sample}$  presents the *reflectivity of the sample* as well as the probability of the reflected *helium* atoms to enter into the detector. The total reflectivity of a sample will always be 100% since the helium does not stick to the surface. The amount of atoms which are collected by the detector is depending on different parameters: The first major distinction is between crystalline and non-crystalline surfaces. For simplicity we assume below that this corresponds to pure specular reflection without



any loss to diffraction peaks. This will hold for metal surfaces, but not for insulators, where a loss through diffraction peaks can be expected.

- if the investigated surface is crystalline, yielding no diffraction peaks, big compared to the focal spot size, and the surface normal of the sample is in the middle of the detector opening all reflected atoms will reach the detector  $\Rightarrow R_{sample} = 1$ .
- if the investigated surface is crystalline, yielding no diffraction peaks, big compared to the focal spot size, and the surface normal of the sample is tilted compared to the center-line of the detector opening only some amount of the reflected atoms are detected, depending on the tilt angle of the surface  $\Rightarrow R_{sample} < 1$ .
- if the investigated sample is not crystalline, the atoms will scatter diffusely and less than 100% of the reflected atoms are collected, regardless of the orientation of the surface normal  $\Rightarrow R_{sample} < 1$

A conservative estimate for the detected intensity from a non-crystalline sample can be described by assuming that the sample is perfectly rough on the atomic scale (diffuse scattering). With a reflectivity corresponding to a  $180^\circ$  cosine intensity distribution (see figure 2.7). The corresponding surface area is given by a half sphere:

$$A_S = \frac{1}{2} \cdot 4 \cdot \pi \cdot R^2$$

The detector aperture with a diameter of  $d_D$  placed at a distance  $l$  from the

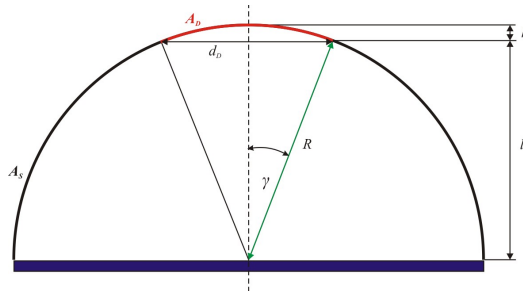


Figure 2.7: Cosine distribution of the reflection intensities for a diffuse scattering sample, illustrating the geometrical relation for the surface area of a spherical cap.

sample surface is cutting out a solid angle ( $\gamma$ ) of this spherical distribution. The corresponding surface area  $A_D$  of the spherical cap (see figure 2.7) is given by:

$$A_D = \pi \cdot (r^2 + h^2) \quad (2.17)$$

with

$$\begin{aligned} r &= d_D/2 \\ l &= \sqrt{R^2 - r^2} \\ h &= R - l \\ R &= \sqrt{r^2 + l^2} \end{aligned}$$

This leads to:

$$R_{sample} = \frac{A_D}{A_S} \quad (2.18)$$

A graph representing the calculated  $R_{sample}$  values for varying sample-detector distances  $l$  is shown in figure 2.18. For example for a detector aperture

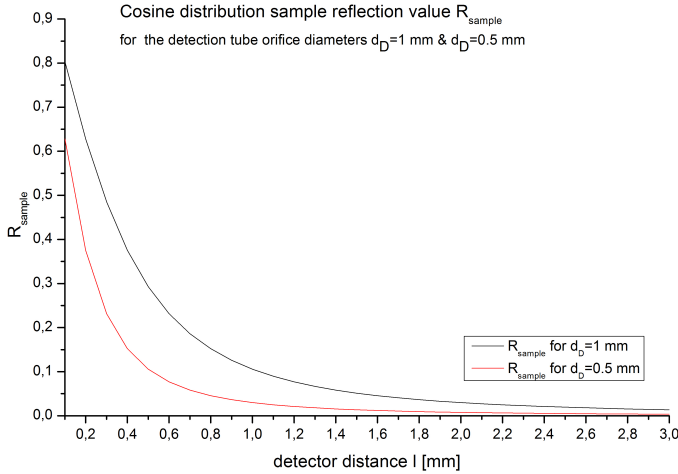


Figure 2.8:  $R_{ssample}$  for varying sample-detector distances  $l$  presented for a assumed cosine distribution of the reflection.

diameter  $d_D = 1$  mm and a sample-detector distance  $l = 1$  mm, the fraction entering the detector is  $R_{sample} = 0.105$ .

The case above is an extreme case. In practice the scattering profile for a sample will be material dependent and can vary strongly between different materials. For example if the surface exhibits the properties of an *Lambertian diffuser* the reflectivity will correspond to a cosine squared distribution perpendicular to the sample normal and hence the reflectivity factor  $R_{sample}$  is higher than calculated above [66]. It will be part of the further development work to determine the scattering profiles for various materials and to determine in detail the contrast properties of NEMI.

#### 2.1.5 Comparison of determined helium flow values $\dot{N}_R$ entering the detection system

Several different variations and combinations of  $\dot{N}_o(x)$ ,  $T_{ZP}$  and  $R_{sample}$  are listed in table 2.6. The worst case flow rate comes from a room temperature beam generated by a  $d_N = 3 \mu\text{m}$  nozzle using a middle-stop  $d_{MS} = 50 \mu\text{m}$  ZP.

#### 2.1.6 Pressure increase in the PITOT TUBE detector

This section will provide the determination of the expected pressure increase in the PITOT TUBE, utilized as a He-detector for the NEMI system. This pressure rise can be related to the amount of He-atoms entering the tube through its small aperture opening. The working principle of this setup is presented in detail in chapter 5.

The principle idea behind this method is the formation of an equilibrium state between the sample chamber and the *pitot tube* volume, expressing itself by a pressure difference between the sample chamber pressure and the pressure in the detection tube. Since the scattered beam particles enter the tube with a preferential forward direction, the vacuum conductance factor can be neglected for this case. It is assumed that the whole beam flow simply passes through without being affected by the pin hole barrier. For the He-atoms flowing out of the tube due to the pumping via the pinhole aperture, the vacuum conductance factor is strongly influenced by the diameter of the pinhole, since the atoms don't have a preferential forward direction any more. At some point an equilibrium state between the *in-* and *out-*flow for the tube will arise.

$$Q_{Beam} = Q_T \quad (2.19)$$

PARTICLE FLOW $\dot{N}_R$ ENTERING THE DETECTION SYSTEM			
[s <sup>-1</sup> ]			
	$\dot{N}_o(x)$	$\dot{N}_{R10\%}$ ( $R_{sample} = 0.1$ )	$\dot{N}_{R80\%}$ ( $R_{sample} = 0.8$ )
$d_{N_1} = 3 \mu\text{m}, d_{MS} = 50 \mu\text{m}, T_o = 300 \text{ K}$	$3.3383 \cdot 10^{11}$	$2.6706 \cdot 10^9$	$2.1366 \cdot 10^{10}$
$d_{N_1} = 3 \mu\text{m}, d_{MS} = 50 \mu\text{m}, T_o = 100 \text{ K}$	$5.7822 \cdot 10^{11}$	$4.6257 \cdot 10^9$	$3.7006 \cdot 10^{10}$
$d_{N_2} = 5 \mu\text{m}, d_{MS} = 20 \mu\text{m}, T_o = 300 \text{ K}$	$9.8399 \cdot 10^{11}$	$7.8719 \cdot 10^9$	$6.2976 \cdot 10^{10}$
$d_{N_2} = 5 \mu\text{m}, d_{MS} = 20 \mu\text{m}, T_o = 100 \text{ K}$	$1.7043 \cdot 10^{12}$	$1.3634 \cdot 10^{10}$	$1.0908 \cdot 10^{11}$

Table 2.6: Determined He-particle flow  $\dot{N}_R$  into the detection system following equation 2.1. For different zone plate middle-stop diameters  $d_{MS}$ , varying nozzle diameters of  $d_{N_1} = 3 \mu\text{m}$  and  $d_{N_2} = 5 \mu\text{m}$  and the two different nozzle temperature conditions of  $T_o = 300 \text{ K}$  and  $T_o = 100 \text{ K}$  respectively. The nozzle pressure is set to  $p_o = 180 \text{ bar}$ . The transmissivity of the ZPs is given by  $T_{ZP} = 0.08$  whereas the sample reflectivity again is varied for the two different values of  $R_{sample} = 0.1$  and  $0.8$  respectively.

with  $Q_T$  the particle flow back-out (*out-flow*) from the PITOT TUBE and  $Q_{Beam}$  the beam flow into the tube (*in-flow*).

At this equilibrium state there will be an increase of the pressure  $p_T$  within the *pitot tube*, compared to the pressure in the sample chamber  $p_{SDC}$ . This value is a measure for the number of particles entering the detector itself. To determine the expected pressure increase within the detector tube, the following equations and considerations can be applied.

Together with the IDEAL GAS LAW (eq.2.24, and eq. 2.35) one can find:

$$Q_T = L(p_T - p_{SC}) = \frac{\Delta N}{\Delta t} \cdot k \cdot T = \dot{N} \cdot k \cdot T \quad (2.20)$$

$$\dot{N} = \frac{L(p_T - p_{SC})}{k \cdot T} \quad (2.21)$$

$$p_T = p_{SDC} + \frac{\dot{N} \cdot k \cdot T}{L} \quad (2.22)$$

with  $\dot{N}$  the particle-flow-throughput (2.26), and  $T$  the sample-chamber/PITOT-TUBE temperature (RT).

$L$  is the vacuum conductance factor for the pin hole aperture between the sample chamber and the tube for molecular flow conditions (see D.1), and is defined as:

$$L = \frac{\bar{c}}{4} \cdot A \quad \bar{c} = \sqrt{\frac{8kT}{\pi m_{He}}} \quad (2.23)$$

Where  $A$  stands for the pin hole surface and  $\bar{c}$  for the average (mean) velocity of the gas particles [61, 62]. It has to be mentioned that all this considerations just apply for the boundary condition of a constant and equal temperature  $T$  (sample-chamber temperature = *pitot-tube* temperature).

Assuming an ideal background pressure in the *sample/detector chamber (SDC)* i.e.  $p_{SC} = 0$ , one can calculate the expected partial pressure increase within the PITOT TUBE detector with equation 2.22.

The calculated detector pressure increase values  $p_T$  for two different cases of helium flow rates  $\dot{N}_R$  into the detection system (see table 2.6) are listed in tables 2.7 and 2.8. The detector aperture diameter is set to  $d_D = 1$  mm. Thereby the just mentioned particle-flow-throughput entering the detector tube  $\dot{N}_R$  is

PARTIAL PRESSURE INCREASE $p_T$ IN THE PITOT TUBE FOR $\dot{N}_R = 7.8719 \cdot 10^9 \text{ s}^{-1}$
$d_{ph} = 1 \text{ mm} \Rightarrow A = 7.8536 \cdot 10^{-7} \text{ m}^2$
$\bar{c} = 1260 \text{ m/s}$
$L = 2.473 \cdot 10^{-4} \text{ m}^3/\text{s}$
$p_T = 1.3182 \cdot 10^{-7} \text{ Pa} = 1.32 \cdot 10^{-9} \text{ mbar}$

Table 2.7: Partial pressure increase  $p_T$  in the detector PITOT TUBE, and corresponding vacuum conductance factors, achieved with a pinhole aperture diameter of  $d_D = 1 \text{ mm}$ ,  $d_N = 5 \mu\text{m}$  and 8% ZP efficiency as well as 10% sample reflectivity.  $p_o = 180 \text{ bar}$ ,  $T_o = 300 \text{ K}$  and  $d_{MS} = 20 \mu\text{m}$ .

PARTIAL PRESSURE INCREASE $p_T$ IN THE PITOT TUBE FOR $\dot{N}_R = 6.2976 \cdot 10^{10} \text{ s}^{-1}$
$d_{ph} = 1 \text{ mm} \Rightarrow A = 7.8536 \cdot 10^{-7} \text{ m}^2$
$\bar{c} = 1260 \text{ m/s}$
$L = 2.473 \cdot 10^{-4} \text{ m}^3/\text{s}$
$p_T = 1.0546 \cdot 10^{-6} \text{ Pa} = 1.05 \cdot 10^{-8} \text{ mbar}$

Table 2.8: Partial pressure increase  $p_T$  in the detector PITOT TUBE, and corresponding vacuum conductance factors, achieved with a pinhole aperture diameter of  $d_D = 1 \text{ mm}$ ,  $d_N = 5 \mu\text{m}$  and 8% ZP efficiency as well as 80% sample reflectivity.  $p_o = 180 \text{ bar}$ ,  $T_o = 300 \text{ K}$  and  $d_{MS} = 20 \mu\text{m}$ .

inserted in equation 2.22<sup>2,3</sup>.

To conclude the evaluation of the detector system it can be said that with the chosen PITOT TUBE system good signal intensities can be expected when the background pressure in the source chamber is in the low  $10^{-9} \text{ mbar}$  range.

## 2.2 LAY-OUT OF THE PUMPING SYSTEM

Within this chapter the considerations and final design decisions regarding the layout of the ultra high vacuum pumping system for the new microscope are presented. Such an assembly of high vacuum chambers is necessary to provide

- 
- 2 Note: For the determination of the the detector entering particle-flow-throughput  $\dot{N}_R$  the beam temperature value  $T_o$  has to be used, whereas regarding the average gas particle velocity for the conductance factor of a pinhole is related to the PITOT TUBE/ sample-chamber temperature which is set to room temperature. This is the case because equation 2.20 is established for the molecular particle flow of He-atoms back-out from the PITOT TUBE through the detector aperture into the sample chamber.
  - 3 Also note that for the PITOT TUBE system utilized in this microscope setup the conditions for an effusive source are fulfilled. (see chapter 2.2.1.2)

an atmosphere with a long enough mean free path. It is needed to enable the helium beam atoms to travel without experiencing any disturbing interactions on their way to the sample surface. Therefore a beam column with sufficiently good enough vacuum conditions has to be provided. Furthermore it has to be able to handle the high helium flow rates due to the beam.

### 2.2.1 Some vacuum technology and flow basics

The two first sub-chapters 2.2.1.1 and 2.2.1.2 present some basic equations describing vacuum and ultra high vacuum (UHV) conditions.

#### 2.2.1.1 Ideal gas law

In the following all considerations are carried out with the simplification on an *ideal gas*. The *Ideal Gas Law* is defined as:

$$p \cdot V = N \cdot k \cdot T \quad (2.24)$$

with  $p$  the pressure,  $V$  the volume,  $N$  the number of particles,  $T$  the temperature in [K] and  $k$  the BOLTZMANN-constant.

The conditions for an ideal gas<sup>4</sup> will not exactly apply for our system, but it will give a sufficiently close estimate of the situation. First some parameter and value definitions [61, 62]:

$$\text{Volume-Flow-Throughput } \dot{V} \quad q_v = \frac{\Delta V}{\Delta t} = \dot{V} \quad (2.25)$$

$$\text{Particle-Flow-Throughput } \dot{N} \quad q_N = \frac{\Delta N}{\Delta t} = \dot{N} \quad (2.26)$$

$$\text{Pressure-Volume-Throughput } q_{pV} \quad q_{pV} = p \cdot \dot{V} \quad (2.27)$$

$$\text{Pumping-Speed } S \quad S = \dot{V} \quad (2.28)$$

$$\text{Pump-Throughput } \dot{Q} \quad \dot{Q} = p \cdot S \quad (2.29)$$

with  $p$  the pressure,  $V$  the volume,  $N$  the number of particles,  $T$  the temperature in [K],  $k$  the BOLTZMANN-constant and  $t$  the time.

<sup>4</sup> Ideal gas: (a): *point particles*: molecules/atoms are minute spheres; (b): very small sphere volume compared to the actually occupied volume by the gas; (c) *non-interacting* in terms of no forces exerted upon each other; (d): *randomly-moving*: traveling along straight paths; (e): perfectly elastic collisions between the molecules.( see [60])

### 2.2.1.2 Effusion

The particle flow throughput  $\dot{N}$  through a small round opening from a chamber with the pressure  $p$  into another chamber with a low pressure ambient background is given by [61]

$$q_N = \dot{N} = \frac{n \cdot \bar{c}}{4} \cdot A \quad (2.30)$$

with  $n$  the particle density ( $n = N/V$ ),  $V$  the volume,  $N$  the number of particles,  $\bar{c}$  the average (mean) particle velocity<sup>5</sup> and  $A$  the surface area.

This equation is just valid in case the temperature  $T = const.$ , and when the opening in the wall is small (opening diameter  $D \ll \lambda$ )[63]. Also the condition of molecular flow (see D.1) has to be fulfilled. As a more detailed definition for effusive sources M. KAPPES and S. LEUTWYLER state in [67] that in an effusion source the mean free path length  $\lambda$  within the chamber has to be an order of one magnitude bigger than the diameter of the orifice  $D$ , in other words  $\lambda/D > 10$ .

### 2.2.2 System setup

Figure 2.9 presents a sketch of the selected pumping system setup for the instrument. Four different types of pumps are used. Each chamber has at least one *turbomolecular pump* (TP) with magnetic bearings, the so called MAG W Pumps from OERLIKON/LEYBOLD. The decision for the implementation of magnetically born turbo-pumps has been made for the reason of vibrational minimization of the system. Since the *source chamber* pumps will have to deal with the biggest amount of helium flow and throughput, two of the MAG W 600 pumps are mounted here. Their pumping speed for *helium* is given by  $550 \text{ ls}^{-1}$  for each of them. The following *pumping stage* as well as the chamber holding the ZONE PLATE are set up with a MAG W 300 TP respectively. Each of these pumps is presented with  $260 \text{ ls}^{-1}$  pumping speed. Finally the sample chamber is assembled with a MAG W 600 TP.

All the backing pumps for the system are SCROLLVAC SC 30 D oil free scroll-pumps, with a pumping speed of  $30 \text{ m}^3\text{s}^{-1}$  and an achievable ultimate pressure

---

<sup>5</sup>  $\bar{c} = \sqrt{\frac{8 \cdot k \cdot T}{\pi \cdot m_T}}$ , with  $m_T$  the atom mass of a single helium atom [61]



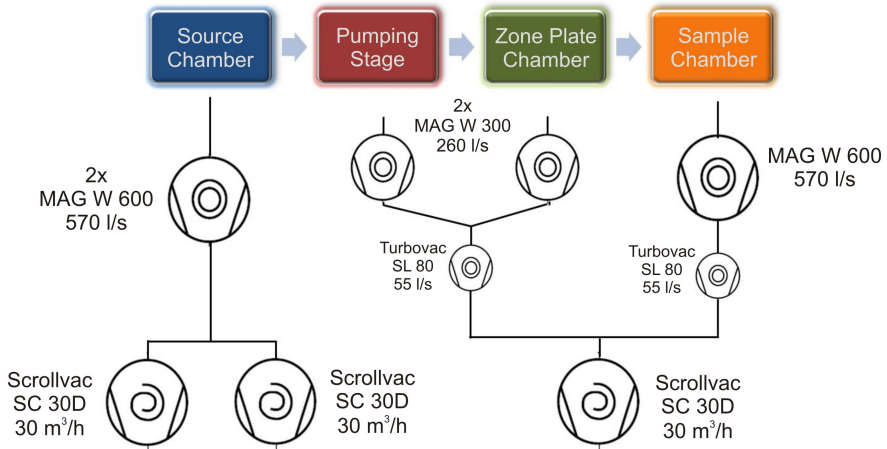


Figure 2.9: Schematic of the pumping system setup for NEMI.

of  $\leq 0,01$  mbar. The crucial factor for the assignment of these scroll-pumps, is the goal of setting up a completely oil free pumping system.

The He flow is highest within the *source chamber*, therefore this chamber has its own prevacuum line working with two of the SCROLLVAC pumps. A third backing pump is used on the *pumping stage*, the *zone plate chamber* and the *sample chamber* together. To further reduce the He back-flow into the system, the *pumping stage/ZP-chamber* as well as the *sample chamber* prevacuum lines respectively, have an additional small SL80 *turbomolecular pump* implemented preliminary to the SCROLLVAC backing pump.

The next step is to estimate the partial pressure increases in the chambers, so to say in the *pumping stage chamber (PST)*, the *ZP chamber (ZPC)* and the *sample/detector chamber (SDC)*, based on the pressure originating from the *helium* atoms entering the *source chamber (SC)* through the nozzle. Figure 2.10 gives a principle sketch of the chamber and pumping situation.

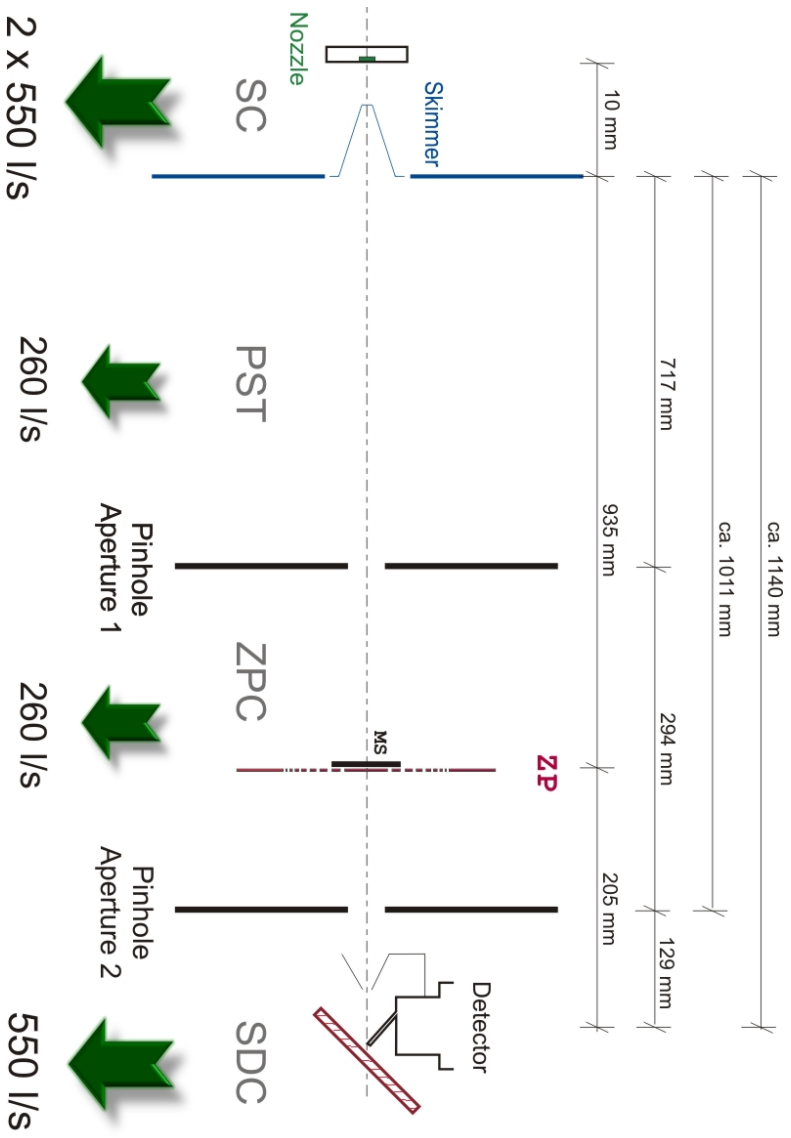


Figure 2.10: Detailed setup sketch for the evaluation of the ultra high vacuum part of the pumping system.

### 2.2.3 Partial helium pressure increase in the UHV system

The starting point for all the calculations is the *free-jet expansion* within the *source chamber (SC)*. The arising pressure conditions within this chamber are considered in the following sub-section 2.2.3.1. Two different processes contribute to the partial *helium* pressure increase in the rest of the *Nemi* system. For one part a helium gas *diffusion process* from one chamber to the next takes place which is based on the pressure situation in the respective foregoing chamber. That means that the finally achieved *source chamber* pressure arising from the *helium* expansion leads to a consequent diffusion of helium atoms into the adjacent *pumping stage chamber (PST)* and so on. This *diffusion* process though is independent from the *helium* atoms which are traveling with the beam itself into the following chambers. The partial helium pressure increase based on those beam atoms will make up the above mentioned second process which is influencing the final *total partial pressure increase* in each chamber. Therefore the total partial *helium* pressure rise in each chamber is a combination of the pressure increase due to the *diffusion* process  $p_{diff}$  and the pressure rise which originates from the *probe beam*  $p_{beam}$ .

$$p_{total} = p_{diff} + p_{beam} \quad (2.31)$$

In the following the effects of this two different processes will be considered separately for each chamber and in the end of the section 2.2 the final *total pressure increase* in each chamber will be presented.

#### 2.2.3.1 Source chamber (SC)

First the partial source chamber pressure  $p_{SC}$  due to the inlet of the *helium* gas has to be evaluated. The particle density  $n_o$  of helium atoms entering through the nozzle pinhole was evaluated in section 2.1.2.3 with the IDEAL GAS LAW 2.16.

$$n_o = \frac{N_o}{V_o} = \frac{p_o}{k \cdot T_o} \quad (2.32)$$

Picturing the He-*nozzle* as a pressurized reservoir with the boundary conditions of a pressure  $p_o$ , and the Temperature  $T_o$ , as picture 2.11 indicates, it is

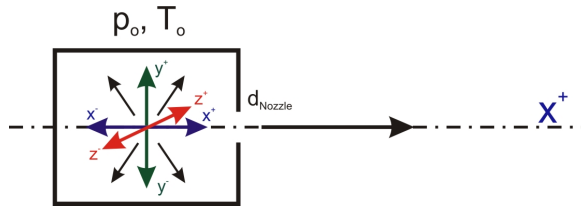


Figure 2.11: principle sketch for the flow rate estimate of the nozzle

possible to determine the expected pressure rise within the source chamber as follows:

According to [61], the helium atoms are moving with  $1/3 \cdot N$  particles in all 3 space dimensions  $x, y, z$  in positive and negative direction, respectively. Considering the case of a small nozzle pinhole at the end of this reservoir, the share of He-atoms passing through the nozzle orifice can be roughly estimated by those atoms traveling in positive  $x$  direction, i.e.  $1/6 \cdot N$  atoms are entering the chamber through the nozzle. This assumption will alter equation 2.10 to

$$\dot{N}_o = C_N \cdot n_o \cdot \bar{v}_{He} \cdot A \quad (2.33)$$

with  $C_N = 1/6$  the factor for the positive  $x$  direction,  $A$  the nozzle surface and  $\bar{v}_{He}$  the mean velocity of the He atoms derived from the KINETIC THEORY OF GASES [61] under standard conditions.

$$\bar{v}_{He} = \sqrt{\frac{3 \cdot k \cdot T_o}{m_{He}}} \quad (2.34)$$

Deriving equation 2.24 over the time  $t$  one can find

$$p_{SC} \cdot \dot{V} = p_{SC} \cdot \frac{\partial V}{\partial t} = \frac{\partial N}{\partial t} \cdot k \cdot T = \dot{N} \cdot k \cdot T \quad (2.35)$$

which can be also written as

$$p_{SC} = \frac{\dot{N}_o \cdot k \cdot T}{\dot{V}} = \frac{\dot{N}_o \cdot k \cdot T}{S_{CH}} \quad (2.36)$$

with  $\dot{N}_o$  from equation 2.33,  $S_{CH}$  the pumping-speed of the source chamber turbo-molecular pumps and  $T$  the temperature of the chamber which is in the room temperature (RT) range.

The pumping speed  $S$  for *helium* for the two MAG W 600 turbo-molecular pumps is given by  $S_{CH} = 2 \cdot 550 \text{ ls}^{-1} = 1100 \text{ ls}^{-1}$ . Hence the partial source chamber pressure  $p_{SC}$  can be determined from e.q. 2.36. Figure 2.12 represents a diagram of the calculated source chamber pressure values for rising nozzle pressures  $p_o$ . Additionally the specifically calculated values of  $p_{SC}$  for different system setup parameters are presented in table 2.9. Since this evaluation is performed for the worst case scenario regarding the particle load on the pumping system, all further presented values are calculated for a nozzle pressure of  $p_o = 200 \text{ bar}$  if nothing else mentioned.

SOURCE CHAMBER PRESSURE $p_{SC}$ AT $p_o = 200 \text{ bar}$		
[mbar]		
	$d_{N_1} = 5 \mu\text{m}$	$d_{N_2} = 10 \mu\text{m}$
$T_o = 300 \text{ K}$	$8.1 \cdot 10^{-4}$	$3.3 \cdot 10^{-3}$
$T_o = 100 \text{ K}$	$1.4 \cdot 10^{-3}$	$5.6 \cdot 10^{-3}$

Table 2.9:  $p_{SC}$ , partial source chamber pressures for different starting conditions  $d_N$  and  $T_o$ .

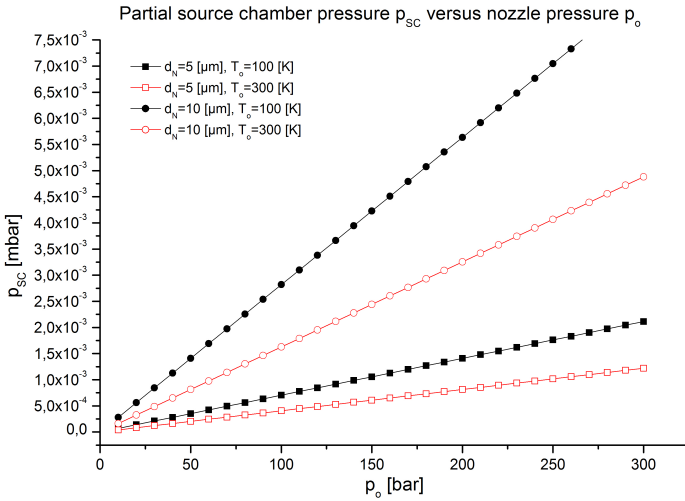


Figure 2.12:  $p_{SC}$ , partial source chamber pressures versus nozzle pressure  $p_o$  for the two different nozzle diameters  $d_N = 5 \mu\text{m}$ , and  $d_N = 10 \mu\text{m}$  at the two different nozzle temperatures  $T_o = 100 \text{ [K]}$ , and  $T_o = 300 \text{ [K]}$  respectively.

#### 2.2.4 Partial pressure increase due to the helium diffusion process from the source chamber $p_{diff}$

The partial pressure increase in the different ultra high vacuum (UHV) chambers is due to the *helium* gas which is injected via the nozzle into the source chamber. This chapter will deal with the partial pressure rise due to a *diffusion* processes between the different UHV chambers which originates from the pressure increase in the source chamber due to the inlet of helium gas through the nozzle. The diffusion process can be pictured as an *effusive source* at the entrance aperture of each chamber.

As a next step the originating partial helium pressures in the remaining chambers, consequential to the source chamber pressure are calculated. This means that for the moment the additional pressure rise due to the He-beam is neglected.

Generally the *gas diffusion* from a chamber 1 with the parameters  $p_1$  and  $T_1$  through an opening into an adjacent chamber 2 with a low pressure ambient background and pumped with a pumping speed  $S_2$  is considered. Since the system is in the ultra high vacuum (UHV) range the conditions for the molecular flow regime are valid. This leads to the two following equations for the condition of “*equilibrium state particle flow between two chambers through a pinhole with a small diameter*” [62]:

$$p_2 = \frac{\dot{N} \cdot k \cdot T}{S_2} \quad (2.37)$$

$$\dot{N} \cdot k \cdot T = L \cdot (p_1 - p_2) \quad (2.38)$$

Hereby equation 2.37 is derived the same way like equation 2.36 on the basis of the *ideal gas law* (e.q. 2.24). Equation 2.38 embraces the diffusion passage between the two chambers by describing the molecular flow through a pinhole with a small diameter. The factor  $L$  states the vacuum conductance factor for a pinhole (with the surface area  $A$ ) in the molecular flow regime:

$$L = \frac{\bar{c}}{4} \cdot A = \frac{\sqrt{\frac{8kT}{\pi m_{He}}}}{4} \cdot A$$

Combining equation 2.37 and 2.38 leads to

$$p_2 = \frac{L}{S_2 + L} \cdot p_1 \quad (2.39)$$

which describes the expected pressure increase in chamber 2 due to gas diffusion through a small opening from chamber 1. By inserting the corresponding values for each of the chambers following the *source chamber*, it is possible to determine the  $p_{diff}$  values for each of them. The respective calculations are presented in the following three sub-chapters 2.2.4.1, 2.2.4.2 and 2.2.4.3.

#### 2.2.4.1 Pumping stage chamber (PST)

The chamber adjacent to the *source chamber* (SC) is the *pumping stage chamber* (PST). The connection part between this two chambers is the *skimmer* (SK), whose orifice diameter generally lies in the range between 1 – 5  $\mu\text{m}$  (see figure 2.10).

The pressure  $p_1$  from equation 2.39 hereby is given by the *source chamber pressure*  $p_{SC}$  which was calculated in section 2.2.3.1. The pumping speed  $S$  is represented by the PST MAG W 300 turbo-pump which is stated by the manufacturer to be  $S_{PST} = 260 \text{ l s}^{-1}$ . The corresponding values evaluated for the most likely used setup parameters of  $d_{N_1} = 5 \mu\text{m}$ ,  $T_o = 100 \text{ K}$  and  $p_o = 200 \text{ bar}$ , and for the worst case setup parameters regarding the flow rate, present at  $d_{N_2} = 10 \mu\text{m}$ ,  $T_o = 100 \text{ K}$  and  $p_o = 200 \text{ bar}$  are stated in table 2.10. For both of this starting parameter sets the calculated partial pumping stage pressure increase due to diffusion is presented for a skimmer diameter of  $d_{Sk_1} = 1 \mu\text{m}$  and  $d_{Sk_2} = 5 \mu\text{m}$  respectively.

$p_{PST} (diff)$ PUMPING STAGE DIFFUSION PRESSURE INCREASE		
[mbar]		
$p_o = 200 \text{ bar}$	$d_{Sk} = 1 \mu\text{m}$	$d_{Sk} = 5 \mu\text{m}$
$d_N = 5 \mu\text{m}, T_o = 100 \text{ K}$	$1,34 \cdot 10^{-12}$	$3,35 \cdot 10^{-11}$
$d_N = 10 \mu\text{m}, T_o = 100 \text{ K}$	$5,35 \cdot 10^{-12}$	$1,34 \cdot 10^{-10}$

Table 2.10:  $p_{PST} (diff)$  *pumping stage* pressure increase due to diffusion for different starting setup parameters:  $p_o$ ,  $d_N$ ,  $T_o$ , and  $d_{Sk}$  respectively.

### 2.2.4.2 Zone plate chamber (ZPC)

The same procedure can be used to determine the partial *helium* pressures increase due to diffusion from the *pumping stage chamber (PST)* into the *zone plate chamber (ZPC)* and furthermore from the *zone plate chamber (ZPC)* into the *sample/detector chamber (SDC)*.

The aperture pinhole placed between the *pumping stage chamber (PST)* and the *zone plate chamber (ZPC)* has a diameter of  $d = 5 \text{ mm}$ .<sup>6</sup>  $p_1$  from equation 2.39 is represented by  $p_{PST}(\text{diff})$  whereas  $p_2$  will be the determined ZPC pressure  $p_{ZPC}(\text{diff})$ . The pumping of this chamber is performed by a MAG W 300 with  $S_{ZPC} = 260 \text{ ls}^{-1}$ .

Table 2.11 states the calculated values for the *diffusion* based pressure rise in the *zone plat chamber*  $p_{ZPC}(\text{diff})$  at the two same starting parameter setups like used before for the pumping stage chamber.

$p_{ZPC}(\text{diff})$ ZONE PLATE CHAMBER DIFFUSION PRESSURE RISE [mbar]		
$p_o = 200 \text{ bar}, d = 5 \text{ mm}$	$d_{Sk} = 1 \mu\text{m}$	$d_{Sk} = 5 \mu\text{m}$
$d_N = 5 \mu\text{m}, T_o = 100 \text{ K}$	$3,11 \cdot 10^{-14}$	$7,78 \cdot 10^{-13}$
$d_N = 10 \mu\text{m}, T_o = 100 \text{ K}$	$1,25 \cdot 10^{-13}$	$3,11 \cdot 10^{-12}$

Table 2.11:  $p_{ZPC}(\text{diff})$  partial *zone plate chamber* pressure increase due to diffusion from the PST chamber for different starting setup parameters:  $d$ ,  $p_o$ ,  $d_N$ ,  $T_o$  and  $d_{Sk}$  respectively.

### 2.2.4.3 Sample/detector chamber (SDC)

An aperture with a diameter of  $d = 5 \text{ mm}$  separates the *zone plate chamber (ZPC)* from the *sample/detector chamber (SDC)*. This leads to the corresponding numbers for  $p_{SDC}(\text{diff})$ , presented in table 2.12. It has to be mentioned here that in case of the *sample/detector chamber* a MAG W 600 turbo-pump is in charge of the pumping. This pump is stated to have a pumping-speed of  $S_{SDC} = 5701 \cdot \text{s}^{-1}$ .

The partial pressure rises in all UHV (ultra high vacuum) chambers due to diffusion from their neighboring chamber pressures has been evaluated. As

<sup>6</sup>  $A = \frac{d^2 \cdot \pi}{4}$



$p_{SDC} (diff)$ SAMPLE/DETECTOR CHAMBER DIFFUSION PRESSURE INCREASE [mbar]		
$p_o = 200 \text{ bar}, d = 5 \text{ mm}$	$d_{Sk} = 1 \mu\text{m}$	$d_{Sk} = 5 \mu\text{m}$
$d_N = 5 \mu\text{m}, T_o = 100 \text{ K}$	$3,34 \cdot 10^{-16}$	$8,35 \cdot 10^{-15}$
$d_N = 10 \mu\text{m}, T_o = 100 \text{ K}$	$1,34 \cdot 10^{-15}$	$3,34 \cdot 10^{-14}$

Table 2.12:  $p_{SDC} (diff)$  partial *sample/detector chamber* pressure rise due to diffusion from the ZPC chamber for an aperture diameter of  $d = 5 \text{ mm}$ , with varying parameters for  $d_N$ , and  $d_{Sk}$  respectively.

one can see from the presented values it is very minor in all chambers behind the source chamber (SC). This can be ascribed to the choice of the aperture diameters between the chambers as well as too the chosen pump setup.

### 2.2.5 Partial pressure increase due to the helium beam $p_{beam}$

The following section considers the pressure increase in the UHV chambers due to the He-beam for every chamber separately.

In general the basic approach is the same for all chambers. The partial pressure increase due to the *micro-probe beam* is based on the residual particle flow  $\dot{N}_{beam}$  after weighing the beam-flow *into* the chamber  $\dot{N}_{IN}$  against the beam-flow *out* of the chamber  $\dot{N}_{OUT}$ . In mathematical terms

$$\dot{N}_{beam} = \dot{N}_{IN} - \dot{N}_{OUT} \quad (2.40)$$

It is known from equation 2.10 that at position  $x$  the particle flow within the beam is given as

$$\dot{N}_o(x) = n(x) \cdot v_{He} \cdot A \quad (2.41)$$

which leads to

$$\dot{N}_{IN} = \dot{N}_o(x_{in}) \quad \text{and} \quad \dot{N}_{OUT} = \dot{N}_o(x_{out}) \quad (2.42)$$

with  $\dot{N}_o(x_{in})$  the beam-particle-flow *into* the chamber at the entrance aperture position  $x_{in}$ , and  $\dot{N}_o(x_{out})$  the beam-particle-flow at its exit aperture position  $x_{out}$  *out* of the chamber.

Using the same approach like in 2.36, one can find  $p_{beam}$

$$p_{beam} = \frac{(\dot{N}_{IN} - \dot{N}_{OUT}) \cdot k \cdot T}{S} \quad (2.43)$$

to be the pressure arising within the chamber just due to the probe beam<sup>7</sup>.

### 2.2.5.1 Pumping stage chamber (PST)

The entrance aperture diameter for this chamber is given by the skimmer diameter  $d_{Sk}$ . The exit diameter of the beam is determined either by the geometrical setup of the system, this means by the widening of the beam at that point, or in case of a very wide beam ( $d_{beam} > d_{app}$ ) by the aperture diameter  $d_{app} = 5$  mm.

From geometrical considerations (see figure 2.13) one can find that as long as the skimmer diameter  $d_{Sk} < 50$   $\mu\text{m}$ , the beam widening is not limited by the pumping stage exit aperture (APERTURE 1) because the beam diameter in this cases stays below 5 mm. Since the small focal spot size of NEMI is based on the usage of *microskimmers* (skimmer diameters between 1 – 5  $\mu\text{m}$ ), the beam is never limited by this aperture. Hence the beam flow leaving the pumping stage chamber through APERTURE 1 is regulated by the geometrical beam opening size  $d_{beam\_App1}$ .

$$d_{beam\_App1} = 2 \cdot \left[ \left( \frac{\frac{d_N}{2} + \frac{d_{Sk}}{2}}{L_{Nozzle-Skimm}} \right) \cdot L_{Nozzle-App1} \right] - d_{Nozzle}$$

To evaluate the pressure rise in the *PST* chamber due to the beam, one has to consider the amount of atoms entering the chamber through the skimmer opening, as well as in principle also the amount of atoms leaving it on the other side through the exiting aperture to the *zone plate chamber*. Since equation 2.10, and the corresponding equation for  $n(x)$  (e.q. 2.13) are both just valid close to the beam axis, they will not deliver a reasonable estimate for the particle flow leaving the chamber, due to the strong broadening of the beam at that point.

<sup>7</sup> Note that the temperature  $T$  in equation 2.43 is the chamber temperature, hence room temperature (RT), whereas for  $\dot{N}_{beam}$  and therefore also for  $\dot{N}_{IN}$  and  $\dot{N}_{OUT}$  the beam temperature  $T_o$  has to be assigned.

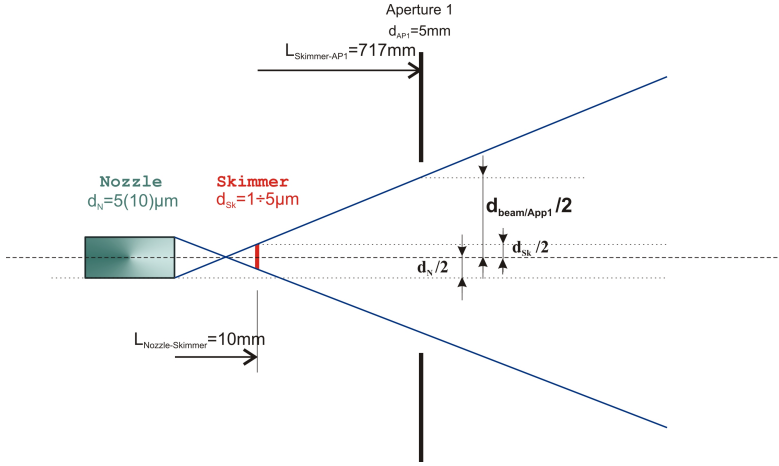


Figure 2.13: Schematic for the geometrical considerations regarding the beam widening at the position of APERTURE 1 between the pumping stage chamber (PST) and the zone plate chamber (ZPC)

Therefore it was decided to do a “worst case” evaluation and consider that all particles entering the pumping stage will participate into the pressure rise of the chamber. In other words, all atoms go in, but none go out. This leads to a change of equation 2.43 to

$$p_{PST}(beam) = \frac{(\dot{N}_{IN_{PST}}) \cdot k \cdot T}{S_{PST}} \quad (2.44)$$

with<sup>8</sup>

$$\dot{N}_{IN_{PST}} = n(Skimmer) \cdot v_{He} \cdot A_{Sk} \quad (2.45)$$

$$n(Skimmer) = 0,16 \cdot n_o \cdot \left( \frac{d_N}{L_{Nozzle-Skimmer}} \right)^2 \quad (2.46)$$

$$n_o = \frac{N_o}{V_o} = \frac{p_o}{k \cdot T_o} \quad (2.47)$$

The calculated pressure numbers for the before mentioned combinations of the two different nozzle diameters, as well as the two different skimmer diameters are presented in table 2.13.

<sup>8</sup> In the case of the participation of the beam’s particle flow to the total chamber pressures the mean velocity of the He-atoms is presented by the atoms final average speed originating from the *free-jet-expansion* and hence defined by  $v_{He} = \sqrt{\frac{5kT_o}{m_{He}}}$  (for details see chapter 3.4).

$p_{PST} (beam)$ PUMPING STAGE CHAMBER BEAM PRESSURE-RISE [mbar]		
$p_o = 200 \text{ bar}$	$d_{Sk} = 1 \mu\text{m}$	$d_{Sk} = 5 \mu\text{m}$
$d_N = 5 \mu\text{m}, T_o = 100 \text{ K}$	$7,39 \cdot 10^{-11}$	$1,85 \cdot 10^{-9}$
$d_N = 10 \mu\text{m}, T_o = 100 \text{ K}$	$2,96 \cdot 10^{-10}$	$7,39 \cdot 10^{-9}$

Table 2.13:  $p_{PST} (beam)$  pumping stage chamber pressure rise due to the beam for varying  $d_N$  and  $d_{Sk}$  respectively.

### 2.2.5.2 Zone plate chamber (ZPC)

In the *zone plate chamber* most of the incoming *helium* atoms are blocked out of the beam by the *zone plate*. Thus the simplification of all atoms participating into the chamber pressure fits even better than for the *PST*. Another approximation is that all beam atoms entering the pumping stage chamber will go directly through this chamber, and enter into the *ZPC* chamber. Therefore the beam inlet flow *into* the *ZP* chamber is equal to  $\dot{N}_{IN_{PST}} = \dot{N}_{IN_{ZPC}}$ . Hence the pressure rise within the *ZP* chamber due to the beam can be estimated to be

$$p_{ZPC} (beam) = \frac{(\dot{N}_{IN_{ZPC}}) \cdot k \cdot T}{S_{ZPC}} = \frac{(\dot{N}_{IN_{PST}}) \cdot k \cdot T}{S_{ZPC}} \quad (2.48)$$

Since the turbo molecular pump mounted to the *ZP* chamber is the same model like the one pumping the pumping stage chamber (MAG W 300,  $S_{ZPC} = 260 \text{ ls}^{-1}$ ), the calculated pressure rise values due to the beam within the *ZP* chamber are the same like for the *PST* which are presented in table 2.13.

### 2.2.5.3 Sample/detector chamber (SDC)

For the *sample/detector chamber pressure* it is assumed that maximum 10% of the particle flow impinging on the *zone plate* are transmitted further into the *sample/detector chamber*. Also there is no particle flow leaving the chamber since it is the last chamber of the system, hence  $\dot{N}_{OUT_{SDC}} = 0$ . This modifies equation 2.40 and 2.43 to

$$\dot{N}_{IN_{SDC}} = \dot{N}_{IN_{ZPC}} \cdot 0,1 \quad (2.49)$$

$$p_{SDC} (beam) = \frac{(\dot{N}_{IN_{SDC}}) \cdot k \cdot T}{S_{SDC}} = \frac{(\dot{N}_{IN_{ZPC}} \cdot 0,1) \cdot k \cdot T}{S_{SDC}} \quad (2.50)$$

In the case of the *sample/detector chamber*, the pumping is performed by a MAG W 600 turbo molecular pump with  $S_{SDC} = 570 \text{ ls}^{-1}$ . The corresponding values determined for  $p_{SDC}(\text{beam})$  are listed in table 2.14.

$p_{SDC}(\text{beam})$ SAMPLE/DETECTOR CHAMBER BEAM PRESSURE-RISE [mbar]		
$p_o = 200 \text{ bar}$	$d_{Sk} = 1 \mu\text{m}$	$d_{Sk} = 5 \mu\text{m}$
$d_N = 5 \mu\text{m}, T_o = 100 \text{ K}$	$3,37 \cdot 10^{-12}$	$8,43 \cdot 10^{-11}$
$d_N = 10 \mu\text{m}, T_o = 100 \text{ K}$	$1,35 \cdot 10^{-11}$	$3,37 \cdot 10^{-10}$

Table 2.14:  $p_{SDC}(\text{beam})$  *sample/detector chamber* pressure rise due to the beam for varying  $d_N$  and  $d_{Sk}$  respectively.

### 2.2.6 Total partial pressure increase due to the helium beam and diffusion

For the determination of the total partial helium pressure increase developing within the chambers, the two amounts  $p_{diff}$  and  $p_{beam}$  have to be added up like stated in equation 2.31. The pressure values due to diffusion between the chambers  $p_{PST}(\text{diff})$ ,  $p_{ZPC}(\text{diff})$  and  $p_{SDC}(\text{diff})$  are calculated in paragraph 2.2.4. Together with the pressure rises due to the probe beam which were determined in section 2.2.5 one can evaluate the total partial pressure increase within each subsequent chamber.

#### 2.2.6.1 Total pumping stage chamber (PST) pressure

The pressure rise due to diffusion from the neighboring source chamber has been found to be  $p_{PST}(\text{diff}) = 1,34 \cdot 10^{-10} \text{ mbar}$  for the worst case setup scenario of a diameter  $d_N = 10 \mu\text{m}$  nozzle combined with a  $d_{Sk} = 5 \mu\text{m}$  skimmer orifice at the beam settings of  $p_o = 200 \text{ bar}$  and  $T_o = 100 \text{ K}$ . This  $p_{PST}(\text{diff})$  pressure value is used as a basis for further considerations.

The calculated values for the total pressure arising in the pumping stage chamber  $p_{PST}$ , can be found by combining the values from the pressure increase due to the beam  $p_{PST}(\text{beam})$  listed in section 2.2.5 and from the diffusion process  $p_{PST}(\text{diff})$  which were stated in section 2.2.4. Corresponding values are shown in table 2.15.

$p_{PST}$ PUMPING STAGE CHAMBER TOTAL PRESSURE-RISE [mbar]		
$p_o = 200 \text{ bar}$	$d_{Sk} = 1 \mu\text{m}$	$d_{Sk} = 5 \mu\text{m}$
$d_N = 5 \mu\text{m}, T_o = 100 \text{ K}$	$7,52 \cdot 10^{-11}$	$1,88 \cdot 10^{-9}$
$d_N = 10 \mu\text{m}, T_o = 100 \text{ K}$	$3,01 \cdot 10^{-10}$	$7,52 \cdot 10^{-9}$

Table 2.15:  $p_{PST}$  pumping stage total chamber pressure for varying  $d_N$  and  $d_{Sk}$  respectively.

### 2.2.6.2 Total zone plate chamber (ZPC) pressure

The same procedure is performed to gain the total pressure increase in the ZPC. Also it is worth to mention that the total pressure rise within the ZP chamber is mainly due to the beam flow since the increase due to diffusion is at most in the lower  $10^{-12}$  mbar range and therefore insignificant. Table 2.16 presents the total pressure values arising within the ZP chamber.

$p_{ZPC}$ ZONE PLATE CHAMBER TOTAL PRESSURE-RISE [mbar]		
$p_o = 200 \text{ bar}$	$d_{Sk} = 1 \mu\text{m}$	$d_{Sk} = 5 \mu\text{m}$
$d_N = 5 \mu\text{m}, T_o = 100 \text{ K}$	$7,39 \cdot 10^{-11}$	$1,85 \cdot 10^{-9}$
$d_N = 10 \mu\text{m}, T_o = 100 \text{ K}$	$2,96 \cdot 10^{-10}$	$7,39 \cdot 10^{-9}$

Table 2.16:  $p_{ZPC}$  total zone plate chamber pressure rise due to the beam and the first estimated pressure for different  $d_N$  and  $d_{Sk}$  respectively

### 2.2.6.3 Total sample/detector chamber (SDC) pressure

The same way as for the zone plate chamber, the part of the diffusion pressure increase in the sample detector chamber  $p_{SDC} (diff)$  is negligible small compared to  $p_{SDC} (beam)$ . Hence the resulting total pressure rise values for the SDC which are presented in table 2.17 are nearly the same as the values just for the increase due to the beam. As one can see from the numbers in table 2.17 the total pressure increase in the sample/detector chamber is very low. Compared to the in chapter 2.1.6 calculated expected detector/PITOT TUBE pressure rise due

$p_{SDC}$ TOTAL SAMPLE/DETECTOR CHAMBER PRESSURE-RISE [mbar]		
$p_o = 200 \text{ bar}$	$d_{Sk} = 1 \mu\text{m}$	$d_{Sk} = 5 \mu\text{m}$
$d_N = 5 \mu\text{m}, T_o = 100 \text{ K}$	$3,37 \cdot 10^{-12}$	$8,43 \cdot 10^{-11}$
$d_N = 10 \mu\text{m}, T_o = 100 \text{ K}$	$1,35 \cdot 10^{-11}$	$3,37 \cdot 10^{-10}$

Table 2.17:  $p_{SDC}$  total *sample/detector chamber* pressure rise due to the beam and the first estimated pressure for varying  $d_{Nozzle}$  and  $d_{Skimmer}$  respectively.

to the signal from the sample<sup>9</sup>, it can be seen that for a worst case scenario<sup>10</sup> the expected detector/PITOT TUBE pressure rise is one order of magnitude higher than the background pressure increase in the chamber as long as a small skimmer diameter is used. For an easy comparison the corresponding numbers are presented in table 2.18.

$p_{SDC}$ TOTAL SAMPLE/DETECTOR CHAMBER PRESSURE-RISE & PRESSURE RISE IN THE DETECTION TUBE $p_T$ [mbar]			
$p_o = 200 \text{ bar}$	$d_{Sk} = 1 \mu\text{m}$	$d_{Sk} = 5 \mu\text{m}$	$p_T$
$d_N = 5 \mu\text{m}, T_o = 100 \text{ K}$	$3,37 \cdot 10^{-12}$	$8,43 \cdot 10^{-11}$	$2,39 \cdot 10^{-9}$
$d_N = 10 \mu\text{m}, T_o = 100 \text{ K}$	$1,35 \cdot 10^{-11}$	$3,37 \cdot 10^{-10}$	$9,56 \cdot 10^{-9}$

Table 2.18: Comparison  $p_{SDC}$  total *sample/detector chamber* pressure rise against *detection pressure* increase in the PITOT TUBE  $p_T$  for a worst case sample reflection of 10% and a ZP middle stop diameter of  $d_{MS} = 50 \mu\text{m}$ , with the starting parameters  $p_o$ ,  $T_o$ ,  $d_N$  and  $d_{Sk}$ .

### 2.3 LAY-OUT OF THE PREVACUUM SYSTEM

The NEMI prevacuum system is based on three SCROLLVAC SC30 D scroll pumps, and two SL80 turbomolecular pumps. A detailed presentation of the calculations regarding the dimensioning of the backing pump system is presented in appendix D. Within this chapter the fundamental starting consideration for the layout of the prevacuum system are considered and their final outcome and conclusions based on the calculations of appendix D is presented in the end of this section.

<sup>9</sup> corresponding to the in table 2.17 chosen starting parameters  $p_o$ ,  $d_N$ ,  $d_{Sk}$  and  $T_o$ .

<sup>10</sup> 10% reflection on the sample surface and a  $d_{MS} = 50 \mu\text{m}$  *middle stop* diameter of the *zone plate*.

Basically there are two main points to consider when it comes to the layout of the prevacuum system for NEMI:

1. Are the intended backing-pumps strong enough to deal with the helium flow in the system.
2. Any helium back-flow back into the PST/ZPC/SDC - UHV chambers has to be prevented.

The first point is particularly important in regard to the *source chamber (SC)* prevacuum system. The high *helium* flow from that chamber can lead to a significantly high stress on the backing pump system which as a consequence can lead to a considerable reduction of the pumping performance of the two implemented turbo-pumps for this chamber.

The second point on the other hand is important for all the other UHV chambers of the system especially the *sample/detector* chamber. Possible *helium-backflow* leads to a high background signal for the detection process and hence it will downgrade or even prohibit good measurement results.

It was decided to work with two separate backing-pump systems for the setup. One prevacuum line thereby is in charge of evacuating the high helium flow of the *source chamber*. The other one takes care of the fore-vacuum for the *pumping stage chamber/zone plate chamber* and the *sample/detector chamber* together.

In appendix D a detailed description for the calculation of the vacuum conductance factors for both systems is presented. This calculations are based on the fact that the systems will work in the *knudsen-flow* regime which is the case as also shown in the same appendix. Therefore following [60] the vacuum conductance values for each prevacuum component of the systems can be determined based on

$$C = C_m \cdot J \tag{2.51}$$

with  $C_m$  describing the vacuum conductance for molecular flow, and  $J$  a transformation factor. The exact explanation and relation for this formula is presented in D.3 and the foregoing description for vacuum conductance and flow regimes in appendix D.

Similar to the treatment of electrical connections and their resistance values also in the case of vacuum conductance an overall/total conductance value for the whole prevacuum system can be calculated by summing up each



component's conductance value  $C$  either in a *serial* or a *parallel* connection. In the end this total conductance  $C_{total}$  can be included for the determination of the *effective pumping-speed* of the prevacuum system which is defined as:

$$\frac{1}{S_{eff}} = \frac{1}{S_p} + \frac{1}{C_{total}} \quad (2.52)$$

$S_p$  thereby is the *pumping-speed* of the prevacuum pump which is stated by the manufacturer.

Together with the in section 2.2 calculated helium flow  $\dot{N}_o$  in each UHV chamber it is possible to determine the finally appearing prevacuum pressure of the backing-line (see equation D.35)

$$\bar{p}_{prevac} = \frac{\dot{N}_o \cdot k \cdot T}{S_{eff}} \quad (2.53)$$

Based on this prevacuum pressure on the other hand it is possible to make a statement on point 1 stated in the beginning of this chapter. That is to say if the intended backing-pumps accomplish the demands. For a proper efficiency of the turbo-molecular pumps implemented into the system they need to be provided with a prevacuum pressure below a certain range. Exceeding this backing-pressure value will lead to a progressively collapsing of the turbo-pumps compression ratio and therefore its efficiency. Diagrams provided by the pump manufacturers show the compression ratio characteristic behavior with respect to the provided prevacuum pressure of a system. In general it can be said that a backing-pressure located in the range below ca.  $1 \cdot 10^{-1}$  mbar will not significantly influence the optimum pumping speed and compression of the MAG W turbo pumps.

In the following the conclusions from the evaluation process of the two backing-pump systems for NEMI are presented. The detailed calculations and considerations on which these conclusions are based on can be found in appendix D.

### 2.3.1 *Prevacuum-line source chamber (SC)*

A schematic diagram presenting all the vacuum components building up the prevacuum-line for the *source chamber* is illustrated in figure 2.14. Based on

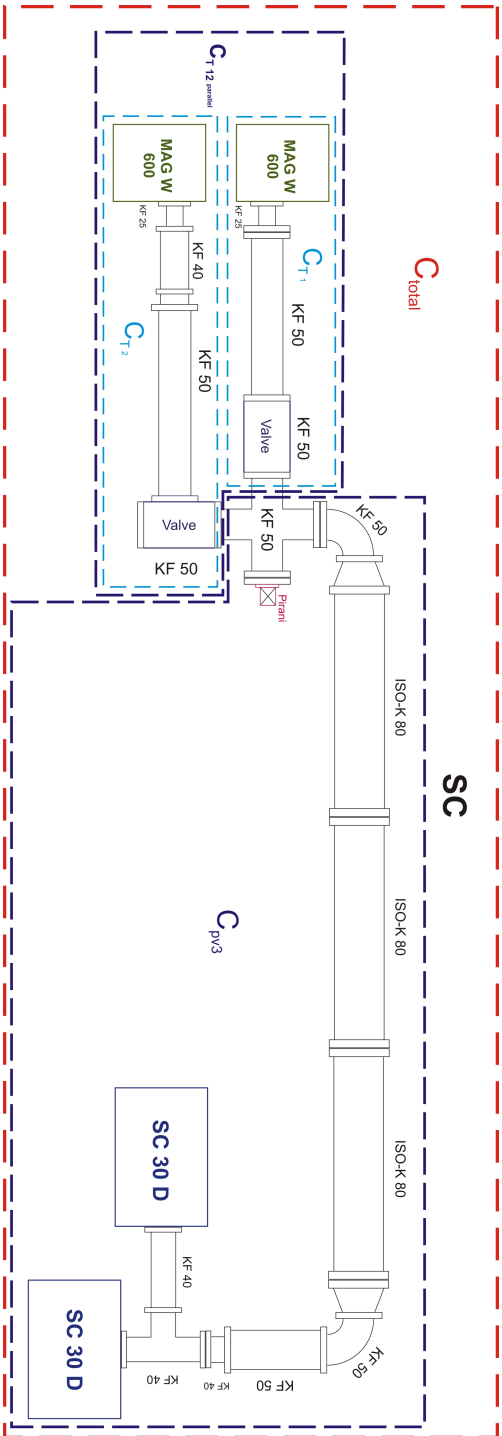


Figure 2.14: Principle sketch of the setup for the Source Chamber prevacuum line components.

this diagram the total conductance of this system  $C_{total}(SC)$  and furthermore the *effective-pumping speed* of this backing-pump line  $S_{eff}(SC)$  is calculated in section D.7.

The crucial point for this fore-vacuum setup is the high *helium* flow originating in the source chamber. Due to this strong load on the backing system it was decided to implement two SC 30 D SCROLLVAC backing pumps. The calculations from appendix D showed that for nozzle parameters of  $d_{Nozz} = 10 \mu\text{m}$ ,  $T_o = 100 \text{ K}$  and  $p_o = 200 \text{ bar}$  the achieved prevacuum pressure will lie in the range of ca. 1 mbar. As a consequence of this high prevacuum pressure the efficiency of the two MAG W 600 turbo-pumps used for the pumping of the source chamber is decreased substantially ( see D.7). The finally achieved end-pressure  $p_{end}$  for the UHV part of the *source chamber* would for this starting conditions be located in the area around  $2 \cdot 10^{-2} \text{ mbar}$  which is not sufficient enough to provide a proper undisturbed *free-jet-expansion*. Consequently for these *beam parameters* the current backing-pump setup is not suitable for high beam pressures  $p_o$ .

The same calculations done for a  $d_{Nozz} = 5 \mu\text{m}$  nozzle (see section D.7) show that for the start parameters of  $p_o = 180 \text{ bar}$  and a liquid nitrogen cooled beam ( $T_o = 100 \text{ K}$ ) the final *source chamber* UHV pressure will be around  $p_{end}(SC) = 2.5 \cdot 10^{-3} \text{ mbar}$ . This means that again for high beam pressures  $p_o$  the limits of the fore-vacuum system are reached but for lower beam pressures  $p_o$  the system is sufficiently strong enough which is also established by the measurements results presented in section 9.1 gained with the NEMI setup. In case of a room temperature beam on the other hand the current prevacuum setup will provide a good *free-jet expansion* even in the high pressure ranges around  $p_o = 200 \text{ bar}$ . Also for this case measurement results are presented in the same section.

Finally it can be said that the prevacuum-system layout for the source chamber is adequate for measurements with a room temperature beam as well as for a liquid nitrogen cooled beam at beam pressures up to  $p_o = 80 \text{ bar}$ . For beam parameters exceeding this numbers the additional implementation of a backing-pump with a higher pumping speed value is suggested, for example an additional roots-pump.

### 2.3.2 *Prevacuum-line pumping stage/zone plate/sample detector chamber (PST/ZPC/SDC)*

In case of the second prevacuum-system the focus is not on a high helium flow but rather on the *helium back-flow*. The previously performed calculations of chapter 2.2 showed that the arising helium flow within the PST/ZPC/SDC all together is rather small compared to the one of the source chamber. Therefore it was decided to use one backing-pump system for all three chambers. A schematic diagram presenting all components of this backing-vacuum line is illustrated in figure 2.15.

The increase in the prevacuum pressure due to the additional helium flow from the *free-jet expansion* is about  $2 \cdot 10^{-6}$  mbar and is negligible small (see section D.8). The measurements performed on NEMI also confirmed this situation as one can see from the diagrams presented in chapter 9.

The significant point regarding this pre-vacuum system is to prevent any *helium gas* back flow from the prevacuum-system back into the UHV chambers since this would lead to an increase in the background-signal for the measurements. For the reason of probably very small pressure rises in the detected measurement signals of our microscope an as low as possible background pressure is needed. This is necessary to ensure that the whole system is sensitive enough for measuring even small signal changes located in the lower  $10^{-10}$  mbar range in the detected reflection signal.

To achieve a prevention for such *helium gas* back-flow two additional small SL 80 turbo pumps are attached into the prevacuum line for this three chambers. Thereby one of them is in charge of the PST/ZPC together whereas the second one covers the most sensitive *sample/detector chamber* itself. In both cases the small turbo-pumps act as a kind of back-flow barrier.

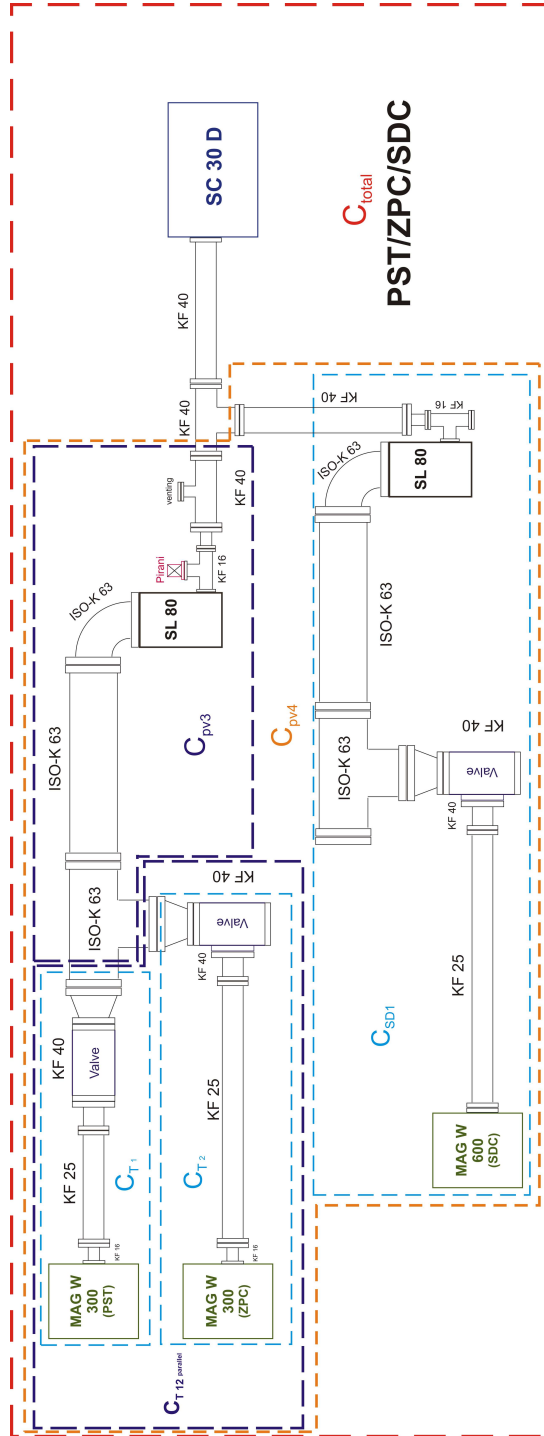


Figure 2.15: Principle sketch of the setup for the pumping stage- / zone plate- / sample detector-chamber prevacuum line components.

## 2.4 ULTIMATE PARAMETERS AND SETTINGS

All considerations done within the prior chapters show that the chosen ultra high vacuum pumps as well as the components determining the backing vacuum system are sufficient to run the system. It was also shown that the expected particle flow within the *helium* detection system is high enough to anticipate good results. The final setup with its pumps and also the optical element parameters like skimmer size and aperture sizes are listed up once more in table 2.19 and 2.20. The respective parameters are presented for the finally used microscope setup, and therefore also the skimmer and nozzle sizes are adjusted to the proper parameters and not the worst case scenarios for the pumping system. A graphic presenting all this elements and their finally chosen parameters is given in 1.3 (see chapter 1).

FINAL NEMI SETUP PARAMETERS		
	Diameter	Relevant Distance
Nozzle	$d_N = 5 \mu\text{m}$	
Skimmer	$d_{Sk} = 1 - 5 \mu\text{m}$	$L_{Nozzle-Skimmer} = 10 \text{ mm}$
Aperture 1	$d_{App_{PST-ZPC}} = 5 \text{ mm}$	$L_{Skimmer-Ap1} = 0.717 \text{ m}$
Zone Plate (ZP)	$d_{ZP} = 192 \mu\text{m}$	$L_{Skimmer-ZP} = 0.935 \text{ m}$
Aperture 2	$d_{App_{ZPC-SDC}} = 5 \text{ mm}$	$L_{Skimmer-Ap2} = 1.011 \text{ m}$
Sample		$L_{Skimmer-Sample} = 1.140 \text{ m}$

Table 2.19: Final setup parameters and elements for the NEMI helium microscope system

# Final NEMI Setup

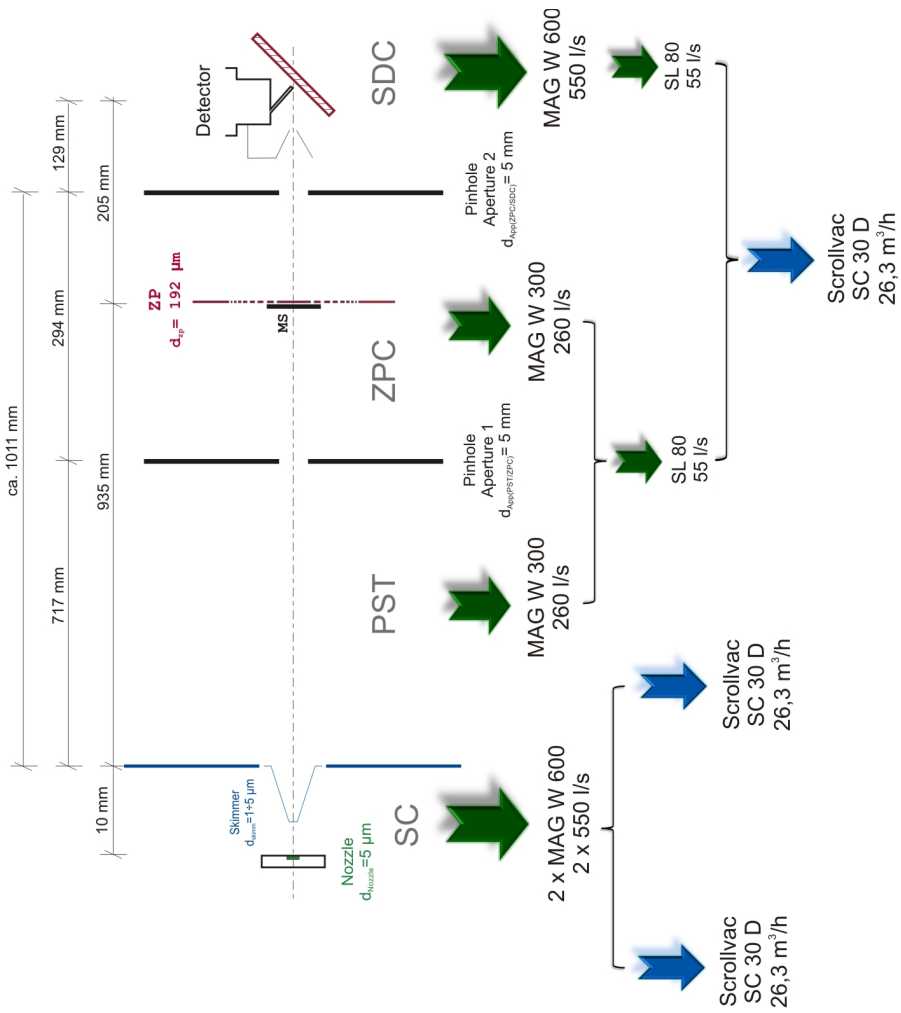


Figure 2.16: NEMI setup sketch with the finally chosen parameters

FINAL NEM1 PUMPING SETUP			
	Ultra High Vacuum (UHV)	Backing Vacuum (BV)	
Source Chamber (SC)	2 x MAG W 600 (2 x 550 l/s)	2 x SCROLLVAC SC30D (26.3 m <sup>3</sup> /h)	
Pumping Stage (PST)	MAG W 300 (260 l/s)	SL 80 (55 l/s)	SCROLLVAC SC30D (26.3 m <sup>3</sup> /h)
Zone Plate Chamber (ZPC)	MAG W 300 (260 l/s)		
Sample/Detector Chamber (SDC)	MAG W 600 (550 l/s)	SL 80 (55 l/s)	

Table 2.20: Final NEM1 pumping setup parameters



## SOURCE

---

The generation of an almost monochromatic neutral gas probe beam is a basic requirement to build up a neutral matter-wave reflection microscope based on zone plate focusing. In this chapter the creation of atomic beams is discussed. Three important concepts, **final average speed**, **virtual source size** and **speed-ratio** are explained.

### 3.1 THEORETICAL BACKGROUND FOR A FREE JET EXPANSION

#### 3.2 EFFUSIVE BEAMS

For an expansion of a gas from a reservoir into a low pressure ambient background chamber via a small orifice one can distinguish between two different regimes [63]. In both cases the gas leaves a reservoir which has the initial equilibrium condition of an internal gas pressure  $p_o$ , a reservoir temperature  $T_o$  and an exiting orifice diameter or nozzle diameter  $d_N$ . The background pressure of the chamber into which the gas expands will be referred to as  $p_B$ . The distinction between the two expansion regimes is based on two parameter values, the *mean-free-path*  $\lambda_o$  of the molecules in the reservoir and its exiting orifice diameter  $d_N$ . The *mean-free-path* is defined as the average traveling distance of an atom (molecule) between successive collisions with other atoms (molecules) (see chapter D.1).

In cases where the *mean-free-path* is longer than the expansion orifice diameter and hence  $\lambda_o \gg d_N$ , the atoms suffer nearly no collision on their way through the nozzle. The beam generated under this conditions is referred to as an *effusive beam* [63]. An *effusive beam* has a velocity distribution for the exiting atoms which is only dependent on the energy they gained from collisions with the reservoir wall. Hence it depends on the reservoir temperature  $T_o$ , as well as on their own mass  $m$ . It can be written as [63]:

$$F(v_x) = \frac{2}{\alpha^4} \cdot v_x^3 \cdot \exp\left(\frac{-v_x^2}{\alpha^2}\right) \quad (3.1)$$

$$\alpha = \sqrt{\frac{2 \cdot k \cdot T_o}{m}}$$

with  $v_x$  the mean velocity at point ( $x$ ),  $k$  the BOLTZMANN constant,  $T_0$  the reservoir temperature and  $m$  the atom (molecule) mass of the beam particles. As one can see equation 3.1 is a MAXWELL BOLTZMANN distribution. The average velocity of the atoms is:

$$\bar{v} = \sqrt{\frac{8 \cdot k \cdot T_0}{\pi \cdot m}} \quad (3.2)$$

### 3.3 FREE JET EXPANSION

The second expansion case is called a *free-jet-expansion* sometimes referred to as *supersonic expansion*. By increasing the gas pressure  $p_0$  within the reservoir or by reducing the expansion diameter  $d_N$ , the *mean-free-path* becomes smaller than the nozzle diameter. When  $d_N \gg \lambda_0$  the atoms/molecules leaving the nozzle experience many collisions. Therefore the assumption of molecular flow is no longer satisfied during the initial stage of the expansion. A high pressure gas expansion of this type is called a *free-jet expansion* and it generates a high intensity particle beam with a comparatively small, nearly monochromatic velocity spread. Following the expanding particles their propagation can be described by the transition between two different flow regimes. At high gas pressures  $p_0$  and with the restriction to short and converging nozzles, effects of gas viscosity namely friction and energy loss due to heat transfer can be neglected. This means that the expansion can be treated as adiabatic and isentropic. Directly after leaving the nozzle the gas density is high. Consequently the collision frequency of the particles is sufficiently high to be assumed that there is an equilibrium state maintained throughout the expansion process [63]. Therefore within this region the particles can be treated with an idealized continuum model. As the free-jet further expands into the vacuum its density decreases rapidly with increasing distance from the nozzle which is described as a transition area from continuum flow to free molecular flow. Due to the low enough background pressure  $p_B$  into which the particles are expanding there will be a point at which the collision frequency of the particles has decreased to such a low value that the continuum model no longer holds - this is called the quasi molecular flow regime. Finally all collisions have ceased, and the particles propagate freely on straight trajectories.

In all the following equations  $m$  stands for the beam particle (atom or molecule)

mass,  $k$  is the BOLTZMANN constant,  $T_o$  the reservoir temperature,  $v_f$  is the final average particle speed, and  $v_x$  the particle velocity in  $x$  direction.

### 3.4 FINAL AVERAGE SPEED OF A MONOATOMIC GAS

Following the literature by M.D. Morse [63] the beam particles energy in the molecular flow region and hence its ultimate flow velocity can be deduced from the assumption that the expansion can be treated as adiabatic and isentropic. Therefore the particle's speed will be directly related to the thermal energy of the atoms. The adiabatic assumption leads to a conservation of the sum of the enthalpy and the kinetic energy of the directed mass flow [63]

$$h + \frac{1}{2}mv^2 = \text{constant} \quad (3.3)$$

where  $h$  states the enthalpy of the expanded gas per atom,  $v$  the average flow velocity of the expanded gas atoms and  $m$  the particle (atom) mass. Since this sum of the enthalpy and the kinetic energy has to be constant it is also equal to the enthalpy of the gas in the source reservoir  $h_o$  (per atom). For a monoatomic ideal gas this is defined as

$$\begin{aligned} h_o &= c_p \cdot T_o \\ &= \frac{\gamma}{\gamma - 1} \cdot k \cdot T_o \\ &= \frac{5}{2}kT_o \end{aligned} \quad (3.4)$$

As equation 3.4 shows the enthalpy  $h_o$  is directly proportional to the reservoir (nozzle) temperature  $T_o$ . Hence a change of the nozzle temperature will lead to a change in the particle beams energy. The constant of proportionality thereby is the *heat capacity for constant pressure*  $c_p$ . It can be found from the heat capacity ratio  $\gamma$  for a monoatomic gas multiplied by the BOLTZMANN constant  $k$ .

$$c_p = \frac{\gamma}{\gamma - 1} \cdot k \quad (3.5)$$

$$\gamma = \frac{f + 2}{f} \quad (3.6)$$

$\gamma$  depends on the *degrees of freedom* of the molecule/atom which in case of helium (a monoatomic gas) is given by three translational degrees of freedom

$f = 3$ .

From equations 3.3 and 3.4 one finds the average final flow velocity  $v_f$  within the particle beam to be

$$h_o = 0 + \frac{1}{2}mv_f^2 \quad (3.7)$$

$$\frac{5}{2}kT_o = \frac{1}{2}mv_f^2 \quad (3.8)$$

$$v_f = \sqrt{\frac{2h_o}{m}} = \sqrt{\frac{5kT_o}{m}} \quad (3.9)$$

Note the difference of  $v_f$  (e.q. 3.9) to the average atom velocity in an effusive source  $\bar{v}$  (see e.q. 3.2). It is possible to say that  $h$  can be set to  $h = 0$  when the gas has fully expanded into the vacuum. This is the case for the molecular flow region of the beam. The final average flow velocity  $v_f$  of the *free-jet expansion* beam is also often referred to as “*terminal velocity*” or “*terminal speed*”. In this thesis further on it is referred to as *final average speed* or *final average velocity*. As shown in chapter 4.3 a de BROGLIE wavelength  $\lambda_{He}$  of the beam can be directly related to this velocity. Also it is possible to calculate the beams energy  $E$  (particle energy) from equation 3.7

$$E = \frac{1}{2}m \cdot v_f^2 \quad (3.10)$$

To get a feeling for the magnitudes of the just mentioned values, a room temperature  $T_o = 300\text{ K}$  neutral helium beam has the following properties:

$$\begin{aligned} v_{fHe} &\approx 1765\text{ m/s} \\ E &\approx 65\text{ meV} \\ \lambda_{He} &\approx 0,565\text{ \AA} \end{aligned} \quad (3.11)$$

### 3.5 VIRTUAL SOURCE

The boundary between the continuum flow and the molecular flow is named “*quitting surface*”. After this surface the particles follow straight trajectories and have a fixed kinetic energy. Hence from this point on it is possible to apply geometrical optics to the beam (straight trajectories, constant particle wavelength for each atom respectively).

If one traces the straight trajectories backwards an area of least confusion can

be found where all atom trajectories passes through a minimum cross section. This cross section defines the spatial intensity distribution of the source, the so called "*Virtual Source*" [68]. It can be seen as the plane defining the source size and position in regard to geometrical optics. The width of the virtual source and its location depends on the nozzle diameter, the source pressure and the source temperature [69]. It can be approximated well by two Gaussian functions [69]. For our application an additional beam size defining element, the skimmer, is placed after the virtual source plane to ensure a small object size entering into the GAUSSIAN LENS FORMULA (see e.q. 4.16). The skimmer in this case defines a new source plane located at the skimmer orifice position. A schematic illustration of the virtual source is presented in figure 3.1. By back tracing the particles stream lines straight from the quitting surface the virtual source plane and its corresponding perpendicular speed distribution can be found. This is presented in figure 3.1 for one direction [69, 70].

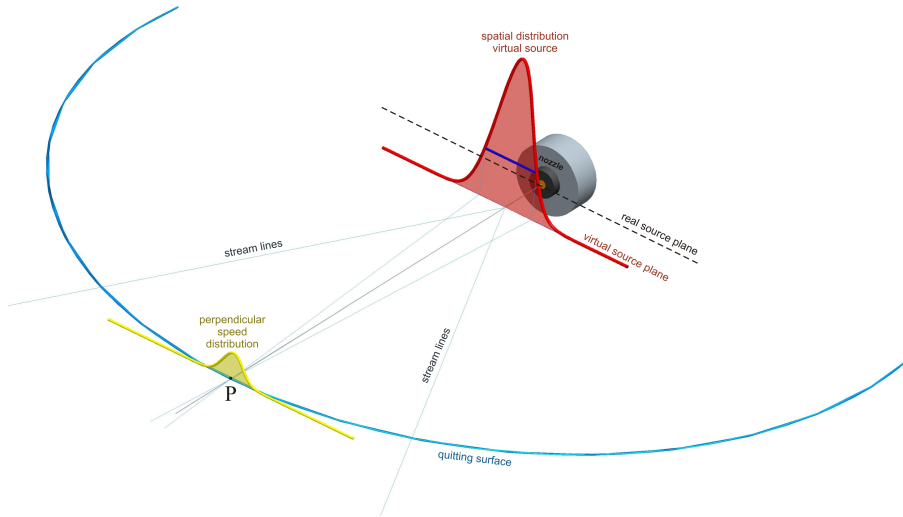


Figure 3.1: Schematic illustration of the relation between the spatial intensity distribution of the virtual source and the perpendicular speed distribution of the particles passing through point  $P$ . From the perpendicular speed distribution of the particles in point  $P$  (located at the quitting surface) it is possible to find the spatial distribution of the virtual source and its source plane. After the gas particles exit the nozzle they initially propagate within a continuum flow regime symmetric around the beam axis. Since during the expansion the density of the gas declines and hence the mean free path length increases the continuum flow regime transforms continuous into a molecular flow regime. After a distance of a view nozzle diameters they reach a point from which it is possible to assume that they propagate further on purely within the molecular flow regime on straight trajectories. The area of this final transition into molecular flow is named *quitting surface*. By back tracing the particles on straight trajectories it is possible to find the location (plane) of the virtual source. Its spatial distribution can be deduced from the perpendicular speed distributions of the particles in point  $P$  following the model presented by Thomas Reisinger et al.[69, 70].

## 3.6 VELOCITY DISTRIBUTION AND SPEED RATIO

Similar to the *effusive beam* the *free-jet beam* is also characterized by a velocity distribution of the participating atoms/molecules. It is common in literature to express the velocity distribution of a *free-jet beam* by two temperatures. The temperature of the beam along the beam axis  $T_{\parallel}$  and the temperature perpendicular to this direction  $T_{\perp}$ . The velocity distribution along the beam direction  $x$  is described by a MAXWELL BOLTZMANN distribution [71]:

$$f(v_x) = \sqrt{\frac{m}{2\pi k T_{\parallel}}} \cdot \exp\left(\frac{-m \cdot (v_x - v_f)^2}{2k T_{\parallel}}\right) \quad (3.12)$$

with the standard deviation of the normal distribution defined by

$$\sigma(v) = \sqrt{\frac{k \cdot T_{\parallel}}{m}} \quad (3.13)$$

A measure for the width of the velocity distribution of atom/molecule beams is given by the “*speed-ratio*”. This parameter is defined by the following equation [59].

$$S = \sqrt{\frac{m \cdot v_f^2}{2 \cdot k \cdot T_{\parallel}}} \quad (3.14)$$

As shown in section 8.2.2 the *speed-ratio* can be directly related to the measured speed distribution using equation 3.15.

$$S = 2 \cdot \sqrt{\ln 2} \cdot \frac{v_f}{\Delta v} \quad (3.15)$$

*Free-jet beams* with small velocity distributions used for example in beam scattering experiments can reach speed ratio values higher than 300.





## FOCUSING ELEMENT

---

*This chapter presents an overview over the theory behind Fresnel zone plates. The final part discusses the fabrication of these elements.*

### 4.1 BACKGROUND

Focusing of neutral atom or molecular beams is based on *de BROGLIE's* theorem of *matter-waves*, stating that any matter particle has a corresponding wavelength and therefore is subjected to the *wave-particle duality* [24]. Hence it is possible to assign a wavelength to atoms and molecules in correspondence to their momentum following *de Broglie's* relation

$$\lambda = \frac{h}{p} = \frac{h}{m \cdot v} \quad (4.1)$$

where  $\lambda$  is the particles wavelength,  $p$  its momentum,  $m$  the particles mass,  $v$  its velocity and  $h$  the PLANCK constant (relativistic effects ignored).

Since the *de Broglie* wavelength of particles (matter waves) lies in the Ångström regime or even below for the energies relevant here, the corresponding diffraction gratings for such waves have to be periodical structures with a lattice constant in the nanometer or even sub-nanometer range.

Therefore only the strong improvement in the field of nano-structuring technology within the last two decades made it possible to start producing transmission diffraction gratings and zone plates for the use as optical elements for atom and molecular beams. One main feature of such diffraction gratings is that they have to be free standing structures to enable the particles to pass through the optical element. This is the main difference to the *zone plate* elements customarily employed for X-ray and neutron optics [51].

A *Fresnel Zone-Plate* (ZP) can be described as a circular diffraction grating with radially increasing line densities. Therefore it can be seen as a pattern

of alternating opaque/impermeable and transparent/transmissive rings [64].

The ring pattern of a “*Fresnel Zone Plate*” is based on the “*Fresnel Zone Construction*” [72, 64, 51]. An easy way to describe this pattern is to picture a spherical propagating wave front originating from an object at point  $P$  (see figure 4.1). This wavefront is divided into a set of *Fresnel zones* by spheres centered at point  $P'$  which are differing in their radius by  $\lambda/2$ . Radiation

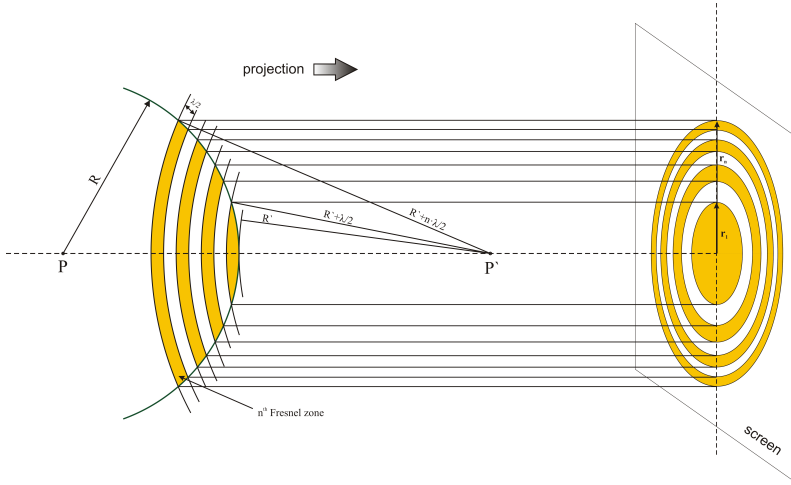


Figure 4.1: Schematic for the *Fresnel zone construction*. A Spherical wave front (radius  $R$ ) which is propagating from point  $P$  is divided into a set of *Fresnel zones* by spheres centered at point  $P'$  with radii  $R' + n \cdot \lambda/2$  for  $n = 1 \rightarrow N$ . The radius of the dividing spheres is increasing with a period of  $\lambda/2$ . The *zone plate* geometry can be pictured as the projection of the originating zones on the divided spherical wavefront onto a screen when every second zone is set to be transmissive.

transmitted from adjacent zones will have opposite signs of phase and will nullify each other (each transmissive or opaque ring is on zone). Hence a blocking/removing of either all even or odd zones will lead to an increase of radiance in point  $P'$  proportional to the number of zones. The ZP geometry is described by the following equation (neglecting the higher power terms) [51, 64, 72]:

$$r_n^2 = n \cdot f_1 \cdot \lambda \tag{4.2}$$

with  $r_n$  the radius of the  $n^{\text{th}}$  zone ( $n = 1, \dots, N$ ),  $f_1$  the first order focal length of the zone plate and  $\lambda$  the particles wave length.

In case of a given/fixed outermost *zone plate* radius  $r_N$  for a ZP with  $N$  zones, equation 4.2 can be transformed to represent a formula for the corresponding first order focal length of the ZP.

$$f_1 = \frac{r_N^2}{N \cdot \lambda} \quad (4.3)$$

Just as any other diffraction grating also *zone plates* have subsidiary diffraction orders so to speak higher-order foci. For the higher order focal lengths of the ZP, equations 4.2 and 4.3 alternate to

$$r_n^2 = m \cdot n \cdot f_m \cdot \lambda \quad \text{and} \quad f_m = \frac{r_N^2}{m \cdot N \cdot \lambda} \quad (4.4)$$

with  $f_m$  being the focal length for the  $m^{\text{th}}$  diffraction maximum ( $m = 0, 1, \dots$ ).

The ZP's focusing function is purely based on a quantum mechanical effect namely on the diffraction of particles on the grating structure. They don't influence the excitation state of the atoms or molecules and they are also not able to break apart bondings within a molecule [51].

As long as there is no strong interaction between the particles and the ZP material, and as long as the particles can be considered to be of point shape it is in principle possible to apply classical optics to the ZP. (point shape is not valid anymore in case of big molecules [73])

The deviations from this classic mechanical point of view can be treated by additional implementation of quantum mechanics and hence taking into account *van der Waals interaction* [74, 75]. In the case of neutral helium atom beams though this additional effect can be ignored [76, 51].

From looking at equations 4.3 and 4.4 it is obvious that a change in the wavelength  $\lambda$  will influence the focal length which means that ZPs suffer from chromatic aberration. By differentiation of the right formula of equation 4.4 with respect to  $\lambda$  one can see that the influence of the chromatic aberration of a ZP gets smaller for higher order foci. A discussion on the impact of this aberration effect on the finally accomplishable focal spot diameter for the microscope setup of *Nemi* is presented in section 4.2.

The diffraction efficiency  $\eta_m$  of every particular order  $m$  is defined as the ratio between the intensity  $I_m$  which is transmitted into the diffraction order and the total intensity  $I_{total}$  which is incident on the ZP. It can be written as [51]

$$\eta_m = \frac{I_m}{I_{total}} = \left( \frac{\sin \left[ \frac{a}{d} m \pi \right]}{m \pi} \right)^2 \quad (4.5)$$

where  $a$  is the width of the transparent zone,  $d$  is the width of a zone pair consisting of an opaque and a transmissive zone and  $a/d$  is defined as the opening ratio of the zone plate.

From the equation it can be found that the diffraction efficiency gets a maximum in case of a  $a/d$  open ratio of 0.5 (meaning that 50% are blocked). The corresponding efficiencies are presented in equation 4.6.

$$\text{Efficiency} = 1/4, 1/\pi^2, 1/9\pi^2, \dots, 1/m^2\pi^2 \quad (4.6)$$

It can be seen that for an optimal ZP 25% of the incident beam intensity goes into the 0<sup>th</sup> order part of the beam, whereas 10.1% are transmitted into the 1<sup>st</sup> order focus. This shows that it is crucial to block out the 0<sup>th</sup> order contribution which overlaps with the first order focal spot. To achieve this an additional *middle stop disc* (central disc) is implemented onto the center of the ZP ring pattern.

#### 4.2 ZONE PLATE ABERRATIONS AND RESOLUTION

The resolution of a ZP and therefore the smallest resolvable distance  $\delta$  between two incoherent point sources is approximately determined by the width of the smallest (outermost) zone [51]. For the first order focal spot this resolution can be more accurately describes by

$$\delta = 1,22 \cdot dr_N$$

with  $dr_N$  being the width of the outermost *Fresnel zone*.

In case of polychromatic radiation impinging onto the ZP the resolution is influenced by the wavelength distribution. This effect of chromatic aberration can be determined from equation 4.3 which shows that the focal length of a

ZP is indirectly proportional to the diffracted wavelength.

The transversal width  $d_p$  of the chromatic *point spread function (PSF)* of a Fresnel ZP is given as [44, 64]:

$$d_p = \frac{r_N}{\lambda/\Delta\lambda} \quad (4.7)$$

Herein  $r_N$  denotes the radius of the ZP and  $\Delta\lambda$  describes the shift in the wavelength  $\lambda$ . This relation can be deduced by the following considerations:

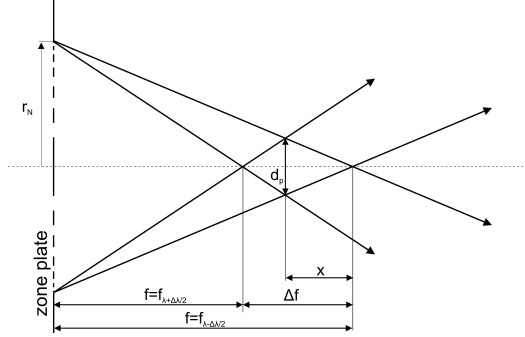


Figure 4.2: Schematic illustrating the point spread function (PSF) of a Fresnel zone plate. The relations between the longitudinal and transversal chromatic aberration are illustrated.

The longitudinal chromatic aberration  $\Delta f$  due to polychromatic illumination with a wavelength shift of  $\lambda + \Delta\lambda/2$  and  $\lambda - \Delta\lambda/2$  is illustrated in figure 4.2 [64]. By looking at the displayed similar triangles it can be seen that

$$\frac{\frac{d_p}{2}}{\Delta f - x} = \frac{r_N}{f} \quad (4.8)$$

and

$$\frac{\frac{d_p}{2}}{x} = \frac{r_N}{f + \Delta f} \quad (4.9)$$

From eq. 4.8 and 4.9 follows

$$d_p = \frac{r_N}{\frac{f}{\Delta f} + \frac{1}{2}} \quad (4.10)$$

Furthermore from figure 4.2 and eq. 4.3 it can be found that eq. 4.11 has to be satisfied.

$$\frac{f}{\Delta f} + \frac{1}{2} = \frac{f_{\lambda + \frac{\Delta\lambda}{2}}}{f_{\lambda - \frac{\Delta\lambda}{2}} - f_{\lambda + \frac{\Delta\lambda}{2}}} + \frac{1}{2} = \frac{\lambda}{\Delta\lambda} \quad (4.11)$$

Finally combining eq. 4.11 and 4.10 leads to relation 4.7.

The speed ratio  $S$  of a molecular/atom beam is a measure for its monochromatic quality [44].

$$S = 2\sqrt{\ln(2)} \frac{v}{\Delta v} \simeq 2\sqrt{\ln(2)} \frac{\lambda}{\Delta\lambda} \quad (4.12)$$

From section 3.6 and 8.2.2 the speed ratio  $S$  of a *free-jet expansion* beam is known to be related to the parallel speed distribution of the beam particles by the left side of equation 4.12. Therefore it can be found that it is likewise related to the *de Broglie* wavelength distribution as denoted on right side of the same equation.

This can be followed by considering

$$\begin{aligned} \Delta v &= \frac{\hbar}{m \cdot (\lambda + \frac{\Delta\lambda}{2})} - \frac{\hbar}{m \cdot (\lambda - \frac{\Delta\lambda}{2})} = \\ &= -\frac{\hbar \cdot 2 \cdot \frac{\Delta\lambda}{2}}{m \cdot \left(\lambda^2 - \left(\frac{\Delta\lambda}{2}\right)^2\right)} = \\ &= -\frac{2 \cdot \hbar \cdot \frac{\Delta\lambda}{2}}{m \cdot \lambda^2 \cdot \left(1 - \frac{\left(\frac{\Delta\lambda}{2}\right)^2}{\lambda^2}\right)} \end{aligned}$$

and further deriving

$$\begin{aligned} \frac{\Delta v}{v} &= \frac{\frac{\hbar}{m \cdot \lambda}}{\frac{2 \cdot \hbar \cdot \frac{\Delta\lambda}{2}}{m \cdot \lambda^2 \cdot \left(1 - \frac{\left(\frac{\Delta\lambda}{2}\right)^2}{\lambda^2}\right)}} = \\ &= -\frac{\lambda \cdot \left(1 - \frac{\left(\frac{\Delta\lambda}{2}\right)^2}{\lambda^2}\right)}{2 \cdot \frac{\Delta\lambda}{2}} = \\ &= -\frac{\lambda}{2 \cdot \frac{\Delta\lambda}{2}} \cdot \left(1 - \frac{\left(\frac{\Delta\lambda}{2}\right)^2}{\lambda^2}\right) \simeq -\frac{\lambda}{2 \cdot \frac{\Delta\lambda}{2}} \quad (\text{for } \lambda \gg \frac{\Delta\lambda}{2}) \end{aligned}$$

Hence for  $\lambda \gg \Delta\lambda/2$  it can be said that

$$\frac{v}{\Delta v} \simeq \left| \frac{\lambda}{\Delta\lambda} \right| \quad (4.13)$$

Therefore it is possible to assess the chromatic broadening  $d_p$  (width transversal PSF) of a ZP's first order focal spot by

$$d_p = 2\sqrt{\ln(2)} \cdot \frac{r_N}{S} \quad (4.14)$$

In the case of focusing a free-jet expansion neutral helium beam this chromatic aberration is the largest aberration effect influencing the ZP and therefore defines the shape and size of the focal spot. From [77] it is known that in order to achieve diffraction-limited focusing, a speed ratio roughly larger than the number of zones on the zone plate is needed. From equation 4.14 it can be also concluded that the higher the speed ratio value  $S$ , the smaller the effect of chromatic aberration. One way to enhance  $S$  is to work with a cooled free-jet beam. A decrease of the zone plate radius  $r_N$  however is no reasonable option since it will be accompanied by a decrease of the focal spot intensity.

Other aberrations such as *spherical aberration*, *coma* and *astigmatism* have an influence [64]. *Spherical* aberration for example leads to a corresponding optimum number of zones for a zone plate which for the first order focus spot is determined by [64]

$$N_{opt} = \sqrt{2} \cdot \frac{r_1}{\lambda} \quad (4.15)$$

with  $r_1$  being the radius of the first zone. We see that for wavelengths in the Ångström range, there is no practical limitation to the number of zones.

#### 4.3 ATOM OPTICAL PARAMETERS

For zone plates with zone numbers  $N$  bigger than 100 the optical properties of a zone plate can be treated the same way as for a thin diffraction lens with the focal length  $f$  [78, 51].

The evaluation of the expected focal spot size basically starts out the same way as for any geometrical optics system and therefore is based on the LENSMAKER'S

equation which is also often referred to as *thin-lens-equation*. Since the ZPs used for the instrument presented within this thesis have zone numbers bigger than  $N = 100$  it is possible to apply the GAUSSIAN LENS FORMULA (4.16) [72].

$$\frac{1}{f} = \frac{1}{g} + \frac{1}{b} \quad (4.16)$$

with  $f$  being the focal length,  $g$  determining the object distance and  $b$  the image distance.

The transverse magnification of the system is given by formula 4.17 [72].

$$M = \frac{b}{g} \quad (4.17)$$

As mentioned in chapter 1.1 one of the main starting points for the development of this microscope was to build it as compact as possible to achieve a high probe beam intensity. The working distance (image distance *ZP-sample*)  $b$ , should in principle be as small as possible for the smallest demagnification factor. Restrictions exist for what can be realized technically to still have enough space for the sample-detector handling. Hence  $b$  was set to a fixed number  $b = 205$  mm. Also the *microskimmer* diameters are preset to  $d_{sk} = 1 - 3$   $\mu$ m. This number is based on a compromise between an as small as possible diameter (this value defines the imaged object size) and still as high as possible flow through the *skimmer* orifice. Since in reality the helium beam source does not correspond to a point source, its extended size has to be included in the atom optical considerations. A more realistic picture of the actual spatial intensity distribution of the *free-jet expansion* source is provided by the size and location of its "virtual source" (see section 3.5). From the work presented by Reisinger et al. [79, 69] it is known that the virtual source size depends on the nozzle diameter, the source pressure and the source temperature. Generally it can be said that it is always bigger than the nozzle diameter. Therefore to achieve small focal spots the size of the virtual source is restricted by a *microskimmer* which is placed into the beam-line approximately 10 – 15 mm after the nozzle. From preliminary measurements this distance was found to be long enough to ensure that for all different applied beam pressures and source temperatures the skimmer shape does not interfere with the *free-jet expansion* whilst still being small enough to provide good beam intensities. Hence the skimmer



orifice position is defining the object plane, and its diameter is a measure for the imaged source size. Also the high helium background flow from the source has to be minimized before the beam hits the target. Therefore the system has to include several differential pumping stages leading to a minimum length of the setup.

Based on this considerations the distance between the *skimmer* and the focusing *zone plate* complies to the object distance  $g$  of the atom optical setup. This parameter is chosen so that a better resolution than with a standard optical microscope can be reached while it is still small enough to provide enough intensity in the focused spot (desired focal spot diameter is in the  $0.3\ \mu\text{m}$  range). Therefore  $g$  was set to a value of  $g = 935\ \text{mm}$ . The magnification of the system can now be determined using equation 4.17 and it is found to be:

$$M = 0.219 \quad (4.18)$$

After deciding on this parameters corresponding *Fresnel zone plates* for room temperature and liquid nitrogen cooled beams were produced [65].

Both types of zone plates have a focal length of  $f = 168.14\ \text{mm}$  if utilized in their temperature range.

The difference between the two types originates from different *Fresnel* zone dimensions (patterns), necessary for the two different helium beam wavelengths. For a *free-jet helium* beam we have:

$$\lambda_{He} = \frac{h}{m_{He} \cdot v_{He}} \quad (4.19)$$

$$v_{He} = \sqrt{\frac{5 \cdot k \cdot T_o}{m_{He}}} \quad (4.20)$$

with  $\lambda_{He}$  the de Broglie wavelength of the helium beam,  $v_{He}$  the average speed of the helium atoms in the beam,  $m_{He}$  the mass of a helium atom,  $T_o$  the atom temperature,  $k$  the BOLTZMANN constant and  $h$  the PLANCK constant<sup>1</sup>.

In both cases the outer diameter of the ZP is predefined to a diameter of  $d_{ZP} = 192\ \mu\text{m}$  by the fabrication process.

<sup>1</sup> Planck constant  $h = 6.62618 \cdot 10^{-34}$  [Js].

To reduce the influence of the  $0^{th}$  order part of the beam onto the first order focus spot, the ZPs designed for Nemi were fabricated with two different *middle-stop disc* diameters in particular  $d_{MS1} = 20 \mu\text{m}$  and  $d_{MS2} = 50 \mu\text{m}$ . The two zone plates have about 1000 and 500 rings respectively (see table 4.1)

Thus the fabricated ZPs can be also distinguished by their middle-stop diameters.

FRESNEL ZONE NUMBERS $N_f$		
	$d_{MS1} = 20 \mu\text{m}$	$d_{MS2} = 50 \mu\text{m}$
$RT = 320 \text{ K}$	991	934
$LN = 100 \text{ K}$	554	522

Table 4.1: List presenting the number of *Fresnel-rings*  $N_f$  for the different *zone plate* types fabricated for NEMI. The outer diameter of all ZPs is  $d_{ZP} = 192 \mu\text{m}$ , and their first order focal length is given by  $f_1 = 168.14 \text{ mm}$ . They are fabricated for two different probe beam temperatures ( $RT=320 \text{ K}$ ,  $LN=100 \text{ K}$ ) and with two different *middle-stop* diameters  $d_{MS1} = 20 \mu\text{m}$  and  $d_{MS2} = 50 \mu\text{m}$  respectively.

A detailed sketch of the atom optical setup for NEMI as well as the corresponding distances is presented in figure 1.3.

The diameter of the geometrical image of the source  $d_{op}$  without considering any aberrations can be determined by the object size (source size) and the magnification factor  $M$  of the system. Since the source size is defined by the skimmer diameter the expected focal spot diameter without any aberration effects lies in the range of app. 200 – 1100 nm.

$$d_{op} = M \cdot d_{skimmer} \quad (4.21)$$

#### 4.4 FOCUSED SPOT SIZE

The total focused spot size is a convolution of  $d_{op}$  and the broadening due to chromatic aberration  $d_p$ . In a simple approximation both of this values can be assumed to have a Gaussian distribution. Therefore the value for

the theoretically predicted focal spot diameter  $d_{th}$  can be determined by the square-root sums of the squares of  $d_{op}$  and  $d_p$ .

$$d_{th} = \sqrt{(d_{op})^2 + (d_p)^2} \quad (4.22)$$

Table 4.2 presents the theoretically expected focused spot diameters for the two different beam temperatures of  $T_o(RT) = 320$  K and  $T_o(LN) = 100$  K for a microskimmer diameter of  $d_{sk} = 1 \mu\text{m}$  and  $d_{sk} = 3 \mu\text{m}$  respectively. The speed ratio values utilized for this determination are based on the numbers evaluated for the measurements presented in section 8.

THEORETICALLY EVALUATED FOCUSED SPOT DIAMETER $d_{th}$		
	$d_{sk} = 1 \mu\text{m}$	$d_{sk} = 3 \mu\text{m}$
RT = 320 K	1.43 $\mu\text{m}$	1.56 $\mu\text{m}$
LN = 100 K	0.38 $\mu\text{m}$	0.73 $\mu\text{m}$

Table 4.2: Theoretically expected focal spot diameters for the two different beam temperatures of  $T_o(RT) = 320$  K ( $S = 113.6$ ,  $p_o = 150$  bar) and  $T_o(LN) = 100$  K ( $S = 521.4$ ,  $p_o = 150$  bar) and the two different skimmer diameters of  $d_{sk} = 1 \mu\text{m}$  and  $d_{sk} = 3 \mu\text{m}$  respectively.

The focused spot size is mainly influenced by the chromatic aberration of the ZP.

#### 4.5 ZONE PLATE FABRICATION

The *free-standing silicon-nitride zone plates* were fabricated by Thomas Reisinger at the MIT NANOSTRUCTURES LABORATORY under the supervision of Henry Smith. They were produced using a *scanning electron-beam lithography* (SEBL) process in combination with reactive ion etching. The fabrication process is described in [65] and [70]. Scanning-electron micrographs of free-standing silicon-nitride zone plates for *Nemi* are presented in figures 4.3 and 4.4. Note that the free standing *Fresnel rings* have to be stabilized and held in place by a support-grid structure (radially orientated rod structures crossing the ring pattern in a star shaped manner).

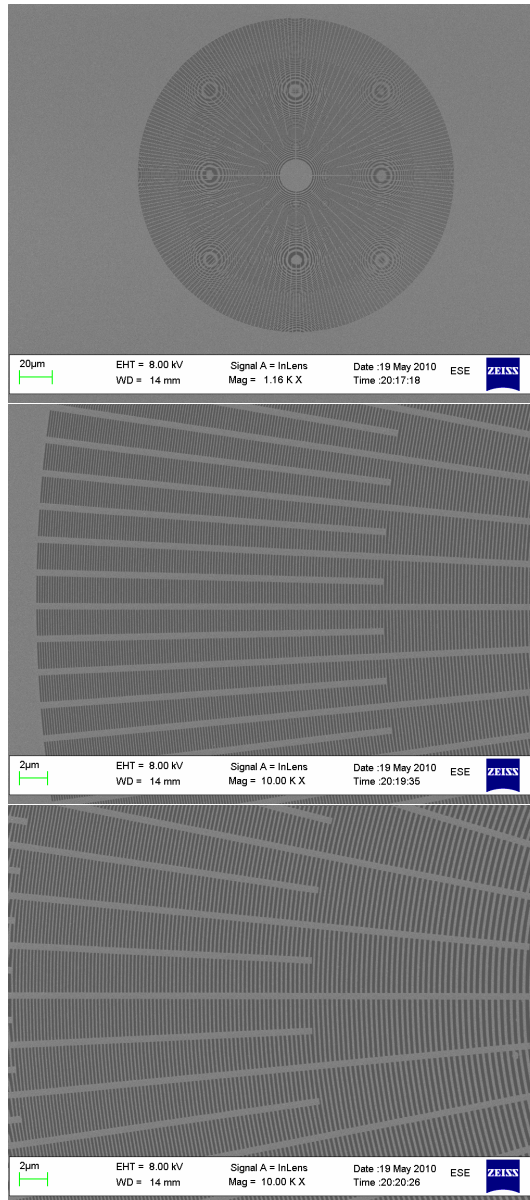


Figure 4.3: SEM images of one of the NEMI *zone plates* (support chip 8, membrane 1). Top: image of the whole *zone plate* with a middle stop diameter of  $d_{MS} = 20 \mu\text{m}$  visible; middle : SEM micrograph of the same *zone plate* in higher magnification showing the outermost *Fresnel zones*; bottom: same *zone plate* in higher magnification showing the middle area *Fresnel zones* of the *zone plate*. (The circular shaped patterns overlying the top image of the whole *zone plate* are imaging artifacts)



Figure 4.4: Scanning-electron micrographs showing the two different *zone plate* types utilized in the NEMI setup representing the difference in the middle stop diameter; top: outer diameter  $d_{ZP} = 192\ \mu\text{m}$  *zone plate* with a middle stop diameter of  $d_{MS} = 20\ \mu\text{m}$  (support chip 8, membrane 2); bottom:  $d_{ZP} = 192\ \mu\text{m}$  *zone plate* with a middle stop diameter of  $d_{MS} = 50\ \mu\text{m}$  (support chip 8, membrane 6). (again the in a circular wave form shaped patterns overlying both micrographs are imaging artifacts)



## DETECTION

---

*The following chapter presents the theoretical considerations which the detection system of the matter wave microscope is based on. It will describe the working principle of a so called **Pitot-tube** detector, as well as the measurement concept of the cold cathode pressure gauge. The corresponding mathematical considerations regarding this detection-method are presented in section 2.1.6 together with the evaluation process for the intensity of the measured reflection signal.*

### 5.1 THEORETICAL BACKGROUND DETECTION SYSTEM

As described in section 1.2.4, the helium atom detection for the NEMI microscope is based on a pressure measurement within an accumulation tube, a so called **Pitot Tube**. This setup became the system of choice because of its robust working principle and simple design demands. A main factor for the application of such a detection system is the fact that there is no need for time resolved and mass selected measurements in NEMI. The intensity of the reflected beam signal is found from the relative pressure-variation within the detector tube.

### 5.2 WORKING PRINCIPLE PITOT TUBE

A **Pitot Tube** is an accumulation tube with a low-conductivity entrance aperture facing the signal to be measured. This aperture connects the small accumulation cell to the surrounding vacuum. A pressure measurement system determining the pressure rise/fall within the accumulation volume is mounted to the opposite side of the tube. Under high-vacuum/ultra-high-vacuum (HV/UHV) conditions the pressure in such an accumulation volume is only dependent on the quality of its evacuation. This means that it depends on the conductance of the opening between the *Pitot tube* and the HV/UHV chamber. As described in section 2.1.6 the atoms/molecules entering the *Pitot tube* have a preferential forward direction into the tube. They will hardly be influenced

by the shape of the entering aperture. Within the tube volume the particles will accumulate bouncing around in all directions. At the same time the *Pitot tube* itself is an effusive source (see section 3.2 and 2.2.1.2) with an *outflow* (*backflow*) of gas particles from the tube (see figure 5.1). After some time an equilibrium state between the *in-* and *out-flow* of the tube arises (see e.q. 2.19) where the same amount of entering atoms/molecules will leave the tube again. The formation of this equilibrium state is connected to an increase of the *Pitot-tube* pressure which can be observed. The value of this pressure increase is a measure for the amount of particles entering the tube and therefore for the beam/signal intensity. The mathematical context of a *Pitot tube* is described in chapter 2.1.6. The final correlation between the *Pitot tube* pressure variation  $p_T$  and the incoming particle flow  $\dot{N}_{in}$  is

$$p_T = p_{SDC} + \frac{\dot{N}_{in} \cdot k \cdot T}{L} \quad (5.1)$$

$T$  states the sample-chamber/PITOT-TUBE temperature,  $p_{SDC}$  the pressure in the sample/detector chamber and  $L$  the vacuum conductance factor for the pinhole entering aperture of the tube.

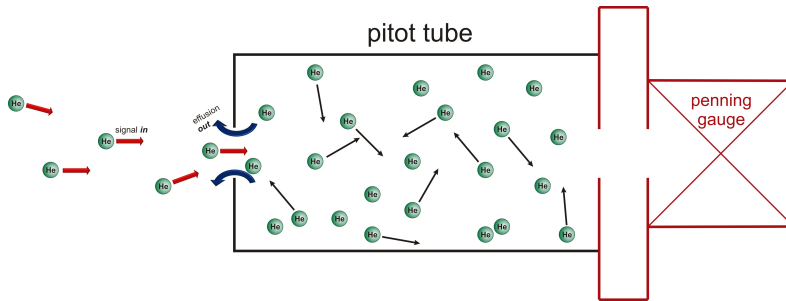


Figure 5.1: Schematic of the working principle of a *Pitot tube*

### 5.3 COLD CATHODE PRESSURE MEASUREMENT GAUGE

A *cold-cathode ionization vacuum gauge* also often referred to as *inverted-magnetron* essentially consists of two electrodes, a cathode and an anode. By applying a high voltage electrical field between this two electrodes a *gas-discharge* can be induced by the electrons traveling between the cathode and



the anode. This leads to an ionizing process of the residual gas within the pressure gauge volume. The *gas-discharge* current is a measure for the pressure. However just at gas pressures above 1 mbar the straight trajectories of the electrons are sufficiently long enough to ionize enough molecules/atoms to keep the gas discharge running. Due to that reason for lower ambient pressures the traveling path of the ionizing electrons has to be extended. This is done by applying an additional magnetic field which forces the electrons to travel on spiral trajectories. The electron paths are extended and consequently the probability for a collision with gas molecules on the electrons traveling path is enhanced strong enough and a stable gas discharge even in the ultra high vacuum region is reached. This type of vacuum gauge can be used for pressure measurements down to the range of  $1 \cdot 10^{-11}$  mbar. An important point to take into consideration is the fact that the measured signal of cold cathode gauges is gas type dependent. They have different sensitivities for different gas types to detect. In case of helium the sensitivity of these gauges is low. The reason for this is that the required ionization energy for helium is high. Most producer companies provide corresponding diagrams and correction numbers for their instrument read-out values for different gas types. In case of the *cold-cathode gauges* used for the *Nemi* microscope the correcting number is stated to be linear in the range below  $10^{-5}$  mbar and is specified to be  $K = 5.9$  for helium. The conversion formula describing the correlation between measured signal and the effective pressure is stated in equation 5.2. Further information can be found in the literature [80, 81] as well as in the technical documentation brochures provided by the different manufacturers.

$$p_{eff} = K \cdot \text{indicated pressure} \quad (5.2)$$



## TECHNICAL REALIZATION

---

*Within the following section the design concept for NEMI with its technical specifications and documentations is presented. This is done by the aid of 3D CAD model images which should provide a better illustration of the technical realization regarding this instrument. Nearly every component implemented in the set-up of NEMI was therefore designed with a computer-aided design (CAD) software called PRO-ENGINEER Wildfire [82]. This kind of approach for the development of a new instrument has the big advantage, that the shape, size and even weight of each component is roughly known before its actual manufacturing process. Therefore the components can be assembled virtually beforehand, which provides a strong tool to evaluate the functionality of a newly designed setup. Also it enables special tailoring of a components shape with regard to other parts of the instrument's setup, as well as an easy communication tool with the mechanical manufacturers of the several customized parts, since most of them also support CAD-model based communication. Later on changes on the system can be easily evaluated first, by adapting the CAD-model of NEMI before the actual change of the parts, as well as it is possible at any time to read out the dimensions of the actual components from the model files. Therefore a big part of the work presented in this thesis concerns the design and development of the instrument based on 3D CAD-modeling. This section covers the engineering point of view regarding the build-up of our matter wave microscope and therefore presents the technical details and requirements needed for this work. It is structured in a way that each of the UHV chambers of NEMI will be treated in a separate section with all components belonging to this chamber described in the same section.*

### 6.1 SOURCE CHAMBER

The basic requirements for the source and the source chamber are to provide a free-jet-expansion from a nozzle element into a HV/UHV chamber. The limitation regarding the nozzle pressure is, for the moment, set by the maximum pressure of commercially available helium (He 6.0) gas bottles of 200 bar.

The vacuum chamber and its corresponding pumping system needs to be able

to deal with the high helium flow rates originating from the expansion (see chapters 2.1, 2.2 and 3).

It was decided to use two turbomolecular pumps with magnetically bearings, whereas the magnetically version was chosen on account of reduction of the vibrational influence on the microscope.

As a main additional requirement the nozzle has to be mounted with free movement in all three ( $X$ - $Y$ - $Z$ ) directions. This boundary condition is demanded by the beam-line alignment. As described in sub-chapter 1.2.2, a *skimmer* is implemented as an exit aperture of the source chamber. This element on the other hand is mounted in a fixed position, defining a center-line for the beam. Therefore the nozzle itself has to be moveable in  $X$ - $Y$  direction to adjust its exit orifice directly in line with the skimmer opening hole.

Additional movement in  $Z$ -direction corresponding to a distance change between the nozzle and the skimmer tip is also required. This is due to possible variations in the optimum distance between the skimmer and the nozzle (see chapter 3).

#### 6.1.1 Nozzle / Source

For the microscope setup presented within this thesis it was decided to work with a standard design concept for the nozzle. It is based on a pinhole aperture which is mounted pressure and vacuum tight against a stainless steel high pressure gas tube. One big change compared to most other neutral helium *free-jet* sources presented in literature and earlier research work is, that the nozzle setup for *Nemi* and hence the beam-line is arranged in vertical direction. The decision of choosing such an upright beam line setup was mainly based on the anticipated easier sample and detector handling within the sample chamber which is located at a standard working height.

However, the principle of the nozzle design presented within this work could also be applied in a horizontal beam line setup<sup>1</sup>.

---

<sup>1</sup> The technical design of the *free-jet* source was developed in collaboration with Kurt Ansperger [83] who also performed the manufacturing of the source components in his mechanical workshop.

### 6.1.1.1 Pinhole aperture - nozzle body

The pinhole aperture utilized for the nozzle setup is a commercially available *Platinum* pinhole aperture disc **(1)**<sup>2</sup> with a diameter  $d = 3.04 (+0/ - 0.02)$  mm and a thickness of  $0.25 (+0/ - 0.02)$  mm. It is purchased by PLANO [84] (article Nr.: **A0300P**, **A0301P**). Two different pinhole aperture diameters were chosen namely  $10\ \mu\text{m}$  and  $5\ \mu\text{m}$ . The  $5\ \mu\text{m}$  diameter aperture is the smallest pinhole diameter available from this company.

3D schematics of an aperture disc are presented in figure 6.1. One side of the nozzle disc has two conical counter-bores. The final micrometer range exiting hole has cylindrical shape. The pinhole accuracy is specified to be  $\pm 1\ \mu\text{m}$  for pinhole sizes between  $5 - 10\ \mu\text{m}$ , and the roundness is stated to be within  $0.1\ \mu\text{m}$ . A scanning electron micrograph of such a  $d_N = 5\ \mu\text{m}$  nozzle disc pinhole aperture is presented in figure 6.2. The left scanning electron microscope (SEM) image in figure 6.2 shows a, with some kind of dirt particles, clogged  $d_N = 5\ \mu\text{m}$  nozzle disc, which was unmounted from *Nemi* and exchanged with a new one.

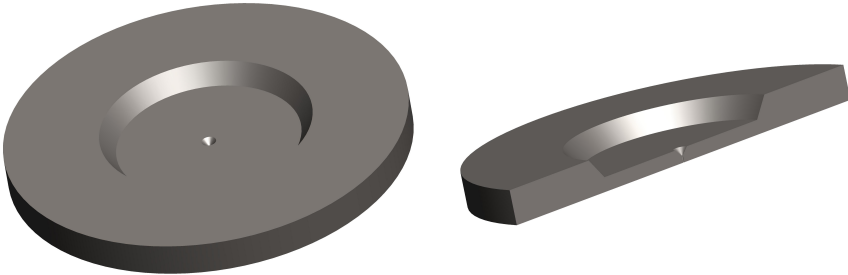


Figure 6.1: Left: principle 3D scheme of the *pinhole aperture nozzle disc (1)*, right: scheme half section of the *nozzle disc*.

The pinhole aperture disc is mounted pressure and vacuum tight against a three millimeter outer diameter stainless steel high pressure *gas tube*. For the tightening mechanism the *nozzle aperture disc (1)* is placed in a *circular holding fixture (2)* made from stainless steel which again is placed in a triangular shaped *nozzle retaining fixture (3)* (see figure 6.5).

<sup>2</sup> Component number for figure 6.5. For simplicity this system is applied for the components in the chapters 6.1.1 and 6.1.2.

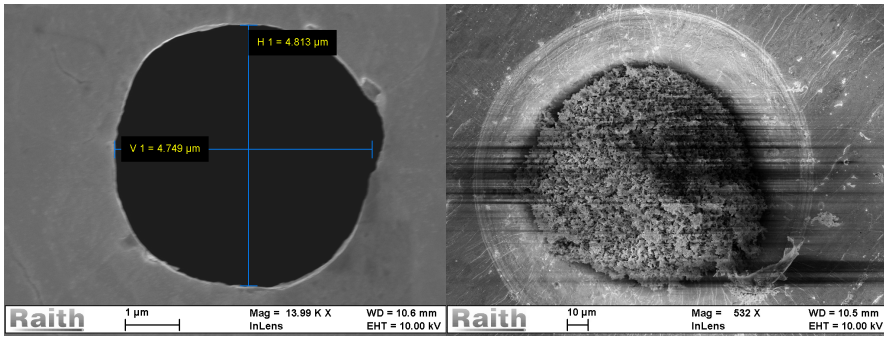


Figure 6.2: Left: SEM micrograph of the aperture pinhole in a  $d_N = 5 \mu\text{m}$  nozzle disc, right: SEM image of a clogged  $d_N = 5 \mu\text{m}$  nozzle disc unmounted from *Nemi*. The black stripes appearing in the image are presumably imaging artifacts due to statically charging of the dust particle during the microscopes scanning process.

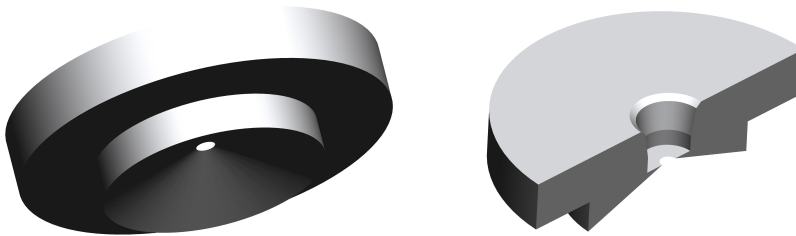


Figure 6.3: Left: Sketch of the *circular holding fixture* (2) for the nozzle disc, right: 3D scheme half section of the *circular holding fixture*.

To seal the *platinum* nozzle disc against the *stainless steel tube* (5) a copper gasket (4) is placed between the tube and the nozzle disc. 3D schematics of the components and the mounting principle are presented in figures 6.1, 6.3, 6.4, 6.5 and 6.6.

As indicated in figure 6.5 the *stainless steel high pressure gas tube* (5) is directly mounted into the copper *nozzle-cooling block* (6). This is done by a specially vacuum proof soldering technique.

That the sealing takes definitely place between the *nozzle disc* and the high pressure *gas tube* is ensured by the fabrication of the triangular shaped *nozzle retaining fixture* (3) and the *circular holding fixture* (2). When this two components are mounted against the *gas tube* and the copper *nozzle-cooling block* (6)

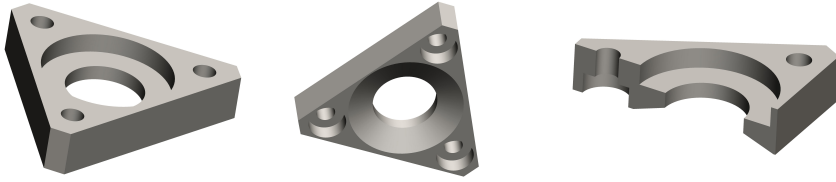


Figure 6.4: Left, middle: Sketch of the triangular shaped *nozzle retaining fixture* (3) for the nozzle disc, right: 3D scheme half section of the *nozzle retaining fixture*.

a free distance between those two components and the *cooling block* is left. In that way it is possible to ensure that the tightening takes place between the *nozzle disc*, the *copper gasket* and the high pressure *gas tube*. This can be seen in detail in the half section scheme of the assembly drawing presented in figure 6.6.

#### 6.1.1.2 Nozzle cooling

Another required boundary condition is the possibility of cooling the nozzle down to enable a change of the beams energy (see section 3). The need for this feature is due to the possible manipulation of the helium beam's wavelength by a change of the nozzle temperature (see chapter 3.4).

The temperature adjustment of the nozzle is done by means of liquid nitrogen. Since it has to be ensured that the nozzle temperature keeps stable over a time-frame of up to several hours at various temperature settings, a stabilization through a counteracting heating element is implemented. The heating element is controlled by a regulating electronic device acting on account of the measured actual nozzle temperature. Note that actually not the *nozzle disc* but the part of the high pressure *gas tube* which is mounted within the *nozzle cooling block* is cooled down. However the distance of this part to the nozzles exiting pinhole is small enough to assume that the gas particles (He-atoms) leave the nozzle with nearly the same thermal energy which they gained during passing the cooled part of the steel pipe.

The cooling of the copper nozzle block is done via a copper braid which is mounted with good thermal contact to a very thin-walled liquid nitrogen filled stainless steel pipe. Figure 6.7 presents a digital photograph of the copper-braid connection between the nozzle-cooling block and the stainless steel tube which on its inside gets filled with liquid nitrogen. One can also see the elec-

trical connection for the vacuum suitable high performance heating cartridge (Type: **HS-4,0**:  $\varnothing=4$  mm, L=20 mm and **12V/8W**, max. 260°C from HS [85]) and the mounting of the K-type thermocouple, which provides the possibility to control the counter heating for a stable regulation of the requested nozzle temperature. This regulation is performed by an *Eurotherm 2404 Controller*<sup>3</sup> [86].

The supply of liquid nitrogen for the cooling mechanism is performed by a round tank also referred to as chicken-feeder which is mounted via a KF-25 connection to the head flange of the nozzle mounting setup (see section 6.1.2.2 and figure 6.11).

### 6.1.2 Nozzle mounting

The nozzle has to be mounted with free-movement in the horizontal X- and Y direction to provide an adjustment possibility of the *nozzle* pinhole and the *skimmer* pinhole for the beam alignment. Since every source chamber venting- or nozzle cooling- procedure will slightly shift the nozzle position, this alignment has to be done frequently and under present vacuum conditions. Therefore it was decided to perform this step automatized by high vacuum compatible stepper motors.

The requirements for the positioning system are a vacuum compatibility down to a pressure below  $1 \cdot 10^{-6}$  mbar, a travel range in two axes of minimum 5 mm with a resolution of 0.5  $\mu\text{m}$  and maximal physical outer dimensions of approximately 160 mm  $\times$  160 mm  $\times$  100 mm (X,Y,Z).

Additionally a vertical Z-adjustment for the distance between the *nozzle* and the *skimmer* has to be provided. Former experiments performed with our other neutral helium scattering instrument have shown that a skimmer-nozzle distance between 10-12 mm results in a good beam performance. In the following two sub-chapters a detailed description of the technical solution for this horizontal and vertical adjustment is presented.

#### 6.1.2.1 X-Y movement

The system of choice for *Nemi* became a combination of two stepper motors from *Zaber* (micro linear actuators with built-in controllers) with 25 mm travel

<sup>3</sup> 2404-CG-VH-HZ-XX-XX-XX-XX-A2-XX-ENG-K-250-1300C



and RS-232 controlled together with two low vacuum compatible translation stages with 28 mm travel from *Zaber* [87]. The linear actuator models are one actuator of the type **KT-NA08A25-SV-ENG1243** acting as a master device and one **T-NA08A25-SV-ENG1244** actuator working in slave mode. The notation for the two stage components is **TSB28-MV**. The main specifications for the actuators are presented in table 6.1. Digital photographs of this components are presented in figure 6.8. The two linear translation stages are mounted on top of each other with 90° rotation to provide the X/Y motion.

ZABER LINEAR ACTUATOR SPECIFICATIONS			
Microstep Size (Default Resolution)	0.047625 $\mu\text{m}$	Maximum Current Draw	350 mA
Travel Range	25.4 mm	Power Supply	12-16 VDC
Accuracy	+/- 8 $\mu\text{m}$	Mechanical Drive System	Precision leadscrew
Repeatability	< 1 $\mu\text{m}$	Limit or Home Sensing	Magnetic hall sensor
Backlash	< 4 $\mu\text{m}$	Manual Control	No
Maximum Speed	8 mm/s	Axes of Motion	1
Minimum Speed	0.00022 mm/s	Vacuum Compatible	10 <sup>6</sup> mbar
Peak Thrust	65 N	Operating Temperature Range	0 to 50 degrees C
Maximum Continuous Thrust	50 N	Weight	0.13 kg

Table 6.1: Detailed specifications for the **KT(T)-NA08A25-SV-ENG1243** linear actuators

The mounting of the above described source setup onto the X/Y stage is done with a specially manufactured *nozzle mounting plate* which is fixed to the *Zaber* stage by four M6 screws. It has to be ensured that the thermal contact between the copper *nozzle-cooling block* and the X/Y stage is as small as possible. Therefore spacing cylinders with low temperature conductance made of *MACOR* are implemented between the copper nozzle block and the *nozzle mounting plate*. Figure 6.9 and 6.10 present sketches and digital photographs of the real components of the described X/Y adjustment setup for the source.

#### 6.1.2.2 Z movement

Due to the less frequently required vertical Z-movement of the nozzle, this motion is performed manually, but still under present vacuum conditions. Figure 6.11 shows a sketch of the Z-movement mechanism in combination with the X/Y-Stage and the nozzle-setup.

This graphic should explain the working principle for the vertical adjustment of the source. The whole X-Y-Z alignment setup for the nozzle is mounted

via a CF-200 *source mounting flange* onto (into) the *source chamber*. The X/Y table is fixed inside the vacuum chamber whereas the Z-movement is adjusted from outside. An *edge welded CF-100 bellow* ensures the possibility for the Z-movement of the source under vacuum conditions.

Without any counteracting-force, the vacuum conditions within the source chamber would compress the edge welded bellow together. To work against this compression, several *flat spring sets* are placed around three circular symmetrically arranged M10 thread rods which are connected with Z-axial free movement to the top *nozzle head flange* holding the source.

By tightening of the *Z-adjustment screws* on-top of this three M10 thread rods, the vacuum bellow is stronger compressed and the nozzle moves relatively to the *fixed source mounting flange* further down in its Z-position. To enable also a backwards movement of the source to a higher Z-position, the above mentioned *flat spring sets* provide a restoring force against the vacuum when the *Z-adjustment screws* are loosened.

In this way it is possible to move the source position over a range of approximately 20 mm in the vertical Z-direction. Three additional M10 threaded rods, also arranged in a circular position around the bellow, allow an adequate guidance of the *nozzle head flange* during this Z-movement, and furthermore they can be used for the fixation of the final Z-position. For an easy horizontal adjustment of the *head flange* a small circular spirit level is implemented on the top side of the flange. Also the connection for the liquid nitrogen tank (also referred to as *chickenfeeder*) for the nozzle cooling is shown in figure 6.11.

Figure 6.12 presents more 3D sketches of the whole nozzle mounting for the “*in vacuum*” X/Y/Z movement.

### 6.1.3 *Skimmer*

The *skimmer* is a conical shaped aperture with its small orifice facing the source. The diameter of the skimmer orifice has to be in the lower micrometer range to achieve a micrometer or even sub-micrometer focal diameter with *Nemi* (see chapter 4.3). Therefore the orifice diameters of the skimmers designed for this instrument are in the range between 1 – 5  $\mu\text{m}$ . Such skimmers are called “*microskimmers*”.

However for the first beam characterizing experiments also bigger skimmer diameters between 10 – 400  $\mu\text{m}$  have been used.

The microskimmers are produced by performing a glass pulling process similar to the one used to fabricate patch clamps for biological cell and tissue studding [88, 89].

The ones used for *Nemi* were manufactured here in our group at the IFT in Bergen [54]. They consist of such a glass pulled *skimmer* tip, which is glued with a high vacuum suitable two-component adhesive into the small hole at the top of a thin walled conical shaped copper body. The glass puller used for this application was a NARISHIGE PP-830 model [54]. A picture of one of the *Nemi* skimmers is shown in the left side of figure 6.13, whereas the middle and the right part of this figure presents an electron microscope (SEM) micrograph of the glass tip from a skimmer similar to the ones used for *Nemi*.

To mount the *skimmer* element into the source chamber it will be fixed with the *skimmer fixation ring*, three M1.6 thread rods and hex-nuts to a *skimmer mounting ring*. This ring is mounted on top of a specially reworked *CF-150 vacuum blind flange* (VITON sealing). To enable the beam to pass undisturbed through the skimmer orifice into the next chamber the *skimmer mounting ring* is also formed conically. The specially reworked *CF-150 flange* on the other hand has a cylindrical transition hole. A sketch of this three components is presented in figure 6.14. The blind flange is fitted vacuum tight (with a VITON gasket) into the source chamber in a way that it provides the *skimmer* to be the exiting aperture of the chamber. To exchange the *skimmer* only the *skimmer fixation ring* which is held by the three M1.6 hex-nuts has to be unmounted and after the *skimmer* exchange it simply is remounted again.

#### 6.1.4 Complete source chamber

Finally the above mentioned elements (*source/nozzle* and *skimmer*) are implemented into a *CF-200 Cube* from VACOM [90] which is acting as the *source* chamber. This cube holds six CF-200 connections providing one connection for the source mounting, two ports for the two 600l/s MAG W-600 turbo molecular pumps, one opening for a *CF-quick access door* with view-port, one connection for a *CF-4 port cluster flange* and one opening for the *skimmer mount*, which at the same time acts as connection to the adjacent *pumping stage* chamber. For a better illustration of the assembly figure 6.15 shows an exploded 3D sketch of the just mentioned components. The two MAG W turbo pumps are assembled

to the *cube* via a *CF-200/CF-150 reducer flange*. Also the *4xCF-40 cluster flange* with the main flange dimension of *CF-150*, as well as the *CF-150 quick access view-port* are mounted to the chamber with the same reducer flanges. The view-port enables a fast access possibility for a *skimmer* or *nozzle* exchange. Since the required vacuum conditions for the source chamber lie only in the  $10^{-6}$  mbar range, the VITON gasket of the view-port is not an issue. The *cluster flange* is used to provide additional ports for vacuum feed-throughs and pressure measurement gauges. At the moment just one of these *CF-40* flanges is equipped with a PFEIFFER [91] **PKR-251** active pirani/cold cathode transmitter (specifications see appendix C.1) for pressure monitoring of the chamber.

The *source* is directly mounted to the chamber via the *CF-200 source mounting flange*. To fix the *skimmer* to the source chamber and enable a connection to the adjacent pumping stage chamber, a  $L = 105$  mm long *CF-200/CF100* reducer flange from the company VAB [92] is used. This reducer flange is mounted to the bottom *CF-200* sealing of the cube. The specially reworked *CF-150 skimmer mounting flange* on the other hand is fixed on the top side of the just mentioned VAB reducer flange with a VITON gasket implemented for the vacuum sealing. Therefore the *skimmer mounting flange* together with the *skimmer mounting ring* and the *skimmer* will end up inside the *CF-200 source chamber cube* when the VAB reducer flange is attached via a copper gasket sealing to the cube. Two schematics showing the concept of the final *skimmer* and *nozzle* (source) position are presented in figure 6.16.

For a better image of the whole source chamber assembly figure 6.17, 6.18 and 6.19 present further schematic views of the assembly of the source chamber setup.

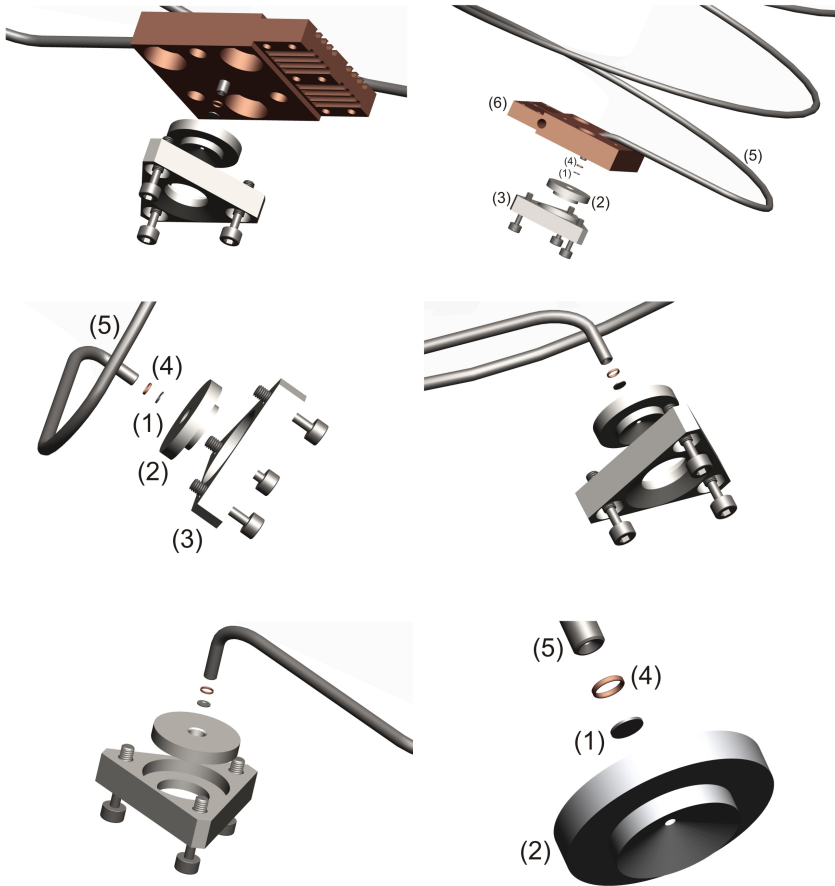


Figure 6.5: Exploded assembly drawing of the *nozzle disc* mounting. The *nozzle disc* (1) is placed in the *circular holding fixture* (2) and sealed by a *copper gasket* (4) against the high pressure *gas tube* (5). To tighten this sealing the *circular holding fixture* gets placed within the triangular shaped *nozzle retaining fixture* (3) which again is tightened by three M3 stainless steel screws into the copper made *nozzle-cooling block* (6). The stainless steel high pressure *gas tube* (5) on the other hand is mounted by a specially vacuum proofed soldering technique directly into this copper *nozzle-cooling block* (6).

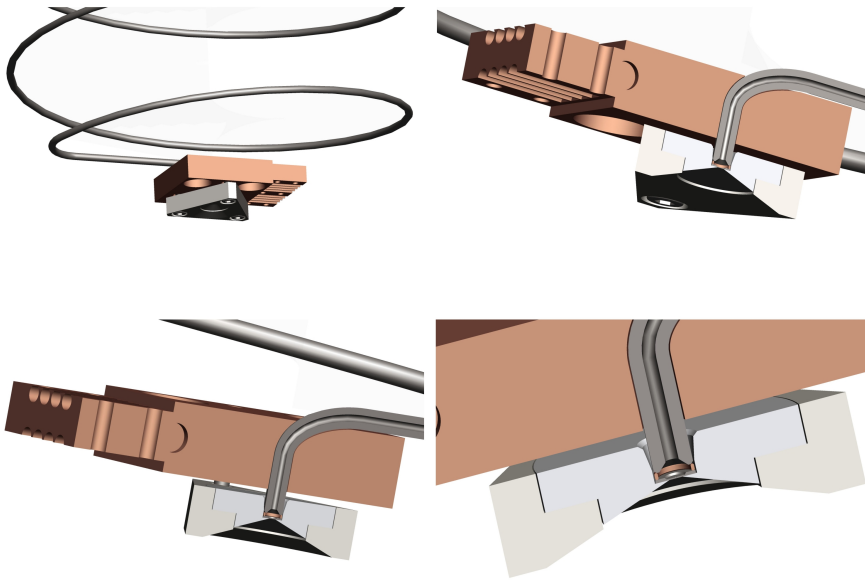


Figure 6.6: Scheme of the assembled nozzle. Top left: assembled nozzle; top right, bottom left, bottom right: 3D half section scheme of the assembled nozzle. Note: the vacuum and high pressure tight sealing takes place between the *nozzle disc* (1), the *chopper gasket* (4) and the *high pressure gas tube* (5).

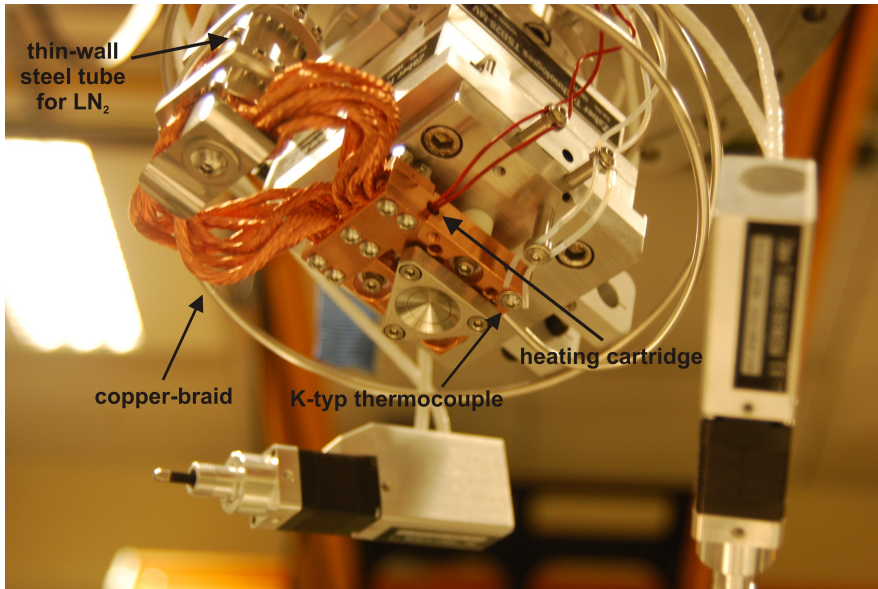


Figure 6.7: Picture of the nozzle cooling system displaying the copper-braid connection between the copper nozzle-cooling block and the liquid nitrogen filled stainless steel tube. The two red wires are the electrical connection for a high performance heating cartridge which is inserted into the nozzle-cooling block. The thermic connection between the tube for the liquid nitrogen ( $LN_2$ ) and the copper braid is done by high force clamping of the braid wires onto the outer diameter of the tube.

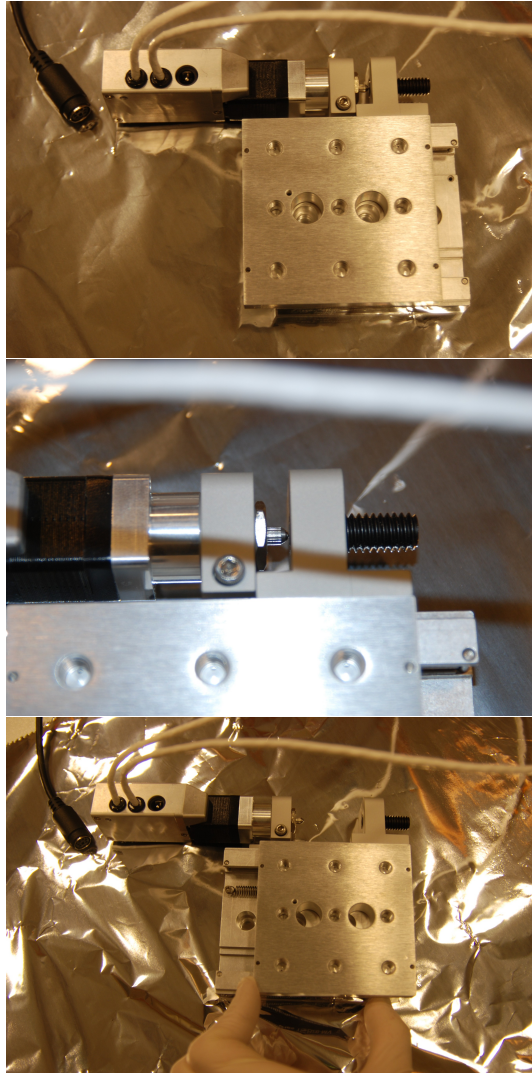


Figure 6.8: Digital images of the *Zaber* stage components. Top: vacuum compatible **TSB28-MV** linear translation stage with mounted **KT-NA08A25-SV-ENG1243** linear actuator; middle: detail picture of the actuator pin which performs the linear motion and bottom: picture of the pull back mechanism (return spring) for the stage.



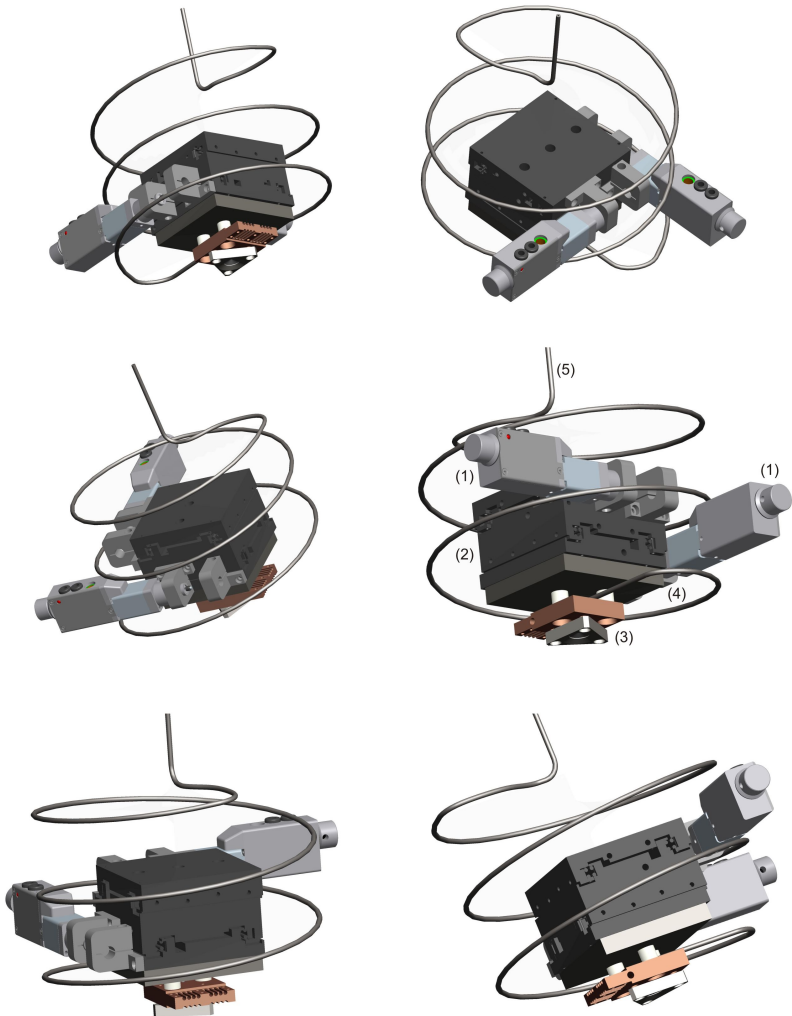


Figure 6.9: 3D schematics of the X/Y nozzle adjustment based on two perpendicularly assembled *Zaber linear stages* (2) in combination with two *Zaber linear actuators* (1). The *nozzle setup* (3) is mounted via three *Macor spacers* (white) onto the *nozzle mounting plate* (4) which again is fixed by four M6 screws onto the *X/Y translation stage* (2). Also shown in this sketches is the high pressure helium supply *gas tube* (5) of the source. (3D CAD model *Zaber linear stages* (2) & *linear actuators* (1) provided by *Zaber* [87])

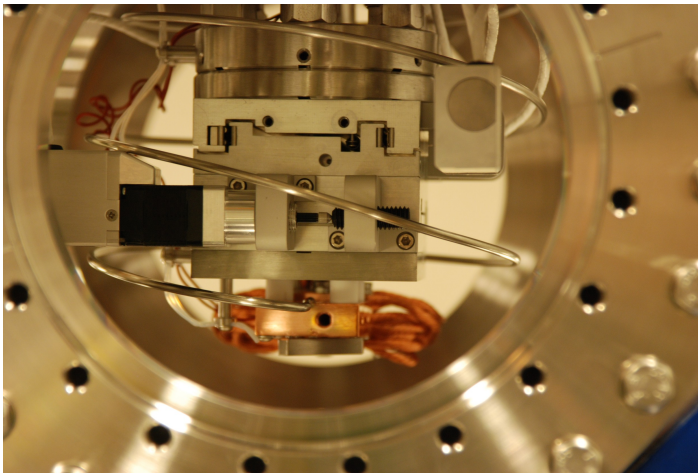


Figure 6.10: Photograph of the actual *Nemi* nozzle mounting showing the *Zaber* stages and linear actuators for the X/Y adjustment of the source.

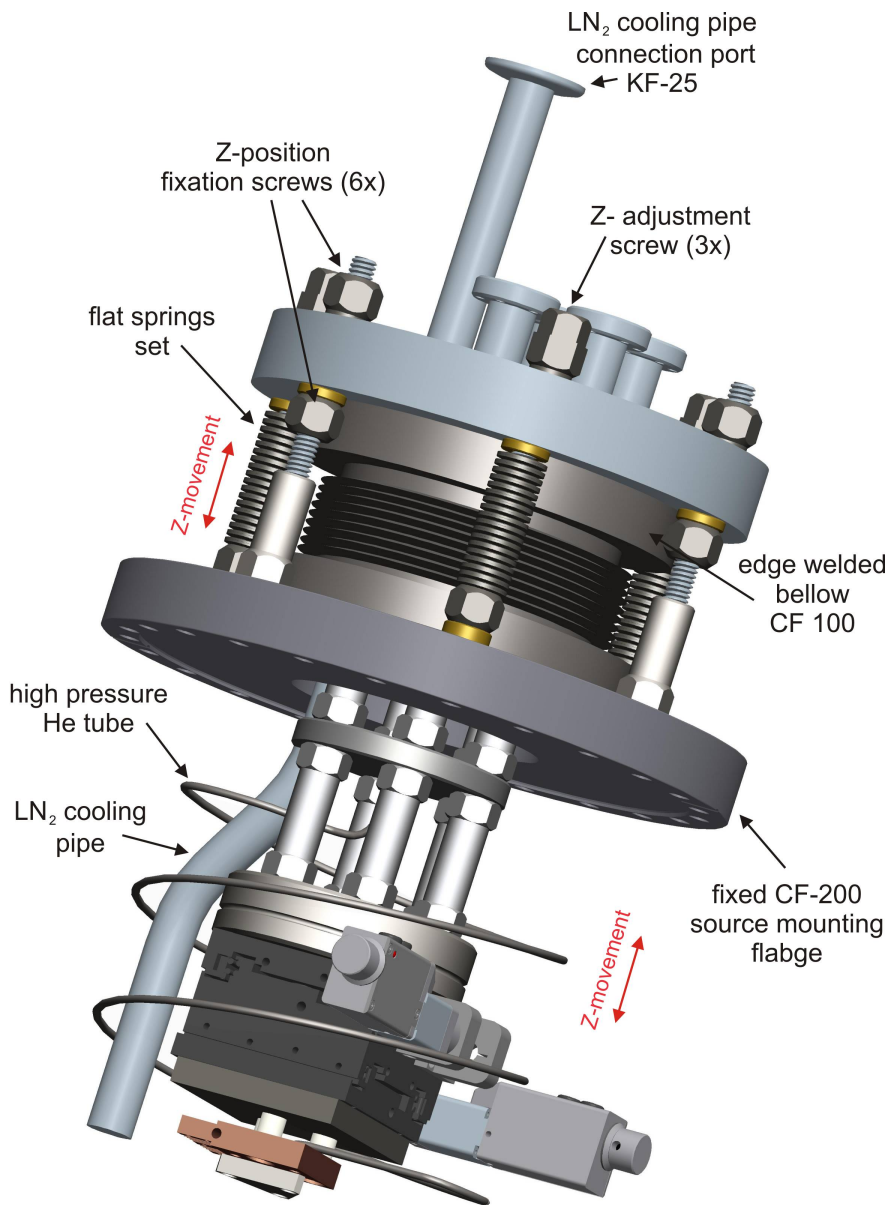


Figure 6.11: 3D sketch of the Z-axis source movement mechanism.

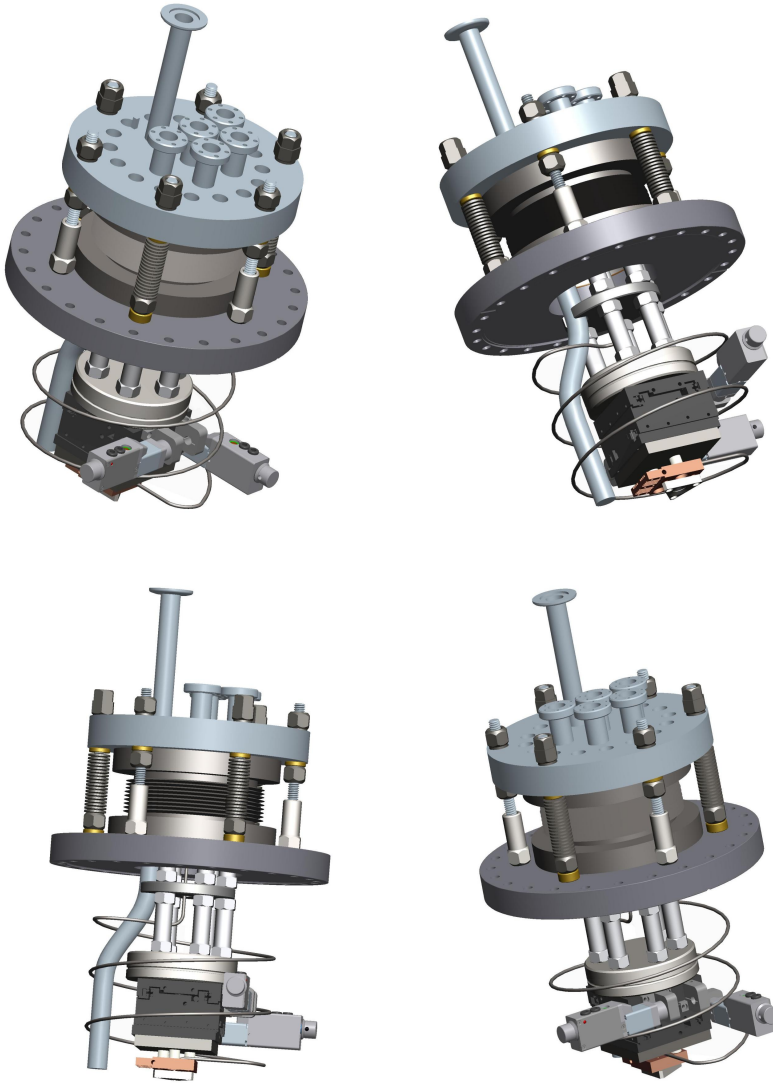


Figure 6.12: 3D sketches of the whole nozzle (source) setup with free movement in X/Y and Z direction.

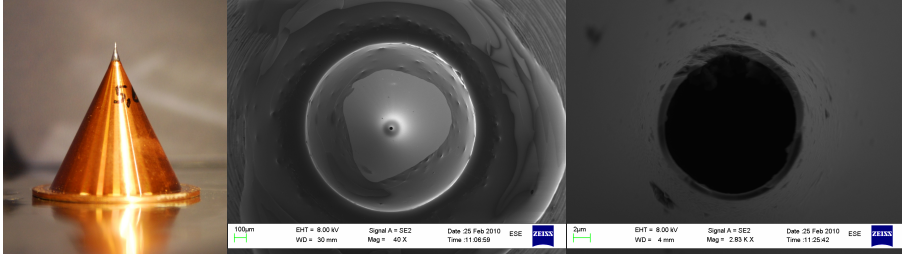


Figure 6.13: Left: photograph of a skimmer for *Nemi*; middle, right: SEM micrograph of a glass tip from a skimmer similar to the ones used in *Nemi*. The SEM images were taken by Thomas Reisinger and Martin Greve.

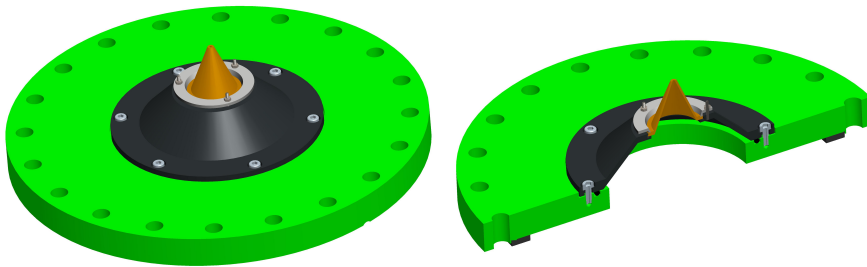


Figure 6.14: Sketches of the skimmer mounting on the CF-150 vacuum blind flange. Left: *skimmer* (gold), *skimmer fixation ring* (light-gray) *skimmer mounting ring* (dark-gray) and specially reworked *CF-150 blind flange* (green) for skimmer mount; right: 3D scheme half section to provide a better understanding for the conical shape of the components. The half section sketch also shows the VITON sealing (black) for the vacuum tight mounting of the skimmer mount flange into the source chamber.

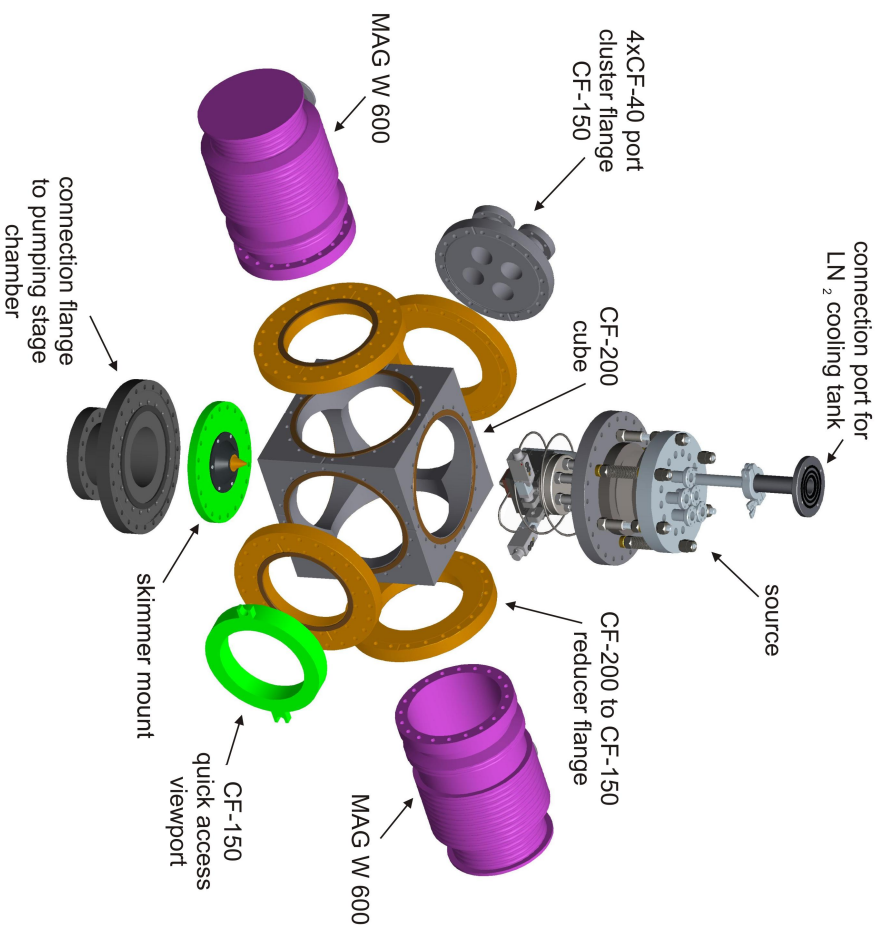


Figure 6.15: 3D explosion sketch of the source chamber. Also pictured in this scheme is the connection port for the liquid nitrogen (LN<sub>2</sub>) cooling tank

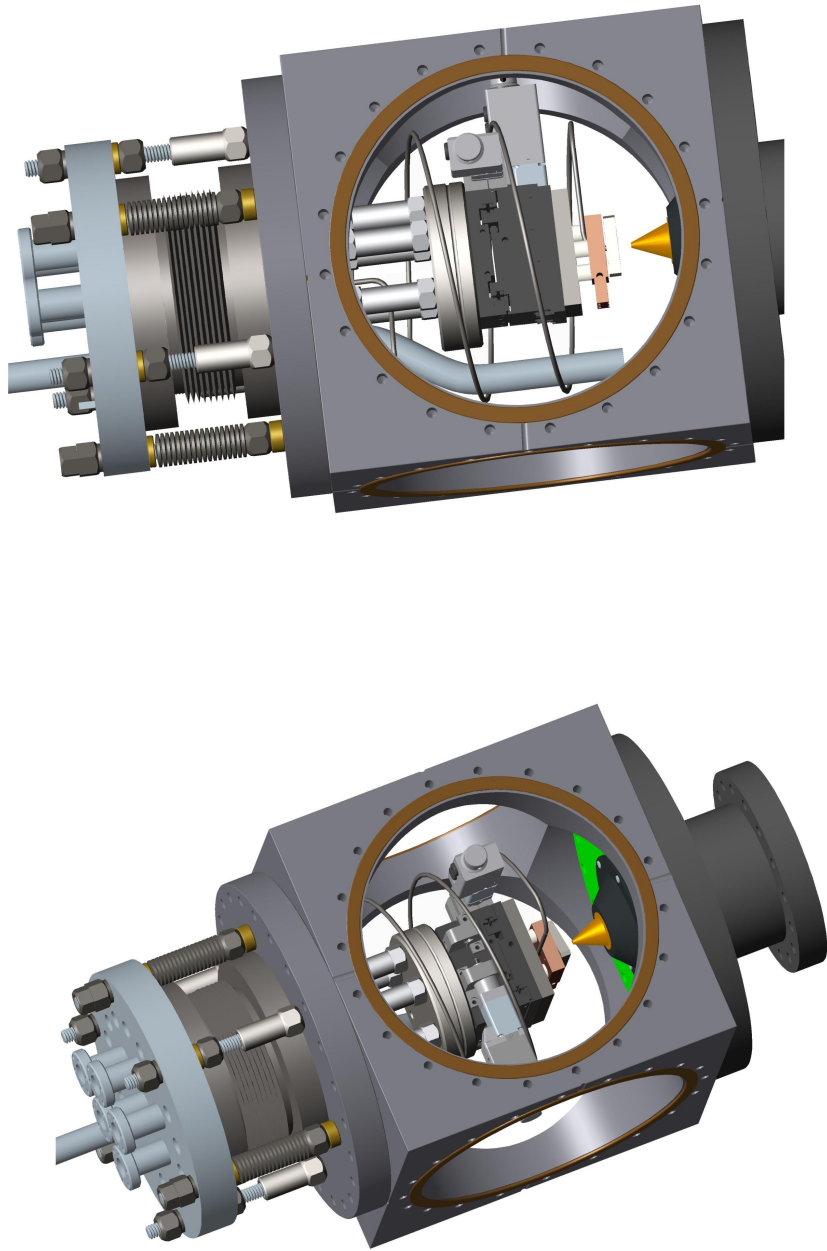


Figure 6.16: Sketches presenting the final skimmer and source position after mounting into the source chamber cube. For a better understanding components like the MAG W 600 turbo pumps, the 4-port cluster flange and the quick access view port are not displayed in this images.

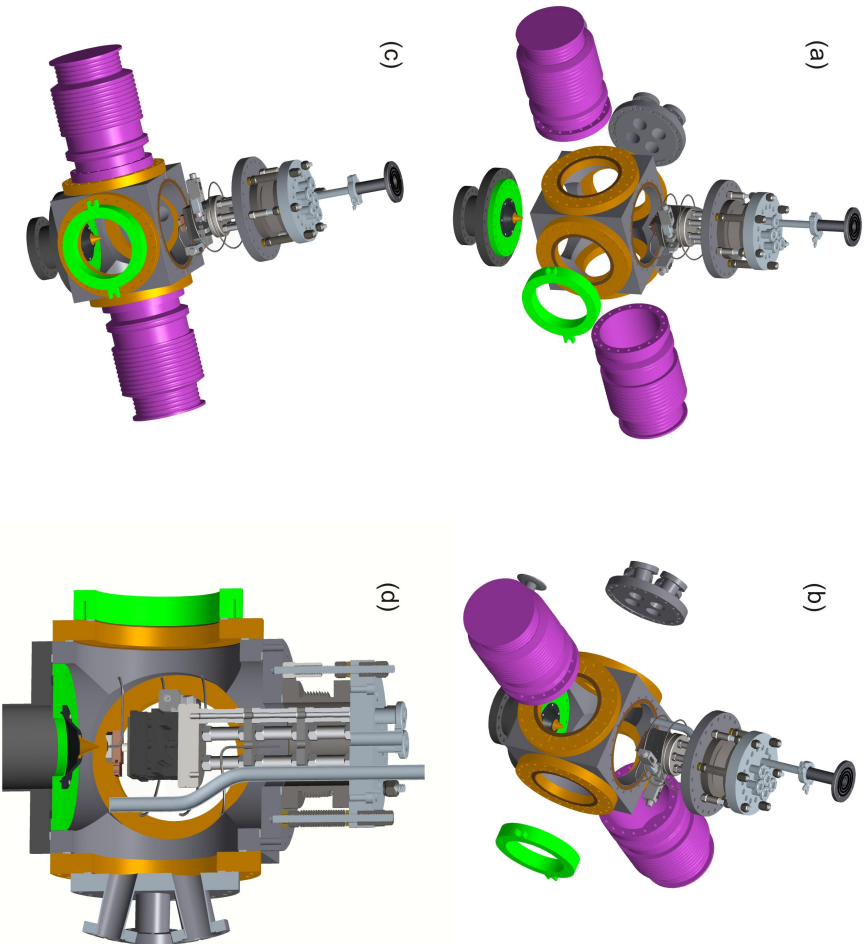


Figure 6.17: Sketch of the source chamber assembly steps. (a), (b), (c) displaying three different assemble steps chronologically arranged, (d) representing a half section sketch through the vertical middle plane of the source chamber (MAC W 600 not displayed)



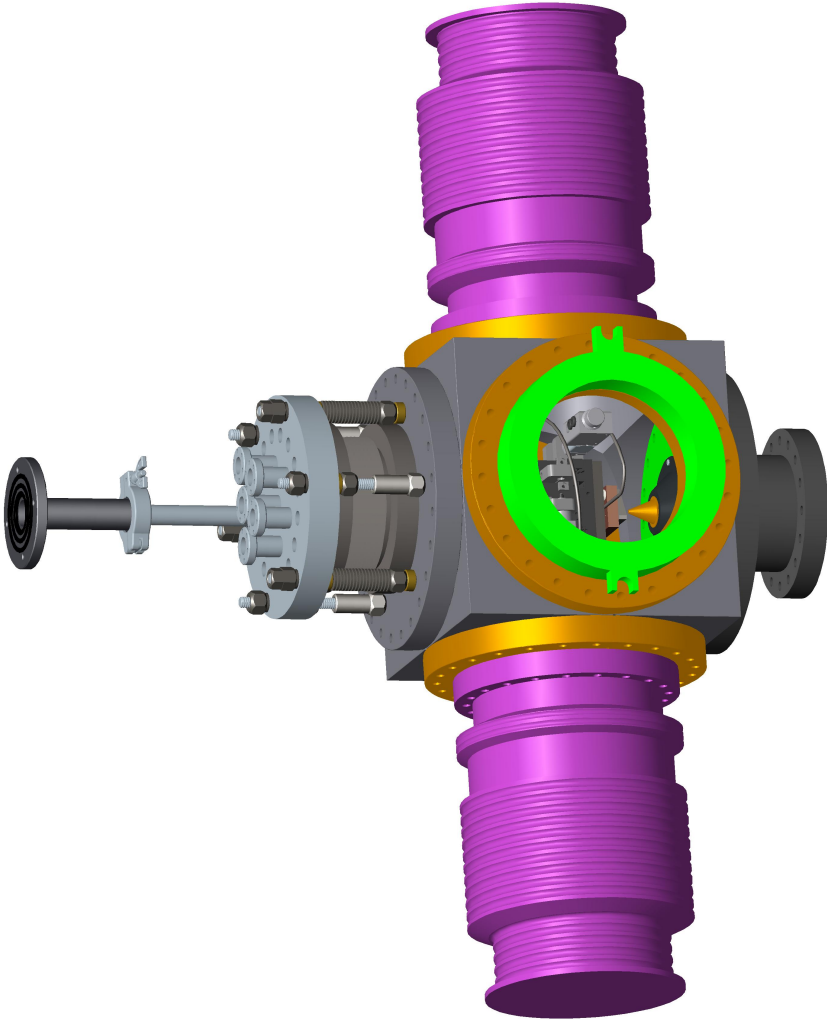


Figure 6.18: Schematic of the assembled source chamber.

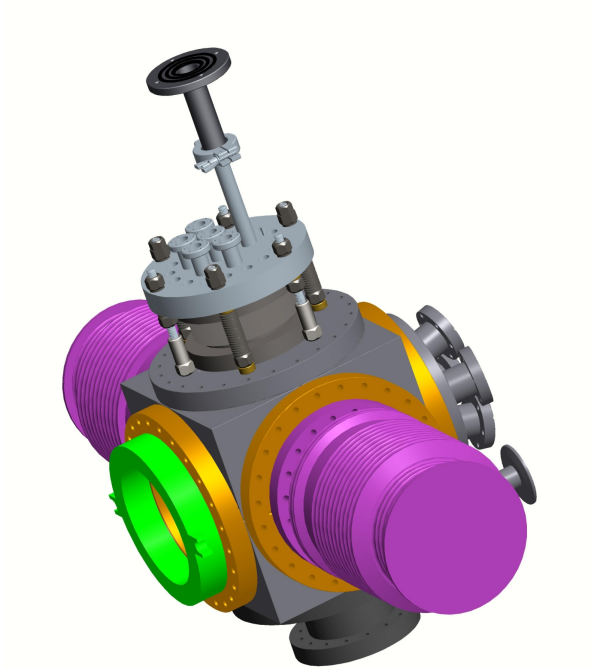
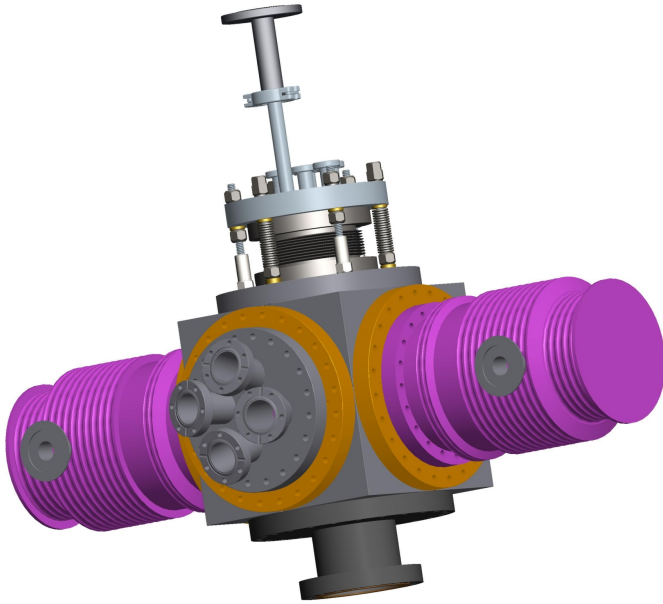


Figure 6.19: Sketches of the assembled source chamber from different view directions.

## 6.2 PUMPING STAGE CHAMBER AND ZONE PLATE CHAMBER

Chapter 1.1 already briefly mentions that the here presented microscope system requires differential pumping to enable a strong enough background gas reduction along the beam line. Especially when the beam hits the focusing *zone plate* and even more important in the sample chamber where the focused beam spot hits the *sample*, the surrounding vacuum conditions have to be in the ultra high vacuum range with very low helium gas background. Therefore the system is build up by several differential pumping stages represented by the different chambers. They are separated by different aperture openings. A discussion on the amount of helium diffusion between the chambers along the beam line is presented in chapter 2.2. The technical setup of the two next adjacent chambers following the source chamber is presented in the following.

### 6.2.1 Pumping stage chamber (PST)

The passage (aperture) between the source chamber and the adjacent pumping stage chamber is represented by the small skimmer orifice. This implies that the majority of the helium gas background from the source chamber will be pumped out of the system by the source chambers own pumping setup, since the skimmer orifice is in the low micrometer range. Due to diffusion processes there is still some amount of helium gas entering the next chamber besides the helium atoms in the beam itself. As a first differential pumping stage the so called *pumping stage chamber* (PST) is implemented into the system.

The main purpose of this chamber is to reduce the helium background in the system, and additionally it also serves as a spacer between the *skimmer* and the *zone plate*.

The connection between the source chamber (SC) and the PST is a CF-100 manual stainless steel *gate valve* from VACOM [90]. The chamber itself is a combination of a standard *CF-100 tee piece* <sup>4</sup> together with a *CF-100 reducer cross* with two CF-40 slots from VAB [92]. As passage aperture to the following *zone plate chamber* (ZPC) a CF-100 copper gasket *pinhole aperture* is used. The pinhole/aperture diameter for that connection is 5 mm.

---

<sup>4</sup> purchased also from VACOM [90].

Figure 6.20 represents sketches of the *PST* setup. A MAG W 300 turbo-pump pumps this chamber. As shown in figure 6.20 it is directly mounted onto the *CF-100 tee piece*. One of the CF-40 connections from the *CF-100 reducer cross* is utilized for the UHV pressure measurement of the chamber. The implemented pressure measurement gauge is an **IKR-270** active cold cathode transmitter from PFEIFFER [91] (specifications see C.1). The remaining CF-40 connection on the reducer cross is at the moment unoccupied, but it provides a further connection possibility.

### 6.2.2 *Zone plate chamber (ZPC)*

The requirements for the *zone plate chamber* are for one part to provide a second stage of differential pumping along the beam path, and for the other part to locate the actual beam focusing element namely the *zone plate*. The helium background and flow situation for this chamber can be looked up in chapter 2.2.

The chamber is pumped by a MAG W 300 turbo pump, which is connected to the CF-100 side flange of the specially manufactured *zone plate chamber CF-100 cross*. The *CF-100 cross* is shown in figure 6.21. Additionally to the connection flange for the turbo pump, this chamber also holds the mounting flange for the *zone plate* holding mechanism. The *ZP mounting CF-63 flange* is located at a position so that after the connection of the *zone plate chamber cross* into the system, the center axes of this flange lies in the horizontal *zone plate* location plane (within a tolerance of  $\pm 5$  mm). The position of this plane in respect to the *source* and the *skimmer* is defined in chapter 1.3.

There is an additional CF-40 connection flange welded to the *zone plate chamber cross* which provides the connection port for the ultra high vacuum pressure measurement gauge for this chamber. A **IKR-270** active cold cathode transmitter from PFEIFFER [91] is used for pressure monitoring.

As an additional spacer between the *zone plate chamber cross* and the *pumping stage chamber* a *CF-100 distance flange* with four attached CF-16 ports is implemented. Generally the *zone plate chamber cross* could have been manufactured in the exactly needed length to place the *zone plate connection port* in the right horizontal distance from the source. But by implementing this additional standard part from VAB [92] it was possible to build the *zone plate chamber cross* on the basis of a standard CF-100 tee piece, which simplified the production

and therefore reduced the costs for this component. Another beneficial effect is that the added *CF-100 distance flange* holds four more CF-16 connection ports for the system. This enables the implementation of additional feed-throughs into the *zone plate* chamber which for example could provide features like temperature monitoring.

The exiting aperture and connection of the *zone plate* chamber to the adjacent *sample chamber* of NEMI is provided by a diameter 5 mm CF-100 copper gasket aperture. A sketch showing the implementation of the exiting aperture as well as the four-port VAB *distance flange* to the other ZPC components is presented in figure 6.22.

#### 6.2.2.1 *Zone plate mounting & X-Y movement*

The second requirement to the *zone plate* chamber is, as mentioned in section 6.2.2, to hold the *zone plate* (ZP) itself. Tied to this requirement is the demand of a horizontal X-Y adjustment possibility for the ZP<sup>5</sup>.

The fabrication process of the *zone plates* provides a silicon nitride *chip* holding up to nine zone plates. A principle sketch showing such a *chip* and its mounting can be found in figure 6.23. The *chip* is attached to the *ZP holding plate* which on the other hand will be mounted onto the *zone plate holder* itself by six M4 hexagon socket screws. Figure 6.24 shows a detailed schematic of the mounting for the *ZP holding plate*. Another feature implemented onto the *ZP holding plate* is a *beam adjustment inset*. The position of this inset is also shown in figure 6.24. With the help of this inset it is possible to set a X and Y reference axis for the in chapter 7.1.2 described *zone plate adjustment* with the beam line.

The attachment of the *zone plate chip* onto the *ZP holding plate* takes place with three fitting springs shown in figure 6.25.

To make sure the focused helium beam can pass unaffected further on into the sample chamber the *ZP holding plate* as well as the *zone plate holder* itself have milling grooves. A sketch and a photograph of the *ZP holding plate* mounted onto the *zone plate holder* showing these milling grooves is depicted in figure 6.26.

The *zone plate holder* is fixed to a rotatable CF-63 flange (*zone plate holder flange*) on its back end. Due to the rotation feature it is possible to align the *ZP holding*

---

<sup>5</sup> Manufacturing of the *zone plate holder* parts has been performed by Kurt Ansperger [83].

*plate* into a horizontal position after the *zone plate holder* is mounted into the *ZP* chamber. To find this horizontal position, a small circular spirit level is attached to the outside of the *zone plate holder flange* (see figure 6.27). The fastening of the rotatable part of this flange against the fixed mounted outer ring of the flange is done via three radially placed *grub screws*.

Figures 6.27 and 6.28 present two sketches of the completely assembled *zone plate holder* from different view directions.

To mount the *zone plate holder* with a variable adjustment option in X&Y direction, the CF-63 flange of the *zone plate holder* is not directly mounted to the CF-63 *zone plate mounting flange* on the *zone plate chamber cross*. Instead an additionally X/Y/Z ultra high vacuum stage (XYZT64-50-H from UHV DESIGN [93]) is implemented in-between those two components. A sketch of this ultra high vacuum stage is presented in figure 6.29. The X&Y travel of the stage is  $\pm 12$  mm from the center position whereas the travel range in Z-direction is 50 mm. An additional design drawing with more detailed specifications for this UHV stage can be found in Appendix B.1.

Assembly sketches presenting the whole *zone plate chamber* together with the mounted *zone plate holder* as well as a mounted MAG W 300 turbo pump can be found in the figures 6.30 and 6.31. In the later figure the *zone plate chamber CF-100 cross* is faded out to enable a presentation of the *zone plate holder* position within the chamber and in respect to the blue marked beam center line. As indicated in this figure the front side of the *zone plate holder* is not interfering with the beam when located in the outermost Z-position of the *zone plate positioning X/Y/Z* stage. This enables a beam alignment of the unfocused helium beam without any interference from the *zone plate* and the *zone plate holder*. The 50 mm travel range and the length of the *zone plate holder* are designed so that all *zone plates* on the *zone plate chip* can be inserted into the beam line (indicated by a blue line in figure 6.30 and 6.31). The stage's Y travel range of 12.5 mm is big enough so that it is possible to reach all nine *zone plate* locations on the chip.

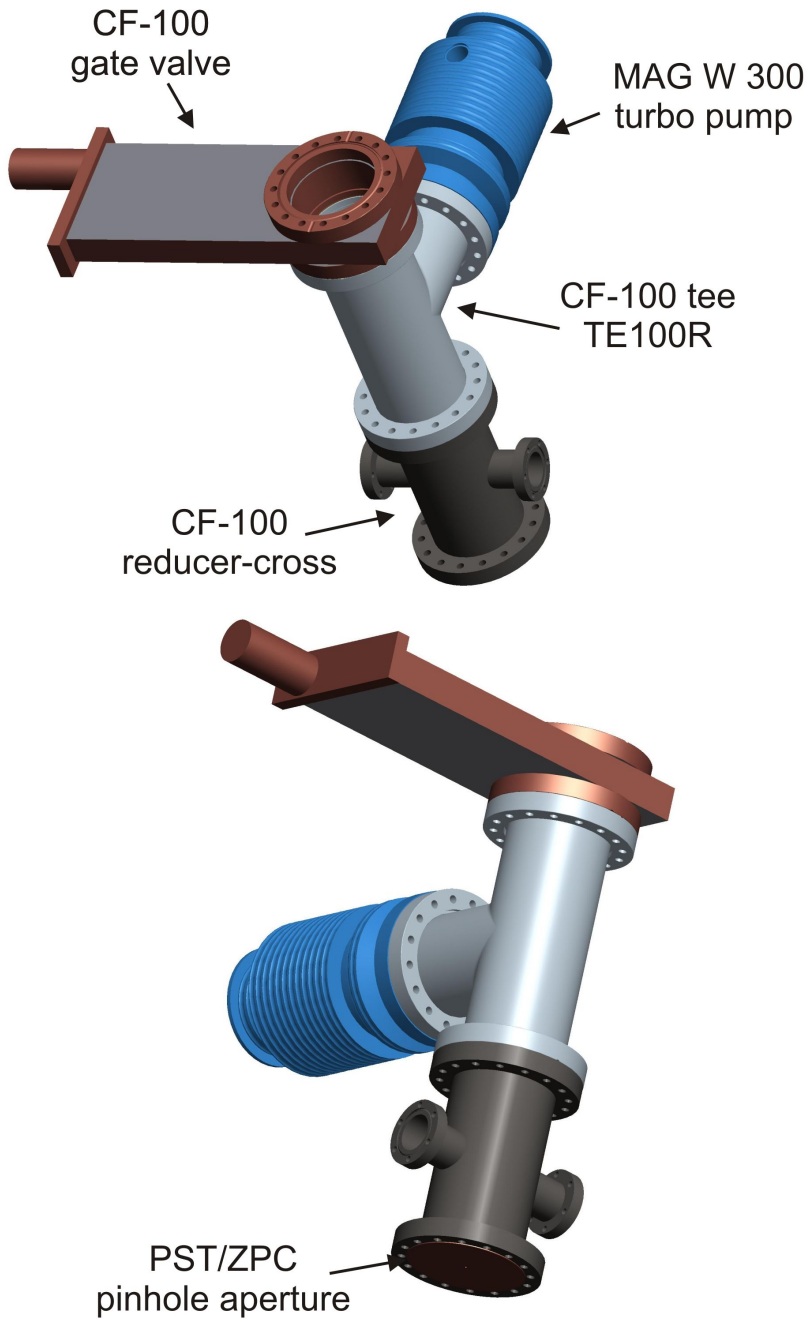


Figure 6.20: Schematics of the components building up the *pumping stage chamber (PST)*. A *CF-100 gate valve* is connected with a *CF-100 tee piece* and a *CF-100 reducer cross*. The exciting aperture from the *PST* into the *ZPC* is a *CF-100 copper gasket* with a diameter 5 mm pinhole.

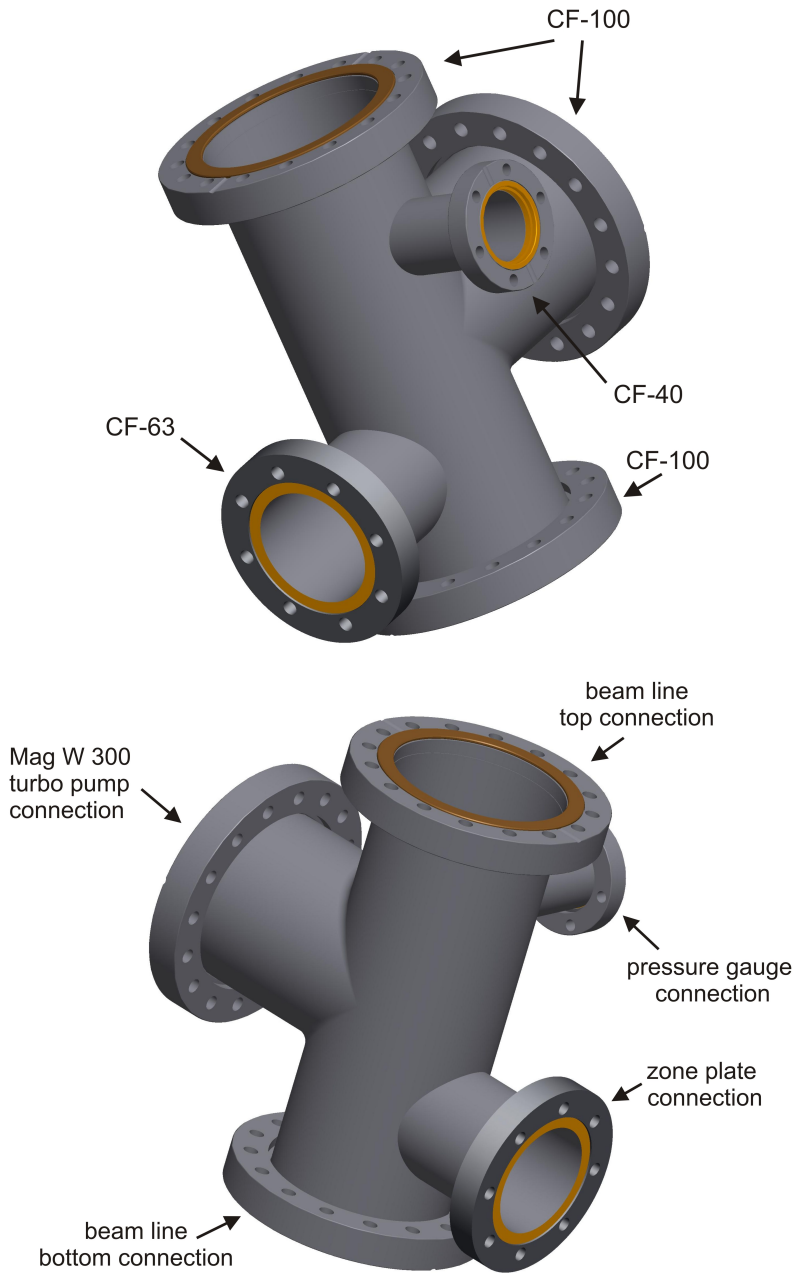
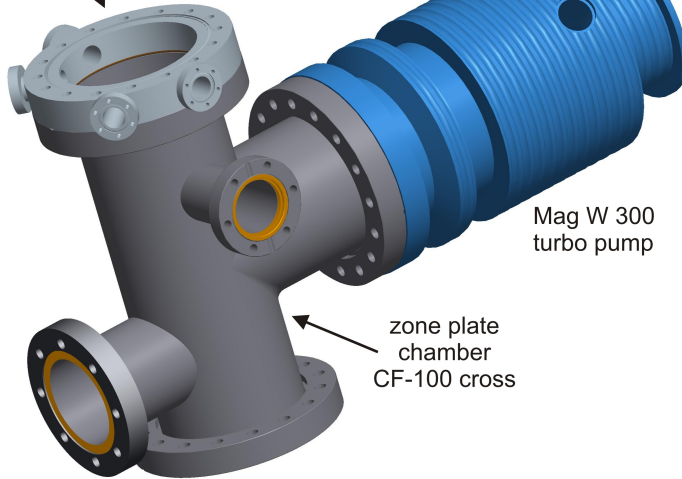


Figure 6.21: Sketches of the *zone plate chamber CF-100 cross* showing the two CF-100 connection flanges along the instruments beam line, the CF-100 connection side flange for the MAG W 300 turbo pump, the CF-63 side connection flange to implement the *zone plate* holding mechanism as well as the CF-40 side flange to connect the pressure measurement gauge for the chamber. (all CF-connections are pictured with CF- copper gaskets)

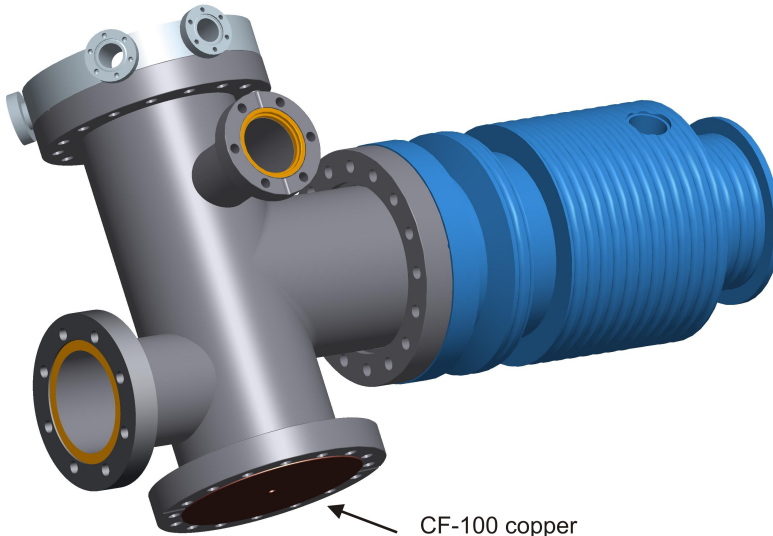


VAB CF-100  
distance flange  
with four CF-16  
ports



Mag W 300  
turbo pump

zone plate  
chamber  
CF-100 cross



CF-100 copper  
zone plate chamber  
exiting aperture

Figure 6.22: Sketches of the VAB CF-100 four port distance flange connected to the VAB specially manufactured CF-100 *zone plate* chamber cross. Also shown in this figure is a schematic of the MAG W 300 turbo pump and the CF-100 copper exiting aperture.

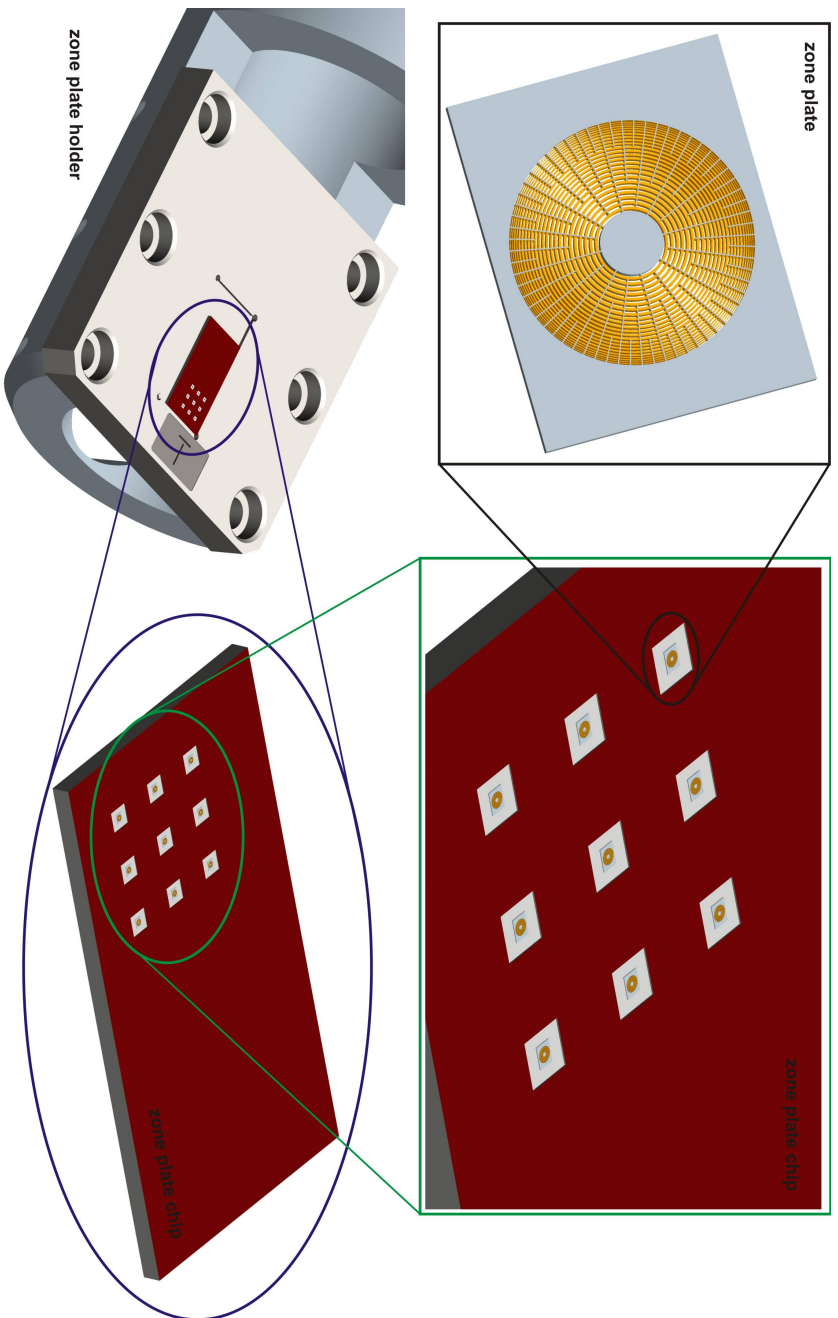


Figure 6.23: Sketch of the *zone plate holder*. The figure represents a sketch of the positioning for the *zone plate chip*. For better explanation of the principle magnified sketches of the components are shown. The *zone plate* shown in the top left part of the image is located on the *zone plate chip* (top and bottom right image). Such a chip can hold up to 9 zone plate patterns. It is attached to the *ZP holding plate* which is shown in bright gray in the bottom left picture.

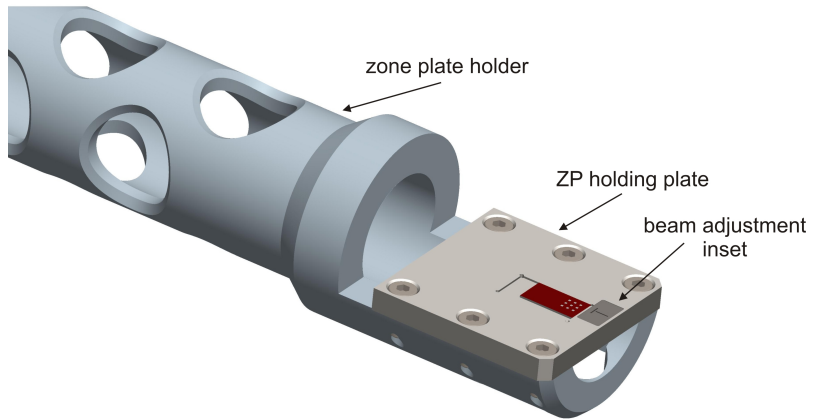


Figure 6.24: Schematic representing the assembled *zone plate holder*. The *zone plate chip* is attached onto the *ZP holding plate* which is mounted by six hexagonal socketed screws.

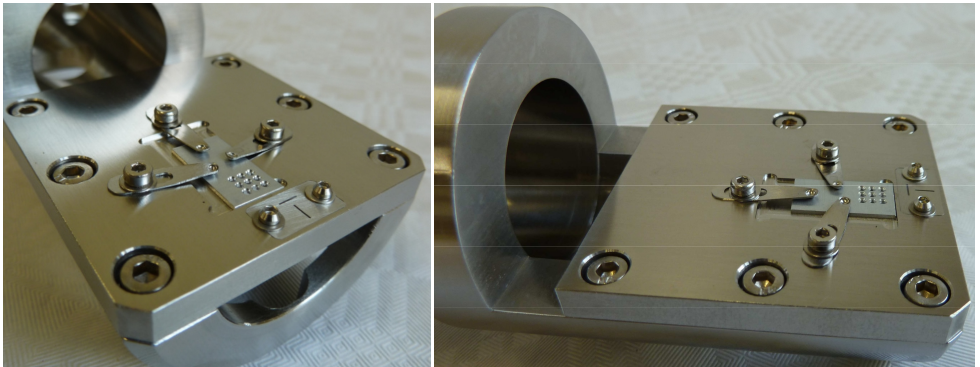


Figure 6.25: Photographs of the *zone plate holder* especially describing the attachment process for the *zone plate chip*. This attachment is done via three fitting springs which are connected to the holder plate through hexagon socketed screws. (Fitting spring concept developed by Kurt Ansperger [83])

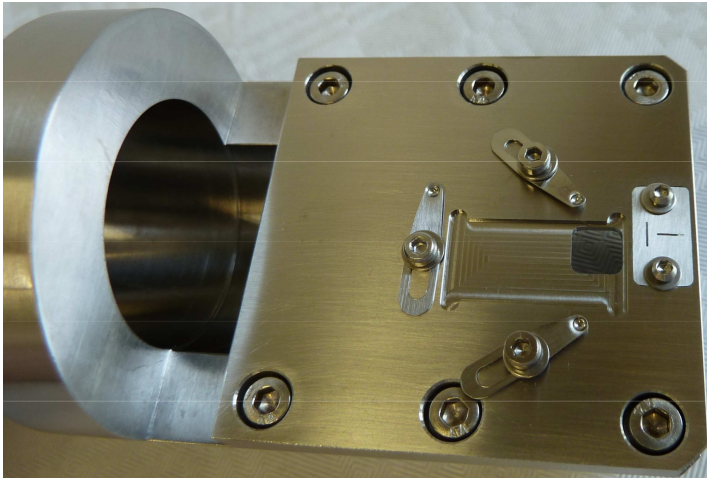
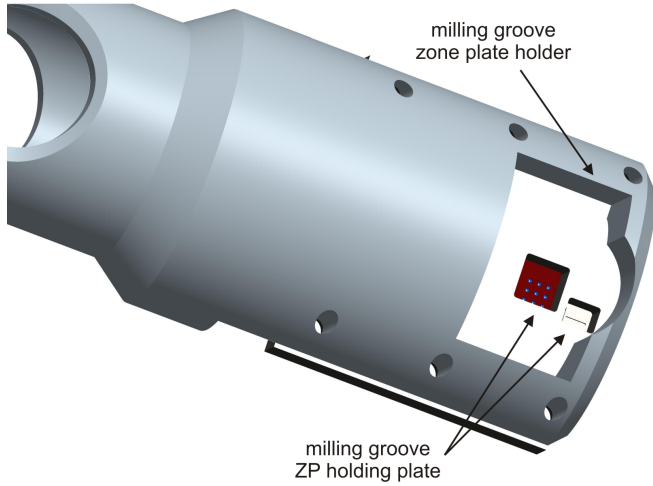


Figure 6.26: 3D sketch (top) and photograph (bottom) of the *ZP holding plate* and the *zone plate holder* showing the milling grooves in both parts. They are necessary to ensure that the focused helium beam can pass unhindered further on into the sample chamber. The image in the bottom presents the *zone plate holder* without a mounted *zone plate chip*.

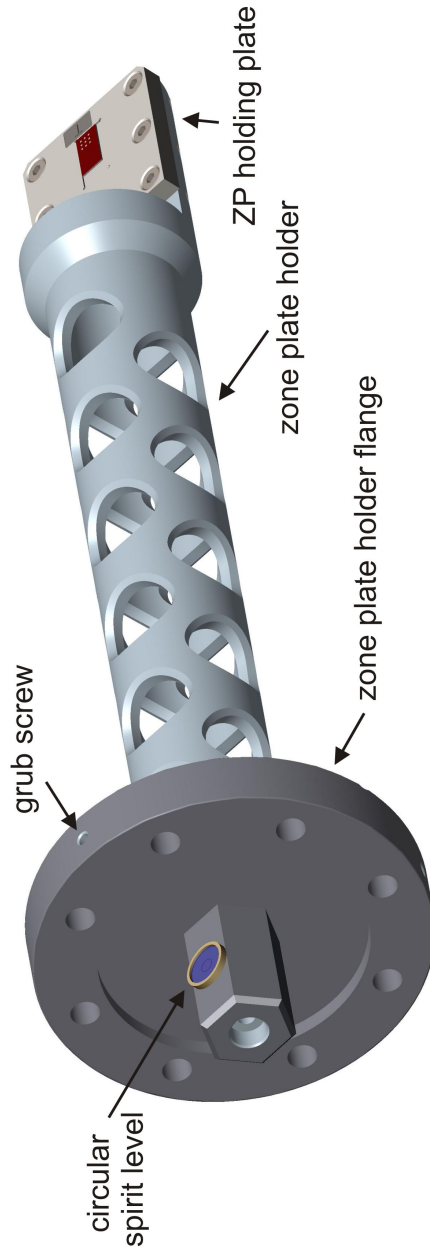


Figure 6.27: Assembly sketch of the *zone plate holder* with attached *ZP holding plate*, *zone plate holder flange*, and *zone plate chip*. Also indicated is the circular spirit level as well as the grub screws fixing the rotatable part of the CF-63 flange against the fixed outer ring of the flange after the horizontal adjustment of the *ZP holding plate*.



Figure 6.28: Assembly sketch of the zone plate holder with attached ZP holding plate, zone plate holder flange, and zone plate clip from a different view direction.

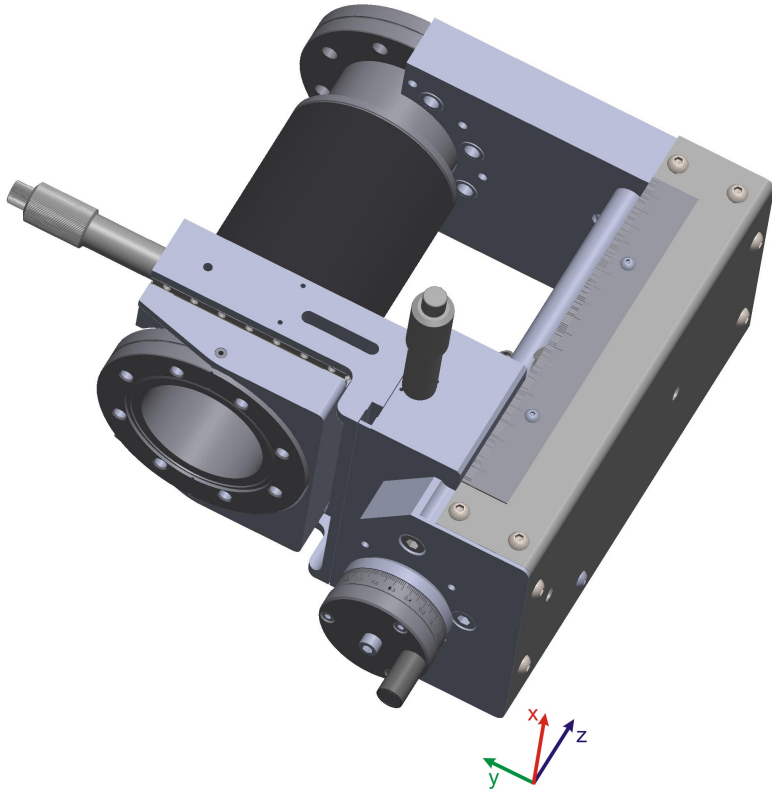


Figure 6.29: 3D sketch XYZ stage **XYZT64-50-H** from the company UHV DESIGN. (3D CAD model provided by UHV Design)

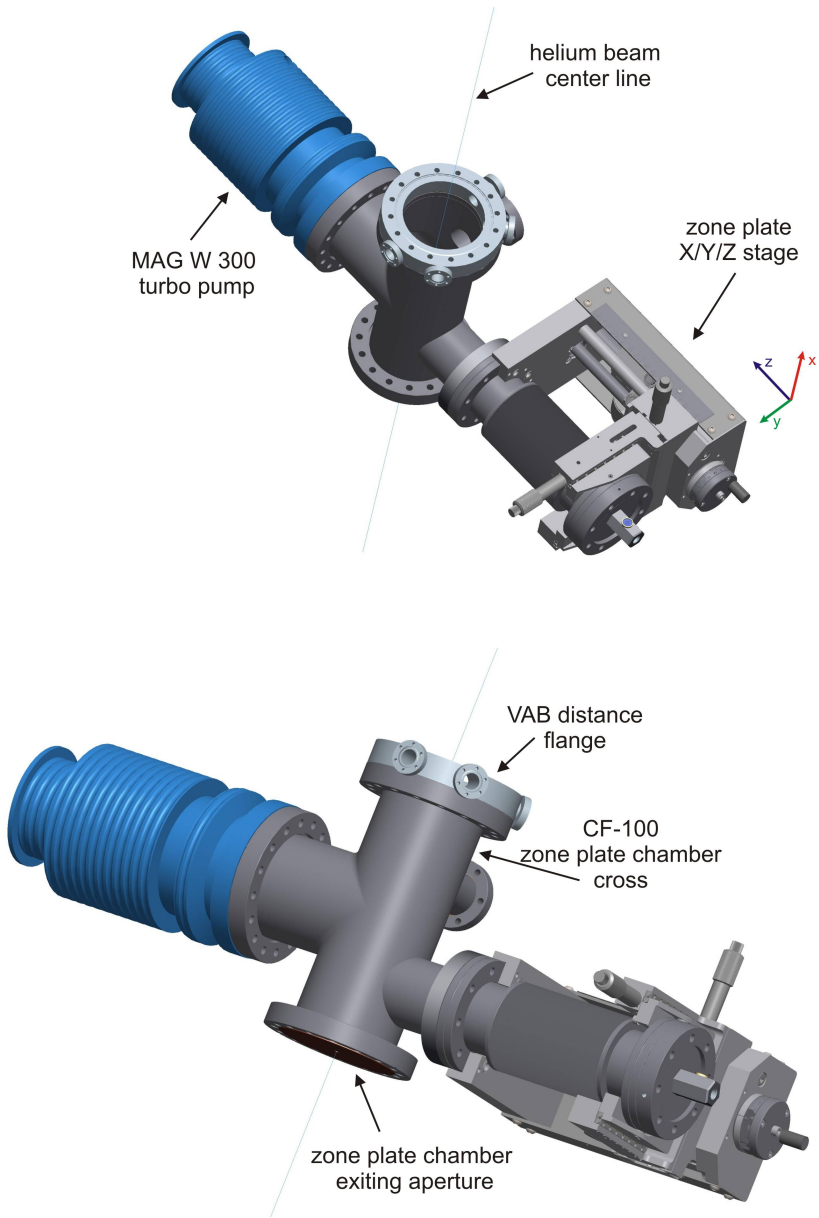


Figure 6.30: Assembly sketch of the *zone plate chamber* with a mounted *zone plate holder* attached to the UHV X/Y/Z stage as well as with a mounted MAG W 300 turbo pump presented with different view directions (top, bottom).



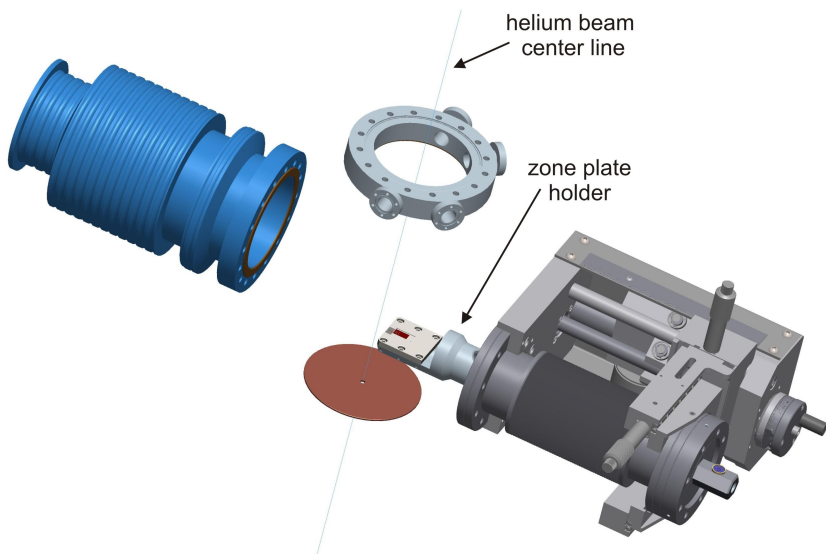


Figure 6.31: Sketch of the *zone plate holder* and the Y/X/Z zone plate adjustment stage within the zone plate chamber setup. For a better description the CF-100 *zone plate chamber cross* is faded out of the graphic. To indicate the position of the helium beam the beams center line is marked by the blue line passing through the VAB distance flange and the copper exiting pinhole aperture of the zone plate chamber.

### 6.3 SAMPLE AND DETECTOR CHAMBER

Following to the *zone plate chamber (ZPC)* is the *sample and detector chamber (SDC)*. The passage aperture between those two chambers is a copper CF-100 gasket with a 5 mm diameter pinhole aperture.

The aim of this chamber is to hold the *sample* which is mounted with free *X,Y,Z* movement and a 360° rotational freedom to place it under different beam incident angles. The sample chamber of NEM1 also contains the whole *detector setup*. This is due to the detection principle which is based on a *pitot tube* system (see chapter 5). When using this detection principle the distance between the sample surface and the *pitot tube* entrance aperture has to be in the range of 1 mm or below (see section 2.1.4) for diffusive reflecting samples. This implies that the detector itself has to be located within the sample chamber, and it has to be adjustable in its position with respect to the sample surface. Since the sample performs the scan process the detector, ones adjusted for each sample, can be left in the same position during the whole imaging process.

Another requirement due to the detection principle is the achievement of very good ultra high vacuum conditions within the chamber ( $10^{-9} - 10^{-10}$  mbar). The background vacuum conditions need to be one order of magnitude better than the measured pressure signal from the detector (see chapter 2.1).

The following section will address the technical design concepts for the *sample implementation*, the *detector setup* and *positioning* as well as the design of the *sample/detector chamber* itself.

#### 6.3.1 Sample implementation

The requirements for the sample implementation were to provide an as flexible as possible sample mount onto a sample holder with free movement in *X,Y,Z* direction and 0-90° rotational adjustment against the impinging beam line. The demanded vacuum conditions for the sample chamber are a pressure in the  $10^{-10}$  mbar range.

### 6.3.1.1 *Sample holder*

The sample holder<sup>6</sup> is, as shown in figure 6.32, build up by a diameter 65 mm stainless steel disc which is 2 mm thick. It has two additional disc levels on it's back side. One level with a diameter of 35 mm times 1 mm thick and the second one with a diameter of 16 mm times 2.5 mm thick. In the center of the *sample holder* a diameter 6 mm hole provides the possibility to use the sample holder also for transmission scans of a sample. From the bottom side of the sample holder a M12 tread enables the mounting of different apertures with special cylindrical M12 inset rings. The outer diameter of the aperture discs has to be between 9 – 10 mm. With such an aperture disc it will for example be possible to gain a profile scan of the helium beam focal spot diameter.

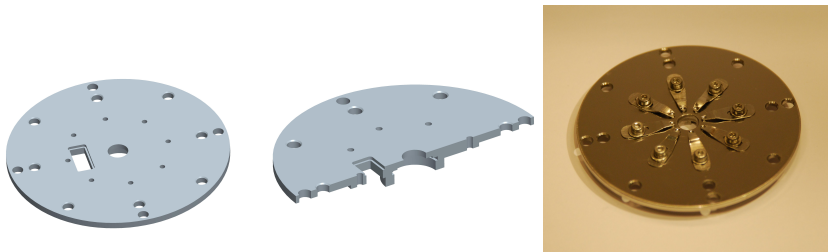


Figure 6.32: Left: Sketch of the *sample holder*; middle: schematic half section *sample holder*; right: photograph of the sample holder. The photograph also shows the eight flexible adjustable sample retaining springs attached to the sample holder with M2 socket head screws.

Several diameter 3.3 mm clearance holes provide a variable mounting option for the attachment of the *sample holder* to the *piezo table* by M3 screws. For detailed information on the design dimensions see the technical drawing attached in appendix B.1. To provide the possibility to set a reference position on the *sample holder* this component is equipped with a *position adjustment inset* (see figure 6.33). A thin rectangular metal plate with two small slit apertures arranged perpendicular to each other is attached to the *sample holder* in a way that it is possible to find a reference position of the whole sample mounting setup in transmission mode of the beam. A detailed description of the reference point adjustment process for the *sample holder* is presented in section 7.1.4.

<sup>6</sup> The *sample holder* is manufactured by Kurt Ansperger [83].

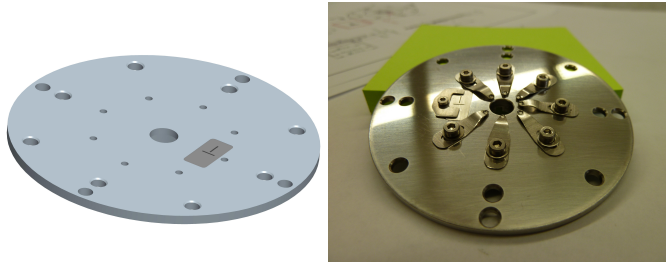


Figure 6.33: Left: sketch of the *sample holder* with the attached *position adjustment inset*; right: the same component shown in a photograph.

### 6.3.1.2 *Sample holder mounting and scanning process*

For the scanning process a *piezo table* from the company PIEZOSYSTEM JENA [94] is utilized. A sketch of this ultra high vacuum compatible **PXY 102 CAP ID40** high resolution xy-positioner with integrated capacitive measure system is presented in figure 6.34, as well as a photograph in figure 6.35.

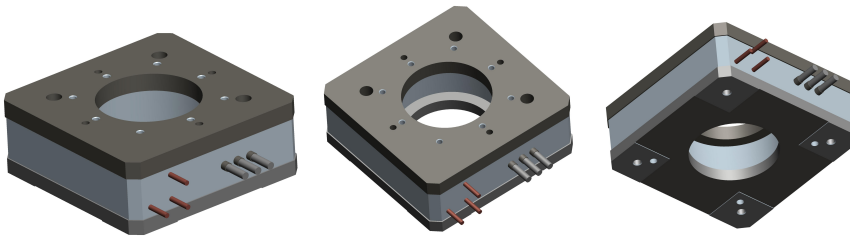


Figure 6.34: 3D sketches of the UHV compatible high resolution xy-positioner from different view directions. The sketches show the diameter  $d = 40\text{ mm}$  aperture opening in the middle of the *piezo table*, enabling also scanning processes with the helium beam in transmission mode.

The technical drawing provided by the manufacturer is attached in appendix B.1. A listing with the specifications of this component is presented in table 6.2. The stepping (scanning) process is performed with a 3-channel piezo amplifier with integrated closed loop controller. The above described sample holder is mounted to the piezo table with M2 screws. A schematic of the mounted *sample holder* together with the *piezo table* is depicted in figure 6.36. A blue rectangular plate representing the sample position is also indicated in the drawing. To better explain the working principle for transmission measurements, half

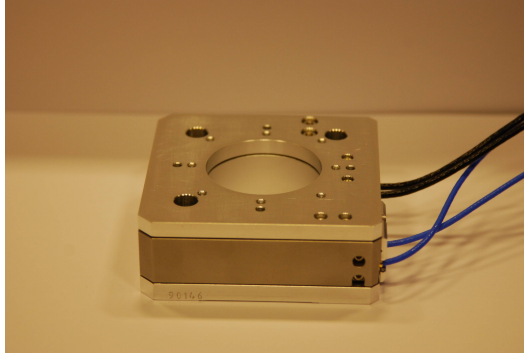


Figure 6.35: Photograph of the UHV compatible high resolution xy-positioner.

section sketches of the *sample holder* and the *piezo table* are provided at the right side of the same figure.

### 6.3.1.3 Sample positioning

A specially manufactured ultra high vacuum compatible XYZR stage system from ALIO [95] provides the X/Y/Z and rotational positioning of the sample. This stage was purchased by LASER 2000 [96] and has the article number: **XYZR Laser 2000 PO 1004704**. It consists of a combination of three standard stage systems from ALIO which are listed in table 6.3.

3D sketches of this three stage components are presented in figure 6.37. Figure 6.38 presents schematics of the assembled XYZR system from different view directions. As one can see the linear Z-travel stage is mounted on top of the X-Y stage, whereas the rotary 360° stage option is attached to the mounting surface of the Z-stage. The three linear movement axes X,Y and Z are provided with a step resolution of 0.02 μm through the encoder interface. Additional design drawings of all three *stage components* provided by the manufacturer are attached in appendix B.1.

For the attachment of the *sample holder* and the *piezo table* to the XYZR movement unit, a *sample attachment unit* was designed<sup>7</sup>. Schematics of this *sample attachment unit* are presented in figure 6.39. The bottom of this figure also shows photographs of this component.

The above described *piezo table* with the attached *sample holder* is placed on this *sample attachment unit* which on the other hand is mounted directly

<sup>7</sup> Fabrication at [83]

SPECIFICATIONS PXY 102 CAP ID40 PIEZO TABLE		
Stroke closed loop (each axis)	$\mu\text{m}$	80
Stroke open loop (each axis)	$\mu\text{m}$	100
Resolution	nm	2
Repeatability	nm	18
Dimension: length	mm	80
width	mm	80
height	mm	30
Aperture diameter	mm	40
Maximum baking temperature	$^{\circ}\text{C}$	150
Integrated capacitive feedback sensor		

Table 6.2: Specifications ultra high vacuum compatible **PXY 102 CAP ID40** high resolution xy-positioner

ALIO XYZR STAGE SYSTEM		
XYZR Laser 2000 PO 1004704		
<b>AIO-HR4-5000E-050-XY-UHV</b>	integrated XY-linear stage	50 mm travel in X/Y
<b>AIO-D8-2500E-CB-UHV</b>	integrated linear Z-stage	25 mm
<b>AIO-40R-D-UHV</b>	360° continuous rotary stage	Ø130 mm table

Table 6.3: List of the implemented stages for the XYZR vacuum compatible sample stage system.

to the rotational stage component of the ALIO motion system. For a better description of the mounting steps the sketches of figure 6.40 as well as figure 6.41 are presented. Figure 6.40 shows the assembly of the *sample holder*, the *piezo table* and the *sample attachment unit*. Whereas figure 6.41 depicts this three components further assembled to the XYZR stage. As shown in figure 6.40 also the *sample attachment unit* holds the necessary notch to permit a free beam line in transmission mode. Note that the 360° rotary stage has a **maximum bake-out temperature of 35°C** since it contains ceramic components. The two other linear stages are able to withstand bake-out temperatures of up to 110°C.

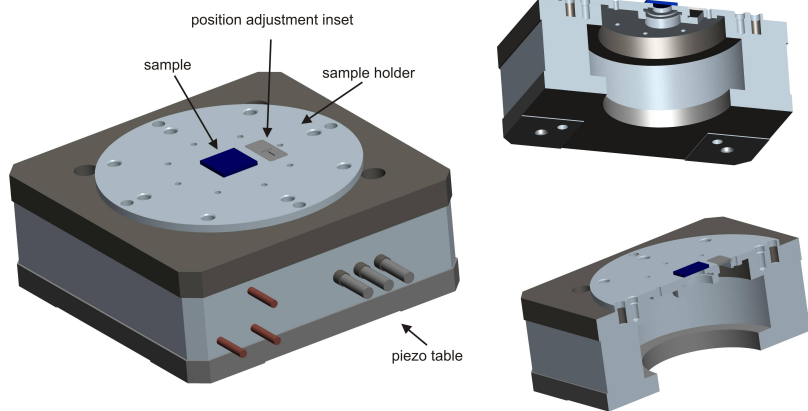


Figure 6.36: Left: sketch of the attachment of the *sample holder* to the *piezo table*. The sample is indicated by the blue rectangular plate placed in the middle of the sample holder; right: schematic half section sketch of the *sample holder* attached to the *piezo table* at different view directions.

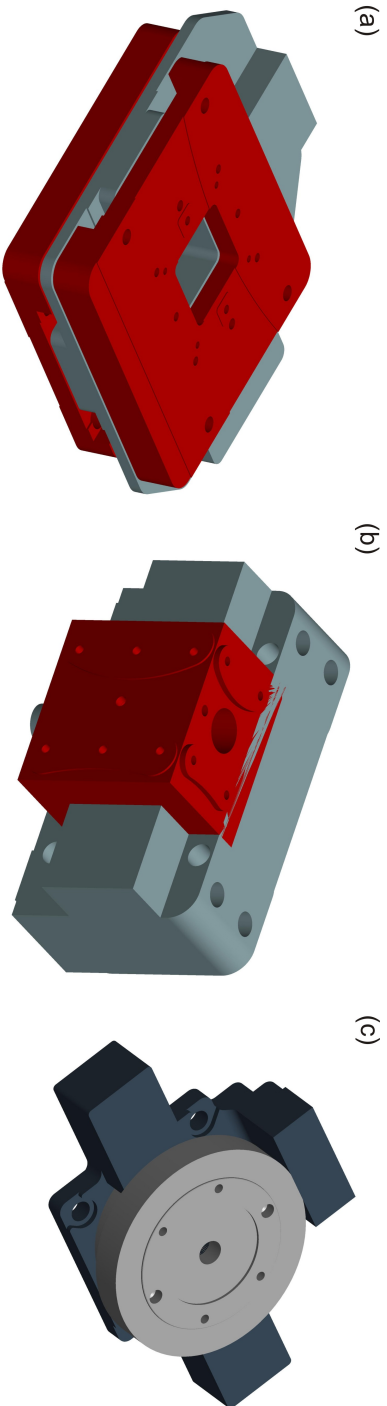


Figure 6-37: Schematics of the three Ario stage components. (a): **AIO-HR4-5000E-050-XY-UHV** XY-linear stage, (b): **AIO-D8-2500E-CB-UHV** integrated linear Z-stage and (c): **AIO-40R-D-UHV** 360 degree rotary stage. (3D CAD model provided by Ario Industries)



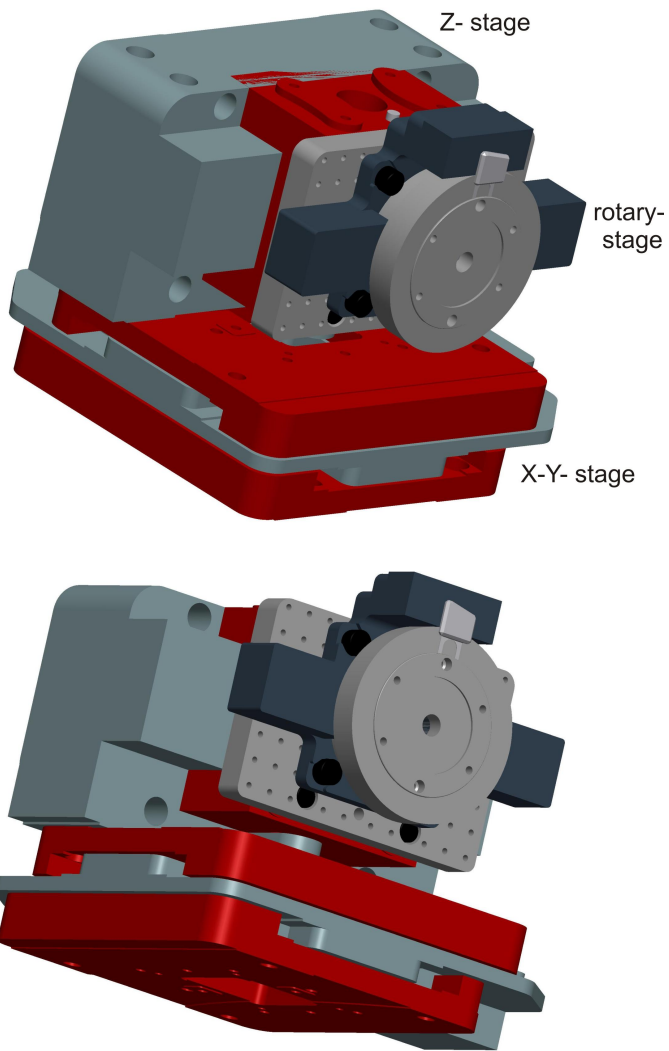


Figure 6.38: 3D sketches of the assembled XYZR stage from ALIO. (3D CAD model provided by ALIO Industries)

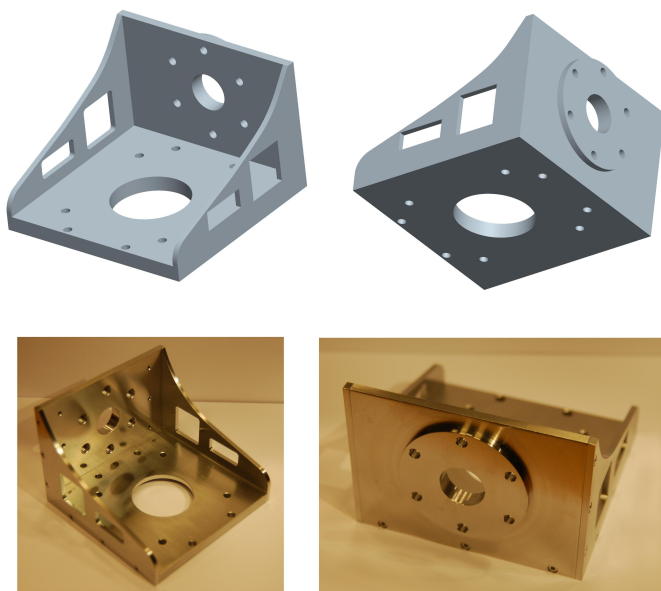


Figure 6.39: Top: Sketches of the *sample attachment unit* from different view directions; bottom: photographs of the *sample attachment unit*.

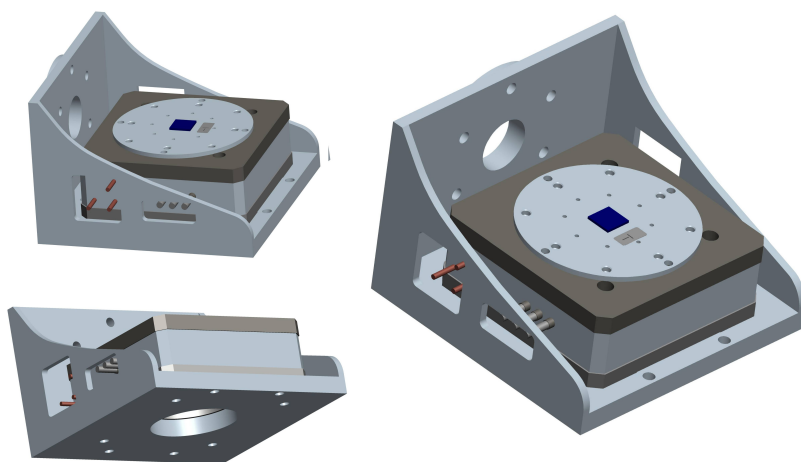


Figure 6.40: Sketches of the assembled *sample attachment unit* with the *piezo table* and the *sample holder* from different view directions. Note in the bottom left view that the *sample attachment unit* also holds a cylindrical notch to permit a undisturbed path for the helium beam line in transmission mode.

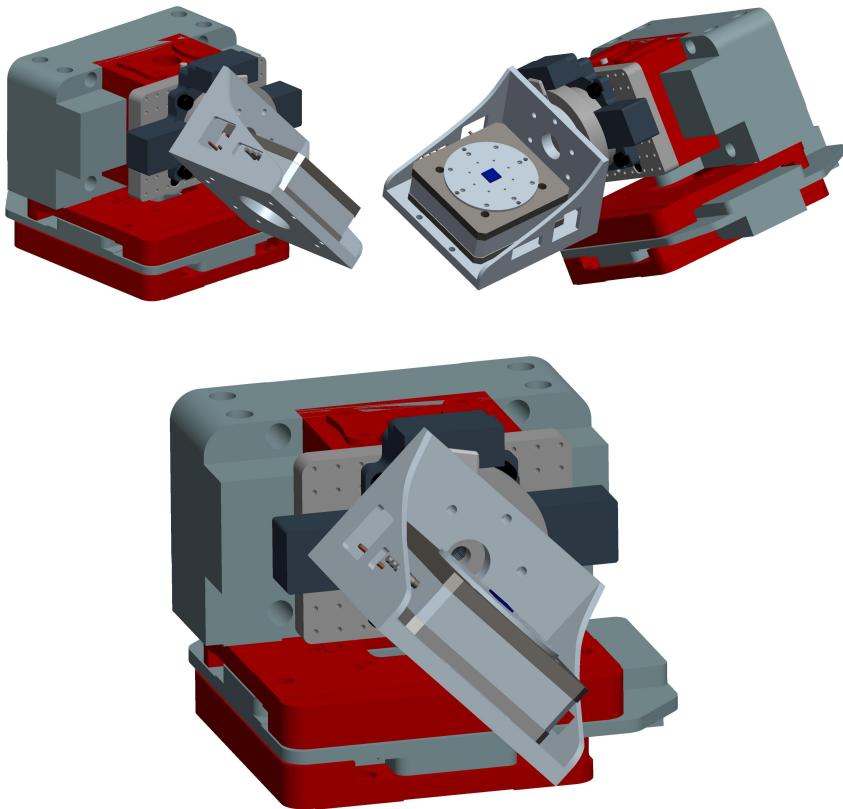


Figure 6.41: 3D schematic of the complete sample stage assembly consisting of the XYZR stage assembled with the *sample attachment unit*, the *piezo table* and the *sample holder* from different view directions.

### 6.3.2 Detection

Chapters 1.2.4, 2.1.6 and 5 presented a detailed description of the working principle for the detector. In the following the technical realization for this component will be presented<sup>8</sup>. The detection of the reflected helium atoms is performed with a *pitot tube* system. Actually there are two different *pitot tube* detectors implemented in the microscope setup. One *reflection detector* and one *transmission detector*. The second one is simply provided by the attachment of an additional *cold-cathode ionization gauge* with a small entrance aperture placed directly into the straight beam line (see sub-section 6.3.2.3). The main detector is the device utilized for the reflection mode of the system.

#### 6.3.2.1 Reflection detector & X-Y-Z movement

As mentioned in the beginning of this chapter (6.3) for diffuse samples it is necessary to place the entrance aperture of the *pitot tube* detection very close to the reflecting surface ( $\leq 1$  mm). Therefore it was decided to build this component on the basis of a “*nose-shape*” like detection system. This will



Figure 6.42: Sketches of the *detector nose* presented from different view directions (left, middle); right: half section sketch of the same component.

ensure sufficient clearance between the sample and the detector to still provide a free sample movement for the scanning and adjustment process (see figure 6.45).

The *detector* is assembled by four different main components, the *detector head*, the *detector nose*, the *0-order aperture mounting setup* and the *cold-cathode gauge*. Sketches of the three first mentioned components are presented in figures 6.43, 6.42 and 6.55. The two main components of the *pitot tube* part are the *detection nose* and the *accumulation cylinder*. These two components are sealed

<sup>8</sup> Technical design developed in collaboration with [83].

vacuum tight against each other with a gold gasket. The *nose* is mounted via four socket head screws.

As shown in figure 6.45 the *detector nose* is shaped in a way that it is possible to tilt the sample and the whole sample holding setup in the range of nearly 0 – 90 degree in respect to the incident helium atom beam. The *detector nose* has been manufactured twice with an entering aperture orifice diameter of 1 mm and 0.5 mm respectively. The entering aperture of the *detector nose* is followed by an approximately 2 cm long cylindrical channel which in the mounted state is opening out into the bigger also cylindrical shaped main part of the *pitot tube* accumulation volume within the *detector head* (see figure 6.43).

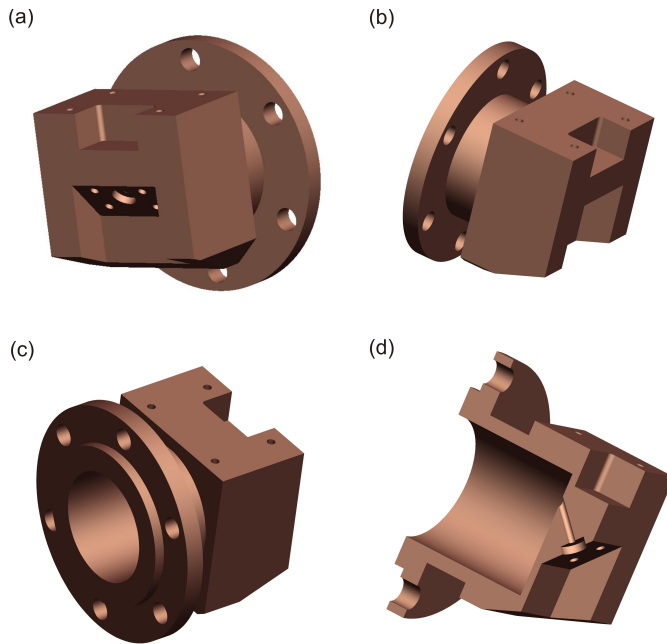


Figure 6.43: Sketches of the *detector head* presented from different view directions in (a), (b) and (c); (d) represents a half section sketch from the same component.

Another set of images illustrating the assembled *detector head* together with the *detector nose* and the 0-order *aperture mounting setup* are shown in figure 6.44. A half-section sketch of the *detector head* is presented in the bottom right image of figure 6.44 (d). It should provide a picture of the traveling path for the detected helium atoms. For a better understanding of the helium particle path and the detector position in respect to the sample figure 6.46 shows additional

sketches of the *sample/detector* arrangement. Before hitting the sample surface the helium probe beam passes through the *0-order sorting aperture* whereby the bigger share of the unfocused *0-order* part of the probe beam is blocked by the aperture (see chapter 6.3.2.2). The unaffected focused part of the helium beam impinges on the sample and the helium atoms are, depending on the surface structure, reflected in different directions. The amount of reflected helium atoms entering the *detector nose* via its aperture therefore will depend on the samples surface shape and roughness. They will further travel-on into the *detector head* where they are accumulated and consequently give rise to a detectable change in the pressure signal of the *detector*.

To improve the sensitivity of the detection system the whole detector body is made from copper, providing the possibility to cool it down to liquid nitrogen temperature. In this way the detector background vacuum condition within the accumulation volume is improved furthermore compared to the surrounding ambient pressure conditions in the sample chamber. This improvement is due to freezing distillation of background gas particles to the detector walls. As a consequence a higher sensitivity of the detector for small pressure changes can be achieved.

The cooling is performed with an outwards mounted liquid nitrogen tank. It has a pipe entering partly into the source chamber via a CF-63 flange and the cooling is further transferred via a copper cord directly to the copper made main body of the *reflection detector*. The thermal connection thereby is provided by a clamping mechanism for the cords braids onto the liquid nitrogen filled tube, as well as onto the detector body itself. To further provide a possibility for a back-out procedure, an additional heating system based on wire resistance heating is added to the detectors main body. Photographs explaining this cooling and heating options for the *reflection detector* are provided in figure 6.47. The connection of the CF-63 cooling feed-through to the cooling tank (liquid nitrogen tank, LN<sub>2</sub>) is done by a special flexible tube proved for low temperature made of **Polytetrafluoroethylene (PTFE, also known as TEFLON)**. This tube connects the stainless steel pipe of the CF-63 feed through to the mounting panel for a ball-shaped LN<sub>2</sub> tank also referred to as "chicken-feeder". Digital photographs of these components are presented in figure 6.48 .

To provide the option that the whole *reflection detector* can be placed in the correct position with respect to the sample's surface, it is mounted onto a

X/Y/Z UHV translation stage (**MAX 25**) from VAB [92] (see figure 6.49).

This linear translation stage is directly connected from outside to the sample chamber (see figure 6.60). Since the detector has to be located within the sample chamber an additional *extension* is implemented for its placing. A detailed sketch of the shape of this *extension* and the accompanying detector placement is presented in figures 6.50 and 6.51.

Together with this extension tube and the stage it is possible to adjust the *reflection detector* in X-Y-and Z direction relative to the sample (see figure 6.53 and 6.54). Figure 6.52 presents the schematics of the mounting of the *detector extension* into the X-Y-Z stage. It illustrates how the UHV-tight mounting into the stage takes place. Note that this mounting needs to be done before the *reflection detector head* is assembled to the *extension tube*.

The figures 6.53 and 6.54 present sketches of the mounted *reflection detector* assembled to the *extension tube* and the Y/X/Z UHV stage. The *sample attachment unit*, the *piezo table*, the *sample holder* and a mounted *sample* are also shown in this figure. Also the helium probe beam line is indicated in this graphics. For better illustration the *detection system* meaning the *detector head* and the *extension tube* as well as the cold-cathode gauge are presented in a half section sketch in figure 6.54.

The detector adjustment stage has a travel range of 25 mm in X and Y direction respectively. In Z-direction the travel is 50 mm which corresponds to a movement of the detector further into the sample chamber and therefore more close to the sample. With the long travel range in Z-direction it is possible to remove the detection setup completely from the direct beam line and the sample.

The *cold-cathode* pressure gauge used as the detector is mounted onto the inside CF-40 flange of the *extension tube*. Since the count rates (relative He pressure increase in the detector due to the reflected signal) may be very low, it is necessary to have a pressure detection gauge working even in the lower UHV range. Therefore the **IKR-070** *Module line* cold cathode gauge head from PFEIFFER [91] became the system of choice. The measurement range of this instrument is stated to be between  $5 \cdot 10^{-3} - 1 \cdot 10^{-11}$  mbar. Detailed gauge specifications are presented in appendix C.1.

### 6.3.2.2 0-Order sorting aperture

One major issue with using a transmissive *Fresnel zone plate* for the helium

beam focusing is the 0-order part of the beam also passing through the *zone plate*. The 0-order has a quite high intensity compared to the focal spot (see chapter 4) and therefore needs to be blocked before the beam is hitting the sample. On the other hand this blocking system should not interfere with the focused part of the helium beam. Therefore the blocking is done in two steps. The first step is performed by the middle stop disc of the *zone plate* itself. It stops the innermost part of the beams 0-order. The second blocking step is done with the help of a separate 0-order *sorting aperture*. This sorting aperture consists of a *skimmer*, placed reversed into the beam line at a relatively short distance before the sample. To ensure that the detector nose will be positioned correctly under this sorting aperture, it is mounted on-top of the detectors main body. A schematic picture of this setup is presented in figure 6.55 and 6.44.

The alignment of the skimmer aperture and the detector nose has to be performed before the detector is mounted into the sample chamber. It is not possible to do a realignment once the detector is mounted into the chamber (see section 7.1.3).

### 6.3.2.3 “in line” Transmission detector

For the “in line” *transmission detector* a *cold-cathode measurement gauge* (PFEIFFER [91] IKR-060, specifications see appendix C.1) is assembled via a CF-100 to CF-40 reducer adapter to the *sample chamber lid*. This is done in a way that the direct helium beam will enter the cold-cathode gauge through the center of a diameter 1 mm pinhole aperture placed directly in-front of the pressure gauge. Therefore it is also referred to as “in line” detector. Figure 6.56 shows a sketch of the “in line” *transmission detector* setup. The figure on the top right side hereby represents a half section sketch of the whole setup, whereas the figures in the bottom right and left for better illustration just show a half section sketch of the sample chamber lid and the reducer adapter, against what the cold-cathode gauge and the pinhole aperture (“in line detector”) are presented in a full sketch. The top left figure represents a full sketch of this components.



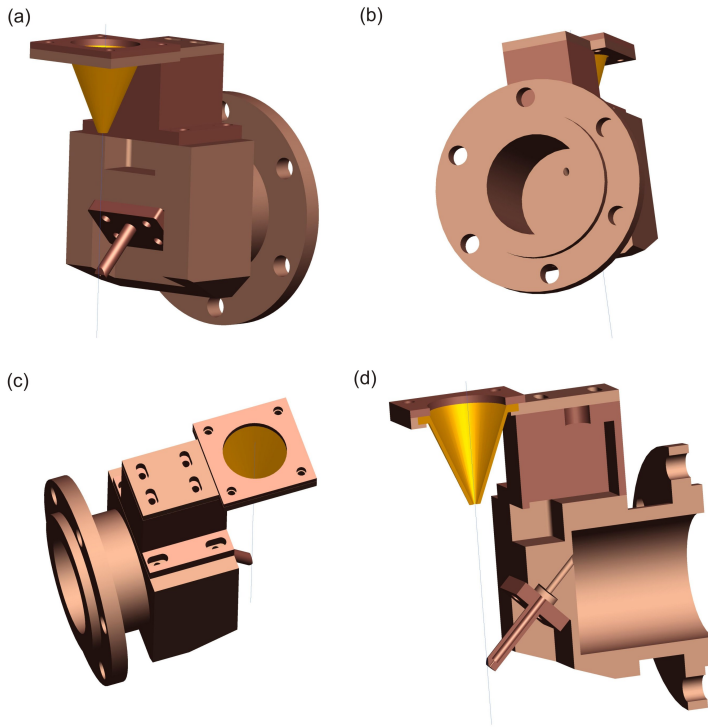


Figure 6.44: Sketches of the assembled *detector* presented without the *cold-cathode gauge*. (a), (b), (c) different view directions, (d) half section sketch. The center-line of the helium probe beam is indicated by the blue line passing through the *0-order aperture orifice*. From the sample surface reflected helium atoms enter the detector through the pinhole aperture in the *detector nose* and travel further on through the *nose* into the *detector head's* accumulation volume. The assignment for the *0-order sorting aperture* is to block out the bigger part of the *0-order* share of the helium probe beam.

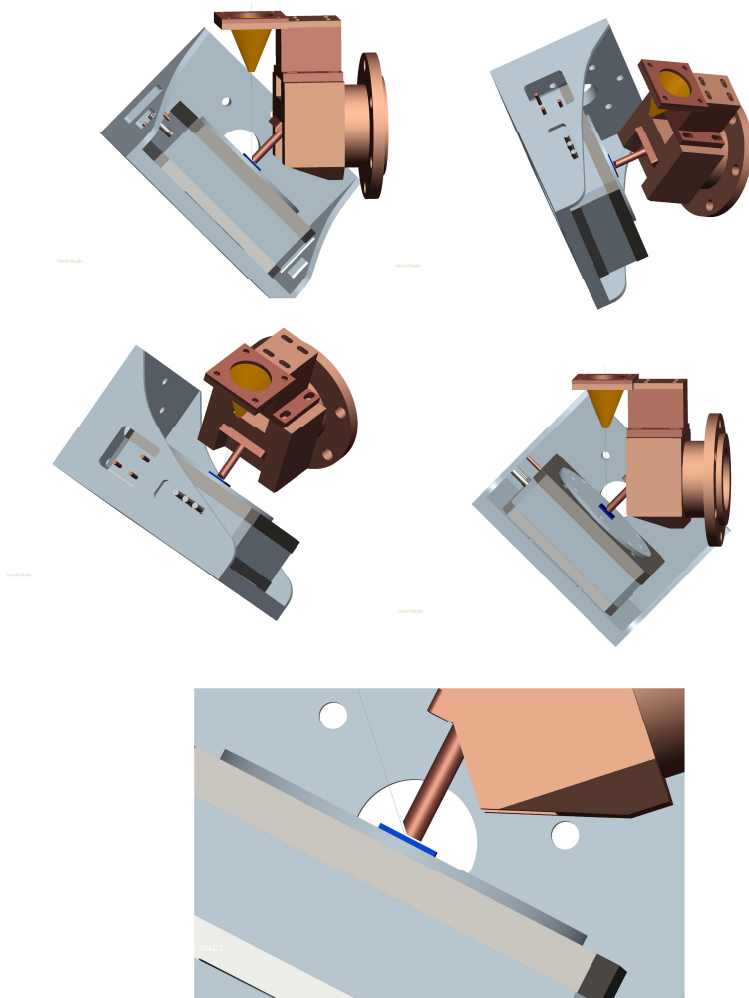


Figure 6.45: Sketches to show the idea for the arrangement of the *nose detector* and the mounted *sample*. The sample itself is indicated by the blue plate mounted on-top of the *sample holder* which is attached to the *piezo table*, which again is mounted onto the *sample attachment unit*. The incident helium beam is indicated by the blue line.

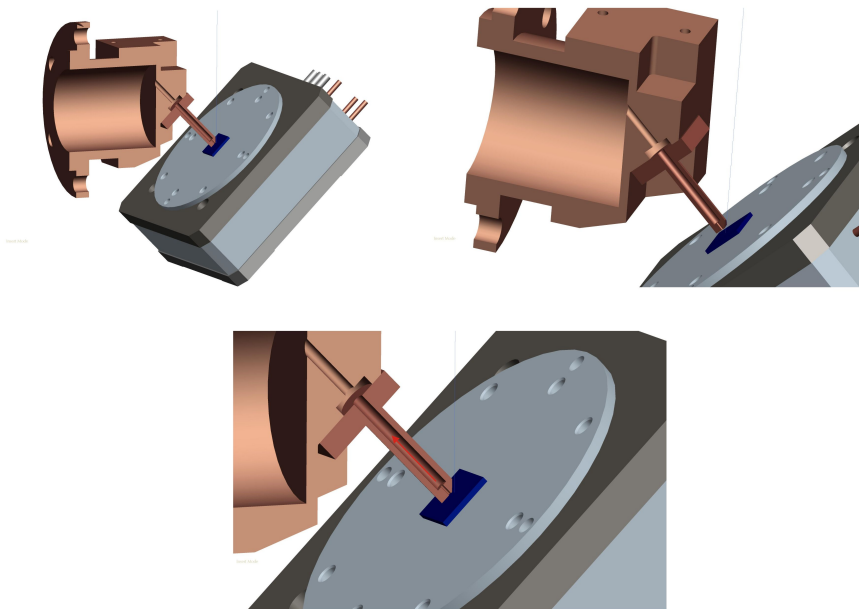


Figure 6.46: Sketches of the *sample/detector* arrangement from different view directions. For a better understanding of the traveling path for the reflected helium atoms the *reflection detectors front part* is shown in a half section sketch. The on the sample impinging helium beam is indicated by the blue line whereas the travel path of the reflected helium atoms within the detector nose is indicated in the bottom image by the red arrow.

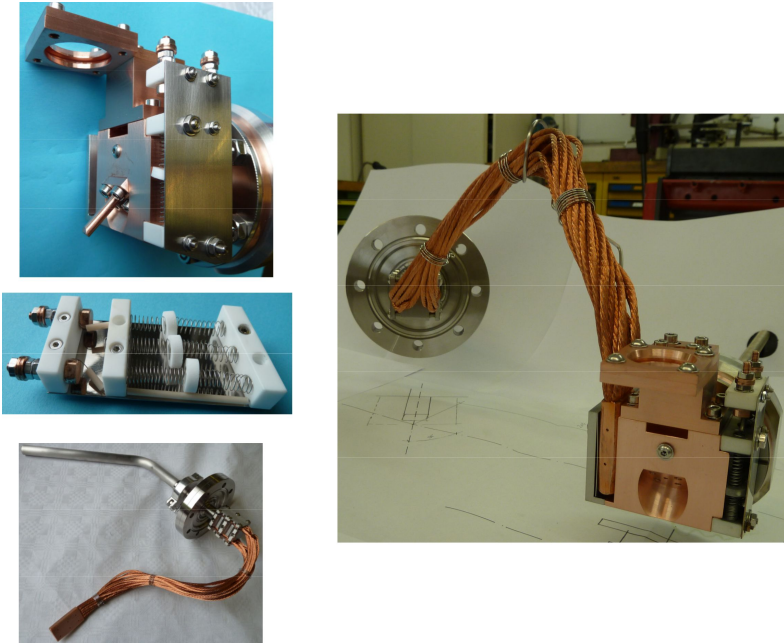


Figure 6.47: Photographs of the *reflection detector* with the connected cooling- and heating -setup for this component (top left, right); as well as photographs of the cooling- (bottom left) and heating- (middle left) setup respectively.

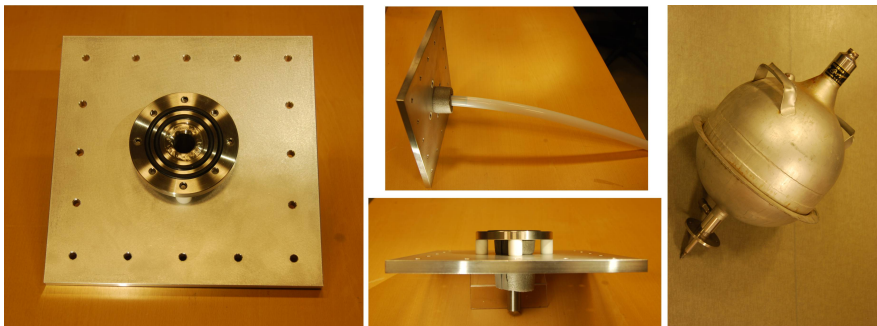


Figure 6.48: Photographs of the mounting panel for the LN<sub>2</sub>tank (chicken-feeder) (left, middle bottom); middle top: mounting panel with attached PTFE connection pipe; right: LN<sub>2</sub>tank (chicken-feeder)

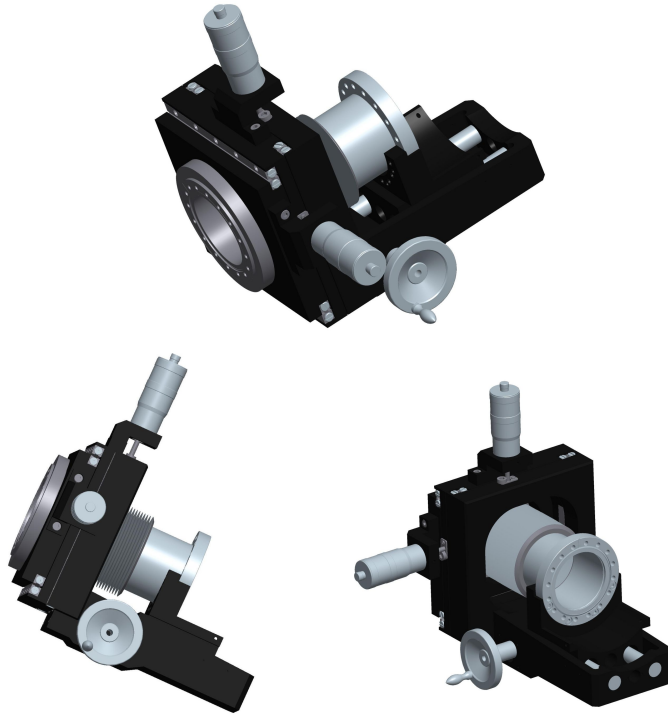


Figure 6.49: Sketch of the *reflection detector* positioning stage from VAB, presented from different view directions. (3D CAD model provided by VAB vakuum Anlagenbau GmbH)



Figure 6.50: Sketch of the *extension* for the *reflection detector* mounted to the stage from different view directions (top); bottom: half section sketch of the same component.

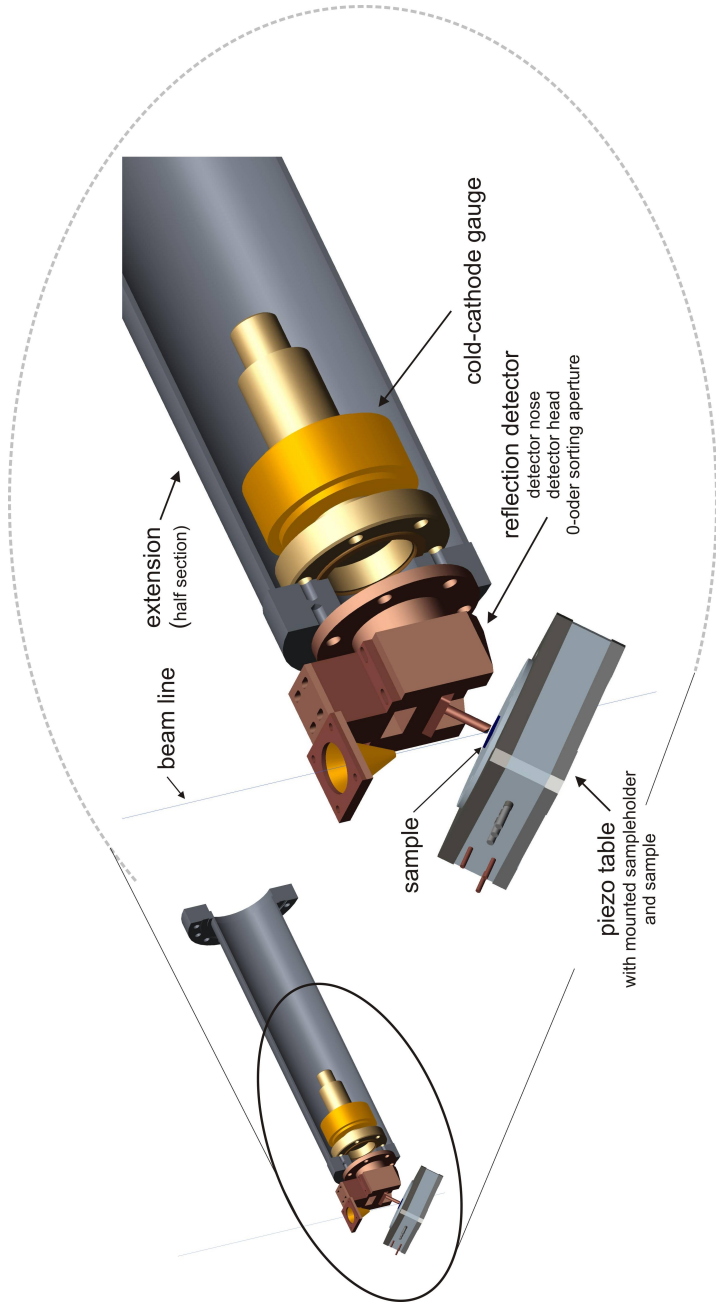


Figure 6.5.1: Sketch of the reflection detector mounted to the extension tube. The figure presents the reflection detector, the piezo table with mounted sample holder and sample, the cold-cathode gauge for the pressure measurement and the extension tube. For a better understanding the extension tube is represented in a half section sketch. The helium beam line is indicated by the blue line.

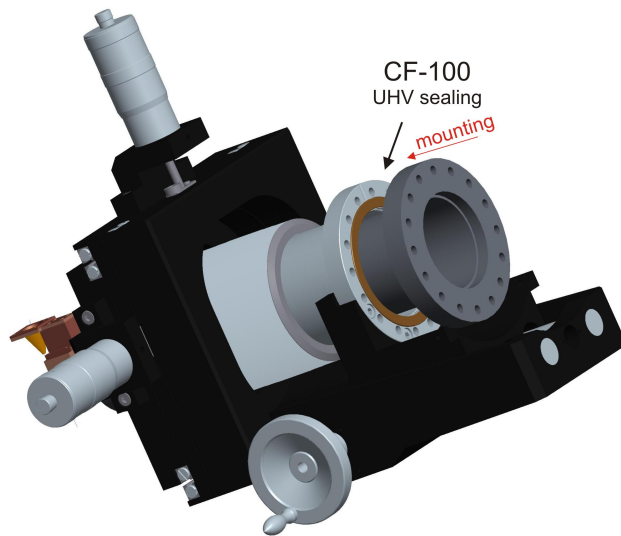


Figure 6.52: Sketch describing the UHV tight mounting of the *detector extension* into the VAB X/Y/Z stage. The sealing is a CF-100 copper gasket. Note that the mounting of the *reflection detector head* has to be done after assembling the *extension tube* into the stage.



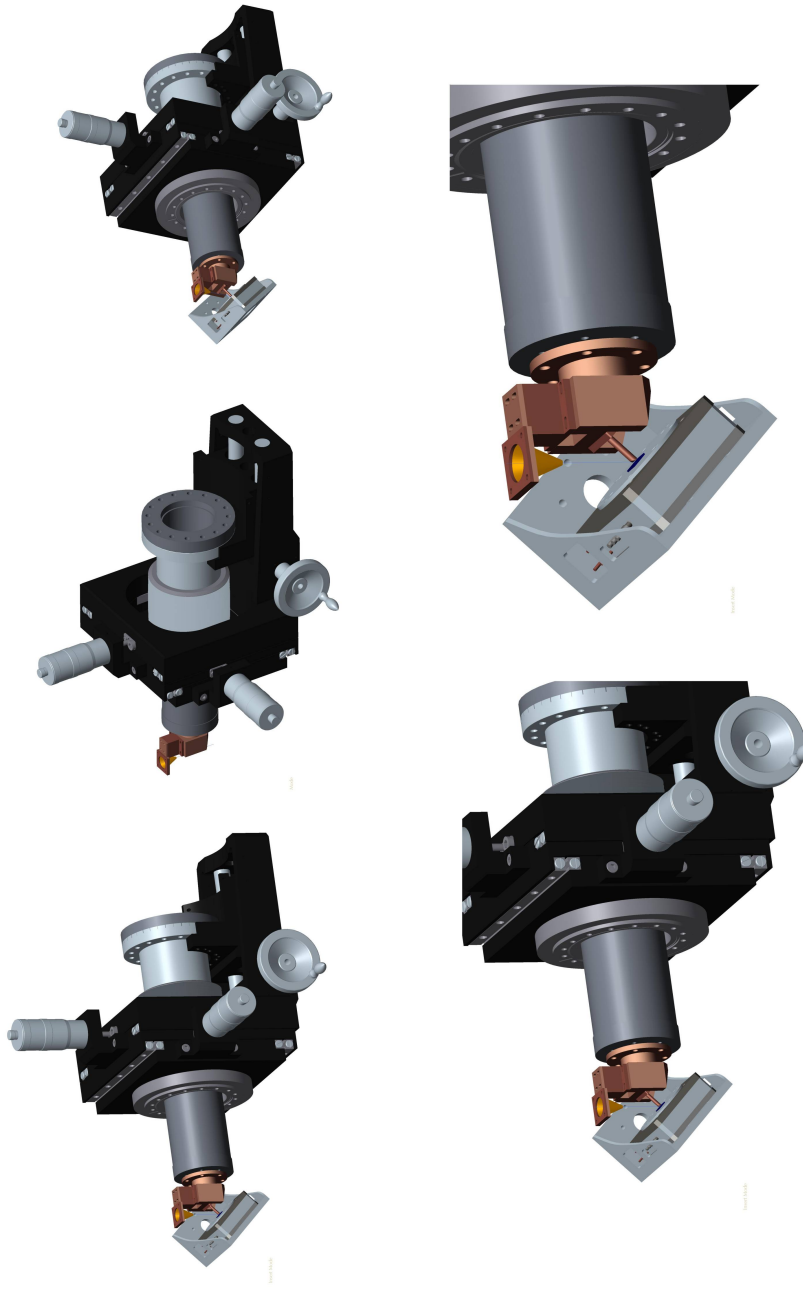


Figure 6.53: Sketches of the *reflection detector mounting* from different view directions and with different magnifications. The stage will be mounted from outside on the sample chamber (see section 6.3.3).



Figure 6.54: Sketches of the reflection detector mounting from different view directions and with different magnifications with the reflection detector and the extension tube shown in a half section sketch for better illustration. The stage is mounted from outside on the sample chamber (see section 6.3.3).

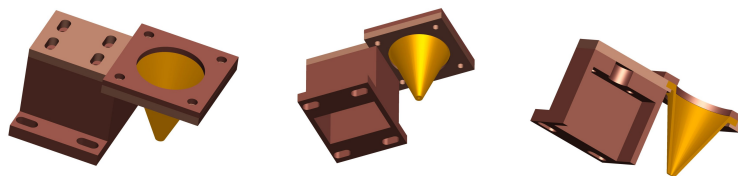


Figure 6.55: Sketches from different view directions (left, middle) of the 0-order aperture mounting setup presented with an attached skimmer for better explanation; right: half section sketch of the same component.

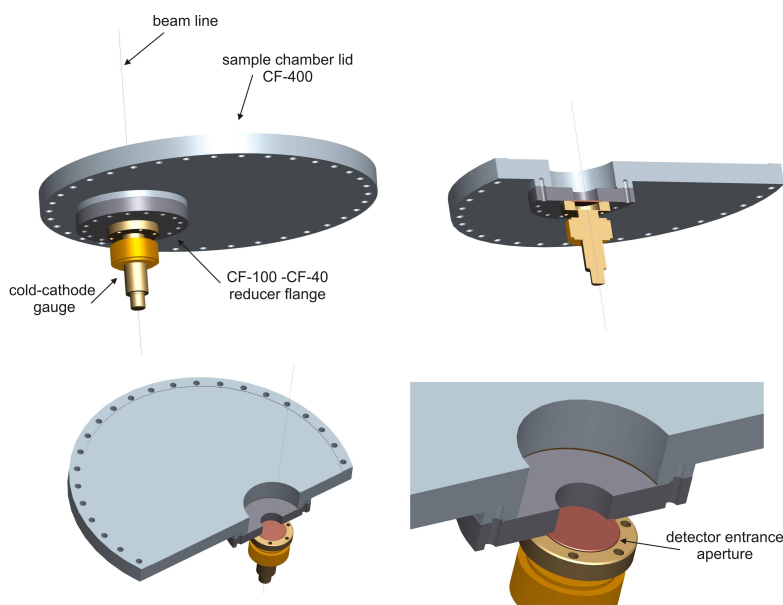


Figure 6.56: Sketch of the “in line” transmission detector setup, representing the cold-cathode gauge assembled via a CF-100/CF-40 reducer flange directly to the sample chamber lid. The entrance aperture for the detection system is a CF-40 copper sealing with an diameter  $d = 1$  mm orifice opening in the middle. Top left: full sketch of the assembled components; top right: half section sketch of all components; bottom left and right: half section sketch of the sample chamber lid and the reducer adapter as well as full sketch of the cold-cathode gauge and the entrance aperture.

### 6.3.3 Sample chamber

The *sample chamber* and its *lid* are a custom-made UHV chamber designed for the special requirements of the *Nemi* system. They were manufactured by VAB [92] according to our technical drawings (Design drawings see appendix B.1).

Schematic drawings of this chamber are presented in figures 6.57, 6.58 and 6.59. Also depicted in this figures are the corresponding dimensions for each connection flange. The *sample chamber lid* is depicted in a sketch in figure 6.57.

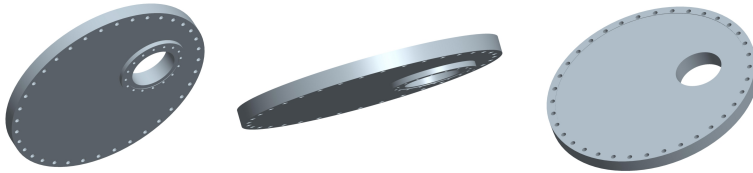


Figure 6.57: Sketch of the *sample chamber lid* from different view directions. It is a CF-400 blind flange with an added CF-100 connection on its bottom side which is centered in the direct beam line position.

The *sample chamber* is shown in figure 6.58. It is based on a CF-400 main chamber with a big CF-400 opening on the bottom which after mounting and assembling of all microscope components is closed by the CF-400 *sample chamber lid*.

The components assembled to the respective connection flanges are depicted in figure 6.59 which shows the *sample chamber* assembled with the *sample chamber lid*. It has to be mentioned that the main adjustment flange, namely the CF-100 flange on the top part of the chamber is centered at the beam line, and it is also aligned with the CF-100 outlet flange of the *sample chamber lid*.

The components assembled to the sample chamber which are not just CF-blank flanges, CF- port views or CF-feed-through connections are the *reflection detector*, the *transmission detector*, the *MAG W 600 turbo pump* and the *liquid nitrogen (LN<sub>2</sub>) cooling* for the *reflection detector*. Assembly sketches of all mentioned components are presented in the figures 6.60, 6.61. For better illustration the CF-blank flanges, view-ports and electrical feed-throughs are not implemented in this drawings. Figure 6.60 herein shows assembly sketches of the *reflection*

*detector* and the *transmission detector* as well as the *MAG W 600 turbo pump* and the *CF-63 liquid nitrogen cooling adapter flange*, assembled to the *sample chamber*.

Figure 6.61 also includes an attached *zone plate chamber* with its turbo pump and the *zone plate adjustment stage*. A complete sketch of the whole assembled setup of all UHV chambers for NEMI is presented in figures 6.62, 6.63, 6.64 and 6.65.

The chamber pressure is monitored by a **IKR-270** active cold cathode transmitter from PFEIFFER [91] (specifications see C.1).

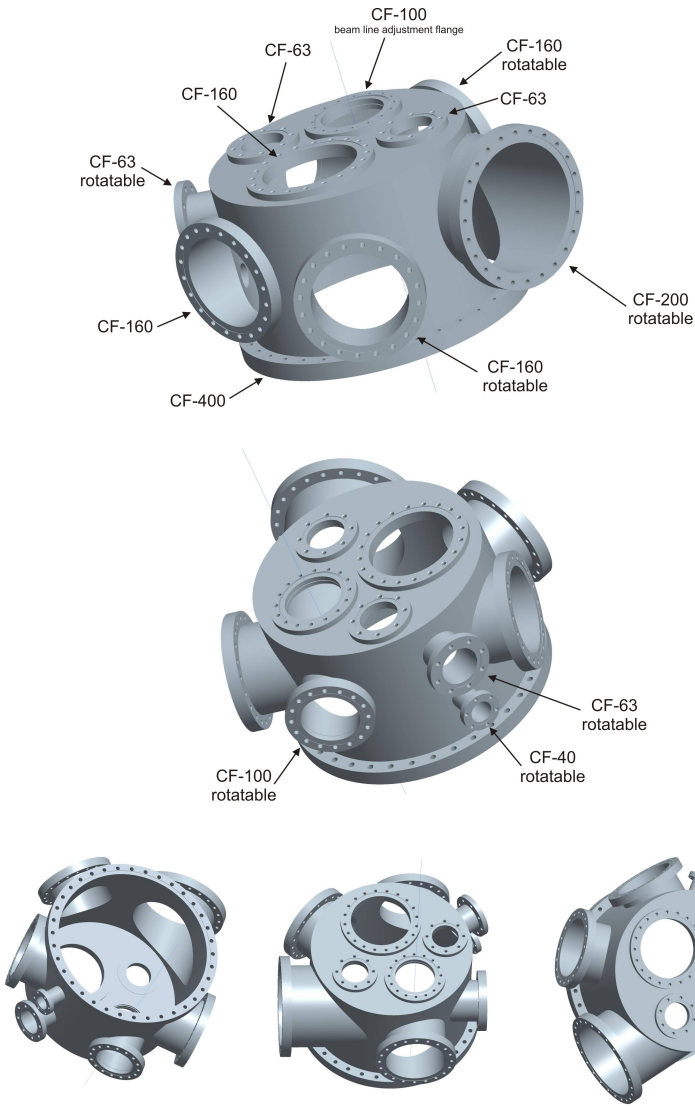


Figure 6.58: Sketches of the *sample chamber* from different view directions.

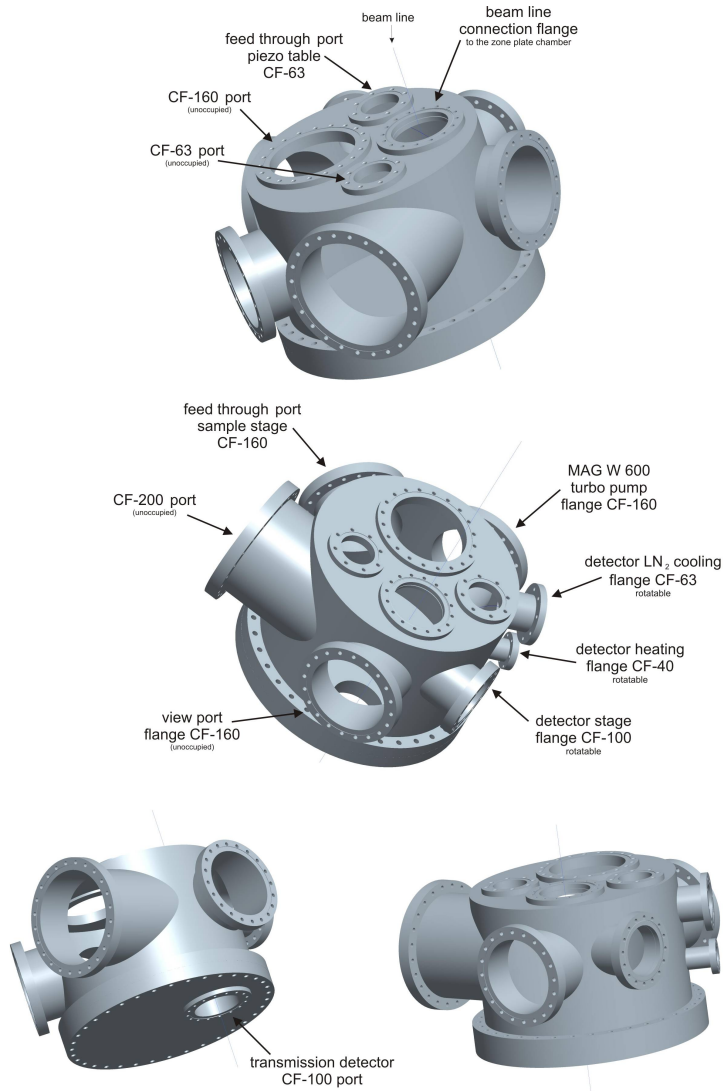


Figure 6.59: Sketches of the *sample chamber* and the mounted *sample chamber lid* from different view directions.

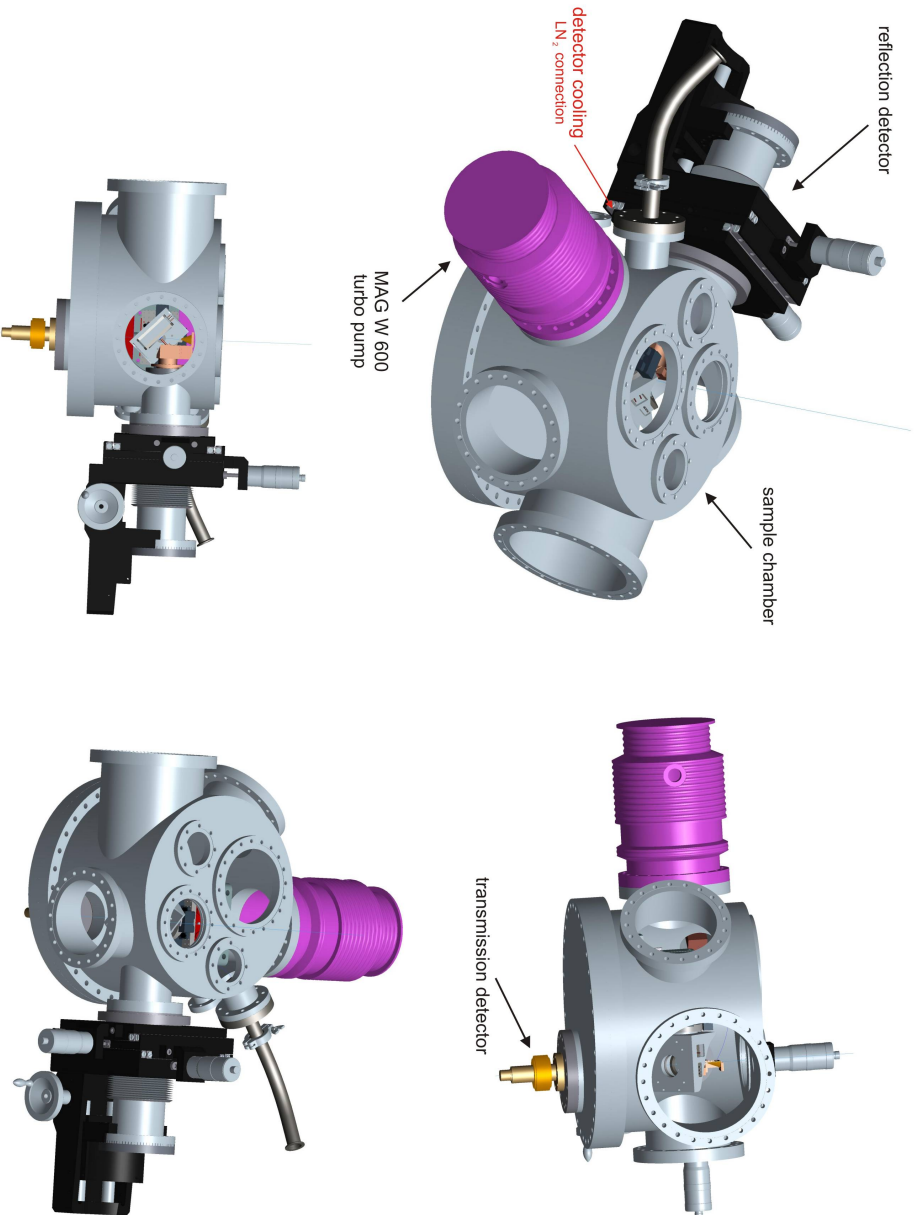


Figure 6.60: Assembly sketch of the *sample chamber* with the attached *reflection detector*, *transmission detector*, *MAG W 600 turbo pump* and the *CF-63 connection flange for the liquid nitrogen cooling (LN<sub>2</sub>)* of the *reflection detector* from different view directions. For better illustration, the remaining *CF-blank flanges*, *CF-view ports* and the electrical *CF-feed-throughs* are not displayed.



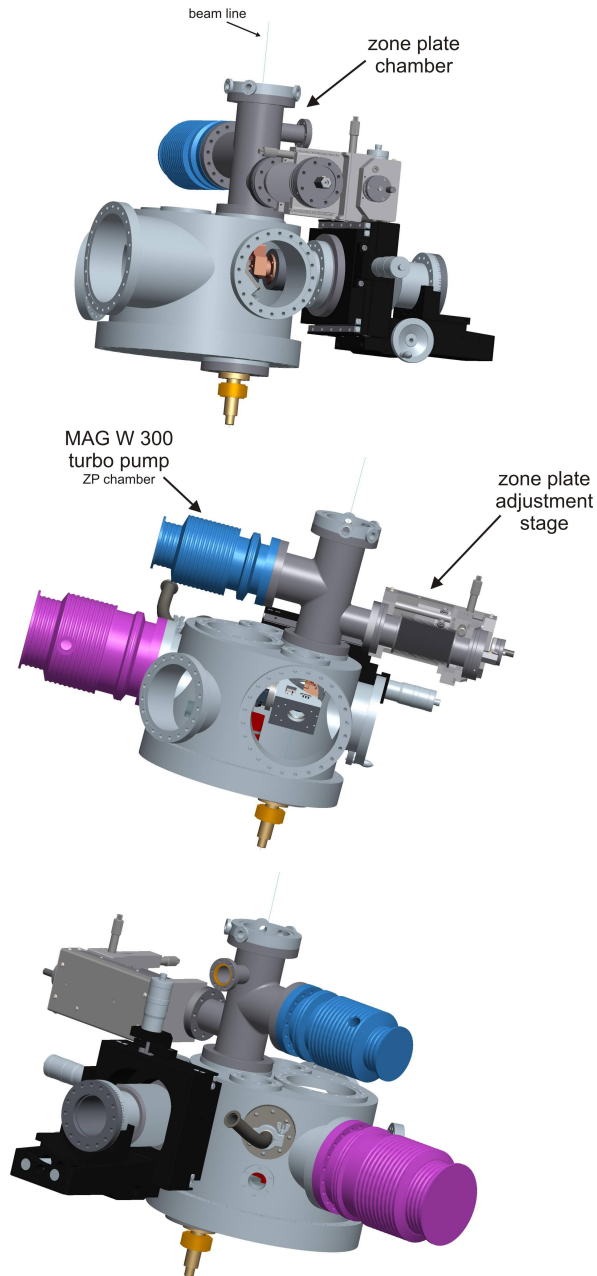


Figure 6.61: Sketches of the partly assembled *sample chamber* attached to the adjacent *zone plate chamber* from different view directions. Also apparent in this figure are the *MAG W 300 turbo pump* for the (ZP) chamber and the *UHV X/Y/Z translation stage* for the zone plate adjustment.

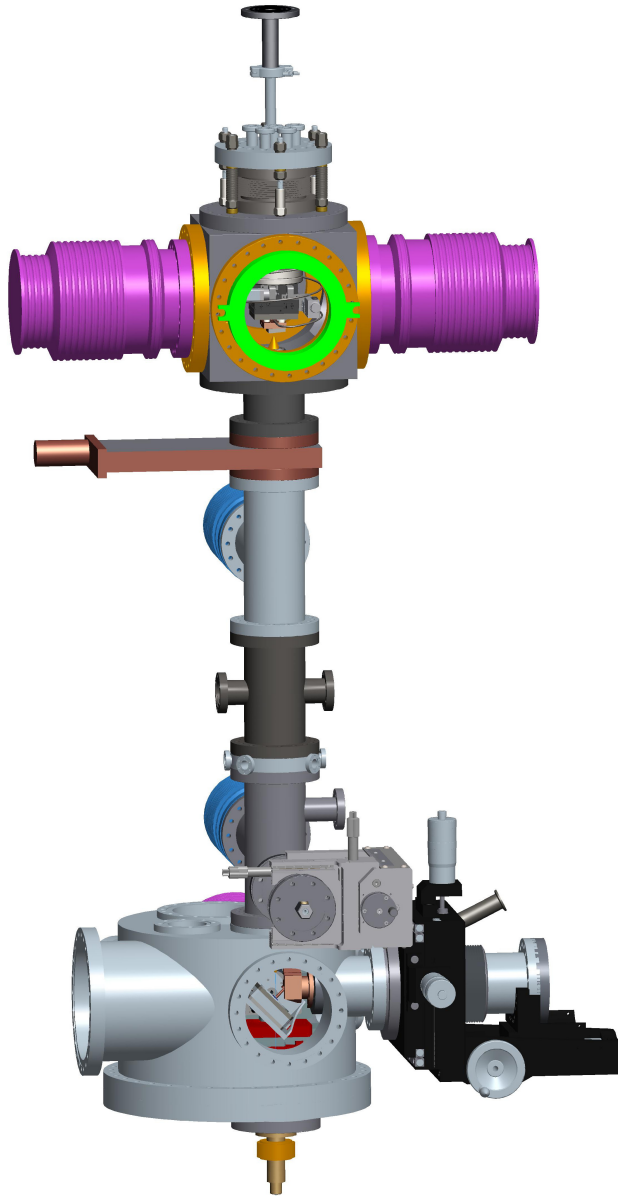


Figure 6.62: Sketch of the assembled NEMI UHV chambers, *sample chamber, pumping stage chamber, zone plate chamber, sample/detector chamber.*

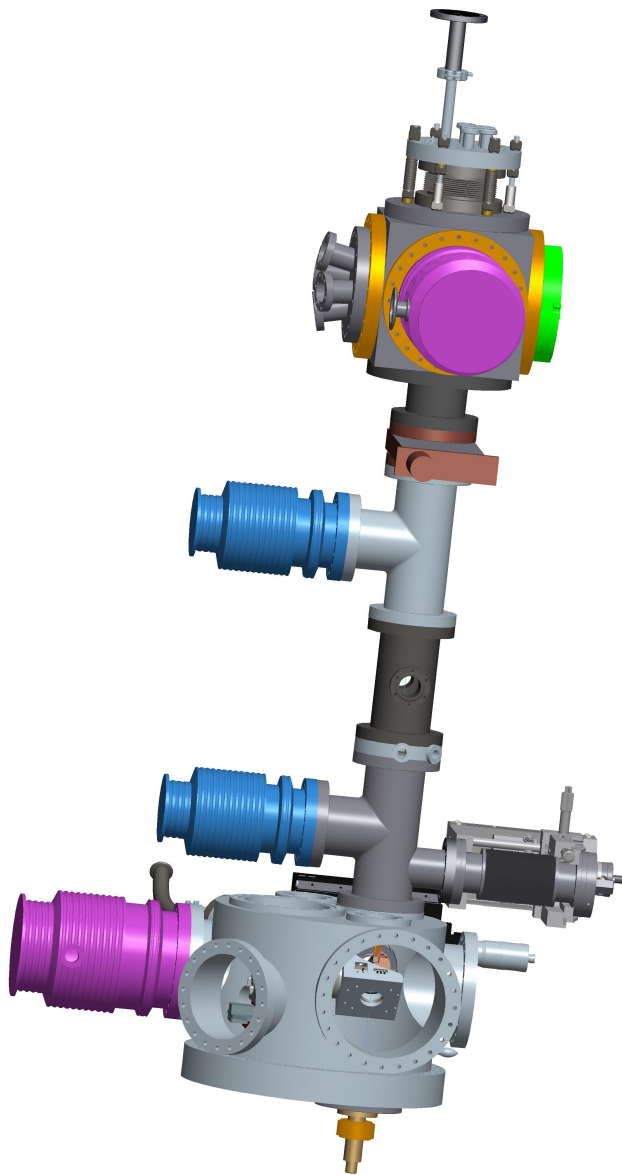


Figure 6.63: Sketch of the assembled NEMI UHV chambers, *sample chamber, pumping stage chamber, zone plate chamber, sample/detector chamber* from a different view direction.

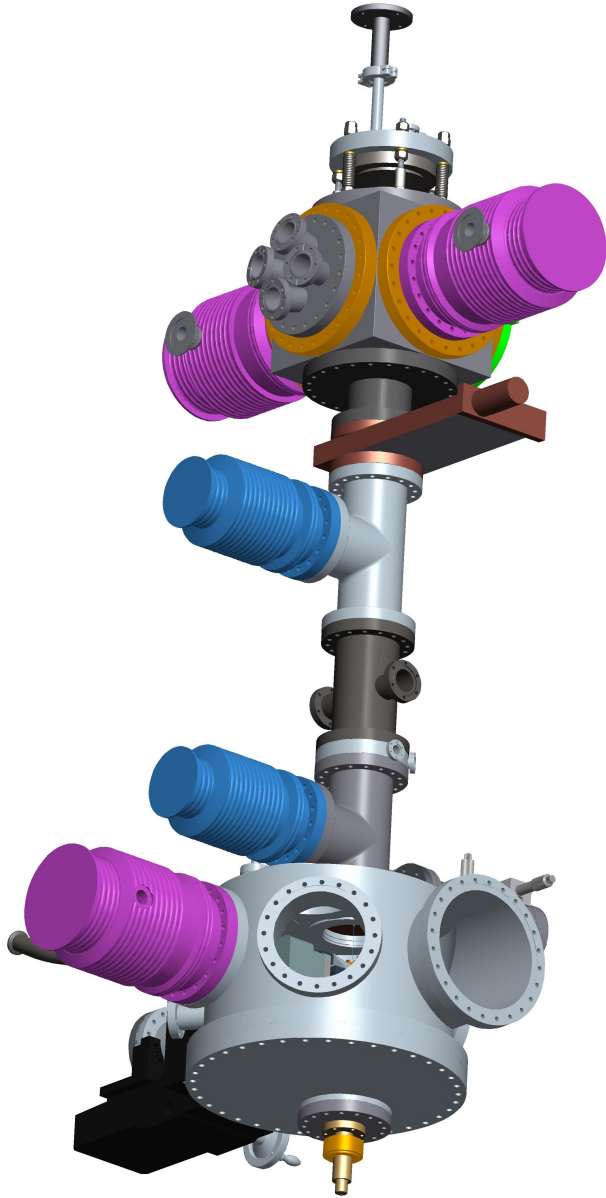


Figure 6.64: Sketch of the assembled NEMI UHV chambers, *sample chamber, pumping stage chamber, zone plate chamber, sample/detector chamber* from a different view direction.

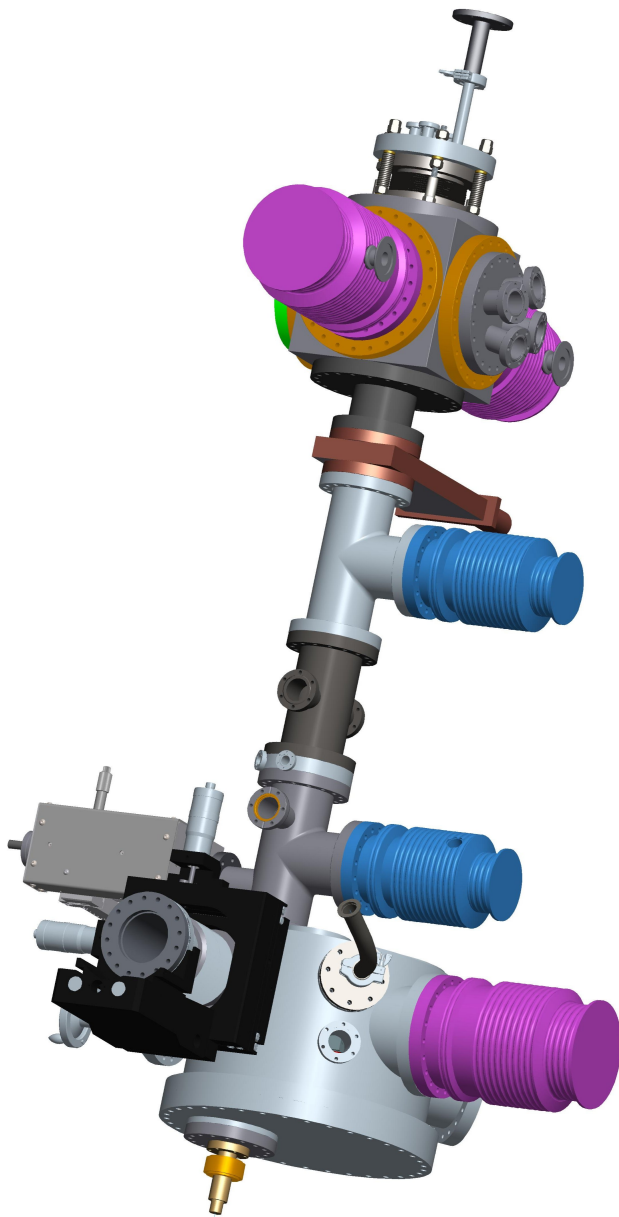


Figure 6.65: Sketch of the assembled NEMI UHV chambers, *sample chamber, pumping stage chamber, zone plate chamber, sample/detector chamber* from a different view direction.

## 6.4 INSTRUMENT PLACING

The NEMI microscope setup is placed on-top of an optical table from the company BFI OPTILAS [97]. It is a **Series 784 (Clean Top II) optical table with honeycomb core** with the dimensions 1000 mm x 2000 mm x 300 mm. The 300 mm corresponds to the table thickness. The pneumatic nitrogen gas damping system is provided by a **support system with 300 mm height tie bars** consisting of 4-posts vibration isolators<sup>9</sup>.

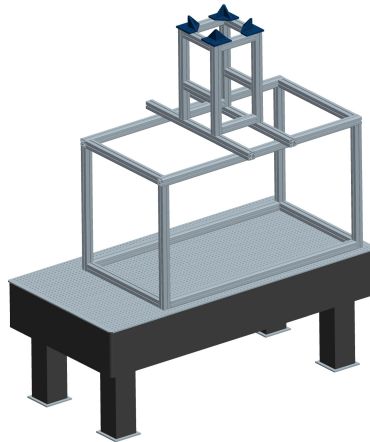


Figure 6.66: Sketch of the **series 784 (Clean Top II) optical table with honeycomb core** from BFI OPTILAS with the mounted ALUFLEX profile framework for holding the microscope setup in a hanging position.

The vertical microscope setup is mounted on-top of this optical table with a flexible sectional ALUFLEX profile framework (see figure 6.66). It holds the instrument in a free hanging position. To illustrate the suspension of the microscope, figure 6.67 presents a sketch of the NEMI setup attached to the ALUFLEX framework and the optical table.

<sup>9</sup> 4-posts vibration isolation system Micro-g piston gimbal.

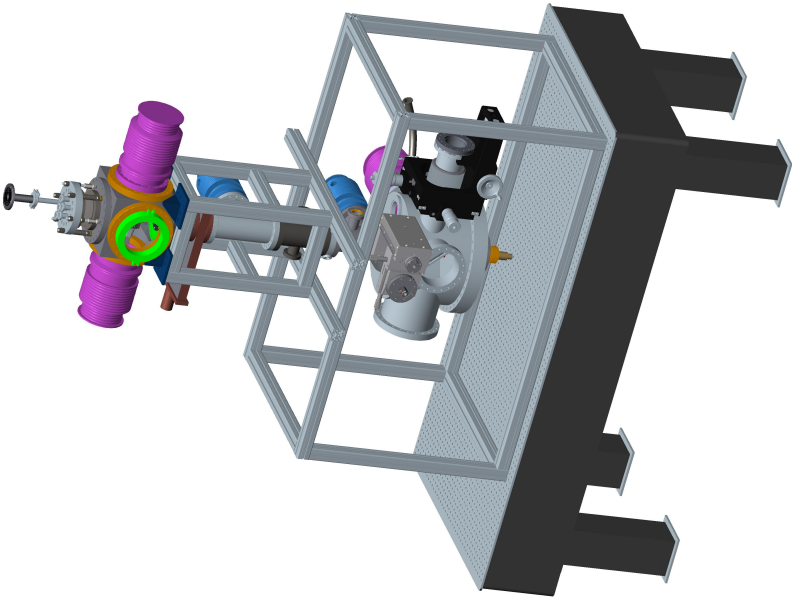


Figure 6.67: Sketch of the microscope NEMT setup attached to the ALUFLEX framework and the optical table.





## BEAM ALIGNMENT

---

*This chapter describes the beam alignment with regard to the different components involved in this process. Starting from the top this is the **nozzle-adjustment** against the skimmer orifice, the **zone-plate adjustment** into the beam line and finally the **reflection-detector and sample adjustment**.*

### 7.1 BEAM ALIGNMENT

Before the first measurements can be performed a beam alignment is necessary. This alignment process will be performed in five different steps, arranged from the top of the NEMI setup to the bottom. Hence the alignment will start in the source chamber and the last alignment step will be the sample-detector alignment within the sample chamber at the end of the helium particles travel path.

#### 7.1.1 Skimmer nozzle adjustment

The skimmer nozzle adjustment against the skimmer orifice in X/Y is performed by two linear actuators (see chapter 6.1.2). They are controlled via a LABVIEW program. It is based on an intensity comparison of the detected pressure signal at the transmission (*in-line*) detector. The skimmer-nozzle alignment is carried out before the *zone plate* is placed into the beam line. In this way it is possible to work with higher detection signals. The alignment is performed in two different program setups. First there is a raw search which is performed with a linear scanning movement of the nozzle leading to a final rectangular detection field. The raw search process stops when a significant signal increase compared to the background signal is reached. The **raw search** is performed with a rectangular scanning process, since the view port in the source chamber allows a visual pre-adjustment of the nozzle and the skimmer position in the Y-direction. Hence the scan length in Y-direction can be minimized which shortens the search time. A screen shot picture of such a rectangular *raw-search*

scan can be found in figure 7.1 .

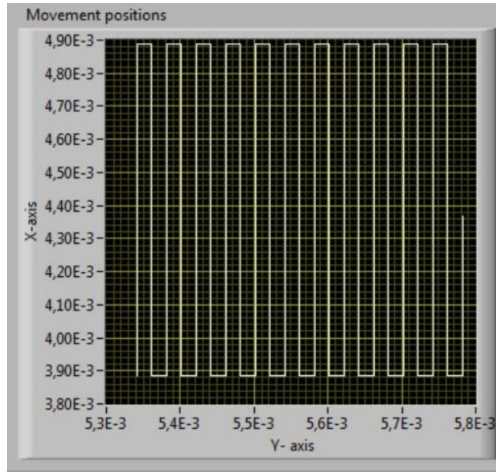


Figure 7.1: Screen shot image of the LABVIEW *nozzle-skimmer* adjustment program taken after performing a rectangular *raw-search* scanning process on NEMI.

Then there is a **fine search** which is performed with a circular/spiral stepping process of the nozzle, starting with stepping along a small radius circle at the starting position and followed by an linear increase of the radius after every finished circle. This fine search finds the maximum position of the scan by scanning in small steps. The fine search scan can be performed repeatedly to refine the maximum position more accurate with each search routine. A screen shot picture of a circular fine-alignment scan is presented in figure 7.2.

### 7.1.2 Zone plate adjustment

The next beam alignment step is the adjustment of the *zone plate* into the beam line. This is done manually with the X/Y/Z zone plate alignment stage. To find a starting position for this alignment the zone plate holder is equipped with the *beam adjustment inset*. (see section 6.2.2.1)

To illustrate the alignment process figure 7.3 shows the *zone plate holder* with the attached *ZP holding plate* and the *beam adjustment inset*. This *beam adjustment inset* has basically two different alignment slots. The first one is orientated in Z-direction and the second one is rotated by an angle of  $90^\circ$  and therefore is aligned with the Y-movement direction of the stage. By a

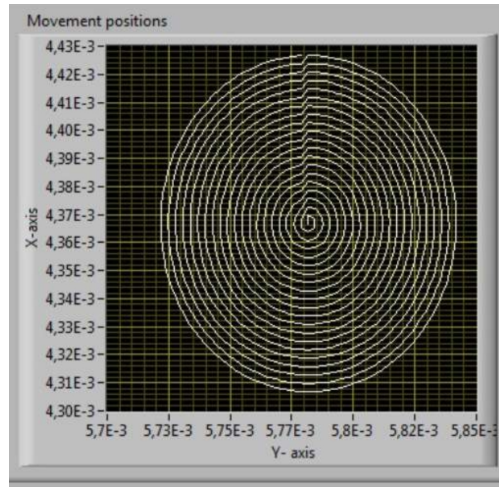


Figure 7.2: Screen shot image of the LABVIEW nozzle-skimmer adjustment program taken after performing a the circular scanning process for the fine-adjustment of the *nozzle-skimmer* position of the NEMI Source.

movement of the *zone plate holder* with the X/Y/Z stage in Z-direction into the beam line and simultaneously reading out the pressure signal of the “*in-line*” detector, one can find the position where the *zone plate holder* for the first time completely blocks the beam.

By moving the *zone plate holder* for approximately further 3 mm into the beam-line, it is possible to be sure that the Z-position for finding the first alignment slot is reached. Now the *zone plate holder* is adjusted in Y-direction until the signal in the transmission detector reaches a maximum. In this way the Y-direction reference point (value) on the translation stage scale is determined.

As a next step the reference value for the Z-direction has to be found. This is done by the help of the second alignment slot. First the Y-value of the stage is readjusted until the signal in the detector is a minimum (only background signal left). This movement should not be more than 2 mm to ensure that it is still possible to hit the Z-adjustment slot in Z-direction. Then the *zone plate holder* is moved further into the beam line until the detected signal rises again for the first time. In the same way as for the Y-direction the Z-direction reference point (value) can be found by determining the first intensity maximum in the read out signal of the “*in-line*” detector. With this adjustment procedure an exact reference position of the *zone plate holder* in Y/Z direction

with respect to the beam line can be found. Note that the positions of the nine possible zone plate locations on the respective *zone plate chip*, in relation to this X/Z reference point on the *zone plate holder*, first have to be evaluated after the attachment of the chip onto the *ZP holding plate* before the final mounting of the *zone plate holder* into the *zone plate chamber* takes place. With this knowledge it is possible to approach each of the nine zone plate locations on the chip.

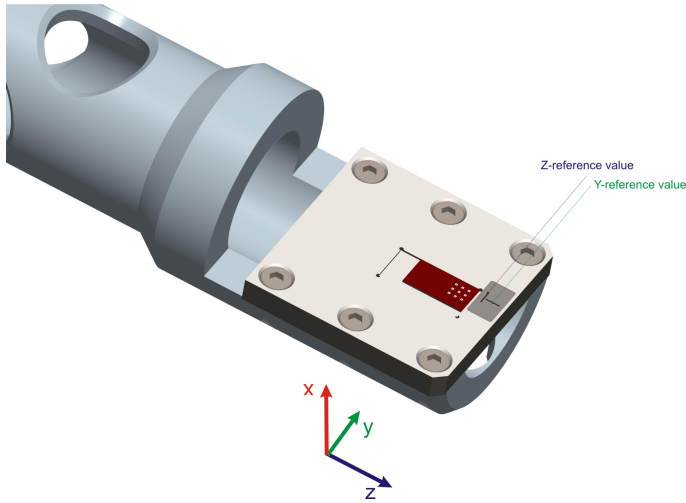


Figure 7.3: Sketch to illustrate the *zone plate* alignment.

### 7.1.3 Reflection detector adjustment

To adjust the *reflection detector* to its correct position within the beam-line the crucial component is the *0-order sorting aperture* on the top of the detector. Before assembling the detector into the *sample chamber* the *sorting aperture's* orifice needs to be adjusted with the *detector nose* entrance aperture. This has to be done with an optical microscope. Since the mounting connections for the *sorting aperture* to the *detector head* are manufactured with elongated holes, it is possible to align this two components against each other. Note that the *0-order sorting aperture orifice* diameter has to be equal or smaller than the middle stop of the *ZP* to achieve optimal 0-order blocking. After this adjustment the *reflection detector* is attached to the *extension tube* within the sample chamber. The beam alignment is performed in a 4-step procedure (see figure 7.6):

1. The *zone plate* is moved into the beam-line.
2. The *reflection detector* is moved with the *X/Y/Z detector translation stage* (see figure 7.6) into the beam line at a *Z*-position which is definitely located above the focal plane. The *X/Y* position is adjusted so that the signal in the *in-line detector* becomes a **minimum** for the second time in both axes. This corresponds to a position where the beam is completely blocked by

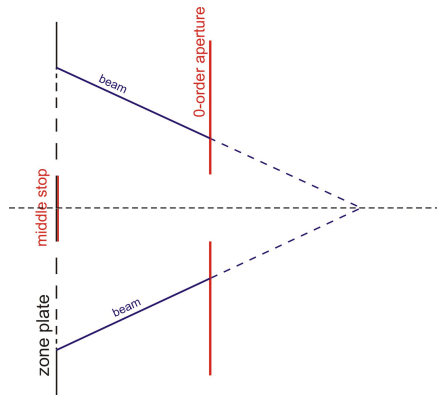


Figure 7.4: Schematic 0-order aperture alignment.

the *middle-stop* of the *ZP* and the *0-order sorting aperture* (see figure 7.4).

3. The *reflection detector* is moved down in *Z*-direction to the point *P* where a **maximum** signal (plateau) arises after a signal increase occurs (see figure

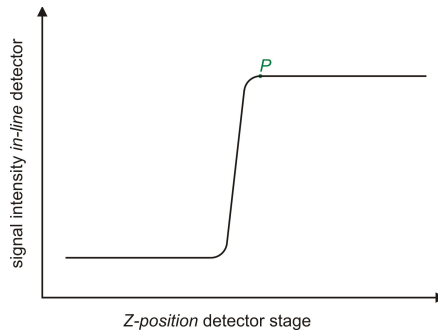


Figure 7.5: Reflection detector *Z*-alignment

7.5). This corresponds to the position where the focused beam signal is a maximum whereas the 0<sup>th</sup>-order part of the beam is blocked best.

4. The *reflection detector* is moved out of the beam line again.

This procedure provides a reference position for the *reflection detector* in X and

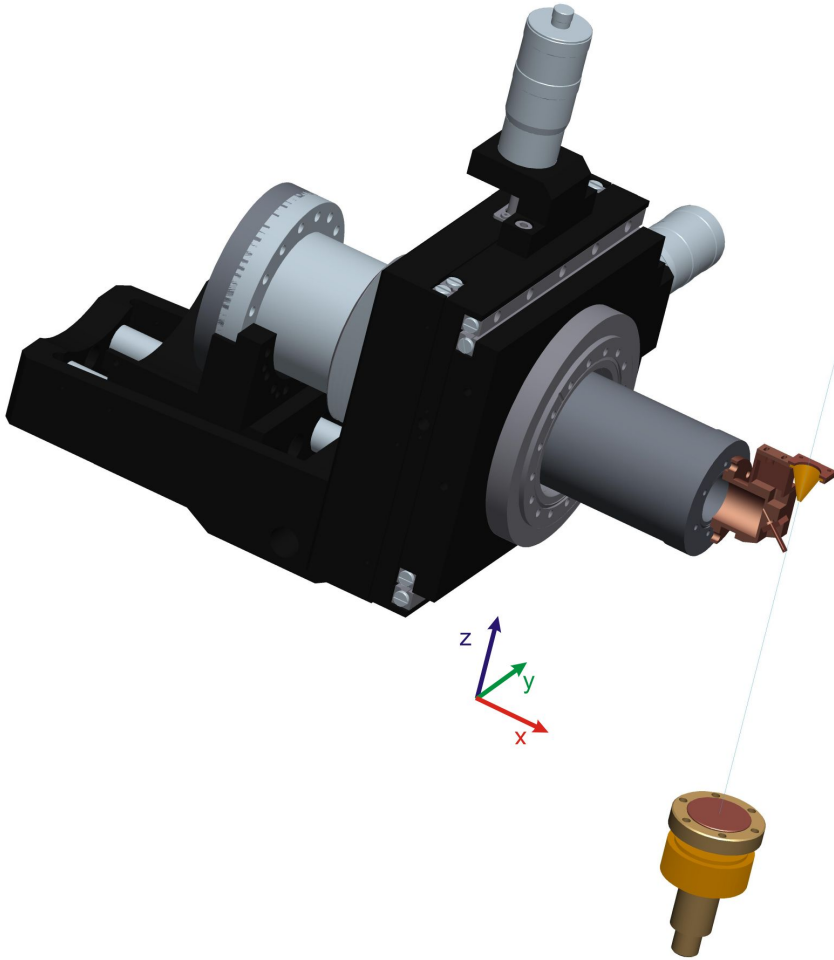


Figure 7.6: Detector stage directions for the alignment.

Y direction and additionally a reference point for the optimum Z-position of the reflection detector. Now the *reflection detector* is moved out of the beam line to adjust the sample holder to the focal plane.

#### 7.1.4 Sample holder adjustment

The first step for the *sample adjustment* is to set the *X/Y reference point* of the sample holder. To achieve that, the *sample holder* is also equipped with an *adjustment inset* similar to the one for the *zone plate adjustment*. With the help of the two small adjustment slits which are arranged in  $90^\circ$  to each other and

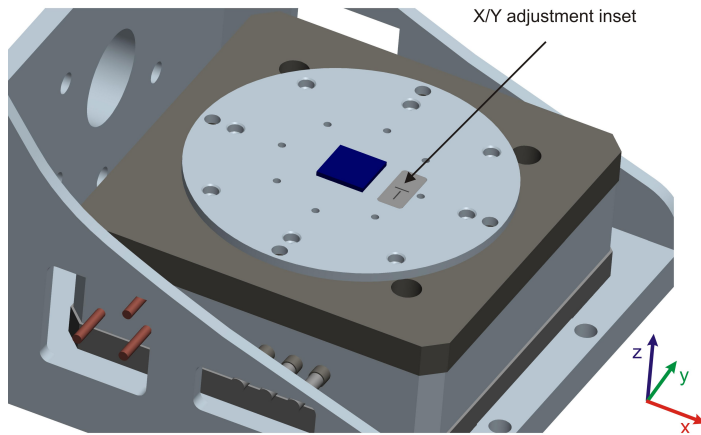


Figure 7.7: Sketch for the illustration of the *X/Y position adjustment* of the sample holder.

by stepping of the X-Y axis of the XYZR-ALIO *sample positioning stage* a *X/Y reference position* on the sample holder is found (see figure 7.7). Thereby the detected beam signal in the *in-line detector* is used to perform this adjustment. After once defining this *X/Y reference position* of the *sample holder* also the *Z-position* has to be adjusted. By performing a linear scan process with one of the two *adjustment slits* on the *sample holder* it is possible to take line scans of the focal spot diameter. For easier handling this reference point adjustment should be performed without the *reflection detector* positioned in the beam line. The adjustment steps are:

1. The *X/Y reference positions* of the *sample holder* are determined with the *adjustment inset* (sample holder) by maximizing the beam signal in the *in-line detector*. The corresponding positions are stored in the *sample stage program*.

2. With one of the slits in the *X/Y adjustment inset* on the sample holder the focal spot size is determined by a slit-scan performed with the *piezo-table* of the *sample holder*. A variation of the *Z-position* of the *sample holder* is used to **minimize** the focus spot diameter. A minimum of the focus spot diameter corresponds to the *sample holder Z-reference position* where the *adjustment inset* is located in the focal plane. (note that the 0<sup>th</sup>-order part of the beam is not blocked at the moment and hence overlays the signal)
3. Then the *sample* is moved into the beam line with a corresponding *X/Y/Z sample stage* movement and is tilted to the desired scan angle. Note that the *Z movement* is necessary since the sample surface is at a higher position than the *adjustment inset* on the *sample holder*.

#### 7.1.5 *Sample-reflection detector alignment*

Finally the *reflection detector* is adjusted to the sample.

1. The *sample holder* is moved down approximately 5 mm in its *Z-position* to ensure that there is no collision with the *reflection detector* when it is moved back in the beam line.
2. The *reflection detector* is moved back into the beam line to its *X/Y/Z reference position*.
3. The sample approaches “step by step” its *Z-axis reference point*. A visual control via the CF-flange view ports in the source chamber ensures that there is no collision between sample and detector-nose. If necessary the the *Z-position* of the *reflection detector* has to be slightly readjusted.



## FIRST SUB-MICRON HELIUM FOCAL SPOT

---

*To determine the capability of fresnel zone-plate diffraction for the implementation as the atom beam focusing tool in NEMI, preliminary focusing measurements were carried out. They were performed with zone-plates produced in a similar manner to the ones that will be used in NEMI, but with different focal lengths to fit our already existing apparatus MAGIE. The results are presented in a paper submitted to New Journal of Physics (see Appendix A ). They include the first sub-micrometer focusing of a He-beam. Additionally the velocity distribution of a He-beam as a critical parameter for the focal spot size is discussed in detail. A new method for determining narrow velocity distributions is described.*

### 8.1 SUB-MICRON FOCUSING OF NEUTRAL HELIUM BEAM (PAPER A)

Since the *fresnel zone-plates* are one of the main components for the NEMI setup, preliminary focusing experiments with such circular diffraction gratings were carried out. The goal of these experiments was to achieve, for the first time, a sub-micrometer neutral helium beam focus spot by the usage of a *fresnel zone-plate* similar to the ones utilized later in NEMI. The corresponding results are presented in the attached paper A (see Appendix A).

One of the required values for the analysis of the measurement data is the in chapter 3.6 described *speed ratio*  $S$  of the atom beam, so to say the beam's velocity/energy distribution. For the paper it was finally decided to implement theoretically evaluated speed ratio values gained by simulations based on the LENNARD-JONES potential [98, 99, 100]. They were performed by Gianangelo Bracco from the Department of Physics at the University of Genova, Italy.

But also an additional set of measurements to experimentally evaluate the speed ratio of a roughly room temperature beam was performed which is presented in the following sections.

## 8.2 EXPERIMENTAL SPEED RATIO DETERMINATION

The experimental speed ratio determination for the neutral helium beam is based on the *time-of-flight* (TOF) measurement technique. This technique is the common method to determine the kinetic energy of the atoms/molecules in a particle beam [101, 102]. In the following is presented: The experimental setup for the TOF-measurements performed on MAGIE (8.2.1), the basic relation of the measured TOF-spectra and the speed distribution of the beam (8.2.2), the standard deconvolution method used to determine the speed-ratio values  $S$  from the measurements (8.2.2.1), a new evaluation procedure which allows to determine  $S$  for narrow speed distributions (8.2.2.2) and the measurement results from this new speed-ratio evaluation technique for a room temperature beam (8.2.3).

The reason for a new evaluation procedure is, that for beams with a narrow speed distribution (high speed-ratios) the standard deconvolution procedure cannot be applied. Narrow in that case means that the broadening of the TOF-spectrum due to the transmission function of the chopper slit is big compared to the actual speed distribution of the beam.

### 8.2.1 Experimental setup for Speed Ratio determination

The *time-of-flight* (TOF) technique is based on the measurement of the flight time the atoms need to travel a certain distance  $L$ . Just as for the NEMI setup MAGIE is also equipped with a *free-jet* expansion source. But in contrast to the new microscope setup, MAGIE is also provided with a so called *chopper-disc* to enable TOF measurements. This disc which holds one or several slit openings is implemented into the beam line to chop the beam into short beam pulses. Additionally the instrument itself is equipped with the necessary electronics to measure the flight times of this pulse segments. Figure 8.1 presents a sketch of the TOF measurement setup. To chop the *free-jet-expansion* beam the *chopper-disc* rotates with the frequency  $f$ . Thereby the chopper defines the spatial and the time-wise starting point of the measurement ( $L_1 = 0$  and  $t_1 = 0$ ). The disc can be moved into the beam-line with a vertical translation stage which provides a read-out/adjustment possibility for the actual vertical position of the chopper (chopper slit) with regard to the beam. The chopped beam pulses subsequently travel undisturbed through the rest of the ultra high vacuum

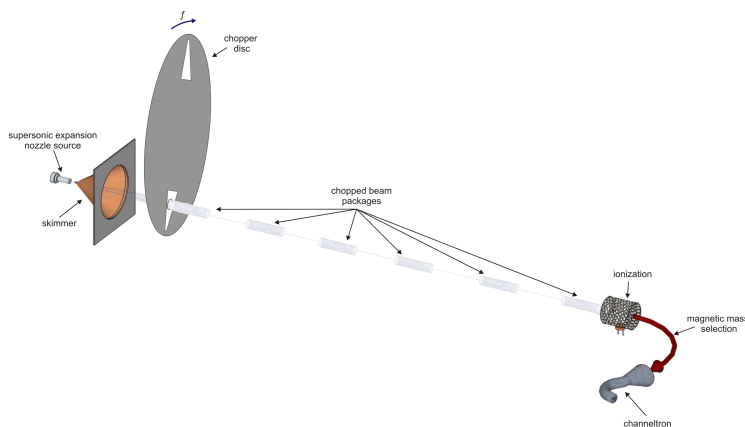


Figure 8.1: Sketch for the *time-of-flight* (TOF) measurement setup on the MAGIE apparatus. A chopper disc rotating with the frequency  $f$  and equipped with two trapezoidal shaped chopping slits is implemented into the neutral helium beam line to chop the beam into small beam packages. The flight time of this beam packages between chopper and ionization detector is measured and together with the given flight distance of the beam (between chopper and detector) it is possible to determine the speed distribution (*speed ratio*) of the beam.

setup and finally are detected time-resolved by the *TOF* electronics. To gain enough signal intensity in the course of this time resolved detection the beam's signal is integrated over several incoming beam pulses. From the broadening of the time resolved detected beam pulses it is possible, with the knowledge of the flight distance  $L$  between the chopper and the detector, to find the velocity/energy distribution of the beam's atoms. Due to the different traveling velocities of the beam particles (speed distribution of the beam) the former small packages at the chopper exhibit a broadening during their propagation over the distance  $L$ . Faster particles will arrive earlier, slow ones later. With the corresponding *TOF* electronics the incoming particle intensities in the detector are recorded time-resolved. From this flight-time distribution the related velocity distribution can be found.

As shown in figure 8.2 the chopper wheel has two trapezoidal shaped slits arranged with  $180^\circ$  spacing between each other. Additionally two small rectangular shaped slits are located in ca. 4 mm distance to each of the chopping

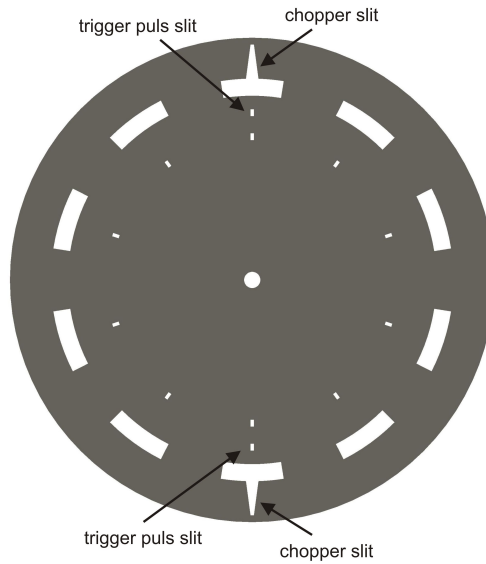


Figure 8.2: Sketch of the *chopper wheel* implemented for the *TOF* measurements. The disc is equipped with two slits of trapezoidal shape arranged  $180^\circ$  to each other. They are accounted to chop the beam. Additionally it also has two small rectangular slit openings in radial direction to the center of the disc. They deliver a trigger pulse to the *TOF* measurement electronics based on the signal of a photo-diode. All the other features present on the chopper wheel, so to say the ten elongated wide slits as well as their corresponding small rectangular shaped trigger slits, are not used for the *TOF* measurements presented here.

trapezoidals in radial direction to the center of the disc. They are assigned to deliver a trigger signal to provide the *TOF* electronics with a starting pulse for the counting process. This trigger pulse is generated by a light-emitting-diode (LED)/photo-detector combination mounted in a fixed position relative to the chopper wheel. Always when a beam package passes through the chopping trapezoidal this LED-photodetector system will deliver a starting pulse to the measurement electronics. After a certain previously appointed delay time  $t_d$  following this trigger pulse the electronics start to accumulate the signal from the incoming helium atoms at the detector in certain predefined time-bins with increasing time-line. Together with the knowledge of the flight distance  $L$ , the start time for each beam package and the detected signal intensities per time-bin it is possible to determine the flight time distribution.

A graph showing one of the acquired *TOF*- spectra is presented in figure 8.3.

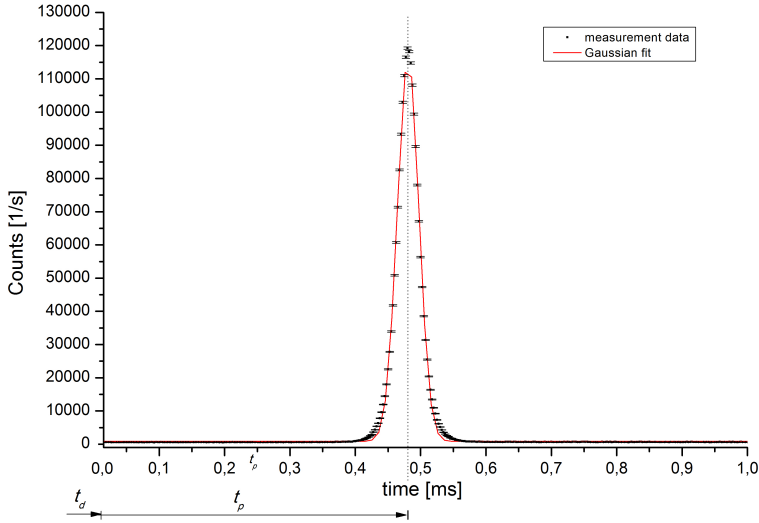


Figure 8.3: Flight time spectrum of the *free-jet expansion* helium beam. This measurement was taken with a  $T_0 = 295$  K,  $p_0 = 81$  bar beam at a chopper frequency of  $f = 270$  Hz and a vertical chopper height position of 0.835 inch. Particle traveling distance (chopper-detector) of  $L_{\text{chopp-det}} = 2046$  mm. (file: TOF3297)

### 8.2.2 Speed ratio evaluation

As one can see from figure 8.3 the measured time-of-flight signal of the direct beam can be well fit by a GAUSSIAN (normal) distribution. It is directly related to the velocity spread of the beam's helium atoms. This is in good accordance with the in literature described velocity distribution of a free-jet expansion source [59]. The center-line of the *Gauss-peak* can be related to the final average velocity  $v_f$  of the beam with a corresponding actual flight time  $t_f$ . An exact explanation for how  $t_f$  is determined can be found in Appendix E.

To determine the actual velocity distribution of the helium particles from the gained TOF-spectra, one has to know that the *speed ratio*  $S$  of a molecular beam is related to the *full-width-half-maximum* of the measured time distribution and the particles final average velocity  $v_f$ <sup>1</sup>.

As described in section 3.6 the velocity distribution of the beam is based on a MAXWELL BOLTZMANN distribution which from the mathematically point of

<sup>1</sup> note that  $v_f = L/t_f$

view corresponds to a GAUSSIAN shaped (normal) distribution of the particles velocities  $v$  with a standard deviation of [59]

$$\sigma_v = \sqrt{\frac{k \cdot T_{\parallel}}{m}} \quad (8.1)$$

where  $m$  stands for the beam particle (atom or molecule) mass,  $k$  is the BOLTZMANN constant and  $T_{\parallel}$  the beam temperature parallel to the beam axis.

The *full-width-half-maximum* (FWHM) of a *normal* (or GAUSSIAN) distribution is defined as  $FWHM = \sqrt{2 \cdot \ln 2} \cdot 2\sigma$ . Together with the *speed-ratio* definition from equation 3.14 this leads to the following consideration:

$$\begin{aligned} S = \sqrt{\frac{m \cdot v_f^2}{2kT_{\parallel}}} &\Rightarrow S^2 = \frac{v_f^2}{2} \cdot \frac{m}{kT_{\parallel}} = \frac{v_f^2}{2} \cdot \frac{1}{\sigma_v^2} = \\ &= \frac{v_f^2}{2} \cdot \left( \frac{2 \cdot \sqrt{2 \cdot \ln 2}}{FWHM} \right)^2 \Rightarrow \\ S &= \frac{v_f}{\sqrt{2}} \cdot \frac{2 \cdot \sqrt{2 \cdot \ln 2}}{FWHM} = \frac{v_f \cdot 2 \cdot \sqrt{\ln 2}}{FWHM} = \\ &= 2 \cdot \sqrt{\ln 2} \cdot \frac{v_f}{FWHM} = 2 \cdot \sqrt{\ln 2} \cdot \frac{v_f}{\Delta v} = S \end{aligned}$$

One can see that the beam's *speed ratio*  $S$  is related to the TOF-measurements in the form

$$S = 2 \cdot \sqrt{\ln 2} \cdot \frac{v_f}{\Delta v} = 1,66 \cdot \frac{v_f}{\Delta v} \approx 1,66 \cdot \frac{t_f}{\Delta t} \quad (8.2)$$

with  $v_f$  the final average velocity corresponding to the actual flight time  $t_f$  of the atoms within the package and  $\Delta v$  and  $\Delta t$  the FWHM of the measured TOF spectrum.

The last part of equation 8.2 can be stated that way due to the following considerations:

$$\begin{aligned} \Delta v &= \frac{L}{t_f + \frac{\Delta t}{2}} - \frac{L}{t_f - \frac{\Delta t}{2}} = \\ &= \frac{L \cdot (t_f - \frac{\Delta t}{2}) - L \cdot (t_f + \frac{\Delta t}{2})}{(t_f + \frac{\Delta t}{2})(t_f - \frac{\Delta t}{2})} = \frac{L \cdot (t_f - \frac{\Delta t}{2}) - L \cdot (t_f + \frac{\Delta t}{2})}{t_f^2 - \left(\frac{\Delta t}{2}\right)^2} = \\ &= \frac{-2 \cdot L \cdot \frac{\Delta t}{2}}{t_f^2 \cdot \left(1 - \frac{\left(\frac{\Delta t}{2}\right)^2}{t_f^2}\right)} \end{aligned}$$

and further considering

$$\begin{aligned}
 \frac{v}{\nabla v} &= \frac{\frac{L}{t_f}}{-2 \cdot L \cdot \frac{\Delta t}{2}} = \\
 &= \frac{t_f^2 \cdot \left(1 - \left(\frac{\Delta t}{2}\right)^2 / t_f^2\right)}{-2 \cdot \frac{\Delta t}{2}} = \\
 &= \frac{1}{t_f} \cdot \frac{t_f^2 \cdot \left(1 - \left(\frac{\Delta t}{2}\right)^2 / t_f^2\right)}{-2 \cdot \frac{\Delta t}{2}} = \\
 &= \frac{t_f}{-2 \cdot \frac{\Delta t}{2}} \cdot \left(1 - \left(\frac{\Delta t}{2}\right)^2 / t_f^2\right) \simeq \frac{t_f}{-2 \cdot \frac{\Delta t}{2}} \cdot 1 \quad (\text{for } t_f \gg \frac{\Delta t}{2})
 \end{aligned}$$

Since in case of the here evaluated TOF measurements the condition  $t_f \gg \frac{\Delta t}{2}$  is valid it is also possible to state

$$\Rightarrow \frac{v_f}{\Delta v} \simeq \left| \frac{t_f}{\Delta t} \right| \quad (8.3)$$

Therefore the *speed ratio* of the nearly monochromatic molecular beam can be directly evaluated from the TOF measurements with the read out of their actual flight time  $t_f$  and the *FWHM* of the curves.

Of course it also has to be taken into account that the *FWHM* of the measured TOF-spectra in reality is put together by a convolution of the actual velocity distribution of the beam and a broadening due to the measurement technique, which results in a broadening of the real velocity distribution.

### 8.2.2.1 Standard deconvolution process

Generally the full-width-half maximum (FWHM) of the measured TOF-spectrum  $\Delta t_M$  provides a measure for the particles energy/velocity spread. Since the pulse packages are chopped by a finite slit width additional broadening will be overlaid onto the Gauss peak's width<sup>2</sup>. Also the detection process provides some smearing of the measured flight time distribution. The spatial location of the particle detection within the electron bombardment ionization detector is defined by its ionization-volume with the length  $L_D$ . This is described by a spatial ionization-probability of the detector. The total distribution of the measured TOF signal  $T_M$  is therefore generated by a convolution of the actual velocity

<sup>2</sup> Note that an optimal chopper slit would be indefinitely small so that there is no big influence on the chopper transmission function. Such small slit widths are not reasonable since the detected beam intensities would be too small.

spread of the beam's particle (corresponding flight time distribution  $T(v)$ ), the width of the chopper slit (chopper-transmission function) and the spatial distribution of the particle detection. For simplicity the chopper-transmission and the ionization probability of the detector are approximated by two Gauss functions  $C(x)$  and  $D(x)$  respectively.

For free-jet expansion beams where the FWHM of the real velocity distribution of the beam  $T(v)$  is broad compared to the FWHM of the chopper-transmission function  $C(x)$ , the real velocity spread (speed ratio of the beam) can be determined with a standard deconvolution procedure like described in literature [102].

The FWHM of the actual velocity spread of the beam particles is defined as  $\Delta t_v$ , the FWHM of the chopper-transmission function as  $\Delta t_C$  and the FWHM of the detector ionization probability function as  $\Delta t_D$ . This leads to [102]

$$\Delta t_M^2 = \Delta t_v^2 + \Delta t_C^2 + \Delta t_D^2 \quad (8.4)$$

with

$$\Delta t_v = L \cdot \frac{\Delta v}{v_f^2} \quad (8.5)$$

$$\Delta t_D = \frac{L_D}{v_f} \quad (8.6)$$

$$\Delta t_C = \frac{w}{2\pi \cdot r_{ch} \cdot f_{ch}} \quad (8.7)$$

with  $L$  the particles flight distance between chopper and detector,  $L_D$  the detector ionization length,  $v_f$  the final average particle velocity (from section 8.2.2),  $\Delta v$  the corresponding FWHM of the real velocity distribution of the beam,  $r_{ch}$  the chopper disc radius at the center of the beam,  $f_{ch}$  the chopper frequency and  $w$  is the chopper slit's width.

From this equation one can find the desired FWHM  $\Delta t_v$  of the actual particles flight-time distribution.

$$\Delta t_v = \sqrt{\Delta t_M^2 - \Delta t_C^2 - \Delta t_D^2} \quad (8.8)$$

The ratio of  $t_f / \Delta t_v$  is thereby a measure for the *speed ratio*  $S$  of the helium beam (see e.q. 8.2).



### 8.2.2.2 Speed ratio evaluation for high speed ratios

When it comes to high speed ratios and hence a small velocity distribution, the above described standard deconvolution procedure cannot be used anymore. For such beams the FWHM of the real velocity distribution of the beam is small compared to the FWHM of the chopper-transmission function. Hence a small error in the determination of the used slit width  $w$  can lead to a significantly high change in the evaluated *speed ratio*  $S$  of the beam. To better explain this circumstances an example is presented in the following:

For a  $T_o = 122.9$  K beam at  $p_o = 81$  bar nozzle pressure, the speed ratio values  $S$  for a chopper slit-width of  $w = 1.83 \pm 0.1$  mm calculated with the standard deconvolution process are presented in table 8.1. As one can see a slit-width

SPEED RATIO $S$ EVALUATED FROM THE TOF-SPECTRUM for a chopper slit width of $w = 1.83 \pm 0.1$ mm	
$w = 1.73$ mm	245.66
$w = 1.83$ mm	286.18
$w = 1.93$ mm	326.62

Table 8.1: Evaluated speed ratio numbers for a  $T_o = 122.9$  K,  $p_o = 81$  bar beam determined from the recorded TOF-spectrum for a  $\Delta w = \pm 0.1$  mm varying chopper slit width.

variation of  $\Delta w = 0.1$  mm leads to a speed ratio deviation by ca.  $\Delta S = \pm 40$ . This number  $\Delta w$  is due to a combination of factors:

- The chopper slit used for the TOF-measurements on MAGIE has a trapezoidal shape, therefore  $w$  is not a fixed value but depending on the height position of the chopper disc (slit) compared to the beam-line. In case of the on MAGIE utilized microskimmers the exact position of the beam line is varying slightly due to the manufacturing process of the skimmer tips. Hence there is no absolute position of the beam-line.
- The vertical translation stage used to position the skimmer into the beam-line has a high inaccuracy especially when it comes to repeatability.
- The manufacturing tolerances of the chopper slight have also an influence on the exact slit width. Those tolerances are small but still have to be mentioned here.

Therefore a new speed ratio evaluation method was developed based on a direct determination of  $S$  without the influence of the chopper slit function. To remove the influence of the chopper slit width, the slit's trapezoidal shape can be utilized. The *speed ratio values*  $S$  at different height positions of the chopper-slit and hence at different slit widths are recorded. Afterwards the ratios  $S$  ( $S = 1.66 \cdot (t_f / \Delta t_M)$ ) determined from the measurement are plotted corresponding to their height positions ( see chapter 8.2.3). By extrapolating the gained curve to the theoretical tip position of the chopper slit ( $P$ ) the corresponding *speed ratio* value for an infinite small slit is found (see fig. 8.4). At this position there is no broadening of the beam's real flight-time distribution due to the chopper-slit's transmission function. Therefore the influence of the the chopper slit's width  $w$  is mostly eliminated<sup>3</sup>.

The accordant evaluation process performed to gain the value of  $S$  for a roughly room temperature beam ( $K = 295$  K) is presented in the following section (8.2.3).

### 8.2.3 Example for the new correction method for a room temperature beam

One of the several rallied TOF spectra gained by measurements taken with a  $T_o = 295$  K,  $p_o = 81$  bar beam and at a chopper frequency of  $f = 270$  Hz is presented in figure 8.3. Equal files were recorded for 19 other height positions of the chopper disc with respect to the beam line. To achieve an accurate knowledge for the respective height position of the slit, the overall helium particle count rates for each TOF-measurement were recorded as well. The chopper-detector distance for the measurements was  $L = 2046$  mm.

Additionally to the count rates at the vertical height positions of each TOF-measurement further count-rates for chopper positions with decreasing slit widths were collected until there was no beam signal left. No beam signal in this case means that due to the trapezoidal shaped form of the chopper slit the beam reaches the position where it leaves the slit at its smaller end (length  $b_1$ ). A sketch representing the chopper slit's dimensions is shown in figure 8.4.

In principle the height position of the chopper disc can be read out from the length scale of the vertical translation stage which the chopper is mounted to. Nevertheless the measurements showed that this position information is not

<sup>3</sup> There might be an error occurring from the manufacturing tolerances of the trapezoidals angle and slit height.

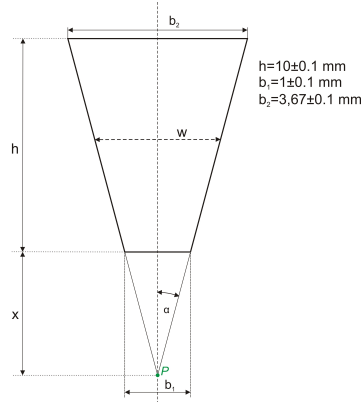


Figure 8.4: Schematic of the chopper slit dimensions. Point  $P$  corresponds to the theoretical position of the tip of the trapezoidal shaped chopper slit.

exact enough and even more inaccurate when it comes to repeatability. Therefore it was decided to perform a more precise determination of the chopper disc's height positions with respect to the beam.

From the curve gained by the intensity/count rate measurements (see figure 8.5) the height values displayed on the scale of the vertical translation stage can be connected with the corresponding height position on the chopper disc. The faster disappearing of the beam signal (steeper slope) is related to the position where the beam is leaving the chopper slit at the trapezoid's smaller end (length  $b_1$ ). The exact slit height position for each TOF measurement can be found by the slit's geometrical dimensions. The corresponding evaluation graph is presented in figure 8.5. Two linear fit curves were created corresponding to the measured signal intensities at different chopper positions. The crossing point of these two linear fits correspond to the beam leaving the trapezoidal chopper slit. Hence the corresponding value on the choppers translation stage can be connected to the chopper slit's smaller end with the length  $b_1$ . By the knowledge of the chopper slit's height  $h$  and the translation stage positions for each TOF measurement the exact height positions of the slit in relation to the beam for each TOF spectrum can be found.

Each TOF-file is analyzed for its speed ratio value  $S(h)$ . This is done by evaluating the actual flight time  $t_f$  and the FWHM  $\Delta t_M(h)$  for each TOF-spectrum. These two values provide the corresponding speed ratio values  $S(h) = 1.66 \cdot t_f / \Delta t_M(h)$  for each measurement. It has to be mentioned here

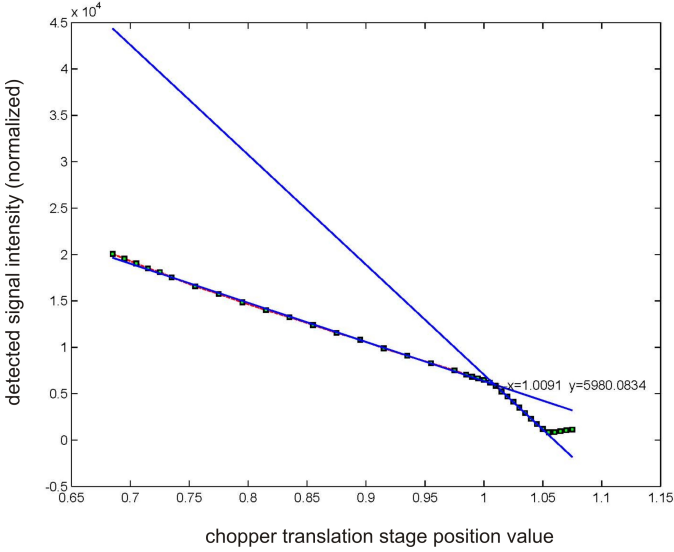


Figure 8.5: Evaluation curve for the position where the beam leaves the slit. This position is found where the two blue linear fit-lines cross. The measured intensities thereby are indicated by the green filled squares connected with the red dashed line.

that the  $S(h)$  numbers are determined without a deconvolution of the real speed distribution and chopper-transmission function. As a next step each  $S(h)$  is plotted on the y-axis versus the chopper slit height position as shown in graph 8.6. A fit through all the  $S(h)$  values is extrapolated to the point  $P$  to eliminate the broadening of the TOF-spectrum due to the finite chopper slit width (see fig. 8.6). This point corresponds to an infinite small chopper slit width ( $w = 0$  mm). Note that the location of point  $P$  is known from the measurement presented in figure 8.5. In this way a more accurate speed ratio determination even for beams with high monochromaticity can be performed.

As for the presented RT beam this measured *speed ratio* value was found to be  $S = 56,2 \pm 0.05$  which agrees well to the speed ratio numbers published in literature [103, 67].

It has to be mentioned here that the measurement/analysis uncertainty for  $S$  is mainly afflicted by the uncertainty of the fitting procedures and the fabrication tolerance of the slit height. By taking a closer look at this values it can be found that the error due to manufacturing tolerances will be in the range of  $\Delta_m S \sim \pm 0.5$  whereas the Gauss fit leads to an error of  $\Delta_{Gauss} S \sim \pm 0.06$ .

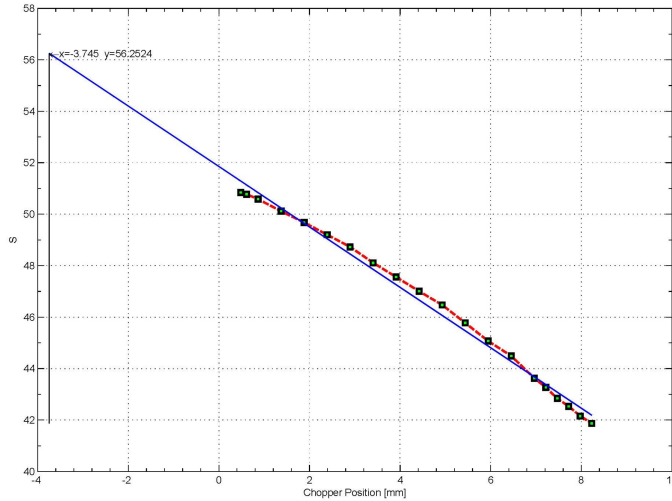


Figure 8.6: Measured *speed ratio* values  $S$  versus their corresponding height position on the trapezoidal chopper slit corresponding to different slit width's  $w$ .

This means that the error due to manufacturing tolerances outweighs the uncertainty of the Gauss fit.

The time resolution predefined by the helium detection principle which is based on electron bombardment ionization of the helium atoms thereby is no limiting factor for speed ratio values below  $S = 240$ . This can be easily explained by the following consideration:

$$\frac{t}{\Delta t} = \frac{L}{\Delta L} = \frac{2046 \text{ mm}}{5 \text{ mm}} \approx 410$$

With a given flight distance between chopper and detector of  $L = 2046 \text{ mm}$  and a length of the atom ionization area of  $5 \text{ mm}$ , the time resolution of the detection setup for speed ratios below  $S \approx 1.66 \cdot \frac{t}{\Delta t} = 1.66 \cdot 410 \sim 247$  is no issue. Since our measured numbers are below this value there is no limitation coming in on behalf of that.



## NEMI MEASUREMENTS

---

Within this part of the thesis the first measurement results gained with the new *neutral helium scattering microscope* setup **Nemi** are presented. In particular it will describe the characterization of the free-jet beam as well as the vacuum chamber pressure responses due to the additional gas flow originating by the beam and its generation. The presented measurements were carried out with an unfocused neutral helium atom beam gained with a diameter  $5\ \mu\text{m}$  nozzle on the assembled beam-column setup of NEMI at two different working temperatures.

### 9.1 CHARACTERIZATION OF THE $5\ \mu\text{m}$ FREE-JET EXPANSION BEAM

The following chapter represents the first measurements regarding the pressure increase within the different NEMI chambers originating due to the helium probe beam at different source (nozzle) pressures  $p_o$ . Also presented are the corresponding pressure rises within a PITOT TUBE detector setup mounted directly into the beam line at the position where later on the sample chamber will be attached. As this indicates these first beam characterizing measurements were carried out before the sample chamber was assembled to the microscope setup. Furthermore they were performed without the beam focusing zone plate element. Nevertheless they provided us with relevant information on the functional capability and the mechanical handling of the system in respect to its beam-column part.

The measurement results gained by the “*in line*” - PITOT TUBE detector allow us to infer on the expected pressure rise within the *reflection detector* as a function of the helium beam’s particle flow. Figure 9.1 shows a principle sketch for this experimental setup.

The PITOT TUBE measuring system which was mounted at the end of the zone plate chamber (ZPC) was built up of a CF-40-DN-flange metal tube (diameter  $D=40\text{mm}$  length app.  $70\ \text{mm}$ ). On one side it was connected to the zone plate chamber by a tube entering aperture with a pinhole diameter of  $d_{\text{pitot}} = 1\ \text{mm}$ . On the other side a cold-cathode high vacuum gauge with a

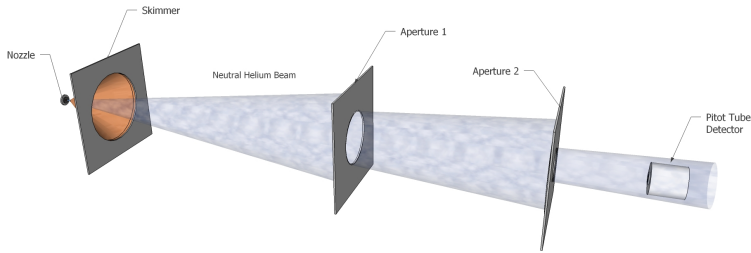


Figure 9.1: Principle sketch of the experimental setup for the first beam flow measurements on the NEMI setup.

CF-40-DN flange connection (distance skimmer to detector entrance aperture:  $L = 1.090$  m) was mounted. This detector setup is similar to the one which will be later implemented onto the sample chamber as the “*in-line*” transmission detector explained in section 6.3.2.3. In the source chamber a *skimmer* with a diameter  $d_{sk} = 9.5 \mu\text{m}$  was mounted and the  $d_N = 5 \mu\text{m}$  *nozzle* was positioned with a distance of 10 mm to this skimmer.

The characteristic curves presented in the following were taken for two different nozzle temperatures  $T_o = 320$  K (RT) and  $T_o = 110$  K (LN) respectively. The two different nozzle temperature settings are in the following also referred to as an app. room temperature beam (RT) and a liquid nitrogen cooled beam (LN) respectively. The cooled beam thereby is of particular interest since the gained speed ratios will be better (less velocity spread, more monochromaticity) for this beam. As a consequence the *zone plate’s* main aberration effect namely the chromatic aberration is reduced in comparison to the focused room temperature beam and the focal spot size diameter can be further scaled down (see chapter 8 and appendix A).

All in the following presented pressure values are background corrected as well as they are adjusted to helium gas values by multiplying the indicated value from the pressure measurement gauges with the corresponding *gas-type-dependent coefficient* provided by the gauge manufacturer. All *cold-cathode principle* based gauges used for NEMI have the same correction coefficient for helium which is stated to be  $k = 5.9$  in the pressure range below  $10^{-5}$  mbar. All the *pirani principle* based prevacuum gauges which are TPR-280 PFEIFFER compact *pirani* gauges (specifications see appendix C.1) have as well a *gas-type-dependency* and their coefficient value for helium is specified to be  $k = 0.8$



in the range below 1 mbar.

The subsequent sub-chapters will treat the measured partial helium pressure increases in the different chambers assembling the beam line and the last section will consider the measured signal intensity in the PITOT-TUBE detection system.

### 9.1.1 Measured source chamber pressures

Figure 9.2 presents the partial helium pressure increase within the source chamber due to the helium beam. Thereby figure 9.2 right shows the partial helium pressure increases in the prevacuum line ( $p_{isc}$  right diagram) whereas the left side of the same figure represents the end pressure of the ultra high vacuum part ( $p_{sc}$  left diagram) of the source chamber. The measurements were performed with a nozzle diameter  $d_N = 5\ \mu\text{m}$  helium *free-jet expansion* beam at different beam pressures  $p_o$ . Both diagrams represent the characteristic curves measured with a room temperature beam and a liquid nitrogen cooled beam respectively. To easily distinguish between these two beam temperatures the corresponding curves are presented in blue/asterisk lines for the cooled beam and red/square ones for the room temperature beam. This assignment of colors will be also maintained until the end of this section.

To compare the actual measured pressure rise to the theoretically expected values (see section 2.2.3.1), the calculated numbers are indicated as dotted/open-symbol lines in the left diagram showing the high vacuum pressure conditions in the source chamber. By comparing those two curves to the measured characteristics it is obvious that the expected linear increase of  $p_{sc}$  is not displayed by the measured lines.

The measured high vacuum pressure values show an upwards bend in the pressure curves with increasing gradient for rising source pressures  $p_o$ . This leads to the assumption that the two turbo pumps which are in charge of the source chamber are losing pumping speed with increasing helium flow into the chamber. An additional indicator for this presumption can be found by studying the prevacuum pressure lines for the source chamber presented at the right side of figure 9.2. As apparent from this curves higher beam pressures  $p_o$  drive the prevacuum pressure values into the  $10^{-1}$  mbar range. The finally achievable UHV pressure of the chamber is depending on the pumping speed of the turbo pumps. This value is not a constant number but depends also

on the provided prevacuum pressure for the system. When the prevacuum pressure exceeds a certain turbo pump specific value it will lead to a decrease of the compression ratio of the TP. This pump specific behavior is stated by characteristic curves provided from the pump manufacturer. Hence a strongly increasing prevacuum pressure of the system will after reaching a certain pressure value always lead to an accompanying rising of the finally achievable lowest end-pressure of the UHV chamber.

For the highest beam pressures with the RT beam we slowly approach this level where the compression ratio of the turbo pumps starts to get affected but the influence is not very strong yet. On the other hand by comparing the  $p_{SC}$  &  $p_{ISC}$  characteristic lines of the RT beam (red/square) and the LN<sub>2</sub> cooled beam (blue/asterisk) it is apparent that the gradient of the cooled beam curve is increasing faster than the one from the room temperature beam (note the scale change for  $p_{SC}$  &  $p_{ISC}$  between the RT and the LN<sub>2</sub> diagram). The same behavior is also obvious for the prevacuum pressure values. From the calculations in section 2.2.3.1 it is expected that a *cooled free-jet expansion* beam will lead to a higher helium flow originating within the source chamber. As a consequence likewise the stress on the pumping system for the source chamber is enhanced faster with the LN<sub>2</sub> cooled beam especially in the region of high source pressures  $p_o$  (ca.  $p_o > 100$  bar). Therefore at a certain point the load onto the prevacuum system reaches a value where the backing pumps are not able to entirely remove all the helium gas arising from the source chamber anymore. The prevacuum pressure in that case approaches the point where it starts to significantly reduce the compression ratio of the two turbo pumps. As a consequence the final end-pressure in the source chamber increases up to a point where the residual helium gas in the chamber starts to interfere with the atoms from the free-jet expansion. At some point the collision frequency between the expansion atoms and the residual gas becomes so high that a further increase of the beam pressure will not lead anymore to an increase in the particle density of the probe beam.

In the case of the room temperature beam we can just make out the beginning of a significant decrease of the turbo pumps pumping speed, therefore for this beam type the pumping setup is sufficient over the whole source pressure range of 0 – 200 bar. However in case of a liquid nitrogen (LN<sub>2</sub>) cooled expansion the situation with the currently applied source chamber pumping setup is different. In this case the final source chamber pressure increases faster and

even reaches the above mentioned pressure limit where the free-jet expansion is strongly disturbed by the residual gas in the chamber. This is indicated by the strong upwards bent of the  $p_{SC}$  pressure curve for the  $\text{LN}_2$  beam at a beam pressure of around  $p_o = 80$  bar.

The consequence of this faster increase in the chamber pressures and the fact that in case of the cooled beam the just described point of strong disturbance of the expansion will be reached is pointed out more clearly by looking at the characteristic curves for the detected signal presented in section 9.1.4. This figure will also explain why the  $\text{LN}_2$  beam measurements are already stopped at  $p_o = 140$  bar.

All together the measurements lead to the assumption that the longer the prevacuum pressure can be kept below the  $10^{-1}$  mbar range, the smaller the slope increase of the high vacuum pressure for the source chamber will be. It is assumed that the prevacuum pressure characteristic has a strong influence on the pumping power of the turbo pumps.

#### 9.1.2 Measured pumping stage chamber pressures

The measured pressure values representing the partial helium pressure increase  $p_{iPST/ZPC}$  and  $p_{PST}$  for the adjacent pumping stage chamber are depicted in figure 9.3. Again the prevacuum characteristic is presented at the right side of the figure whereas the ultra high vacuum pressure curves are shown on the left. As apparent by looking at the two prevacuum curves the helium flow within the pumping stage chamber can be easily handled by the  $30 \text{ m}^3/\text{h}$  scroll-principle backing pump in charge of the pumping stage chamber and the following zone plate chamber. This is obvious since the prevacuum pressure rise for increasing beam pressures is with a maximum of app.  $8 \cdot 10^{-4}$  mbar rather small if not completely negligible since this increase is of the same size as the measurement uncertainty of the *pirani gauges* in this vacuum range. It is also constant after a first increase following the switch-on of the beam which is another indicator that the prevacuum system is not stressed by the raising of the beam pressure. In case of the cooled beam the measurements even showed no partial He pressure increase in the  $p_{iPST/ZPC}$  characteristic line. Of course there will be some amount of pressure increase in the backing pump system but it is minor and therefore lies in the range below the *pirani gauges* sensitivity.

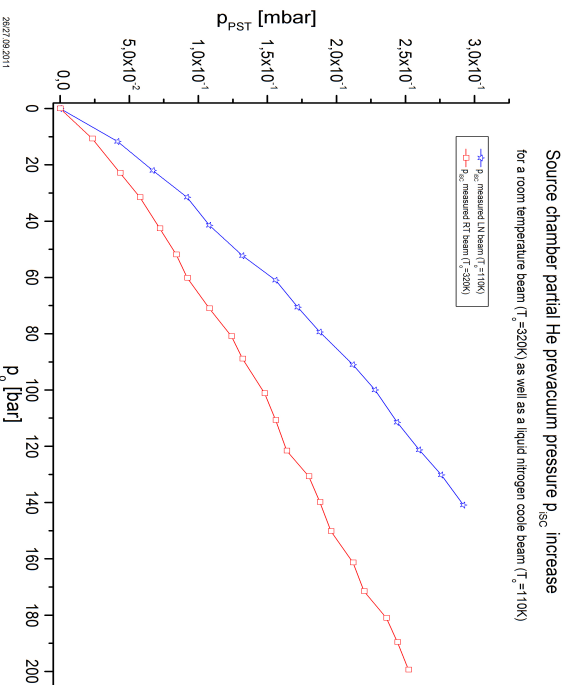
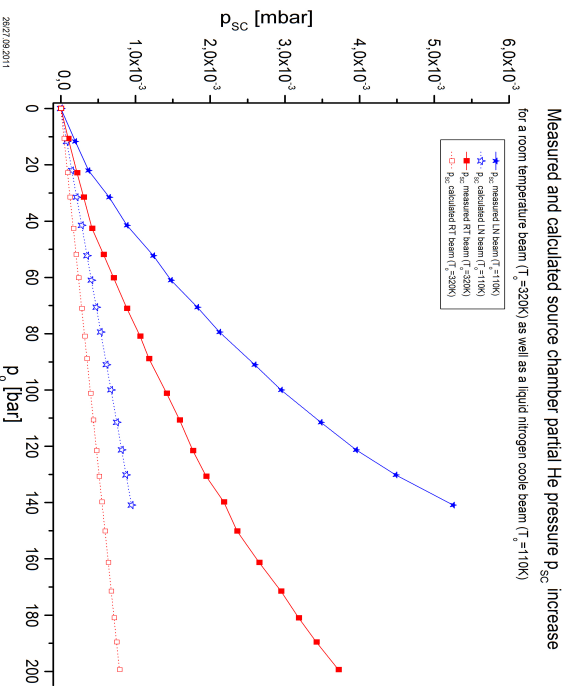


Figure 9.2: Source chamber pressure increases in  $p_{SC}$  &  $p_{PST}$  versus the nozzle pressure  $p_o$ . Left: partial helium pressure increase in the high vacuum part of the source chamber ( $p_{SC}$ ) due to the RT beam (red/square curve) with the theoretical expected pressure rises additionally indicated by the red/dotted/open-squares line and for the LN<sub>2</sub> cooled beam (blue/asterisk curve) with the corresponding theoretically evaluated values in blue/dotted/open-asterisk. Right: partial helium pressure increase in the backing pump vacuum line of the source chamber ( $p_{PST}$ ) for the RT beam (red/open-squares) and the LN<sub>2</sub> cooled beam (blue/open-asterisk). All values are background corrected as well as corrected for helium gas.

As a consequence of this prevacuum behavior it can be seen in the left diagram of figure 9.3 that the ultra high vacuum pressure of the pumping stage  $p_{PST}$  depicts an almost linear increasing slope in contrast to the just before presented source chamber high vacuum pressure  $p_{SC}$ . This behavior leads to the assumption that the pumping speed of the MAG W 300 turbo pump for the pumping stage chamber is not reduced or influenced even by the high beam pressures of  $p_o$ .

The ultra high vacuum pressure curve  $p_{PST}$  of the  $\text{LN}_2$  cooled beam is differing from the RT curve only by slightly enhanced pressure values at the same beam pressures  $p_o$ . This fits the expectations since a higher helium flow rate will naturally lead to a higher partial pressure increase in the chamber.

However comparing the  $p_{PST}$  measurement results to the calculated numbers (dotted-lines/open-symbols) it can be seen that the actual pressure increase is much higher than expected. This circumstances are ascribed to poor sealing between the *source chamber* and the *pumping stage chamber*. The connection between these two chambers should be provided by the *skimmer* orifice. Nevertheless the *skimmer* itself is mounted onto a conical *skimmer-mounting ring* which furthermore is mounted onto a specially reworked CF-150 flange (see section 1.2.2). It is assumed that this *skimmer* fixation onto this *skimmer-mounting ring* is currently not tight enough. A further improvement on this point can be made by an implementation of an additional VITON sealing between this two components.

### 9.1.3 Measured ZONE PLATE chamber pressure

In case of the *zone plate chamber* the same backing pump system as for the *pumping stage chamber* is used. Hence the prevacuum characteristic line for the *zone plate chamber* is the same as presented in the right side of figure 9.3. As discussed there is nearly no influence of the active helium probe beam on the pressure value of this prevacuum line.

The ultra high vacuum pumping of this chamber is provided by a MAG W 300 turbo pump. As shown from the characteristic for the *zone plate chamber* in figure 9.4 the partial helium pressure increase  $p_{ZPC}$  in the ultra high vacuum chamber has a fairly linear tendency. This means that the pumping speed of the turbo pump is unaffected by the additional helium load. The only significant difference between the RT curve and the  $\text{LN}_2$  cooled curve is the

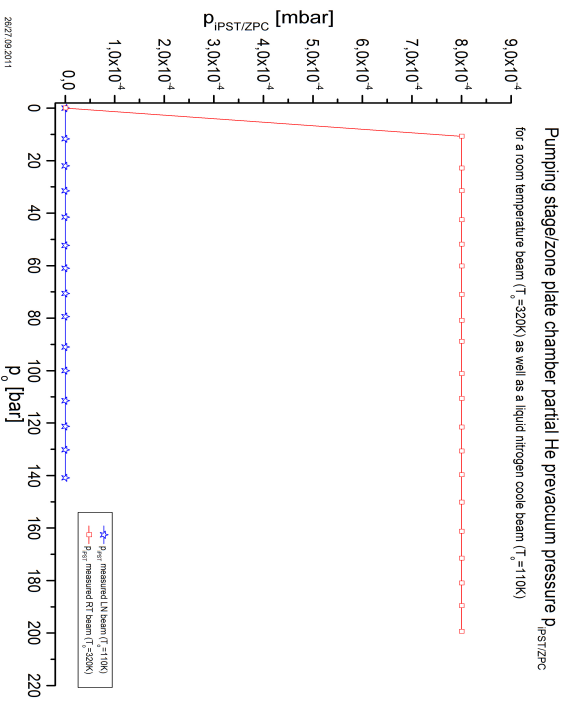
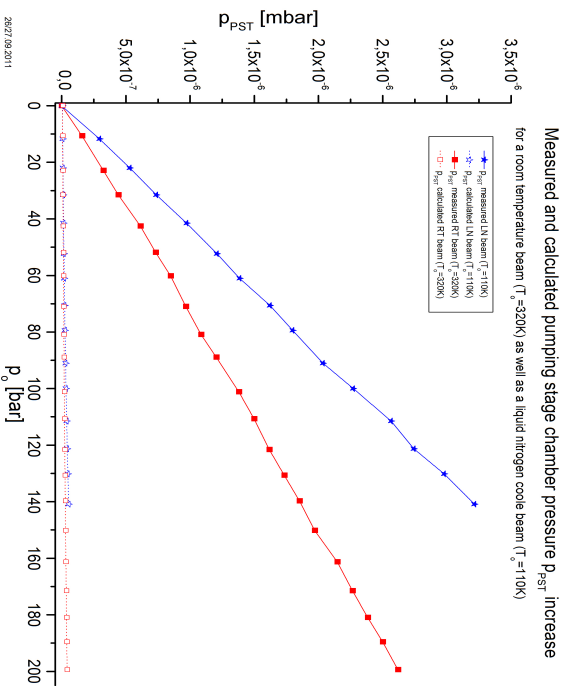


Figure 9-3: Pumping stage chamber pressure increases in  $p_{PST}$  &  $p_{PST/ZPC}$  versus the nozzle pressure  $p_0$ . In both cases only the partial pressure rise due to the helium beam is shown. The left side of this figure represents the ultra high vacuum pressure characteristic for the PST chamber ( $p_{PST}$ ) whereas the right graph depicts the pressure behavior of the prevacuum line ( $p_{PST/ZPC}$ ). RT beam measurements are depicted by red/square lines whereas the characteristics for the LN<sub>2</sub> cooled beam are shown by blue/asterisk lines. The calculated  $p_{PST}$  values for both beam temperature cases are also presented in the left figure by dotted/open-symbol lines. All values are background corrected as well as corrected for helium gas.

higher pressure values at the same beam pressures  $p_o$  for the cooled beam. This complies to the expected behavior due to higher helium flow rates at  $\text{LN}_2$  beam temperatures.

Comparing the calculated pressure rise values for  $p_{ZPC}$  (dotted/open-symbol lines) to the measured characteristics shows that the experimental results are higher then the evaluated numbers. This can be ascribed to the fact that the value for the actual pumping speed of the MAG W 300 turbo pump is not known exactly. The values provided by the manufacturer are standard values which might vary slightly from pump to pump.

Both characteristics however, the measured as well as the calculated one show the same tendency for linear increasing of the  $p_{ZPC}$  pressure values.

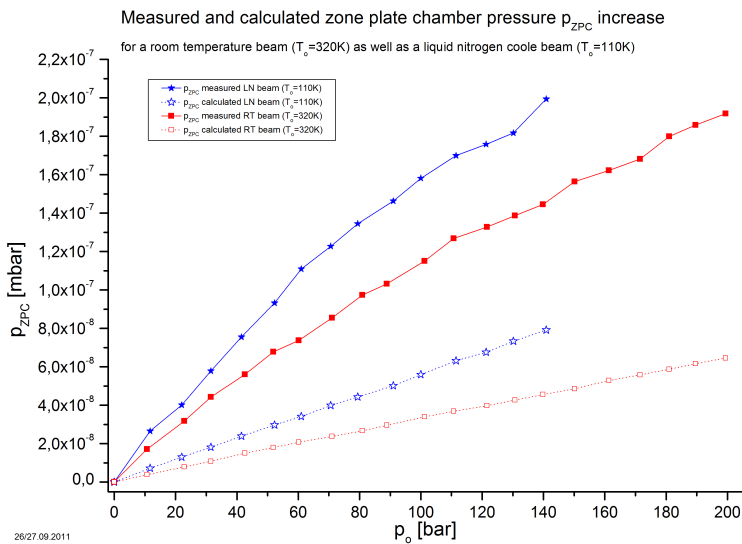


Figure 9.4: Zone plate chamber partial helium pressure increases ( $p_{ZPC}$ ) versus the nozzle pressure  $p_o$ . RT beam measurements are depicted by red/square lines whereas the characteristics for the  $\text{LN}_2$  cooled beam are shown by blue/asterisk lines. The calculated  $p_{ZPC}$  values for both beam temperature cases are also presented by dotted/open-symbol lines. All values are background corrected as well as corrected for helium gas.

9.1.4 Measured “in-line” PITOT tube detector pressure rise

The final pressure characteristics for the beam characterization describe the actual detector behavior. It is represented by the read out from the cold-cathode gauge utilized as the *pitot tube “in-line”* detector. In the case of these measurement results it has to be taken into account that a rising beam pressure  $p_o$  consequently leads to a likewise rising helium background pressure in the detector tube itself. This is due to diffusion of residual helium background gas from the *zone plate chamber* through the pinhole aperture into the detector tube. Therefore an additional detector background measurement has to be recorded for each detector signal and subtracted later on from the measurement results. The following characteristic lines presented in figure 9.5 show the background-corrected detector response curves. They represents the relative helium pressure increases within the *pitot-tube* only due to the helium probe beam. The plot shows a slight downward bend of the measured RT curve in

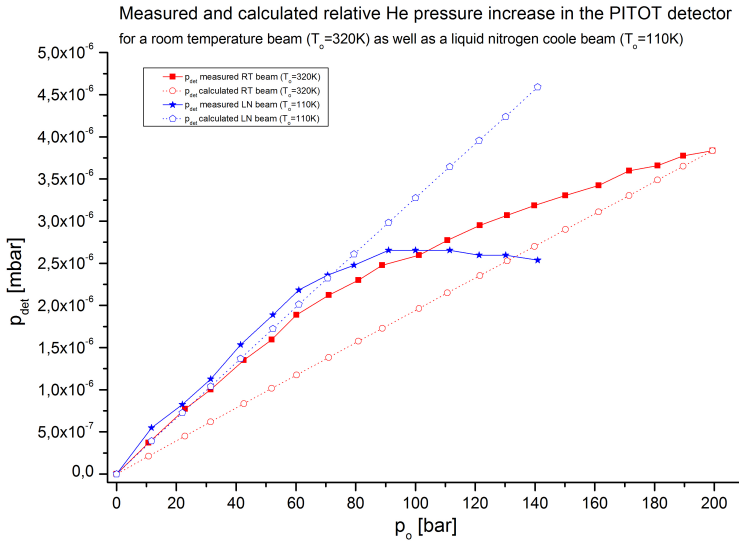


Figure 9.5: Comparison of the “in-line” detector signals of a room temperature (RT) and a liquid nitrogen cooled (LN) beam. The measured detector characteristic of the RT beam is indicated by the red/square line and the corresponding calculated values are indicated by the red/open-circle-dashed line. The blue/asterisk line represents the measured values for the LN beam whereas the blue/open-pentagon-dashed curve corresponds to the calculated values for that case.



the area around approximately  $p_o = 100$  bar, leading into a lower slope of the residual characteristic line against higher beam pressures. By comparing the diagram with the pressure increase behavior of the source chamber (figure 9.2 left) one can see that this bend is located approximately at the same position as the bent towards a steeper rise for the source chamber pressures which appears in the  $p_{SC}$  characteristic line also in the area above ca.  $p_o = 100$  bar. This reinforces the previous argumentation from chapter 9.1.1. In this range above 100 bar beam pressure, for the RT beam the source chamber turbo pumps are starting to struggle with the high helium flow from the source and therefore start to loose pumping speed. As a consequence the source chamber pressure  $p_{SC}$  increases into a range where the residual gas atoms start to interfere with the beam particles from the expansion. More and more collision events with the beam particles occur which furthermore leads to a reduction of the particle density in the probe beam. One can say that the *free-jet expansion* of the beam starts to get slightly disturbed by the higher amount of residual helium gas interaction with the beam. Subsequently also the amount of helium beam atoms reaching the detector is lowered as well. An even further substantiation for this argument is delivered by the beam characterization curves gained with the liquid nitrogen cooled beam shown by the blue/asterisk line in diagram 9.5.

As already indicated (see section 9.1.1) this curve presents the "break down" of the *free-jet-expansion* in the source chamber. This means that the expansion is so strongly disturbed by the residual helium gas that a further increase of the beam pressure does not anymore lead to an increase in the helium-flow within the beam. The presented  $\text{LN}_2$  characteristic curve even shows a decrease of the detected beam intensity by further increasing of the beam pressure above ca.  $p_o = 80$  bar. This indicates strong helium background collisions of the beam in the source chamber which effectively leads to a decrease of the remaining straight forward traveling helium atoms entering the residual beam path.

Also illustrated in this graph is the strong bend in the LN cooled curve at a beam pressure value of about  $p_o = 90$  bar, whereas the RT beam does not show such a strong change. As already explained this behavior is accounted to the fact that in case of the RT beam the pumping setup for the source chamber is still able to cope with the high helium flow in the chamber, whereas in the situation of the LN cooled beam this is not the case anymore for beam pressures above ca. 80 bar. This corresponds also to the strong upwards bend

of the *source chamber pressure*  $p_{SC}$  of the  $\text{LN}_2$  cooled beam which also occurs at the same  $p_o$  pressure range (see figure 9.2). Since in that case the evacuation of the residual helium gas out of the source chamber is not sufficient enough to enable a proper *free-jet expansion*, the slope of the detected signal starts to decline until a point where it even begins to fall again. Therefore with the current vacuum pumping setup the  $\text{LN}_2$  cooled beam can only be used up to beam pressure values around 80 bar.

To additionally display the pressure values which were expected from the theoretical considerations of chapter 2.1.1, they are also indicated in figure 9.5 by the dashed lines. Apparently the characteristic curve measured with the cooled beam corresponds fairly well to the estimated values until it reaches the point where it is assumed that the *free-jet expansion* is strongly disturbed by background collisions in the source chamber.

The measured RT curve on the other hand presents higher pressure values than expected from the theoretical considerations. Up to now I have no suitable explanation for this circumstances and hence I propose further investigations regarding this behavior.

#### 9.1.5 *Summary and discussion of the measurement results*

Altogether it can be concluded that the current pumping setup is strong enough to provide good beam behavior over the whole source pressure range of  $p_o = 0 - 200$  bar for a room temperature beam. Measurements with a liquid nitrogen cooled beam on the other hand are just reasonable until a maximum beam pressure of about  $p_o = 80$  bar. To be able to work with a cooled beam at source pressures higher than this value a further reinforcement on the prevacuum-system for the source chamber has to be made. This could for example be accomplished by an additional implementation of a roots-pump into the backing-line to enable the  $p_{iSC}$  prevacuum pressure to stay below the  $10^{-1}$  mbar range also for higher source pressures  $p_o$ .

Also it was possible to confirm that the *signal detection* with the “*in-line*” PITOT-TUBE detector works as expected.

## OUTLOOK

---

*This final chapter summarizes the work and results presented in this thesis. It lists the next assembling steps for Nemi and a suggestion for the further proceeding of this project. Additionally a discussion of the applications and future possibilities is presented.*

### 10.1 CONCLUSION AND OUTLOOK

A concept and complete technical design for a new neutral matter wave microscope is presented in this thesis. A helium flow calculation for the whole setup was performed to ensure the functionality of the design idea. It could be shown that the expected signal intensity is high enough to achieve good imaging results, and that the designed ultra high vacuum and prevacuum pumping setup will accomplish the demands. All components of the microscope were drawn with a 3D computer-aided design software and assembled to a 3D model of the system. The setup of the beam column with the neutral helium source was completed and its capability and performance was investigated and characterized. The results of this tests are presented and in summary it can be said that the design satisfies all expectations. This investigations also showed the functionality of the accumulation-tube based detection principle for *Nemi*.

All the remaining components of the microscope are manufactured and delivered and ready for assembly.

Measurements to investigate the performance and capability of Fresnel zone plates as beam focusing element for neutral helium beams were carried out. The results are presented in a paper submitted to New Journal of Physics (see appendix A) demonstrating the first sub-micron focusing of a neutral helium beam.

The next step for *Nemi* is to attach the sample chamber and the detection system to the beam column. It is expected that this assembling process will be

finished within the next months, and that first images can be presented within the next half year.

For future applications of *Nemi* an improvement of the source chamber pre-vacuum system is suggested, so that higher beam pressures also for liquid nitrogen cooled beams can be applied. This could for example be accomplished with the installment of an additional roots-pump.

A neutral helium microscope offers the possibility to perform surface investigations without beam induced damage. It can be applied to all materials from metals over semiconductors up to insulating structures. In particular the investigation of polymer nanostructures is a likely first application field. Therefore it is expected that a tool like this will find wide interest.

Although focusing with Fresnel zones plates offers a good approach for neutral helium microscopy on the long term the usage of new highly reflective mirrors might be favorable.

Part I

APPENDIX





## APPENDIX PAPER A

---

### PAPER A - SUB-MICRON FOCUSING OF A NEUTRAL HELIUM BEAM

Sabrina D. Eder, Thomas Reisinger, Gianangelo Bracco, Martin M. Greve, Bodil Holst

submitted to *New Journal of Physics*, December 2011

----- Original-Nachricht -----

Betreff: Acknowledgment of new submission to NJP (temporary ID RANL-8PBDDC)  
Datum: Wed, 7 Dec 2011 11:34:06 +0000  
Von: esubs@iop.org  
Antwort an: esubs@iop.org  
An: sabrina.eder@uib.no

Dear DI Eder

Thank you for submitting your article "Sub-micron focus of neutral helium: A test of free-standing Fresnel zone-plates" to *New Journal of Physics*.

We will contact you if there are any problems with your files, otherwise within a few days you will be sent a permanent article ID so that you can track the progress of your article.

Yours sincerely

The Electronic Submissions Team

This email (and attachments) are confidential and intended for the addressee(s) only. If you are not the intended recipient please notify the sender, delete any copies and do not take action in reliance on it. Any views expressed are the author's and do not represent those of IOP, except where specifically stated. IOP takes reasonable precautions to protect against viruses but accepts no responsibility for loss or damage arising from virus infection. For the protection of IOP's systems and staff emails are scanned automatically.\*

Institute of Physics Registered in England under Registration No 293851  
Registered Office: 76/78 Portland Place, London W1B 1NT

# Sub-micron focus of neutral helium: A test of free-standing Fresnel zone-plates

S D Eder<sup>1\*</sup>, T Reisinger<sup>1</sup>, M M Greve<sup>1</sup>, G Bracco<sup>1,2</sup> and B Holst<sup>1</sup>

<sup>1</sup> Department of Physics and Technology, University of Bergen, Allégaten 55, 5007 Bergen, Norway

<sup>2</sup> CNR-IMEM, Department of Physics, University of Genova, V Dodecanesco 33, 16146 Genova, Italy

E-mail: [sabrina.eder@uib.no](mailto:sabrina.eder@uib.no), [bodil.holst@uib.no](mailto:bodil.holst@uib.no)

**Abstract.** In 2008 we presented the first images obtained with a new type of matter wave microscope: NEutral Helium Atom Microscopy (NEMI). The main features in NEMI are the low energy of the atoms ( $<0.1$  eV) and the fact that they are neutral. This means that fragile and/or insulating samples can be imaged without surface damage and charging effects. The ultimate resolution limit is given by the de Broglie wavelength (around 0.06 nm for a room temperature beam). A particular challenge for neutral helium microscopy is the optical element for focussing. The most promising option is to manipulate neutral helium via its de Broglie wavelength, which requires “classical” optical elements structured to nanometer precision. Here we present an investigation of the helium focussing properties of nano-structured Fresnel zone-plates. Experiments were performed by varying the illuminated area and measure the corresponding focussed spot sizes. The results, which includes the first sub-micron focus of a neutral helium beam, were fitted to a theoretical model. There is very good agreement between model and experiments and we conclude that zone plates can be produced close to theoretical specifications. This is an important step towards nanometer resolution neutral helium microscopy.

AMS classification scheme numbers: 37.20+j, 34.35+a, 37.10.Jk, 03.75.Be

*Keywords:* de Broglie optics, atom optics, molecular beams, neutral helium atom microscopy, matter waves, non-destructive nano-scale imaging

Submitted to: *NJP*



## 1. Introduction

The importance of microscopy in science and technology can hardly be overstated. Matter wave microscopes, where massive particles are used as the imaging probe, have developed rapidly in recent years with major advancements such as helium ion microscopy [1, 2] and atomic resolution transmission electron microscopy [3]. Common for all commercially available matter wave microscopes is that the imaging probe is a beam of charged particles of quite high energy (typically several keV or more) which may charge the sample if it is not conductive and, due to strong interaction with the matter, it is highly probable that energy transfer from the probe to the atomic/molecular species in the sample can cause sample damage. This makes it difficult to image fragile and/or insulating samples, such as for example polymeric nanostructures, insulating coatings, various biological samples etc. In some cases atomic force microscopy or scanning near field optical microscopy can be used instead, but these techniques are not suited for samples with high aspect ratio structures.

In 2008 this group published the first images obtained using a new matter wave microscopy technique (NEMI) where a neutral beam of helium atoms is used as the imaging probe [4]. The low energy of the beam ( $< 0.1$  eV) and the fact that the beam is neutral, makes this technique particularly suited for microscopy of fragile and/or insulating samples. Our original images were shadow images obtained in transmission by focussing a helium beam down to about  $2\ \mu\text{m}$  with a Fresnel zone plate and scanning the focussed beam across a hexagonal copper grid. The image was obtained by recording the signal variation as atoms were transmitted through the grid openings or blocked. Very recently the first neutral helium reflection images were published [5]. The resolution is similar to previous results, but the new reflection images demonstrate beautifully the potential power of neutral helium microscopy as a surface characterisation technique.

A crucial point for high resolution neutral helium microscopy is the optical elements. Because neutral helium in the ground state is not coupled with electric or magnetic fields it is difficult to manipulate it other than via its de Broglie wavelength. The general field of de Broglie matter wave optics, where atoms and molecules are manipulated via their de Broglie wavelength has attracted considerable attention in recent years [6] and has been a topic for several recent publications also in this journal [7, 8, 9, 10]. Very recently the famous Poisson Spot experiment for light was performed for the first time with neutral matter waves, using a  $\mu\text{m}$  size circular plate created with electron beam lithography [10, 11]. de Broglie matter wave optics is characterized by the very small wavelength of matter waves, typically less than  $0.1$  nm. This puts a very large demand on the optical elements. In some cases light fields are used [12], but this is in practice not possible for helium, which means that we are left with the classical optical elements; mirrors and lenses. Mirror focussing has been tried on a couple of occasions [8, 13, 14], but the issue of creating the correct mirror shape remains a limiting factor [15], so that the best 2D focussing obtained with mirrors so far, has only produced a spot size of around  $30\ \mu\text{m}$  diameter [8]. Because the energy of the atoms is so low that they do not penetrate materials, the only possible lenses are so called Fresnel zone plates. A Fresnel zone plate is a special type of axially-symmetric diffraction grating, where the grating period decreases with the distance from the center. Fresnel zone plates are used extensively for example in X-ray optics [16]. A few papers have been published on the application of zone plates in focussing of atoms and molecules [17, 18, 19, 4, 20], but none of these center on the ultimate

performance of the zone plates. Ultimately, the aim for helium microscopy must be to create an instrument with nanometer resolution, but before this can be pursued it must be clear that the optical elements are good enough. This is complex because the zone plate rings have sharp edges that cannot be imaged with high precision in electron or helium ion microscopy due to the increased yield in secondary electron emission at the edges. Thus, the precise characterization of the zone plates can only be performed with the atomic beams themselves:

Here we present a detailed investigation on the focussing properties of two zone plates produced in the group of Prof. Günter Schmahl in Göttingen and in the group of Prof. Henry I. Smith at the Nanostructures Laboratory at MIT (for the rest of the paper they will be referred to as the Göttingen zone plate and the MIT zone plate respectively). Descriptions of the fabrication steps for each zone plate can be found in [21] and in [22]. In both cases the fabrication relies on a combination of electron beam lithography and planar fabrication steps.

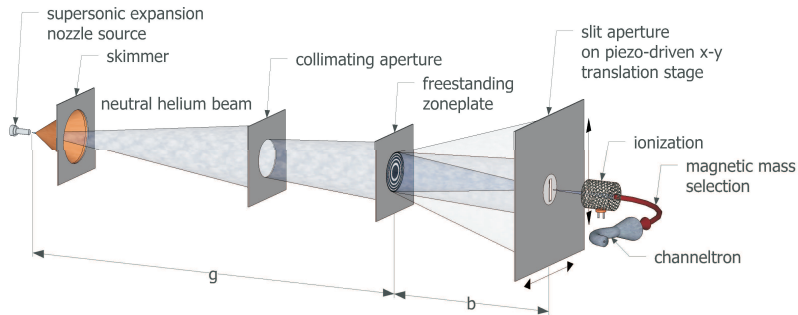
The paper begins with a description of the experimental setup used to measure the focussing properties of the zone plates (section 2), then follow the results (section 3) and a description of the theoretical modeling (section 4). The paper finishes with a conclusion.

## 2. Experimental Setup

The experiments presented here were carried out in the molecular beam apparatus popularly known as MaGIE. For a detailed description see [23]. A diagram of the setup is shown in Figure 1. A neutral, ground-state helium beam is created by supersonic expansion through a 10- $\mu\text{m}$ -diameter nozzle. For the experiments presented here two different settings were used. The measurements with the Göttingen zone plate were carried out using a beam with an average velocity of  $v = (1129 \pm 3) \text{ms}^{-1}$  ( $E \approx 26.5 \text{meV}$ ) and an average wavelength of  $(0.0882 \pm 0.0003) \text{nm}$ . The source pressure was 81 bar. For the MIT zone plate the average beam velocity was  $v = (1036 \pm 3) \text{ms}^{-1}$  ( $E \approx 22.3 \text{meV}$ ) and an average wavelength of  $(0.0961 \pm 0.0003) \text{nm}$ . The source pressure was 110 bar. In both cases the average beam velocity was determined using time of flight (TOF) with a double slit chopper not shown in figure 1.

The central part of the beam was selected using a micro-skimmer. For the Göttingen zone plate a  $(2.5 \pm 0.1)\text{-}\mu\text{m}$ -diameter skimmer was used and for the MIT zone plate a  $(1.1 \pm 0.1)\text{-}\mu\text{m}$ -diameter skimmer. The micro-skimmers were made in house using a glass-pipette-puller (Narishige PP-830) [24]. The distance between the skimmer and zone plate was  $g = (1528 \pm 5) \text{mm}$  (see figure 1). To control the illuminated area on the zone plate two collimating apertures with diameters  $(300 \pm 5) \mu\text{m}$  and  $(150 \pm 5) \mu\text{m}$  were used (National Aperture Inc.). The apertures were mounted on two linear-motion feedthroughs which made it possible to move the apertures into and remove them from the beam-line. The feedthroughs were placed at distances of  $(962 \pm 5) \text{mm}$  and  $(802 \pm 5) \text{mm}$  so that the corresponding illuminated areas in the plane of the zone-plates were  $(478 \pm 11) \mu\text{m}$  and  $(288 \pm 11) \mu\text{m}$  respectively. The MIT zone plate has a diameter of  $188 \mu\text{m}$  and was only tested with full illumination.

To determine the focus spot diameter a  $(25 \pm 2 \mu\text{m}) \times 5 \text{mm}$  slit aperture (CVI Melles Griot) was mounted on a piezo table (PI model Nr. P-731) and scanned across the focussed beam in  $0.1 \mu\text{m}$  steps. In a final experiment the slit aperture was replaced with a transmissive sample, a holy carbon film from Quantifoil (R2/1).



**Figure 1.** Diagram showing the experimental setup used in the measurements presented here. The central part of the supersonic expansion beam is selected with a micro-skimmer. Using different collimating apertures the illuminated area on the zone plate can be controlled. The focussed spot size is determined by scanning a slit aperture across the focussed spot in the image plane. When the helium atoms have passed the slit they are detected in an electron bombardment ionization detector setup. Excluding chromatic aberration the size of the focus is determined by the diameter of the skimmer  $d_{Sk}$ , and the demagnification factor  $b/g$ .

### 3. Results

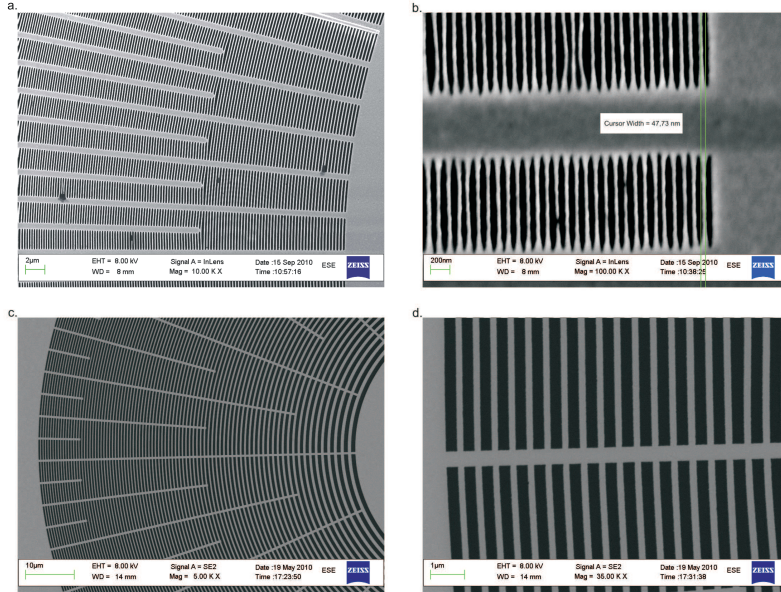
The zone plates used in this experiments can be seen in figure 2. For more than 100 zones the optical properties of a zone plate can be treated similar to a thin refraction lens [25]. The focal length  $f$  of a zone plate depends on the wavelength  $\lambda$  of the incident beam and can be determined using the formula [16]:

$$f = \frac{r^2}{N \cdot \lambda} \quad (1)$$

Where  $r$  is the radius of the zone plate and  $N$  the number of zones.

For a wavelength of 0.088 nm the Göttingen zone plate with  $N = 2700$  and  $r = 270 \mu\text{m}$  has a focal length of 306 mm. For a wavelength of 0.096 nm the MIT zone plate with  $N = 189$  and  $r = 96 \mu\text{m}$  has a focal length of 486 mm. For  $g = (1528 \pm 5) \text{ mm}$  (see Figure 1) this corresponds to image distances of  $b = (383 \pm 2) \text{ mm}$  and  $b = (713 \pm 4) \text{ mm}$  respectively. The optimum image distances were determined experimentally by measuring the focus diameters for different values of  $b$  and they were found to be  $b = (378 \pm 5) \text{ mm}$  and  $b = (712 \pm 5) \text{ mm}$  respectively, in good agreement with the expected values.

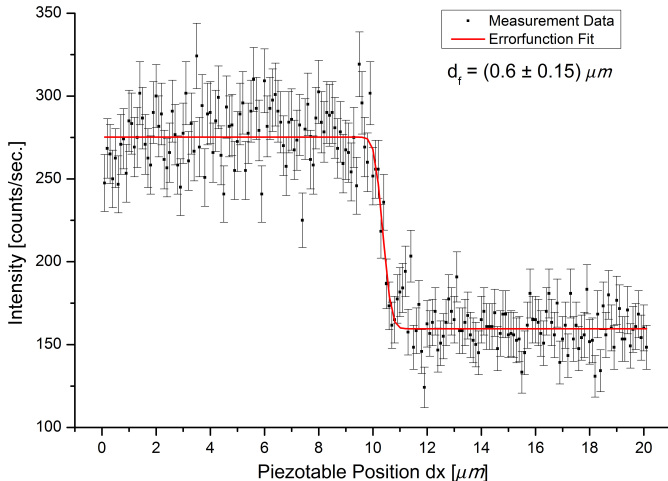
The focussed spot sizes were evaluated following the procedure originally introduced in [19] and further developed in [26]: A  $(25 \pm 2) \mu\text{m}$  wide slit is scanned across the focussed spot in sub-micron steps ( $0.1 \mu\text{m}$ ). As the slit moves across the spot, the measured intensity rises and based on this rise the spot size can be determined by a deconvolution of the measurements with a slit function. Figure 3 shows a typical slit scan. To avoid contributions from temperature fluctuations in the laboratory



**Figure 2.** Scanning electron microscope images of the Göttingen zone plate [21] and the MIT zone plate [22] used in these experiments. The Göttingen zone plate (top images a) and b)) is 540  $\mu\text{m}$  in diameter with a middle stop 162  $\mu\text{m}$  in diameter (blocking the zero-order) and 2700 zones including the blocked middle stop zones. In a) the innermost zones are visible with the middle stop. The radial support rods keeping the rings in place are also visible. In b) the outermost zone with a width of about 48 nm can be seen. The MIT zone plate (bottom images c) and d)) is 188  $\mu\text{m}$  in diameter with a 60  $\mu\text{m}$  diameter middle stop and has 189 zones including the blocked middle zones. The middle stop is visible to the right in c). In d) the outermost zone with a nominal width of 323 nm can be seen. For an ideal zone plate there should be a 1:1 ratio between rings and open space. Both zone plates have slightly wider open zones presumably due to over-exposure or over-etching during fabrication.

the measurements were performed by taking fast scans 0.1  $\mu\text{m}$  steps, 0.5 seconds per measuring point. Each slit scan took about 60 seconds. To reduce the effect of temperature fluctuations several measurements were taken for each spot diameter (7-20 scans).

In a final experiment the slit was replaced by a carbon film with a hexagonal pattern of 2  $\mu\text{m}$  circular holes with a periodicity of 3  $\mu\text{m}$ . This sample was used to create the first sub-micron resolution images obtained with helium microscopy. The images are shown in figure 5.



**Figure 3.** Slit aperture scan across a submicron focussed spot. The scan was performed with  $0.1 \mu\text{m}$  steps. Depicted is the measured intensity (count rate/sec.) versus the slit position on the piezo table weighted with the expected statistical fluctuation of the count rate ( $\sqrt{N}$ ) represented by the error bars. The solid line represents the fit of the data with a Gaussian Error Function. The measurement was taken using the Göttingen zone plate.

#### 4. Modeling the Results

Figure 4 presents the focussed spot measurements obtained with the two zone plates. The focussed spot diameter is plotted versus the diameter of the illuminated area on the zone plates. The results present averages of several measurements (at least 7 per result) as discussed in the previous section. The lines in the diagram present the theoretical model used to predict the focussed spot size  $d_{th}$ . As can be seen there is a good agreement between the theoretical model and the experimental results.

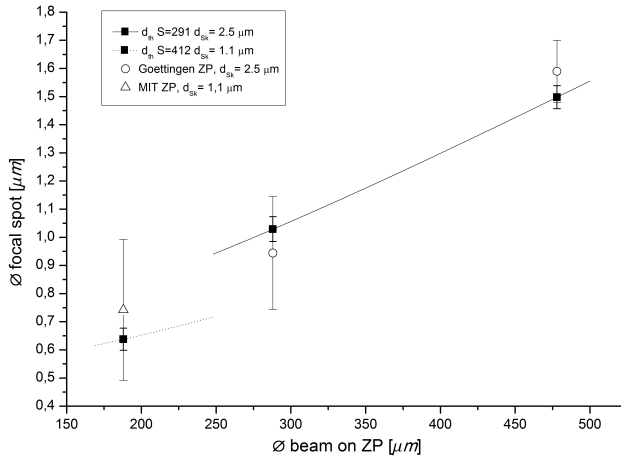
The theoretical model is explained in the following: The spread in wavelength for a supersonic atomic beam can be determined from the speed ratio  $S$  (a measure for the velocity distribution) as [27]:

$$S = 2 \cdot \sqrt{\ln 2} \cdot \frac{v}{\Delta v} \simeq 2\sqrt{\ln(2)} \frac{\lambda}{\Delta\lambda} \quad (2)$$

Here  $v$  is the mean velocity,  $\Delta v$  is the full-width-half-maximum (FWHM) of the velocity distribution and  $\lambda$  and  $\Delta\lambda$  the wavelength and FWHM of the wavelength distribution. The FWHM for a point source (point spread function)  $d_p$  can now be determined using simple geometrical arrangements, see figure 6 and [16]. We get:

$$d_p = \frac{r_i}{\lambda/\Delta\lambda} \simeq 2\sqrt{\ln(2)} \frac{r}{S} \quad (3)$$

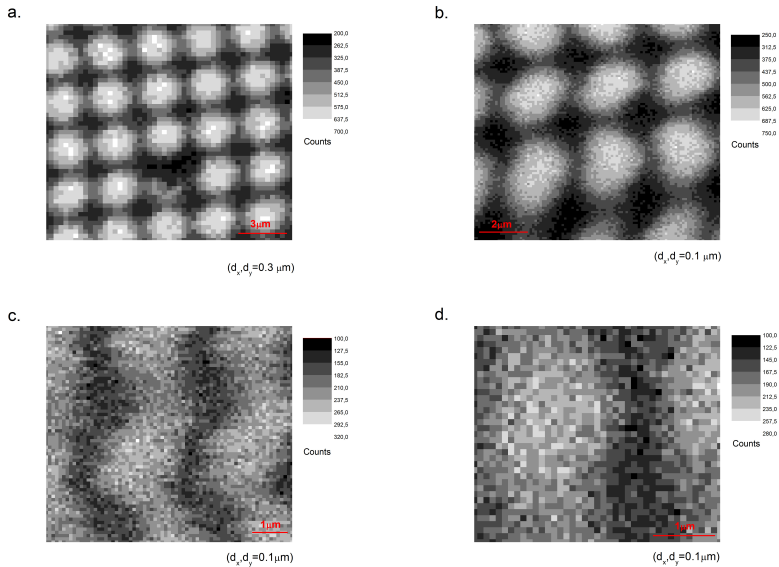
where  $r_i$  is the radius of the illuminated area of the zone plate.



**Figure 4.** Focussed spot diameters measured with three different illuminated areas on the zone plates (diameters:  $\mathcal{O}_1 = 478 \mu\text{m}$ ,  $\mathcal{O}_2 = 288 \mu\text{m}$ ,  $\mathcal{O}_3 = 188 \mu\text{m}$ ). The solid line shows the theoretically calculated focussed spot diameters for a beam with speed ratio  $S=286$  and skimmer diameter  $d_{Sk} = 2.5 \mu\text{m}$ . The dashed line shows the theoretically calculated focussed spot diameters for a beam with speed ratio  $S=408$  and skimmer diameter  $d_{Sk} = 1.1 \mu\text{m}$ . The filled squares are theoretical values including the experimental uncertainties in wavelength, illuminated area and distances (g, b).

The speed ratio  $S$  can in principle be determined experimentally using a TOF measurement. The TOF signal is a convolution of the actual velocity distribution of the beam with the chopper slit and the detector function. For the experiments presented here, the source pressures were rather high and therefore the velocity distribution rather narrow. This meant that the width of the chopper-slit transmission curve was rather large in comparison with the velocity distribution and hence we could not determine the velocity distribution with sufficient accuracy using the standard deconvolution procedure [28, 29]. Therefore we chose to use theoretically determined parameters for the speed distributions calculated using the method of moments with the Lennard-Jones potential [30, 31, 32]. Previous experiments show that there is a very good agreement between theory and experiment in the pressure and temperature range used for these experiments [32].

In reality the source is not a single point. The extended size of the source has to be included to determine the theoretical focus diameter. Previous experiments show that the spatial intensity distribution in a supersonic expansion source (the so called virtual source) can be approximated well with two gaussian functions [33] (a single gaussian function does not describe the tails of the distribution properly). The width of the two gaussian functions depends on the nozzle diameter, source pressure and source temperature. On the other hand, the skimmers used here are smaller than the true virtual source and the beam can be considered as emanating



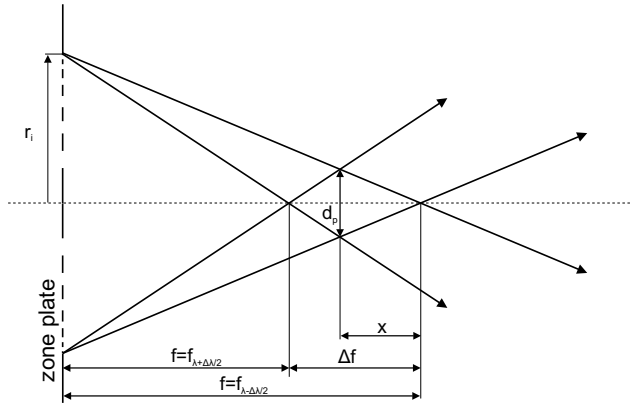
**Figure 5.** 2-D transmission scans of a holy carbon foil QUANTIFOIL® (R2/1). The holes are 2 micron in diameter with a period of 3  $\mu\text{m}$ . All pictures were taken with the Göttingen zone plate. (a) image size 15x15  $\mu\text{m}^2$ , focussed spot diameter < 2  $\mu\text{m}$ , step size 300 nm, 2 s/step (b) image size 10x10  $\mu\text{m}^2$ , focussed spot diameter < 2  $\mu\text{m}$ , step size 100 nm, 2 s/step (c) image size 7x7  $\mu\text{m}^2$ , focussed spot  $\leq 1$   $\mu\text{m}$ , step size 100 nm 1,2 s/step (d) image size 4x4  $\mu\text{m}^2$ , focussed spot diameter  $\leq 1$   $\mu\text{m}$ , step size 100 nm 1 s/step. Image c and d are distorted because of thermal fluctuations, which becomes a factor due to the longer scan times caused by the small step size and the low intensities (a smaller area of the zone plate is illuminated to get the better focus and hence the signal is smaller).

from the skimmer. Therefore a reasonable approximation, which will simplify the following analysis, is to assume a gaussian distribution with FWHM corresponding to the skimmer diameter  $d_{Sk}$ . The FWHM of the geometrical image size of the source is then simply  $d_{op} = (b/g) \cdot d_{Sk}$  (see figure 1). The final theoretical focus diameter  $d_{th}$  can then be obtained as a convolution of two gaussian functions: the geometrical image and the point spread function:

$$d_{th} = \sqrt{(d_p)^2 + (d_{op})^2} \quad (4)$$

## 5. Conclusion

Figure 4 shows that sub micron focussing of a neutral helium beam is possible. Further, Figure 4 shows a very good agreement between the theoretically predicted focus and the experimentally measured values for various zone plate diameters. Even for the



**Figure 6.** This drawing illustrates the geometrical relation between the change in focal length  $\Delta f$  due to a change in wavelength and the resulting point spread function  $d_p$ .  $r_i$  denotes the radius of the illuminated area of the zone plate.

largest illuminated areas there is a good agreement. This is very encouraging and shows that the patterning is precise and transmissive. We thus conclude that the zone plates are patterned to a precision close to specifications paving the way for nanometer resolution neutral helium microscopy. The slit scan measurement shown in Figure 3 illustrates one of the problems that we are still facing. The count rate appears very low - only a few hundred counts. In fact the number of helium atoms arriving at the detector is much higher, but the very low efficiency of present days electron bombardment detectors (less than  $10^{-5}$ ) makes it appear so low. Several groups are currently exploring the possibilities of improving the detector efficiency with various means [34, 35, 36, 37, 38, 39, 40] but so far no breakthrough has occurred. The other crucial issue is thermal drift. This should be possible to solve quite easily, by designing an instrument of smaller dimensions, comparable to a helium ion or a scanning electron microscope, which can be kept in a temperature controlled environment.

### Acknowledgments

This work was supported by Bergens Research Foundation. One of the authors (G.B.) was supported by the Christian Michelsen Center for industrial measurement science and technology (MIMT) in Bergen. The Fresnel zone-plates were fabricated at the institute for X-ray physics, University of Göttingen, by Stefan Rehbein and Günter Schmahl. The other zone plate was fabricated by one of the authors (T.R.) at the NanoStructures laboratory, Massachusetts Institute of Technology, under the supervision of Henry I. Smith. The molecular-beam apparatus MAGIE was originally designed and assembled at the Max-Planck institute (MPI) for fluid dynamics (Now MPI for dynamics and self-assembly) in Göttingen. MAGIE is now located at the



university of Bergen.

- [1] Postek M T and Vladár A E 2008 *Scanning* **30**(6) 457–462
- [2] Scipioni L, Stern L A, Notte J, Sijbransij S and Griffin B 2008 *Advanced Materials & Processes* 27–30
- [3] Haider M, Uhlemann S, Schwan E, Rose H, Kabius B and Urban K 1998 *Nature* **392** 768–769
- [4] Koch M, Rehbein S, Schmahl G, Reisinger T, Bracco G, Ernst W E and Holst B 2008 *Journal of Microscopy* **229** 1–5
- [5] Witham P and Sanchez E 2011 *Rev. Sci. Instrum.* **82** 103705 (pages 9)
- [6] Cronin A D, Schmiedmayer J and Pritchard D E 2009 *Rev. Mod. Phys.* **81**(3) 1051–1129
- [7] Libson A, Riedel M, Bronshtein G, Narevicius E, Even U and Raizen M G 2006 *New Journal of Physics* **8** 77
- [8] Fladischer K, Reingruber H, Reisinger T, Mayrhofer V, Ernst W E, Ross A E, MacLaren D A, Allison W, Litwin D, Galas J, Sitarek S, Nieto P, Barredo D, Fariás D, Miranda R, Surma B, Miros A, Piatkowski B, Søndergård E and Holst B 2010 *New Journal of Physics* **12** 033018
- [9] Eibenberger S, Gerlich S, Arndt M, Tüxen J and Mayor M 2011 *New Journal of Physics* **13** 043033
- [10] Reisinger T, Bracco G and Holst B 2011 *New Journal of Physics* **13** 065016
- [11] Reisinger T, Patel A A, Reingruber H, Fladischer K, Ernst W E, Bracco G, Smith H I and Holst B 2009 *Phys. Rev. A* **79**(5) 053823
- [12] Rasel E M, Oberthaler M K, Batelaan H, Schmiedmayer J and Zeilinger A 1995 *Phys. Rev. Lett.* **75**(14) 2633–2637
- [13] Holst B and Allison W 1997 *Nature* **390** 244–244
- [14] Schewe H C, Zhao B S, Meijer G and Schöllkopf W 2009 *New Journal of Physics* **11** 113030
- [15] Ross A E, MacLaren D A and Allison W 2011 *Journal of Physics D: Applied Physics* **44** 185501
- [16] Michette A G 1968 *Optical Systems for Soft X Rays* (New York: Plenum Press)
- [17] Carnal O, Sigel M, Sleator T, Takuma H and Mlynek J 1991 *Phys. Rev. Lett.* **67**(23) 3231–3234
- [18] Reisinger T, Greve M, Eder S, Bracco G and Holst B *submitted to Phys. Rev. A*
- [19] Doak R B, Grisenti R E, Rehbein S, Schmahl G, Toennies J P and Wöll C 1999 *Phys. Rev. Lett.* **83**(21) 4229–4232
- [20] Oberst H, Kouznetsov D, Shimizu K, Fujita J i and Shimizu F 2005 *Phys. Rev. Lett.* **94**(1) 013203
- [21] Rehbein S, Doak R, Grisenti R, Schmahl G, Toennies J and Wöll C 2000 *Microelectronic Engineering* **53** 685 – 688
- [22] Reisinger T, Eder S, Greve M, Smith H and Holst B 2010 *Microelectronic Engineering* **87** 1011–1014
- [23] Apfelter A 2005 *Wiederaufbau und Test einer He-Streuapparatur und erste Streuexperimente an amorpher sowie kristalliner SiO<sub>2</sub>-Oberfläche* Master's thesis Graz University of Technology
- [24] Braun J, Day P K, Toennies J P, Witte G and Neher E 1997 *Rev. Sci. Instrum.* **68** 3001–3009
- [25] Daniel J, Stigliani J, Mittra R and Semoni R G 1967 *J. Opt. Soc. Am.* **57**(5) 610–611
- [26] Reisinger T and Holst B 2008 *J. Vac. Sci. Technol. B* **26**(6) 2374–2379
- [27] Miller D R 1988 *Atomic and Molecular Beam Methodes* vol 1 (Oxford: Oxford University Press)
- [28] Auerbach D J 1988 *Atomic and Molecular Beam Methodes* vol 1 (Oxford: Oxford University Press)
- [29] Pauly H 2000 *Atom, Molecule, and Cluster Beams 2* vol 2 (Berlin: Springer-Verlag) chap 3.2, pp 156–171
- [30] Toennies J P and Winkelmann K 1977 *The Journal of Chemical Physics* **66** 3965–3979
- [31] Pedemonte L, Bracco G and Tatarek R 1999 *Phys. Rev. A* **59**(4) 3084–3087
- [32] Pedemonte L and Bracco G 2003 *The Journal of Chemical Physics* **119** 1433–1441
- [33] Reisinger T, Bracco G, Rehbein S, Schmahl G, Ernst W E and Holst B 2007 *The Journal of Physical Chemistry A* **111** 12620–12628
- [34] Patton F S, Deponte D P, Elliott G S and Kevan S D 2006 *Phys. Rev. Lett.* **97**(1) 013202
- [35] Riley D J, Mann M, MacLaren D A, Dastoor P C, Allison W, Teo K B K, Amaratunga G A J and Milne W 2003 *Nano Letters* **3** 1455–1458
- [36] Doak R B 2004 *Journal of Physics: Condensed Matter* **16** S2863
- [37] Doak R B, Ekinici Y, Holst B, Toennies J P, Al-Kassab T and Heinrich A 2004 *Review of Scientific Instruments* **75** 405–414
- [38] Holst B, Piskur J, Kostrobij P, Markovych B and Suchorski Y 2009 *Ultramicroscopy* **109** 413 – 417
- [39] Pedemonte L, Tatarek R and Bracco G 2003 *Review of Scientific Instruments* **74** 4404–4409
- [40] Fahy A, O'Donnell K M, Barr M, Zhou X J, Allison W and Dastoor P C 2011 *Measurement Science and Technology* **22** 115902



## APPENDIX TECHNICAL DRAWINGS

---

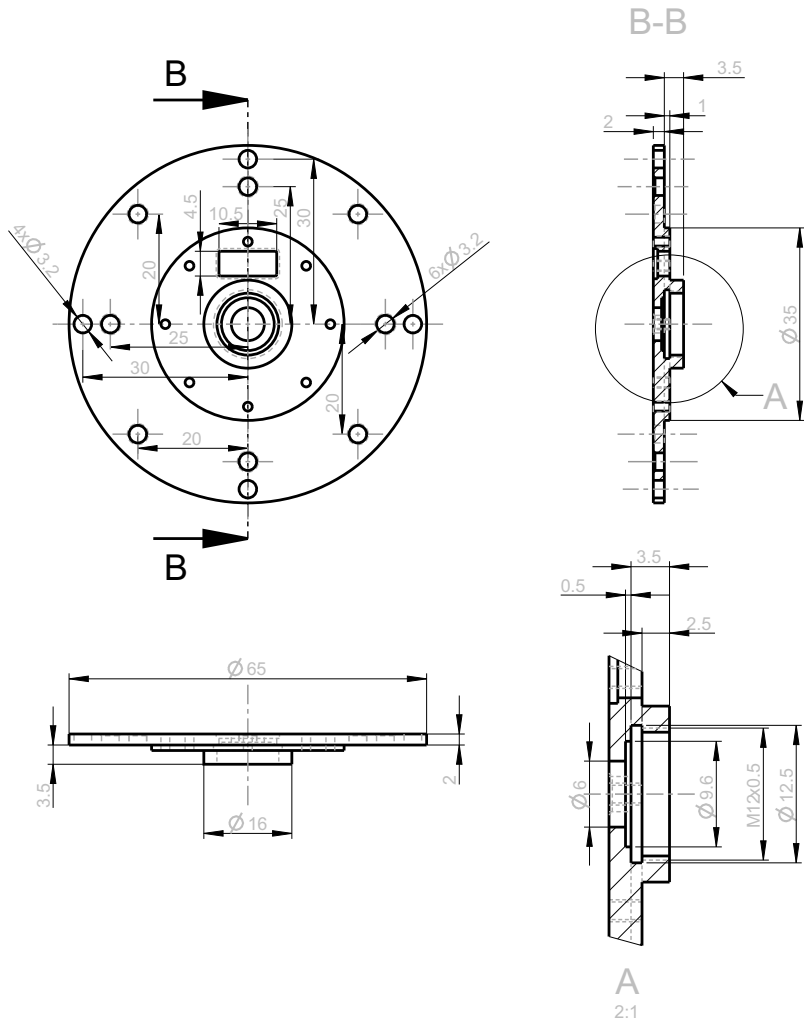
### B.1 DESIGN DRAWINGS AND COMPONENT SPECIFICATIONS

#### B.1.1 *UHV Design XYZT64-50-H XYZ stage*

Design drawing provided by “UHV DESIGN LTD”, England.



B.1.2 *Sample holder*



Item	Qty	Description	Specification	Unit Weight(kg)	Part No. Drw No.	
Sample Holder				Date	07.06.2011	
				Drawn	s.E.	
				Part No./Drwg No	Rev.	Sheet
				NAME: SAMPLEHOLDER, MOUNTING NUMBER: SHM 0001	QUANTITY	4
Specification		Total Weight(kg)	Projection	Format	Scale	
				A4	1:1	



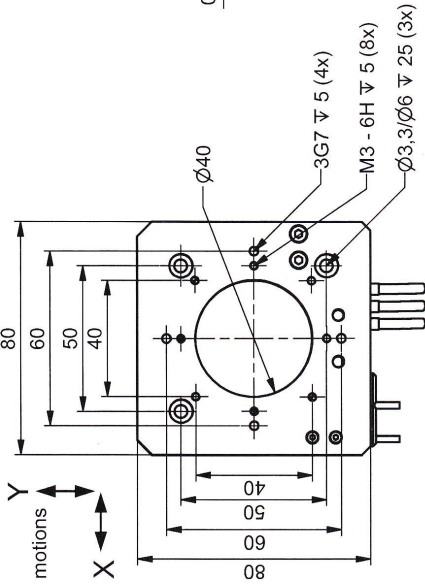




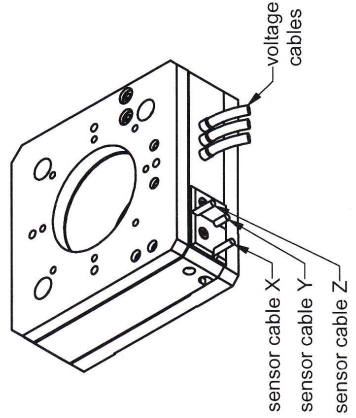
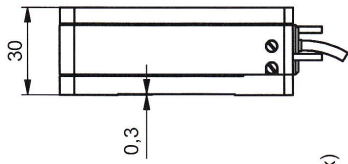
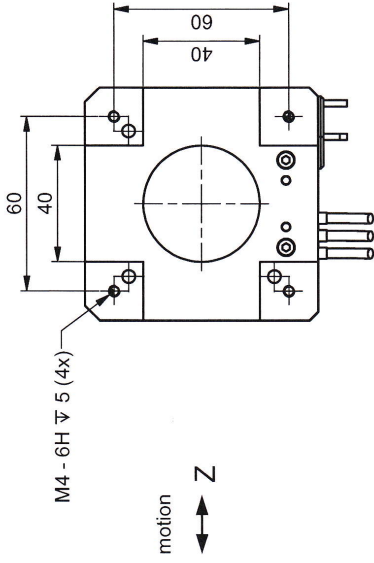
### B.1.3 *Piezo-tabel*

Design drawing provided by "OPTONYX AB", Sweden.

TOP




BOTTOM



**Cables:**  
 standard T-405-06 1.6m (LEMO/LEMO)  
 external version T-405-06E 2m (ODU/LEMO)  
 digital version T-405-06D 2m (D-Sub)

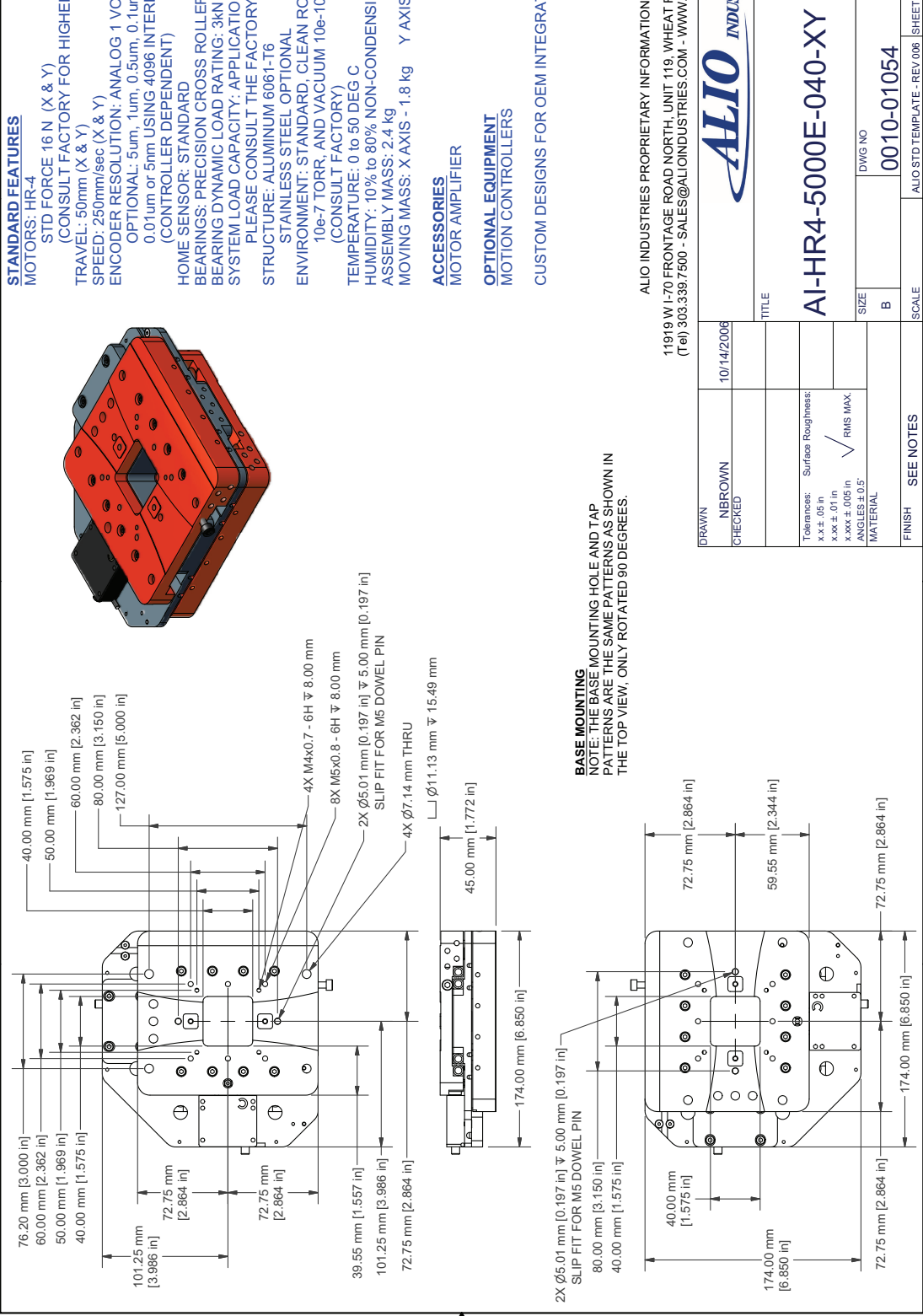
**ORIGINAL**

part.-no.	T-405-06(x)	part.-name	Tritor 102 CAP
file name	PT40506_ÄZ02 REV 1	OK: date/sign.	<i>[Signature]</i> 2010
	scale	1:2	customers drawing
	piezosystem jena		

B.1.4 *Alio XYZR stage*

Design drawings provided by "ALIO INDUSTRIES", USA.

1 2 3 4



**STANDARD FEATURES**

MOTORS: HR-4  
 STD FORCE 16 N (X & Y)  
 (CONSULT FACTORY FOR HIGHER FORCE)  
 TRAVEL: 50mm (X & Y)  
 SPEED: 250mm/sec (X & Y)  
 ENCODER RESOLUTION: ANALOG 1 VOLT, PEAK TO PEAK  
 OPTIONAL: 5um, 1um, 0.5um, 0.1um, 0.05um, 0.02um,  
 0.01um or 5mm USING 4096 INTERPOLATION  
 (CONTROLLER DEPENDENT)

HOME SENSOR: STANDARD  
 BEARINGS: PRECISION CROSS ROLLER  
 BEARING DYNAMIC LOAD RATING: 3kN  
 SYSTEM LOAD CAPACITY: APPLICATION DEPENDENT  
 PLEASE CONSULT THE FACTORY

STRUCTURE: ALUMINUM 6061-T6  
 STAINLESS STEEL OPTIONAL  
 ENVIRONMENT: STANDARD, CLEAN ROOM, VACUUM  
 10e-7 TORR, AND VACUUM 10e-10 TORR  
 (CONSULT FACTORY)  
 TEMPERATURE: 0 to 50 DEG C  
 HUMIDITY: 10% to 80% NON-CONDENSING  
 ASSEMBLY MASS: 2.4 kg  
 MOVING MASS: X AXIS - 1.8 kg Y AXIS - 0.6

**ACCESSORIES**  
 MOTOR AMPLIFIER

**OPTIONAL EQUIPMENT**  
 MOTION CONTROLLERS

CUSTOM DESIGNS FOR OEM INTEGRATION

**BASE MOUNTING**  
 NOTE: THE BASE MOUNTING HOLE AND TAP  
 PATTERNS ARE THE SAME PATTERNS AS SHOWN IN  
 THE TOP VIEW, ONLY ROTATED 90 DEGREES.

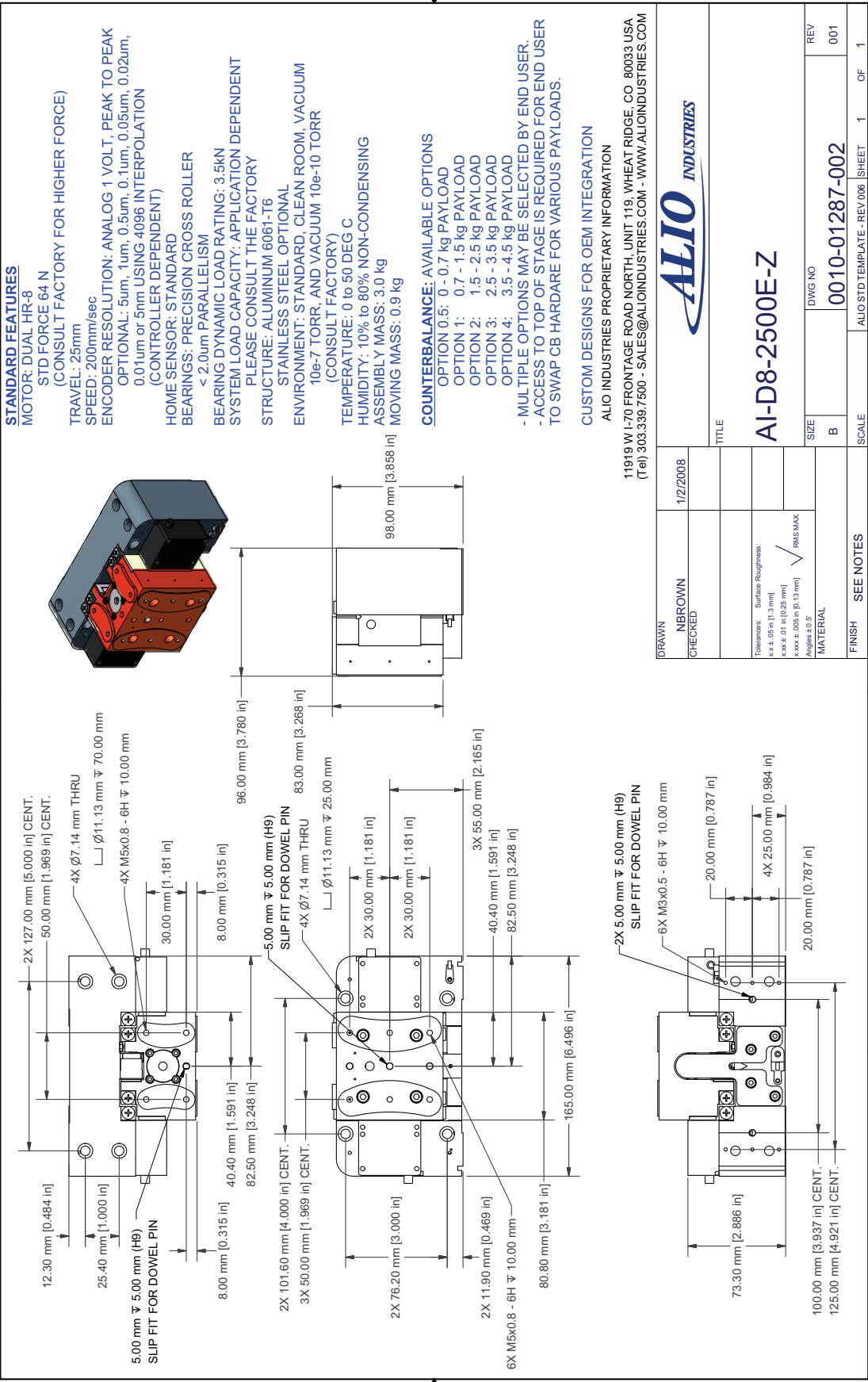
ALIO INDUSTRIES PROPRIETARY INFORMATION

11919 W I-70 FRONTAGE ROAD NORTH, UNIT 119, WHEAT RIDGE, CO. 80033 USA  
 (Tel) 303.339.7500 - SALES@ALIOINDUSTRIES.COM - WWW.ALIOINDUSTRIES.COM

10/14/2006	10/14/2006	10/14/2006	10/14/2006
DRAWN	NBROWN	CHECKED	
TITLE			
AI-HR4-5000E-040-XY			
ALIO INDUSTRIES			
DWG NO			
0010-01054			
REV			
002			
SCALE			
ALIO STD TEMPLATE - REV.006			
SHEET 1 OF 1			

1 2 3 4

1 2 3 4



**STANDARD FEATURES**

- MOTOR: DUAL HR-8
- STD FORCE 64 N (CONSULT FACTORY FOR HIGHER FORCE)
- TRAVEL: 25mm
- SPEED: 200mm/sec
- ENCODER RESOLUTION: ANALOG 1 VOLT, PEAK TO PEAK OPTIONAL: 5um, 1um, 0.5um, 0.1um, 0.05um, 0.02um, 0.01um or 5nm USING 4096 INTERPOLATION (CONTROLLER DEPENDENT)
- HOME SENSOR: STANDARD
- BEARINGS: PRECISION CROSS ROLLER < 2.0um PARALLELISM
- BEARING DYNAMIC LOAD RATING: 3.5KN
- SYSTEM LOAD CAPACITY: APPLICATION DEPENDENT PLEASE CONSULT THE FACTORY
- STRUCTURE: ALUMINUM 6061-T6
- STAINLESS STEEL OPTIONAL
- ENVIRONMENT: STANDARD, CLEAN ROOM, VACUUM 10e-7 TORR, AND VACUUM 10e-10 TORR (CONSULT FACTORY)
- TEMPERATURE: 0 to 50 DEG C
- HUMIDITY: 10% to 80% NON-CONDENSING
- ASSEMBLY MASS: 3.0 kg
- MOVING MASS: 0.9 kg

**COUNTERBALANCE: AVAILABLE OPTIONS**

- OPTION 0.5: 0 - 0.7 kg PAYLOAD
  - OPTION 1: 0.7 - 1.5 kg PAYLOAD
  - OPTION 2: 1.5 - 2.5 kg PAYLOAD
  - OPTION 3: 2.5 - 3.5 kg PAYLOAD
  - OPTION 4: 3.5 - 4.5 kg PAYLOAD
- MULTIPLE OPTIONS MAY BE SELECTED BY END USER.  
 - ACCESS TO TOP OF STAGE IS REQUIRED FOR END USER TO SWAP CB HARDWARE FOR VARIOUS PAYLOADS.

**CUSTOM DESIGNS FOR OEM INTEGRATION**

ALIO INDUSTRIES PROPRIETARY INFORMATION  
 11919 W I-70 FRONTAGE ROAD NORTH, UNIT 119, WHEAT RIDGE, CO 80033 USA  
 (Tel) 303.339.7500 - SALES@ALIOINDUSTRIES.COM - WWW.ALIOINDUSTRIES.COM

DRAWN		1/2/2008	TITLE
NBROWN			
CHECKED			
Tolerances: Surface Roughness: x.x ± .05 in [1.3 mm] x.xx ± .01 in [0.25 mm] x.xxx ± .005 in [0.13 mm] Angles: ±0.5°			
MATERIAL			
SIZE	DWG NO	REV	
B	0010-01287-002	001	
FINISH		SCALE	
SEE NOTES		1	OF 1



**AI-D8-2500E-Z**

1 2 3 4

1 2 3 4

**STANDARD FEATURES**

MOTORS: DUAL HR-2  
 STD TORQUE 0.24 N·m  
 (CONSULT FACTORY FOR HIGHER FORCE)  
 ROTATION: 360 DEGREES CONTINUOUS  
 SPEED: >180 DEG/SEC  
 ENCODER RESOLUTION: 0.03 ARC-SEC TO 27 ARC-SEC  
 0.03 ARC-SEC USING 4096 INTERPOLATION  
 (CONTROLLER DEPENDENT)  
 HOME SENSOR: STANDARD  
 BEARINGS: PRECISION CROSSED ROLLER  
 BEARING DYNAMIC LOAD RATING: 3 kN  
 SYSTEM LOAD CAPACITY: APPLICATION DEPENDENT  
 PLEASE CONSULT THE FACTORY  
 ENCLOSURES: ALUMINUM 6061-T6  
 STAINLESS STEEL OPTIONAL  
 ENVIRONMENT: STANDARD, CLEANROOM, VACUUM  
 10e-7 TORR, AND VACUUM 10e-10 TORR  
 (CONSULT FACTORY)  
 TEMPERATURE: 0 to 50 DEG C  
 HUMIDITY: 10% to 80% NON-CONDENSING  
 ASSEMBLY MASS: 0.56 kg  
 ROTATING MASS: 0.2 kg  
 ROTATING MASS MOMENT OF INERTIA: 140 kg\*mm<sup>2</sup>

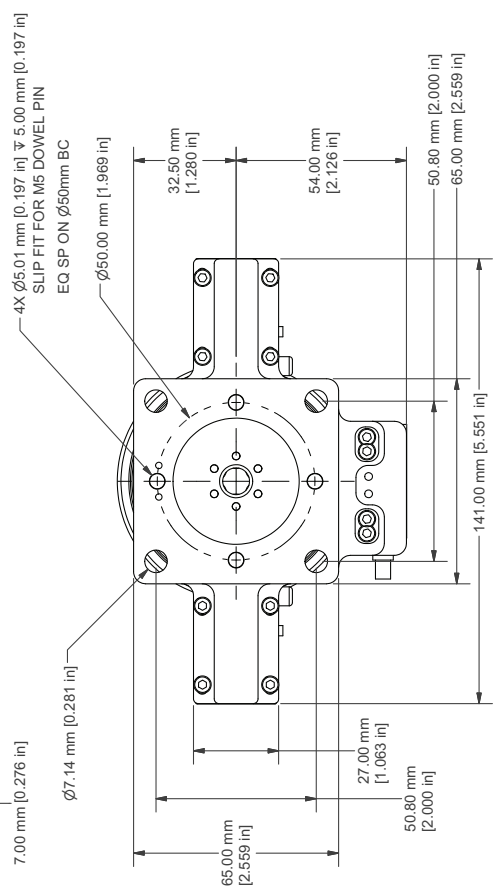
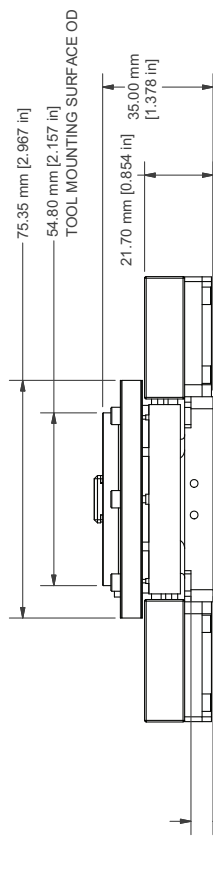
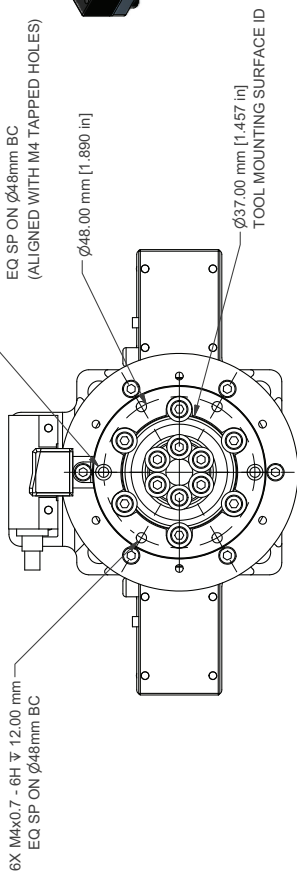
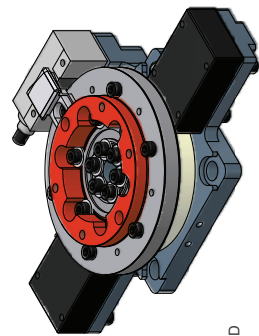
**ACCESSORIES**

MOTOR AMPLIFIER  
 ROTATION LIMIT MARKERS  
 OPTIONAL HARDSTOPS

**OPTIONAL EQUIPMENT**

MOTION CONTROLLERS

CUSTOM DESIGNS FOR OEM INTEGRATION



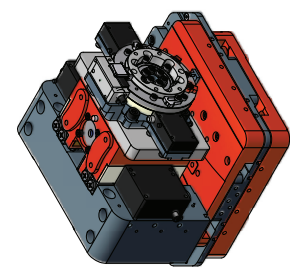
ALIO INDUSTRIES PROPRIETARY INFORMATION  
 11919 W I-70 FRONTAGE ROAD NORTH, UNIT 119, WHEAT RIDGE, CO. 80033 USA  
 (Tel) 303.339.7500 - SALES@ALIOINDUSTRIES.COM - WWW.ALIOINDUSTRIES.COM

DRAWN	1/16/2006	TITLE	
CHECKED	NBROWN	ALIO INDUSTRIES	
Tolerances: x.x $\pm$ .04 in x.xxx $\pm$ .02 in		Surface Roughness: ✓ RMS MAX.	REV
MATERIAL		SIZE	DWG NO
FINISH		B	0010-00267
SEE NOTES		SCALE	1 OF 1
		ALIO STD TEMPLATE - REV.005 SHEET	

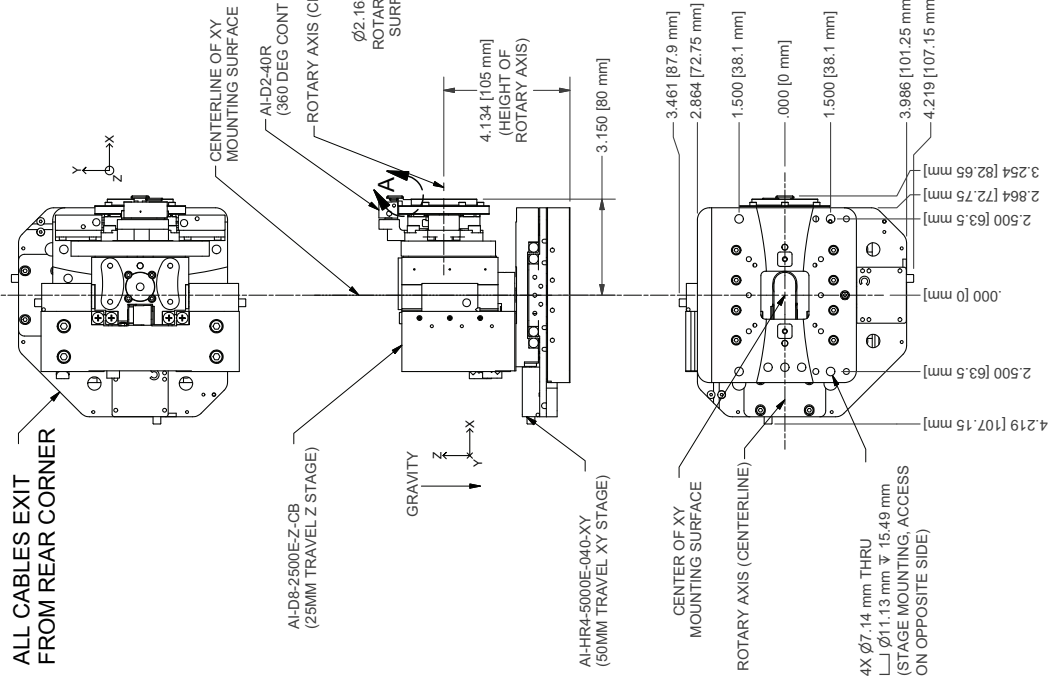
**AI-40R-D**

1 2 3 4

1 2 3 4



ALL CABLES EXIT FROM REAR CORNER



DETAIL A  
SCALE 0.57 : 1

DRAWN	12/21/2010
NBROWN	
CHECKED	
Tolerances: Surface Roughness: x.x ±.05 in [1.3 mm] x.xx ±.01 in [0.25 mm] x.xxx ±.005 in [0.13 mm] Angles ±0.5°	
MATERIAL	RMS MAX.
FINISH	SEE NOTES

TITLE	
XYR LASER 2000 PO 1004704	
SIZE	DWG NO
B	0010-02671
REV	E2
SCALE	ALIO STD TEMPLATE - REV 006
SHEET	1 OF 1



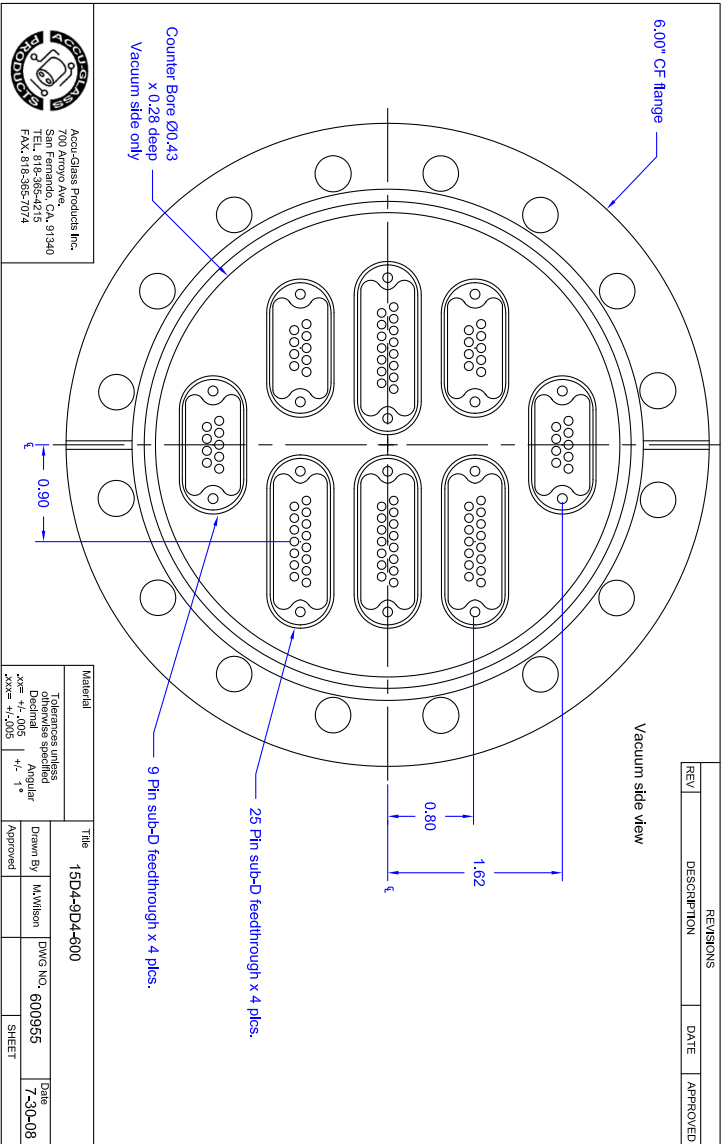
ALIO INDUSTRIES PROPRIETARY INFORMATION  
 11919 W I-70 FRONTAGE ROAD NORTH, UNIT 119, WHEAT RIDGE, CO 80033 USA  
 (Tel) 303.339.7500 - SALES@ALIOINDUSTRIES.COM - WWW.ALIOINDUSTRIES.COM

NOTES: UNLESS OTHERWISE SPECIFIED,  
 1. REF QUOTE: L2G-BERGEN 2010-11-02 r02  
 PO: 1004704

- ALL STAGES SHOWN AT MID-STROKE POSITION. SEE INDIVIDUAL STAGE DATASHEETS FOR STAGE AND MOUNTING DETAILS.
- ALL STAGES UHV.
- ALL VACUUM MOTOR AND ENCODER CABLES ARE 1.5 METERS LONG.
- CUSTOMER MUST SIGNOFF VACUUM FEED THROUGH DRAWING P/N: 600955 WITH THIS DATASHEET.
- Z STAGE PAYLOAD IS ????. Z STAGE PAYLOAD MAY NOT VARY BY MORE THAN 0.15 KG OF LISTED PAYLOAD WITHOUT RISK TO THE Z MOTOR INTEGRITY.
- ROTARY PAYLOAD CENTER OF GRAVITY MUST BE ON THE ROTARY AXIS CENTERLINE.

DESIGN APPROVAL

PRINT NAME \_\_\_\_\_  
 SIGNATURE FOR APPROVAL \_\_\_\_\_  
 DATE OF APPROVAL \_\_\_\_\_  
 PLEASE FAX APPROVED COPY TO 303-339-7501, THANK YOU.



REVISIONS		
REV	DESCRIPTION	DATE

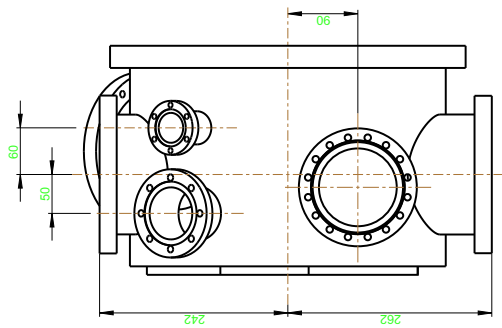
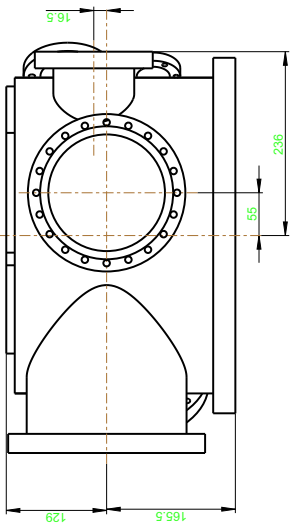
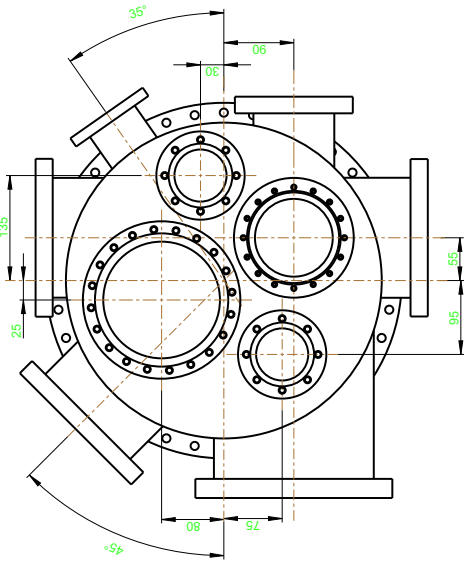
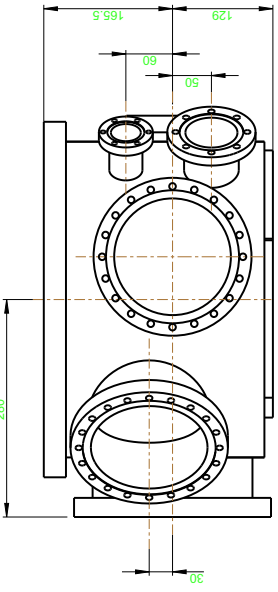
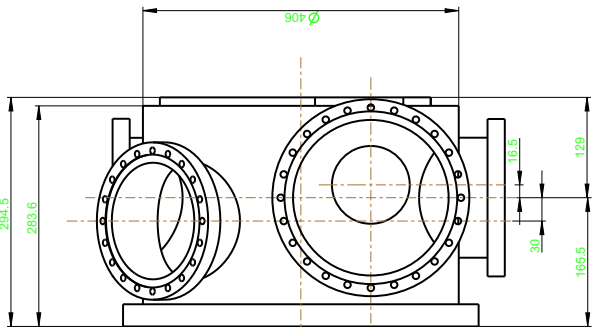
Material		The		15D4-9D4-600		Date
Tolerances unless otherwise specified		Drawn By		DWG NO.		7-30-08
xxmm ±.005	Angular	M.Wilson		600935		
xxdeg ±.25/30	+/- 1°	Approved		SHEET		


  
 Accu-Glass Products Inc.  
 700 Arroyo Ave.  
 San Fernando, CA 91340  
 TEL: 818-366-4215  
 FAX: 818-366-0714

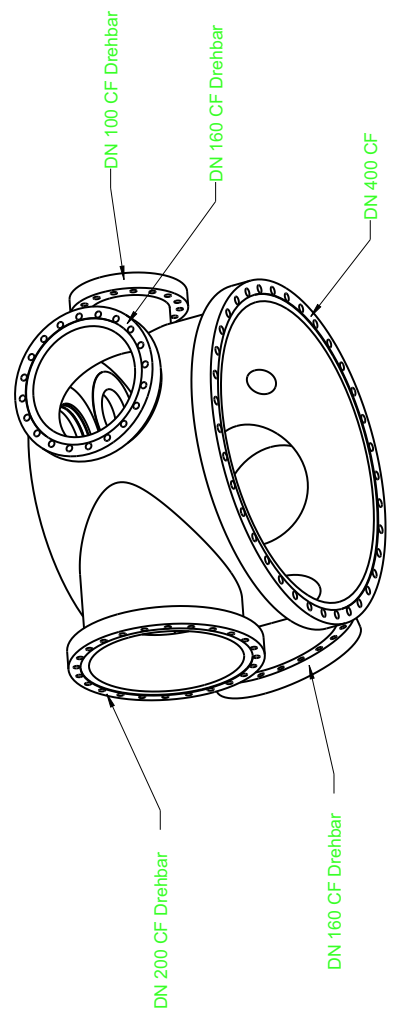
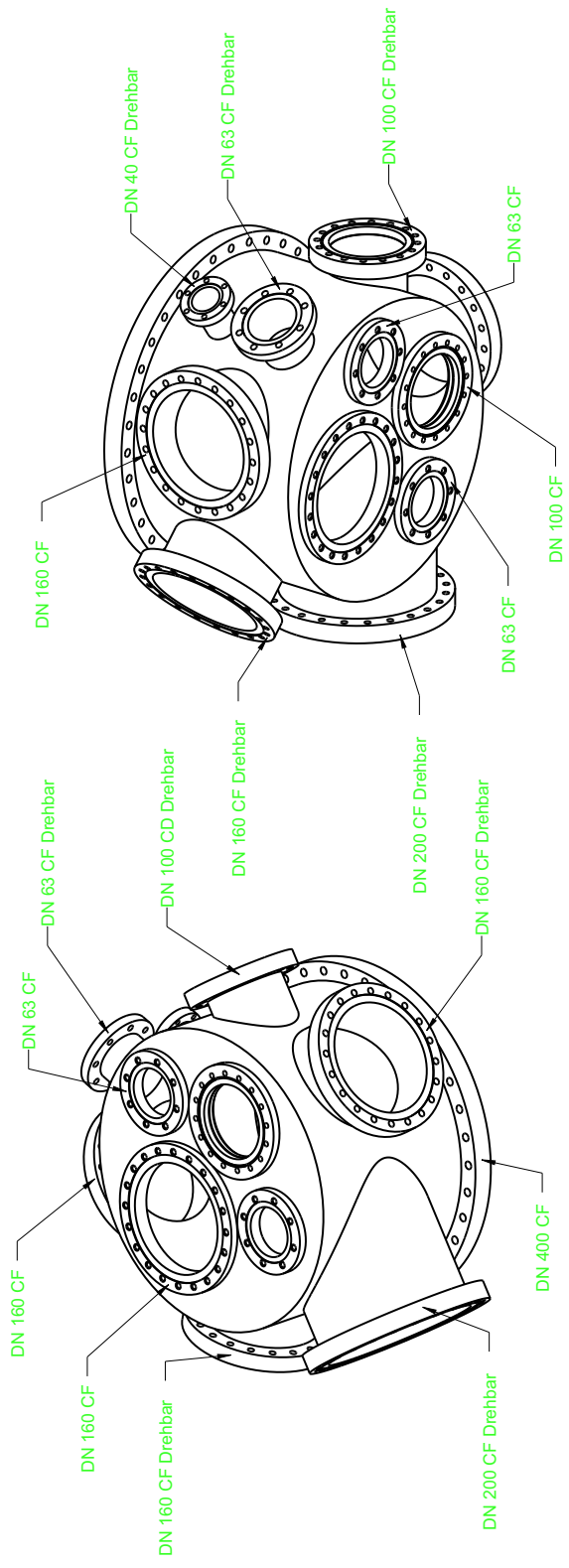


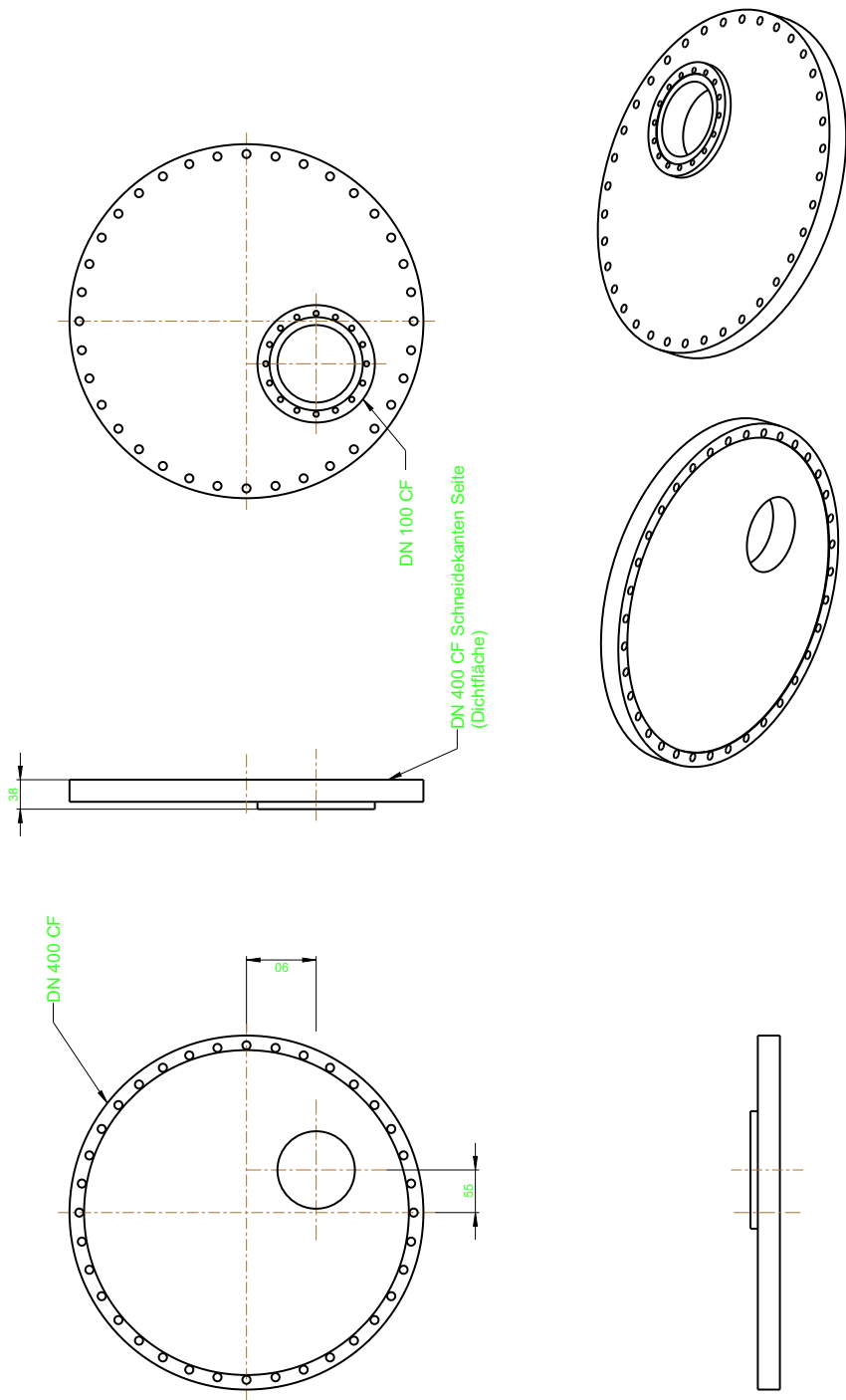
B.1.5 *Sample chamber*

Item No.	280	Draw No.	1
Item Qty	1	Draw No.	1
Description	Sampechamber_A	Draw No.	1
Specification		Draw No.	1
Approval		Draw No.	1
Checked		Draw No.	1
Drawn		Draw No.	1
Scale		Draw No.	1
Sheet No./Total No. of Sheet	1/1	Draw No.	1
Rev.	1	Draw No.	1
Author	Wahid Hidayat	Draw No.	1
Checker	Wahid Hidayat	Draw No.	1
Drawn	Wahid Hidayat	Draw No.	1
Scale		Draw No.	1
Sheet Size	A3	Draw No.	1











## APPENDIX PRESSURE GAUGES

---

### C.1 APPENDIX SPECIFICATIONS PRESSURE MEASUREMENT GAUGES

There are two different systems providing the pressure measurements for NEMI. Both of them are from PFEIFFER Vacuum and correspond to the so called “**Active Line**” and “**Modul Line**” of this manufacturer. The *active line* instruments are connected to a **Maxi Gauge TPG 256 A** controller for 6 transmitters, whereas the *Modul line* instruments have the **TPG-300** controller unit. Each of the two control units additionally provide RS-232 connection ports for external access.

#### C.1.1 *Prevacuum gauges*

There are two different types of prevacuum gauges used for the microscope. One is the *active-line pirani* transmitter from PFEIFFER VACUUM and the other one is a *pirani* gauge head from the same company but the *module-line* version. Both instruments have a *gas-type dependence constant* of  $k=0.8$  in the area  $< 1$  mbar.

##### C.1.1.1 *TPR-280 Active pirani transmitter*

This pressure measurement gauge works on the basis of the *pirani* pressure measurement principle. The specifications of this instrument stated by the manufacturer are presented in the following table.

TPR 280 ACTIVE PIRANI TRANSMITTER SPECIFICATIONS			
Output signal: sensor error below	0.5 V	<b>Measurement range max.</b>	1000 mbar
Output signal: pressure range	2.2-8.5 V	<b>Measurement range min.</b>	$5 \cdot 10^{-4}$ mbar
Output signal: minimum load	10 kOhm	Temperature: operating	+5°C ÷ +60°C
Bake-out temperature	80°C	Temperature: storage	-20°C ÷ +65°C
Seal	metal	Supply: voltage	14-30 V DC
Pressure max.	10 bar	Supply: power consumption max.	1 W
Feed-through	glass	Repeatability: $10^{-3}$ - $10^{-2}$ mbar	±2 %
Flange	stainless steel	Flange (in)	DN 16 ISO-KF
Accuracy: $10^{-3}$ - $10^{-2}$ mbar	±15%	Weight	80 g
Filament	tungsten	Volume	1.5 cm <sup>3</sup>

### C.1.1.2 TPR-010 pirani gauge head

This type of prevacuum gauge is also based on the pirani principle and is from the *modul line*. Its specifications are listed below.

TPR 010 PIRANI GAUGE HEAD SPECIFICATIONS			
Bake-out temperature	100°C	<b>Measurement range max.</b>	1000 mbar
Operating temperature, standard sensor cable	0°C ÷ +70°C	<b>Measurement range min.</b>	$8 \cdot 10^{-4}$ mbar
Weight	0.14 kg	Filament/holder	T/Ni
Isolator	FPM	Chamber wall, inside	AlSiMg
Protective filter	sintered bronze	Flange (in)	DN 16 ISO-KF

### C.1.2 Ultra high vacuum gauges

There are four different types of UHV pressure measurement gauges in use for NEMI. They all have the same *gas-type dependency factor* being stated to be  $k=5,9$  for pressures in the range  $< 10^{-5}$  mbar.

#### C.1.2.1 IKR-270 Active cold cathode transmitter

The IKR 270 active cold cathode pressure gauge is an *active line* instrument. It is based on the cold cathode (inverted magnetron) measurement technique. The specification are listed in the following table.



IKR 270 ACTIVE COLD CATHODE TRANSMITTER SPECIFICATIONS			
Output signal: sensor error below	0.5 V	<b>Measurement range max.</b>	0.01 mbar
Output signal: pressure range	1.8-8.5 V	<b>Measurement range min.</b>	$5 \cdot 10^{-11}$ mbar
Output signal: minimum load	10 kOhm	Temperature: operating	+5°C ÷ +55°C
Bake-out temperature	250°C (electronic removed)	Temperature: storage	-40°C ÷ +65°C
Seal	Ag	Supply: voltage	15-30 V DC
Pressure max.	10 bar	Supply: power consumption max.	2 W
Feed-through	Al <sub>2</sub> O <sub>3</sub>	Repeatability: 10 <sup>-3</sup> -10 <sup>-2</sup> mbar	±5 %
Flange	stainless steel	Flange (in)	DN 40 CF-F
Accuracy: 10 <sup>-9</sup> -10 <sup>-3</sup> mbar	±30%	Weight	950 g
Filament	molybdenum	Volume	20 cm <sup>3</sup>

### c.1.1.2.2 PKR-251 Active pirani/cold cathode transmitter

For the PKR 251 *pirani/cold cathode* transmitter from the *active line*, a *cold cathode* transmitter is combined with a *pirani* principle based one to cover a wide pressure range from nearly ambient pressure down to the middle 10<sup>-9</sup> mbar range. The specification parameters provided by the manufacturer are listed below.

PKR 251 ACTIVE PIRANI/COLD CATHODE TRANSMITTER SPECIFICATIONS			
Output signal: sensor error above	9.5 V	<b>Measurement range max.</b>	1000 mbar
Output signal: sensor error below	0.5 V	<b>Measurement range min.</b>	$5 \cdot 10^{-9}$ mbar
Output signal: pressure range	1.8-8.6 V	Temperature: operating	+5°C ÷ +55°C
Output signal: minimum load	10 kOhm	Temperature: storage	-40°C ÷ +65°C
Bake-out temperature	150°C (electronic removed)	Supply: voltage	15-30 V DC
Seal	FPM	Supply: power consumption max.	2 W
Pressure max.	10 bar	Repeatability: 10 <sup>-3</sup> -10 <sup>-2</sup> mbar	±5 %
Feed-through	Al <sub>2</sub> O <sub>3</sub> , glass	Flange (in)	DN 40 CF-F
Flange	stainless steel	Weight	950 g
Accuracy: 10 <sup>-8</sup> -10 <sup>-2</sup> mbar	±30%	Volume	20 cm <sup>3</sup>
Filament ( <i>pirani/cold cathode</i> )	tungsten/molybdenum	Feature	interior FPM sealed

### c.1.1.2.3 IKR-060/IKR-070 Cold cathode gauge heads

The pressure measurement gauges utilized for the two detection systems (reflection/*in-line* transmission detector) are *module line* instruments. Both of them are connected to the **TPG 300 control unit** via the two corresponding **CP300TT1 measurement boards** which hold one *cold cathode* and one *pirani* gauge connection each. Additionally a third measurement board provides a *RS-232 interface* for external control. Hence it is possible to read out all pressure pa-

rameters via a LABVIEW program. The two sets of instrument specifications regarding the gauges are listed in the tables below.

IKR 060 COLD CATHODE GAUGE HEAD SPECIFICATIONS			
Bake-out temperature	250°C	<b>Measurement range max.</b>	$5 \cdot 10^{-3}$ mbar
Operating temperature, standard sensor cable	5°C ÷ +80°C	<b>Measurement range min.</b>	$1 \cdot 10^{-10}$ mbar
Weight	0.85 kg	Isolator	Al <sub>2</sub> O <sub>3</sub>
Internal seal	silver	Radiation resistance	$1 \cdot 10^7$ Gy
Flange	stainless steel	Flange (in)	DN 40 CF-F

IKR 070 COLD CATHODE GAUGE HEAD SPECIFICATIONS			
Bake-out temperature	250°C	<b>Measurement range max.</b>	$5 \cdot 10^{-3}$ mbar
Operating temperature, standard sensor cable	5°C ÷ +80°C	<b>Measurement range min.</b>	$1 \cdot 10^{-11}$ mbar
Weight	0.85 kg	Isolator	Al <sub>2</sub> O <sub>3</sub>
Internal seal	silver	Radiation resistance	$1 \cdot 10^7$ Gy
Flange	stainless steel	Flange (in)	DN 40 CF-F

## APPENDIX PREVACUUM

## D.1 TYPES OF FLOW REGIMES

There are basically three types of possible flow regimes. Table D.1 states the main properties of them.

VISCOUS FLOW	<b>Low vacuum</b>	$D/\lambda > 110$
INTERMEDIATE FLOW (KNUDSEN)	<b>Fine vacuum</b>	$1 < D/\lambda < 110$
MOLECULAR FLOW	<b>High vacuum</b>	$D/\lambda < 110$

$\lambda$ ...*mean-free-path* stands for the average distance traversed by all the molecules between successive collision with each other, or the average distance traversed between successive collision by the same molecule, in a given time. [60]

With  $T = \text{const.}$ :

$$\lambda \cdot p = \text{const.} = C^* \quad (\text{D.1})$$

where  $p$  stands for the pressure and  $C^*$  is a temperature dependent characteristic value for each gas (see [60]).

$$C_{He}^* = 18 \cdot 10^{-3} \text{ cm} \cdot \text{mbar}$$

Low vacuum	Fine vacuum	High vacuum
particle interaction	Knudsen flow	particle can move without interaction
$\lambda \ll D$	$\lambda \approx D$	$\lambda \gg D$
internal friction (viscosity)	crossover	conductance
laminar / turbulent	viscous-flow / molecular-flow	$C_m \neq f(p)$

Table D.1: Basic properties of the three different flow regimes. The character  $D$  is the pipe/tube diameter and  $\lambda$  is the mean free path length.

$$C_{Air}^* = 6.67 \cdot 10^{-3} \text{ cm} \cdot \text{mbar}$$

⇒ with  $T = 293 \text{ K}$  and  $p = 5 \cdot 10^{-2} \text{ mbar}$  :

$$\lambda_{He(293 \text{ K})} = \frac{C_{He}^*}{p} = 3.6 \cdot 10^{-3} \text{ m} \quad (\text{D.2})$$

For the pipe/tube diameters used in the prevacuum system, the flow regime of NEMI is the **KNUDSEN FLOW REGIME**.  $D/\lambda$  numbers for the most common diameters are listed below.

$D = 50 \text{ mm} \rightarrow \frac{D}{\lambda} = \frac{5 \cdot 10^{-2}}{3,6 \cdot 10^{-3}} \approx 13.8$	<b>Knudsen Regime !</b>
$D = 40 \text{ mm} \rightarrow \frac{D}{\lambda} = \frac{4 \cdot 10^{-2}}{3,6 \cdot 10^{-3}} \approx 11.11$	
$D = 25 \text{ mm} \rightarrow \frac{D}{\lambda} = \frac{2,5 \cdot 10^{-2}}{3,6 \cdot 10^{-3}} \approx 6.9$	

## D.2 INTERMEDIATE - KNUDSEN FLOW

This sections presents the evaluation of the flow regime type for the prevacuum system of *Nemi*. It describes characteristic values and transition points between the viscous and the molecular flow.

### D.2.1 Knudsen's Equation

The conductivity  $C$  [ $\text{l} \cdot \text{s}^{-1}$ ] for a tube in any regime (molecular, intermediate or viscous) is defined by the **KNUDSEN-equation** [60].

$$C = \frac{\pi}{128 \cdot \eta} \cdot \frac{D^4}{L} \cdot \bar{p} + \frac{1}{6} \cdot \left( \frac{2\pi R_o T}{M} \right)^{1/2} \cdot \frac{D^3}{L} \cdot \frac{1 + \left( \frac{M}{R_o T} \right)^{1/2} \cdot D \cdot \frac{\bar{p}}{\eta}}{1 + 1.24 \cdot \left( \frac{M}{R_o T} \right)^{1/2} \cdot D \cdot \frac{\bar{p}}{\eta}} \quad (\text{D.3})$$

with

$$\eta = 0.177 \cdot \bar{p} \cdot \left( \frac{M}{T} \right)^{1/2} \cdot \lambda \quad (\text{D.4})$$

in this equation  $C$  stands for the conductivity [ $\text{l} \cdot \text{s}^{-1}$ ],  $\lambda$  is the mean free path [cm],  $D$  the tube diameter [cm],  $L$  the tube length [cm],  $\eta$  the coefficient of viscosity [poise],  $\bar{p}$  the average pressure [torr],  $R_o$  the universal gas constant ( $R_o = 6.236 \cdot 10^4 \frac{\text{Torr} \cdot \text{cm}^3}{\text{K} \cdot \text{mol}}$ ),  $T$  the temperature [K],

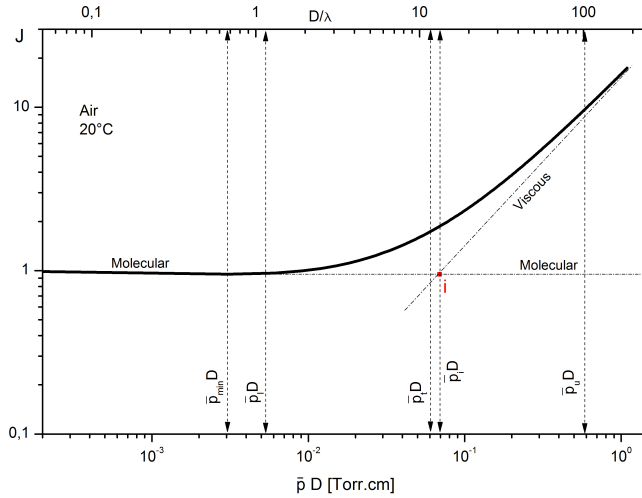


Figure D.1:  $J$  as a function of  $\bar{p} \cdot D$  and the various characteristic values of the different flow regimes. (Figure drawn corresponding to [60])

and  $M$  the molecular weight [ $\text{g} \cdot \text{mol}^{-1}$ ] ( $M_{\text{He}} = 4.003$ ,  $M_{\text{Air}} = 28.98$ )

More information regarding the origin of this equation can be found in chapter D.3 and [60].

### D.2.2 Minimum conductance

Figure D.1 shows a diagram created corresponding to the formulas from [60]. It should provide an illustration for the following considerations. Within the next subsections several specific pressure values for characteristic points from the diagram shown in figure D.1 are discussed. These values and the parameters which are defining them are evaluated following the same basic equations D.5, D.6 and D.7.

$$\bar{p}_x \cdot D = \text{const} \cdot \left(\frac{T}{M}\right)^{1/2} \cdot \eta \quad [\text{Torr} \cdot \text{cm}] \quad (\text{D.5})$$

$$\eta = 0.117 \cdot \bar{p}_x \cdot \left(\frac{M}{T}\right)^{1/2} \cdot \lambda \quad (\text{D.6})$$

$$\lambda = \frac{C^*}{\bar{p}_x} \quad (\text{D.7})$$

with  $C_{He}^*$  the characteristic value for HELIUM [Torr · cm],  $\lambda$  the mean free path [cm],  $D$  the tube diameter [cm],  $\eta$  the coefficient of viscosity [poise],  $\bar{p}_x$  the characteristic pressure value at the point of interest [torr],  $T$  the temperature [K], and  $M$  the molecular weight [ $\text{g} \cdot \text{mol}^{-1}$ ] ( $M_{He} = 4.003$ ,  $M_{Air} = 28.98$ )

They are varying just by different values for the constant. Due to historical reasons the units used in the literature are not standard SI-units. To stay consistent the following equations are also presented in the same non-SI units.

The transition point between molecular flow and intermediate flow is defined by the minimum conductance parameters. The parameter defining this minimum conductance point  $\bar{p}_{min}$  is defined as stated in equations D.5-D.7 with

$$\begin{aligned} \bar{p}_x &\triangleq \bar{p}_{min} \\ const &= 5.47 \end{aligned}$$

For our system the minimum conductance point for He at  $T = 293 \text{ K}$  is of interest<sup>1</sup>.

$$\begin{aligned} \bar{p}_{min} \cdot D &= 5.47 \cdot \left(\frac{T}{M}\right)^{1/2} \cdot 0.177 \cdot \bar{p}_{min} \cdot \left(\frac{M}{T}\right)^{1/2} \cdot \frac{C_{He}^*}{\bar{p}_{min}} \\ &= 8.6398 \cdot 10^{-3} \text{ Torr} \cdot \text{cm} \end{aligned} \quad (\text{D.8})$$

with  $\bar{p}_{min}$  the average pressure at the minimum conductance point [torr].

### D.2.3 Transition pressure

The transition pressure  $\bar{p}_t$  defines the value of pressure for which the viscous part of equation D.3 is equal to its non-viscous fraction. Therefore the transition point pressure describes a mixture of viscous and non-viscous flow. It is situated somewhere in the middle range of the intermediate flow regime as shown in figure D.1. The corresponding equations for the transition point and its pressure value  $\bar{p}_t$  can be found by inserting

$$\begin{aligned} \bar{p}_x &\triangleq \bar{p}_t \\ const &= 95.7 \end{aligned}$$

in equation D.5-D.7.

<sup>1</sup> The corresponding  $C_{He}^*$  stated in section D.1.

For He at  $T = 293$  K:

$$\begin{aligned}\bar{p}_t \cdot D &= 95.7 \cdot \left(\frac{T}{M}\right)^{1/2} \cdot 0.177 \cdot \bar{p}_t \cdot \left(\frac{M}{T}\right)^{1/2} \cdot \frac{C_{He}^*}{\bar{p}_t} \\ &= 15.11 \cdot 10^{-2} \text{ Torr} \cdot \text{cm}\end{aligned}\quad (\text{D.9})$$

with  $\bar{p}_t$  the average transition point pressure [torr].

#### D.2.4 Limits of the intermediate range

If one of the flow conditions predominates, meaning that its influence is of an order of one magnitude more important than the other, we find the corresponding transition point. Hence flow above the upper limit of the intermediate range can be considered as viscous, and flow below the lower limit of intermediate range as molecular flow, respectively [60].

##### Upper limit intermediate range

Is found by solving equations D.5-D.7 with

$$\begin{aligned}\bar{p}_x &\triangleq \bar{p}_u \\ \text{const} &= 942\end{aligned}$$

For He at  $T = 293$  K:

$$\begin{aligned}\bar{p}_u \cdot D &= 942 \cdot \left(\frac{T}{M}\right)^{1/2} \cdot 0.177 \cdot \bar{p}_u \cdot \left(\frac{M}{T}\right)^{1/2} \cdot \frac{C_{He}^*}{\bar{p}_u} \\ &= 14.8 \cdot 10^{-1} \text{ Torr} \cdot \text{cm}\end{aligned}\quad (\text{D.10})$$

with  $\bar{p}_u$  the average upper limit pressure [torr].

Since this value is of particular interest for the layout of the prevacuum system, the following listing present the calculated upper limit pressure values for the most commonly used prevacuum pipe diameters, (ISO-K DN63, KF-DN50, KF-DN40, KF-DN25).

$D = 66 \text{ mm}$	$\bar{p}_u = 2.9 \cdot 10^{-1} \text{ [mbar]}$	$\bar{p} > 2.9 \cdot 10^{-1} \text{ [mbar]} \Rightarrow \text{viscous flow}$
$D = 50 \text{ mm}$	$\bar{p}_u = 3.9 \cdot 10^{-1} \text{ [mbar]}$	$\bar{p} > 3.9 \cdot 10^{-1} \text{ [mbar]} \Rightarrow \text{viscous flow}$
$D = 40 \text{ mm}$	$\bar{p}_u = 4.9 \cdot 10^{-1} \text{ [mbar]}$	$\bar{p} > 4.9 \cdot 10^{-1} \text{ [mbar]} \Rightarrow \text{viscous flow}$
$D = 25 \text{ mm}$	$\bar{p}_u = 6.9 \cdot 10^{-1} \text{ [mbar]}$	$\bar{p} > 6.9 \cdot 10^{-1} \text{ [mbar]} \Rightarrow \text{viscous flow}$

*Lower limit intermediate range*

For the lower limit of the intermediate range the parameters are:

$$\begin{aligned}\bar{p}_x &\triangleq \bar{p}_l \\ \text{const} &= 10\end{aligned}$$

For He at  $T = 293$  K:

$$\begin{aligned}\bar{p}_l \cdot D &= 10 \cdot \left(\frac{T}{M}\right)^{1/2} \cdot 0.177 \cdot \bar{p}_l \cdot \left(\frac{M}{T}\right)^{1/2} \cdot \frac{C_{\text{He}}^*}{\bar{p}_l} \\ &= 1.5 \cdot 10^{-2} \text{ Torr} \cdot \text{cm}\end{aligned}\tag{D.11}$$

with  $\bar{p}_l$  the average lower limit pressure [torr].

A listing presents the lower limit pressure values of the intermediate flow range for the most common pipe diameters (ISO-K DN63, KF-DN50, KF-DN40, KF-DN25).

$D = 66 \text{ mm}$	$\bar{p}_l = 3.0 \cdot 10^{-3} \text{ [mbar]}$	$\bar{p} < 3.0 \cdot 10^{-3} \text{ [mbar]} \Rightarrow \text{molecular flow}$
$D = 50 \text{ mm}$	$\bar{p}_l = 4.0 \cdot 10^{-3} \text{ [mbar]}$	$\bar{p} < 4.0 \cdot 10^{-3} \text{ [mbar]} \Rightarrow \text{molecular flow}$
$D = 40 \text{ mm}$	$\bar{p}_l = 5.0 \cdot 10^{-3} \text{ [mbar]}$	$\bar{p} < 5.0 \cdot 10^{-3} \text{ [mbar]} \Rightarrow \text{molecular flow}$
$D = 25 \text{ mm}$	$\bar{p}_l = 8.0 \cdot 10^{-3} \text{ [mbar]}$	$\bar{p} < 7.99 \cdot 10^{-3} \text{ [mbar]} \Rightarrow \text{molecular flow}$

The intermediate flow range of *helium* therefore extends from ca.  $\bar{p}_u = 7 \cdot 10^{-1} \text{ [mbar]}$  down to ca.  $\bar{p}_l = 3 \cdot 10^{-3} \text{ [mbar]}$ , in other words it extends over a pressure range of app. two orders of magnitude.

#### D.2.5 *The molecular-viscous intersection point*

Figure D.1 depicts point *i* as the intersection point of the line representing the viscous flow, with the one representing the molecular flow. The position of this molecular-viscous intersection point *i* is specific for the kind of gas and its temperature, and it corresponds to  $C_v = C_m$ , with  $C_v$  the conductance for viscous flow and  $C_m$  the one for molecular flow [60]. On that condition it follows that

$$\frac{C_v}{C_m} = 1$$

Together with the equations D.5-D.7 and



$$\bar{p}_x \triangleq \bar{p}_i$$

$$\text{const} = 116$$

one finds for He at  $T = 293 \text{ K}$ :

$$\begin{aligned} \bar{p}_i \cdot D &= 116 \cdot \left(\frac{T}{M}\right)^{1/2} \cdot 0.177 \cdot \bar{p}_i \cdot \left(\frac{M}{T}\right)^{1/2} \cdot \frac{C_{He}^*}{\bar{p}_i} \\ &= 1.83 \cdot 10^{-1} \text{ Torr} \cdot \text{cm} \end{aligned} \quad (\text{D.12})$$

with  $\bar{p}_i$  the intersection point pressure [torr].

The corresponding values for the most common used pipe diameters are:

$D = 66 \text{ mm}$	$\bar{p}_i = 3.59 \cdot 10^{-2} \text{ [mbar]}$
$D = 50 \text{ mm}$	$\bar{p}_i = 4.87 \cdot 10^{-2} \text{ [mbar]}$
$D = 40 \text{ mm}$	$\bar{p}_i = 5.99 \cdot 10^{-2} \text{ [mbar]}$
$D = 25 \text{ mm}$	$\bar{p}_i = 9.73 \cdot 10^{-2} \text{ [mbar]}$

### D.3 GENERAL EQUATION KNUDSEN FLOW

In general the conductance can be written as [60]:

$$C = C_m \cdot J \quad (\text{D.13})$$

In this equation  $C_m$  is the conductance for molecular flow.  $J$  is defined as

$$J = \frac{C_v}{C_m} + \frac{1 + \left(\frac{M}{R_0 T}\right)^{1/2} \cdot D \cdot \frac{\bar{p}}{\eta}}{1 + 1.24 \cdot \left(\frac{M}{R_0 T}\right)^{1/2} \cdot D \cdot \frac{\bar{p}}{\eta}} \quad (\text{D.14})$$

$C_v$  is the conductance for viscous flow:

$$C_v = \frac{\pi}{128 \cdot \eta} \cdot \frac{D^4}{L} \cdot \bar{p} \quad (\text{D.15})$$

and  $C_m$  can be determined from

$$C_m = \left(\frac{1}{6}\right) \cdot \left[\frac{2\pi R_0 T}{M}\right]^{1/2} \cdot \left(\frac{D^3}{L}\right) \quad (\text{D.16})$$

with  $C$  the conductivity [ $\text{ls}^{-1}$ ],  $D$  the tube diameter [cm],  $L$  the tube length [cm],  $\eta$  the coefficient of viscosity [poise],  $\bar{p}$  the average pressure [Torr],  $R_0$  the universal gas constant ( $R_0 = 6.236 \cdot 10^4 \frac{\text{Torr} \cdot \text{cm}^3}{\text{K} \cdot \text{mol}}$ ),  $T$  the temperature [K], and  $M$  the molecular weight [ $\text{g} \cdot \text{mol}^{-1}$ ] ( $M_{\text{He}} = 4.003$ ,  $M_{\text{Air}} = 28.98$ )

In the molecular range the conductance is independent from the pressure, therefore  $J$  becomes  $J = 1$ . The above mentioned equation for  $J$  (eq.:D.14) can also be written as:

$$J = \delta + \frac{1 + 17 \cdot \delta}{1 + 21 \cdot \delta} \quad (\text{D.17})$$

This equation is valid for any gas at any temperature.  $\delta$  is the ratio

$$\delta = \frac{\bar{p} \cdot D}{(\bar{p} \cdot D)_i} \quad (\text{D.18})$$

#### D.4 CONDUCTANCE $c_m$ MOLECULAR FLOW FOR DIFFERENT COMPONENTS

To calculate the conductance of a component we need to calculate its molecular flow conductance first. The following formulas define  $C_m$  for different components and can be found in[60].

##### D.4.1 *Molecular flow conductance of an aperture*

The molecular flow conductance of an aperture  $C_{mA}$  of the area  $A$  [ $\text{cm}^2$ ] is given by

$$\begin{aligned} C_{mA} &= 3.64 \cdot 10^3 \cdot \left(\frac{T}{M}\right)^{1/2} \cdot A \text{ [cm}^3/\text{s]} \\ &= 3.64 \cdot \left(\frac{T}{M}\right)^{1/2} \cdot A \text{ [ls}^{-1}\text{]} \end{aligned}$$

and if the opening is of circular cross section,  $A = \frac{D^2 \cdot \pi}{4}$

$$C_{mA} = 2.86 \cdot \left(\frac{T}{M}\right)^{1/2} \cdot D^2 \text{ [l} \cdot \text{s}^{-1}\text{]} \quad (\text{D.19})$$

with  $D$  the diameter [cm],  $M$  the molecular weight [ $\text{g} \cdot \text{mol}^{-1}$ ] ( $M_{\text{He}} = 4.003$ ,  $M_{\text{Air}} = 28.98$ ) and  $T$  the temperature [K].

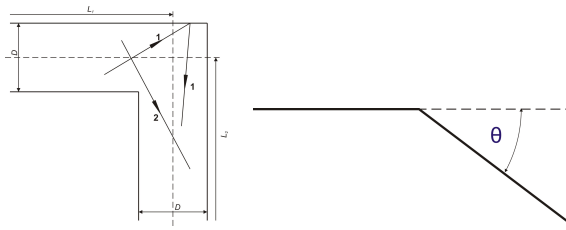


Figure D.2: Molecular flow through an elbow piece (right), and definition of the elbow angle  $\theta$ .

#### D.4.2 Molecular flow conductance of a tube of constant cross section

The conductance of long tubes ( $l \geq 10 \cdot D$ ) at low pressures  $C_{mT}$  (molecular flow) with a uniform circular cross section  $A$  [ $\text{cm}^2$ ] is

$$C_{mT} = 3.81 \cdot \left(\frac{T}{M}\right)^{1/2} \cdot \frac{D^3}{L} \quad (\text{D.20})$$

with  $D$  the tube diameter [ $\text{cm}$ ],  $L$  the tube length [ $\text{cm}$ ],  $M$  the molecular weight [ $\text{g} \cdot \text{mol}^{-1}$ ] and  $T$  the temperature [ $\text{K}$ ].

#### D.4.3 Molecular flow conductance of a short tube of constant cross section

An additional factor of  $1,33 \cdot D$  is added into equation D.20 to consider the *end effect* for a tube length decreasing against zero. Hence the molecular flow conductance of a short tube  $C_{mTs}$  is

$$C_{mTs} = 3.81 \cdot \left(\frac{T}{M}\right)^{1/2} \cdot \frac{D^3}{L + 1.33 \cdot D} \quad (\text{D.21})$$

with  $D$  the tube diameter [ $\text{cm}$ ],  $L$  the tube length [ $\text{cm}$ ],  $M$  the molecular weight [ $\text{g} \cdot \text{mol}^{-1}$ ] and  $T$  the temperature [ $\text{K}$ ].

#### D.4.4 Molecular flow conductance - elbows

The molecular flow passing through an elbow piece is pictured as molecules traveling through the elbow on two different paths (see figure D.2). Therefore

the elbow can be represented as a tube with the diameter  $D$ , and an equivalent length  $L_e$  with the boundary condition of

$$L_{ax} < L_e < (L_{ax} + 1.33 \cdot D)$$

where  $L_{ax} = L_1 + L_2$  is the length measured along the axis of the elbow. The elbow angle is given by the variable  $\theta$  (see figure D.2 right). Thus the equivalent length is

$$L_e = L_{ax} + 1.33 \cdot \frac{\theta}{180^\circ} \cdot D \quad (\text{D.22})$$

and the molecular flow conductance of an elbow  $C_{mEL}$  becomes

$$C_{mEL} = 3.81 \cdot \left(\frac{T}{M}\right)^{1/2} \cdot \frac{D^3}{L_e} \quad (\text{D.23})$$

with  $D$  the tube diameter [cm],  $L_e$  the equivalent tube length [cm],  $M$  the molecular weight [ $\text{g} \cdot \text{mol}^{-1}$ ] ( $M_{He} = 4.003$ ) and  $T$  the temperature [K].

#### D.5 CONDUCTANCE $c$ INTERMEDIATE (KNUDSEN) FLOW REGIME

Combining the general KNUDSEN flow equations from section D.3 with the molecular flow conductance equations from section D.4, the conductance values for our prevacuum system can be determined. From the evaluation of the lower- and upper-limit pressure values for the KNUDSEN regime (see sections D.2.4, D.2.4) it can be reasoned that our backing pump system will mainly work in the KNUDSEN flow range (intermediate).

The calculation for each prevacuum component's conductance value  $C$  is performed following the equations D.13, D.17, D.18 combined with the corresponding molecular flow conductance values  $C_m$ .

The values evaluated for the implemented prevacuum components are listed in the tables representing the setups of the two prevacuum lines used for NEMI i.e. table D.2, D.3 and D.4 respectively.

D.6 TOTAL CONDUCTANCE  $c_{total}$  OF AN INTERMEDIATE FLOW REGIME VACUUM SYSTEM

For vacuum systems which consist of more than one vacuum component, the corresponding conductance values have to be added up. It has to be distinguished between a *serial* and a *parallel* connection of the system parts, similar to the treatment of electrical connections.

For a *serial* connection the overall (total) conductance value  $C_{serial}$  is defined as ( see [60])

$$C_{serial} = \frac{1}{C_1} + \frac{1}{C_2} + \frac{1}{C_3} + \dots + \frac{1}{C_n} \quad (D.24)$$

and in the *parallel* connected case  $C_{parallel}$

$$C_{parallel} = C_1 + C_2 + C_3 + \dots + C_n \quad (D.25)$$

For the final determination of the effective *pumping speed* of the vacuum system, additionally the characteristics of the assembled pumps have to be taken into account. The adequate pump property is the pumps own *Pumping Speed*  $S_p$ , which is specified by the pump manufacturer. The systems *effective pumping speed*  $S_{eff}$  is defined as (see [60])

$$\frac{1}{S_{eff}} = \frac{1}{S_p} + \frac{1}{C_{total}} \quad (D.26)$$

## D.7 CONDUCTANCE PREVACUUM LINE SOURCE CHAMBER (SC)

Graphic 2.14 shows a sketch of the setup for the SC prevacuum line. The pictured components and their corresponding KNUDSEN FLOW properties are listed in table D.2.

The components are presented with their corresponding molecular flow conductance values  $C_m$  as well as with the conductance values  $C$  for the KNUDSEN FLOW regime. They are listed in the order of their connection sequence starting from the turbo molecular pumps. In the end the total value for the vacuum conductance  $C_{total}$  is calculated by considering the setup of the components in parallel and serial connection. Thus  $C_{T_1}$  and  $C_{T_2}$  are the two separate lines connecting each of the two MAG W 600 with the final SC prevacuum line

( $C_{pv_3}$ ), respectively. This means  $C_{T_1}$  and  $C_{T_2}$  are connected parallel and the resulting altogether value  $C_{T_{1,2,parallel}}$  is combined in serial connection with the following pipe system represented by  $C_{pv_3}$ .

$$\begin{aligned}
 C_{T_1} &= \left( \frac{1}{C_1} + \frac{1}{C_2} + \dots + \frac{1}{C_n} \right)^{-1} \rightarrow \text{serial} \\
 C_{T_2} &= \left( \frac{1}{C_1} + \frac{1}{C_2} + \dots + \frac{1}{C_n} \right)^{-1} \rightarrow \text{serial} \\
 C_{T_{1,2,parallel}} &= C_{T_1} + C_{T_2} \rightarrow \text{parallel} \\
 C_{total} &= \left( \frac{1}{C_{T_{1,2,parallel}}} + \frac{1}{C_{pv_3}} \right)^{-1} \rightarrow \text{serial}
 \end{aligned} \tag{D.27}$$

The corresponding effective pumping speed  $S_{eff}$  of the system is

$$\frac{1}{S_{eff}} = \frac{1}{S_p} + \frac{1}{C_{total}} \tag{D.28}$$

where  $S_p$  represents the pumping speed value of the SCROLLVAC prevacuum pump, which is given by  $S_{p1} = 26.3 \text{ m}^3 \text{ h}^{-1} \cong 7.3 \text{ ls}^{-1}$ . There are two of the SCROLLVAC SC30 D backing pumps used for the SC due to the high helium flow, hence  $S_p = 52.3 \text{ m}^3 \text{ h}^{-1} \cong 14.6 \text{ ls}^{-1}$ . The effective pumping speed of the source chamber prevacuum system is  $S_{eff}$  is:

$$S_{eff_{SC}} = 5.778 \text{ ls}^{-1} \tag{D.29}$$

The expected rise in the prevacuum pressure  $\bar{p}_{prevac_{SC}}$  due to the *helium* particle flow penetrating through the chambers turbopumps into the backing pump system can be calculated with the chamber flow rate from section 2.2.3.1,  $\dot{N}_o$  (see equation 2.33) and the effective pumping speed of the prevacuum system,  $S_{eff_{SC}}$ .

WUTZ, [62] states that the particle flow,  $\dot{N} = q_N [\text{s}^{-1}]$  is defined as

$$\dot{N} = \frac{\Delta N}{\Delta t} \tag{D.30}$$

The pressure-volume flow  $q_{pV}$  can be written as

$$q_{pV} = p \cdot \dot{V} \left[ \frac{\text{Pa} \cdot \text{m}^3}{\text{s}} \right] \tag{D.31}$$

$$\dot{N} = q_N = \frac{q_{pV}}{k \cdot T} \tag{D.32}$$


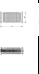

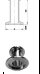

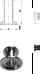
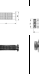




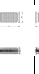
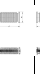
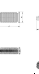






PREVACUUM LINE COMPONENTS SOURCE CHAMBER (SC)				
Component	Dimensions	$C_m$ [ $l\cdot s^{-1}$ ]	$C$ [ $l\cdot s^{-1}$ ]	Component Code
 KF25-KF50 adapter	$D_1=50\text{ mm}, D_2=25\text{ mm}$	83	111	KF50R25-304
 KF50 flexible hose	$D=50\text{ mm}, L=1\text{ m}$	41	75	FX50K100-304
 KF50 valve	$D=50\text{ mm}$		80	XLH 50
$C_{T1,2,parallel}$				
 KF25-KF50 adapter	$D=25\text{ mm}$	83	111	KF50R25-304
 FK40 elbow 130°	$D=40\text{ mm}, \vartheta=130^\circ, L_{akt}=120\text{ mm}$	131	216	n.a.
 KF40 flexible hose	$D=40\text{ mm}, L=250\text{ mm}$	69	113	FX40K25-304
 KF50-KF40 adapter	$D_1=50\text{ mm}, D_2=40\text{ mm}$	257	421	KF50R40-304
 KF50 flexible hose	$D=50\text{ mm}, L=1\text{ m}$	41	75	FX50K100-304
 KF50 valve	$D=50\text{ mm}$		80	XLH 50
$C_{T2}$				
 KF50 4 way cross	$D=50\text{ mm}, L=140\text{ mm}$	424	797	X50K-304
 FK50 elbow 90°	$D=50\text{ mm}, \vartheta=90^\circ, L_{akt}=140\text{ mm}$	235	433	EL50K-304
 ISO-Ko80 to KF50 adapter	$D_1=81\text{ mm}, D_2=50\text{ mm}$	315	580	SK8050/CO
 ISO-K80 flexible hose	$D=81\text{ mm}, L=750\text{ mm}$	202	500	ISO80FX75
 ISO-K80 flexible hose	$D=81\text{ mm}, L=750\text{ mm}$	202	500	ISO80FX75
 ISO-K80 flexible hose	$D=81\text{ mm}, L=750\text{ mm}$	202	500	ISO80FX75
 ISO-K80 to KF50 adapter	$D_1=81\text{ mm}, D_2=50\text{ mm}$	315	580	SK8050/CO
 FK50 elbow 90°	$D=50\text{ mm}, \vartheta=90^\circ, L_{akt}=140\text{ mm}$	235	433	EL50K-304
 KF50 PVC hose	$D=50\text{ mm}, L=1,5\text{ m}$	27	50	PVC50
 KF50-KF40 adapter	$D_1=50\text{ mm}, D_2=40\text{ mm}$	257	421	KF50R40-304
 KF40 equal tee	$D=40\text{ mm}, L=130\text{ mm}$	227	405	TE40K-304
 KF40 PVC hose	$D=40\text{ mm}, L=1,5\text{ m}$	14	23	PVC40
$C_{T3}$				

Table D.2: Vacuum conductance values  $C_m$  and  $C$  for the prevacuum line at the source chamber (SC). (Figures provided by VACOM Vakuum Komponenten & Messtechnik GmbH, product catalog)

with  $k$  the Boltzmann constant  $k = 1.38065 \cdot 10^{-23}$  J/K, and  $T$  the temperature [K]

It is also known from [62], that the throughput  $\dot{Q}$  [ $\frac{\text{Pa} \cdot \text{m}^3}{\text{s}}$ ] of a pump and its pipe system is defined as

$$\dot{Q} = \bar{p} \cdot S_{eff} \quad (\text{D.33})$$

Combining above mentioned equations D.30, D.31, D.32 and D.33, one can find

$$\begin{aligned} q_{pV} &= \dot{Q} \\ \bar{p} &= \frac{\dot{N} \cdot k \cdot T}{S_{eff}} \end{aligned} \quad (\text{D.34})$$

and in the special case of our source chamber backing pump pressure  $\bar{p}_{prevac_{SC}}$

$$\bar{p}_{prevac_{SC}} = \frac{\dot{N}_o \cdot k \cdot T}{S_{eff_{SC}}} \quad (\text{D.35})$$

For a system setup with  $d_{Nozz} = 10 \mu\text{m}$ ,  $T_o = 100 \text{ K}$ ,  $p_o = 200 \text{ bar}$ , which will be a maximum pump load situation, we can find with equations 2.33, D.32 and D.35 that

$$\begin{aligned} \dot{N}_o &= 1.50 \cdot 10^{20} \text{ s}^{-1} \\ q_{pV} &= 6.21 \frac{\text{mbar} \cdot \text{l}}{\text{s}} \\ \bar{p}_{prevac_{SC}} &= 1.08 \text{ mbar} \end{aligned} \quad (\text{D.36})$$

Based on the pressure volume flow and the expected prevacuum pressure of the system, the possible end-pressure in the high vacuum chamber can be determined. For this calculation the compression ratio  $k_o$  of the turbo pump from manufacturer diagrams is used

$$k_o = \frac{\bar{p}_{prevac}}{p_{end}} \Rightarrow p_{end} = \frac{\bar{p}_{prevac}}{k_o} \quad (\text{D.37})$$

The diagrams provided with our pumps show a compression ratio of roughly  $k_o = 50$  at the above mentioned prevacuum pressure of  $\bar{p}_{prevac_{SC}} = 1.08 \text{ [mbar]}$ .



The end pressure in the source chamber under this starting conditions will be around

$$p_{end} \approx 2.15 \cdot 10^{-2} [\text{mbar}] \quad (\text{D.38})$$

This value is pretty high, but the starting conditions are a rather worst case scenario. With this setup though, the helium flow within the source chamber is too high for a proper *free-jet-expansion* of the helium beam. The pumping system is not able to cope with the helium flow arising in the chamber. Hence too much particle interaction of the helium atoms with each other restrain the formation of a suitable probe beam. Measurements carried out with this nozzle starting parameters approve the results of this calculations. They showed an increase to higher beam pressures  $p_o$  ( $p_o < 50 \text{ bar}$ ) with a  $10 \mu\text{m}$  liquid nitrogen cooled nozzle leads to a fast approach of the pumping systems limit. Therefore it was decided to change to a  $d_N = 5 \mu\text{m}$  nozzle setup.

The recalculate values for starting parameters of  $d_{Nozz} = 5 \mu\text{m}$ ,  $T_o = 100 \text{ K}$ ,  $p_o = 180 \text{ bar}$  are:

$$\begin{aligned} \dot{N}_o &= 3.37 \cdot 10^{19} \text{ s}^{-1} \\ q_{pV} &= 1.40 \frac{\text{mbar} \cdot \text{l}}{\text{s}} \\ \bar{p}_{prevacSC} &= 2.42 \cdot 10^{-1} \text{ mbar} \end{aligned} \quad (\text{D.39})$$

As one can see, the prevacuum pressure is now in the lower  $\times 10^{-1} \text{ mbar}$  range. This is still high, but for this case the pumping system is able to handle the particle flow. With the slightly better prevacuum pressure also the compression ratio of the turbopumps will be better. A rough estimate is that it lies in the range of  $k_o = 100$ . Therefore the expected final source chamber pressure will be

$$p_{end} \approx 2.42 \cdot 10^{-3} \text{ mbar} \quad (\text{D.40})$$

The corresponding measurements presented in chapter 9 show that even though the pumping system is at its upper limit, still a proper *free-jet-expansion* is obtain for source pressure values below  $p_o = 80 \text{ bar}$  (LN<sub>2</sub> cooled beam).

As one can see from the measurements presented in section 9 the room temperature beam generated with the current pumping setup provides a fully functioning *free-jet-expansion* beam over the whole range of possible source pressures even up to the higher limit of  $p_o = 200$  bar.

#### D.8 CONDUCTANCE PREVACUUM LINE PST/ ZPC /SDC

The component setup for the backing vacuum line of the *pumping stage/ zone plate chamber* and *sample detector chamber (PST/ZPC/SDC)* is depicted in figure 2.15. All three chambers share one SCROLLVAC SC30D backing pump. The conductance values for the specific components are presented in table form, and can be found in tables D.3 and D.4.

As shown in figure 2.15, the first prevacuum lines after each of the two MAG W 300 pumps yield into a parallel conductance value  $C_{T1,2,parallel}$  for the PST/ZPC chamber combination, derived by summing up the serial connection conductance values  $C_{T_1}$  and  $C_{T_2}$

$$C_{T1,2,parallel} = C_{T_1} + C_{T_2} \quad (D.41)$$

Together with the third serial connection value  $C_{pv3}$  the total vacuum conductance of the pipes until the further parallel connection to the sample chamber prevacuum line can be found to be

$$C_{PST/ZPC_1} = \left( \frac{1}{C_{T1,2,parallel}} + \frac{1}{C_{pv3}} \right)^{-1} \quad (D.42)$$

This conductance factor for the first part of the PST/ZPC prevacuum components  $C_{PST/ZPC_1}$  is added up in a parallel arrangement with the first part conductance factor of the sample/detector chamber prevacuum system  $C_{SD_1}$ . The overall first part conductance factor  $C_{pv4}$  is

$$C_{pv4} = C_{PST/ZPC_1} + C_{SD_1} \quad (D.43)$$

The remaining prevacuum parts for this backing line are the connection KF-40 tee-piece together with the 8 m long KF-40 PVC connection tube to the

scroll pump. Hence the total conductance factor of the prevacuum system for the *pumping-stage-/zone-plate-/sample-detector- chamber* can be found to be

$$C_{totalPST/ZPC/SDC} = \left( \frac{1}{C_{pv4}} + \frac{1}{C_{Tee-piece}} + \frac{1}{C_{KF40Tube}} + \frac{1}{S_{P_{SC30}}} \right)^{-1} \quad (D.44)$$

Regarding this backing pressure system also the two additional little turbo pumps (SL80) have to be considered. They are serially implemented into the pipe system to prevent possible helium gas back-flow from the prevacuum line back into the UHV chambers. This is especially crucial in case of the sample/detector chamber since the helium background in this chamber has to be kept as minimal as possible. Therefore for the calculation of the effective pumping speed the manufacturer pumping speed values of the small turbo pumps  $S_{P_{SL80}}$  are treated as the vacuum conductance values of those pumps, that means  $C_{P_{SL80}} = S_{P_{SL80}}$ . They are directly included in the calculations of  $C_{PST/ZPC_1}$  and  $C_{SD_1}$ .

$$S_{effPST/ZPC/SDC} = C_{totalPST/ZPC/SDC} \quad (D.45)$$

With  $S_{P_{SC30}} = 7.31 \cdot s^{-1}$ ,  $S_{P_{SL80}} = 551 \cdot s^{-1}$  the effective pumping speed of the backing pump line for the PST/ZPC chambers is:

$$S_{effPST/ZPC/SDC} = 2.0025 \text{ ls}^{-1} \quad (D.46)$$

The expected backing system pressure  $\bar{p}_{prevacPST/ZPC/SDC}$  is evaluated with equation D.34, just with the modification that  $\dot{N}$  for this three chambers is not given by  $\dot{N}_0$  but by the particle flow  $\dot{N}_{bIN_{PST}} = \dot{N}_{bIN_{ZPC}}$  plus the particle flow due to the particle diffusion from the source chamber into the PST/ZPC/SDC ( $p_{EPST}$ ,  $p_{EZPC}$  and  $p_{ESDC}$ ). This three values can be found in the sections 2.2.4.1, 2.2.4.2 and 2.2.4.3 respectively.

$$\dot{N}_{PST_{Diff}} = \frac{p_{EPST} \cdot S_{PST}}{k \cdot T} \quad (D.47)$$

$$\dot{N}_{ZPC_{Diff}} = \frac{p_{EZPC} \cdot S_{ZPC}}{k \cdot T} \quad (D.48)$$

$$\dot{N}_{SDC_{Diff}} = \frac{p_{ESDC} \cdot S_{ZPC}}{k \cdot T} \quad (D.49)$$

$$\dot{N}_{PST/ZPC/SDC_{ges}} = \dot{N}_{PST_{Diff}} + \dot{N}_{ZPC_{Diff}} + \dot{N}_{SDC} + \dot{N}_{bIN_{PST}} \quad (D.50)$$















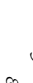


PREVACUUM LINE COMPONENTS PUMPING STAGE / ZONE PLATE CHAMBER (PST/ZPC)						
Component	Dimensions	$C_m$ [ls <sup>-1</sup> ]	C [ls <sup>-1</sup> ]	Component Code		
 KF16-KF25 adapter	D <sub>1</sub> =16 mm, D <sub>2</sub> =25 mm	27	32	KF25R16-304	$C_{T_1}$	$C_{PST/ZPC_1}$
 KF25 flexible hose	D=25 mm, L=500 mm	10	14	FX25K50-304		
 KF25-KF40 adapter	D <sub>1</sub> =25 mm, D <sub>2</sub> =40 mm	83	111	KF40R25-304	$C_{T_1}$	
 KF40 valve	D=40 mm		45	XLH-40		
 ISO-K63 to KF40 adapter	D <sub>1</sub> =66 mm, D <sub>2</sub> =40 mm	180	294	SK63/40CO	$C_{T_1, 2, parallel}$	
 KF16-KF25 adapter	D <sub>1</sub> =16 mm, D <sub>2</sub> =25 mm	27	32	KF25R16-304		
 KF25 flexible hose	D=25 mm, L=1000 mm	5	7	FX25K100-304	$C_{T_2}$	
 KF25-KF40 adapter	D <sub>1</sub> =25 mm, D <sub>2</sub> =40 mm	83	111	KF40R25-304		
 KF40 valve	D=40 mm		45	XLH-40	$C_{PST/ZPC_1}$	
 ISO-K63 to KF40 adapter	D <sub>1</sub> =66 mm, D <sub>2</sub> =40 mm	180	294	SK63/40CO		
 ISO-K63 equal tee	D=66 mm, L=176 mm	782	1695	ISO63TE-304	$C_{P_{160}}$	
 ISO-K63 flexible hose	D=66 mm, L=1000 mm	94	203	ISO63FX100		
 ISO-K63 elbow 90°	D=66 mm, $\vartheta=90^\circ$ , L <sub>ax</sub> =176 mm	426	924	ISO63E-304	$C_{P_{160}}$	
 SL 80 Turbo pump	Flange: ISO-K63/ KF-16	$S_{P_{160}}$	55	SL 80 TP		
 KF16 equal tee	D=16 mm, L <sub>ax</sub> =80 mm $\vartheta=90^\circ$	15	17	TE16K-304	$C_{P_{160}}$	
 KF16-KF40 adapter	D <sub>1</sub> =16 mm, D <sub>2</sub> =40 mm	27	31	KF40R16-304		
 KF40-KF16 unequal tee	D <sub>1</sub> =16 mm, D <sub>2</sub> =40 mm, L=130	114	187	UTF4016K		

Table D.3: Vacuum conductance values  $C_m$  and C for the prevacuum line at the PST/ZPC chamber. (Figures provided by VACOM Vakuum Komponenten & Messtechnik GmbH, product catalog)

PREVACUUM LINE COMPONENTS SAMPLE DETECTOR CHAMBER (SDC) & PUMPING STAGE / ZONE PLATE CHAMBER (PST / ZPC) REST					
	Component	Dimensions	$C_m$ [ls <sup>-1</sup> ]	C [ls <sup>-1</sup> ]	Component Code
	KF25 flexible hose	D=25 mm, L=1000 mm	5	7	FX25K100-304
	KF25-KF40 adapter	D <sub>1</sub> =25 mm, D <sub>2</sub> =40 mm	83	111	KF40R25-304
	KF40 valve	D=40 mm		45	XLH-40
	ISO-K63 to KF40 adapter	D <sub>1</sub> =66 mm, D <sub>2</sub> =40 mm	180	294	SK63/40CO
	ISO-K63 equal tee	D=66 mm, L=176 mm	782	1695	ISO63TE-304
	ISO-K63 flexible hose	D=66 mm, L=1000 mm	94	203	ISO63FX100
	ISO-K63 elbow 90°	D=66 mm, $\vartheta=90^\circ$ , L <sub>ax</sub> =176 mm	426	924	ISO63E-304
	SL 80 Turbo pump	Flange: ISO-K63/ KF-16	S <sub>P,SL80</sub>	55	SL 80 TP
	KF16 equal tee	D=16 mm, L <sub>ax</sub> =80 mm $\vartheta=90^\circ$	15	17	TE16K-304
	KF16-KF40 adapter	D <sub>1</sub> =16 mm, D <sub>2</sub> =40 mm	27	31	KF40R16-304
	KF40 PVC hose	D=40 mm, L=1 m	21	34	PVC40
	KF16 equal tee	D=16 mm, L=80 mm	247	405	TE16K-304
	KF40 PVC hose	D=40 mm, L=8 m	2.6	4-3	PVC40

Table D.4: Vacuum conductance values  $C_m$  and C for the prevacuum line at the SDC & PST/ZPC chamber. (Figures provided by VACOM Vakuum Komponenten & Messtechnik GmbH, product catalog)

As one can see from equation D.50 the particle flow due to the beam is assumed to be the flow which enters the three adjacent chambers at the entrance aperture of the PST chamber. The final backing system prevacuum pressure due to the particle flow is

$$\bar{p}_{prevac_{PST/ZPC/SDC}} = \frac{\dot{N}_{PST/ZPC/SDC_{ges}} \cdot k \cdot T}{S_{eff_{PST/ZPC/SDC}}} \quad (D.51)$$

Looking at the pressure situation with the system parameters  $d_{Nozz} = 10 \mu\text{m}$ ,  $T_o = 100 \text{ K}$ ,  $p_o = 200 \text{ bar}$  one can find:

$$\begin{aligned} \dot{N}_{PST/ZPC/SDC_{ges}} &= 4.72 \cdot 10^{13} \text{ s}^{-1} \\ q_{pV} &= 2.0845 \cdot 10^{-6} \frac{\text{mbar} \cdot \text{l}}{\text{s}} \\ \bar{p}_{prevac_{PST/ZPC/SDC}} &= 2.08 \cdot 10^{-6} \text{ mbar} \end{aligned} \quad (D.52)$$

Of course the PST/ZPC/SDC backing pressure system will not really reach this low pressure value, since the ultimate pressure of the SCROLLVAC SC30 D backing pump is stated to be in the range of  $5 \cdot 10^{-3} - 1 \cdot 10^{-2} [\text{mbar}]$ , but this calculations show that the particle flow will be no problem for this selected backing pump. Hence also the turbopumps of the pumping-stage-/zone-plate-/sample-detector chamber will be able to work at their presented optimum pumping speed. The measurements presented in section 9 also confirm this conclusion.

## APPENDIX FLIGHT TIME CALIBRATION TOF MEASUREMENTS

---

### E.1 FLIGHT TIME $t_f$ CALIBRATION TOF-MEAUSREMENTS

The flight time  $t_f$  is made up by four different parameters. The delay time  $t_d$  for the measured TOF-spectra, preset as a parameter in the TOF-measurement software. The channel width of the recorded signal parts (time bins)  $t_{channel}$ . The actual peak time  $t_p$  which is defined at the center position of the *Gauss* scan and a correction time  $t_c$  which is necessary for the calibration of the TOF-measurements (due to apparatus influences).

$$t_f = t_d + t_p + t_c - \frac{t_{channel}}{2} \quad (\text{E.1})$$

For the evaluation of  $t_f$  half of the channel width  $t_{channel}$  is subtracted to appoint the total count in each channel to the middle of the channels time interval instead of to its end [104].

There are three contributing effects influencing  $t_c$ :

$$t_c = t_1 + t_2 + t_3$$

1.  $t_1$ : Is contributed by the trigger signal which will be delivered from the LED-photo diode setup in connection with the small rectangular shaped trigger slits on the chopper disc. It will always provide a to early signal leading to  $\Rightarrow t_1 < 0$
2.  $t_2$ : Since the photo diode might not be perfectly aligned with the trigger slit on the chopper wheel there is an offset. This offset on the other hand means that the influence of this effect depends on the rotational direction of the chopper wheel and therefore it can be either negative or positive.
3.  $t_3$ : A perfect slit opening would be provided by an nearly infinite small straight line. Since this is not reasonable due to a way to weak signal going through a thin straight line, there is always an offset of the time

due to the finite slit width. This influence is negative for all cases since it does not depend on the rotational direction.

The correction time  $t_c$  is determined experimentally. It is dependent on the rotation frequency and direction of the chopper wheel. The evaluation is done by a measurement of the peak time of the *TOF*-signals for varying chopper frequencies. From plotting the peak times  $t_p$  over the inverse chopper frequency  $f_{chopper}$  a linear increasing curve is found for each spinning direction respectively. The gradient  $\alpha$  of this two curves is related to the correction time like stated in equation E.2.

$$t_c = \frac{\alpha}{f_{chopper}} \quad (\text{E.2})$$



## LIST OF FIGURES

---

- Figure 0.1 First 2D images obtained using a neutral helium atom beam to image a hexagonal copper grating. These pictures were obtained with a (top)  $3\ \mu\text{m}$  diameter and (bottom)  $2\ \mu\text{m}$  focused helium beam spot in a transmission imaging setup [34]. 7
- Figure 0.2 (a) He scattering image of an uncoated pollen grain on a Quantifoil<sup>TM</sup> TEM grid, back side. (b) Magnified area. (c) Line profile taken across linear features in (b), vertical units are gray-scale units, where 255 = white (max. He partial pressure) and 0 = black (min. pressure) published by Philip Witham and Erik Sànches earlier this year [52]. 9
- Figure 1.1 Schematic of the working principle illustrating the main components of the new *NEutral helium scattering MI-croscope* named **Nemi**. The instrument is based on a *Nozzle* for the beam generation, a *Skimmer* for selecting the central part of the beam, a *Zone Plate* as an optical element for beam focusing, and a *Detection System* for detecting the helium beam atoms which are back-scattered from the sample surface. 12
- Figure 1.2 Sketch of a FRESNEL *zone plate* element similar to the ones used in NEMI. The orange highlighted ring system structure represents the FRESNEL ZONES, whereas the gray disc in the middle and the gray rod structures orientated in radial direction represents the so called middle stop disc and the supporting grid structure for holding the ring system in place. The middle stop disc acts as a blocking element for the main part of the zero order fraction (not diffracted) of the beam. A more detailed description of these functions can be found in chapter 4. 15

- Figure 1.3 Diagram of the helium microscope with the main distances and dimensions. 17
- Figure 2.1  $v_{He}$  final average speed of the helium atoms depending on the nozzle temperature  $T_o$ . 23
- Figure 2.2 Particle density  $n_o$  entering the source chamber (SC) directly at the nozzle versus the nozzle temperature  $T_o$  for a nozzle pressure of  $p_o = 180$  [bar]. 24
- Figure 2.3 Particle density  $n_o$  entering the source chamber (SC) directly at the nozzle versus the nozzle pressure  $p_o$  for a nozzle temperature of  $T_o = 100$  [K] and  $T_o = 300$  [K] respectively. 25
- Figure 2.4 Particle density  $n(x)$  at the *zone plate* position  $x = 0.945$  [m] over the nozzle temperature  $T_o$  at a nozzle pressure  $p_o = 180$  [bar] for varying nozzle diameters. 26
- Figure 2.5 Particle density  $n(x)$  at the *zone plate* position  $x = 0.945$  [m] over the nozzle diameter  $d_N$  for the two different nozzle temperatures  $T_o = 300$  K and  $T_o = 100$  K at a pressure of  $p_o = 180$  [bar]. 26
- Figure 2.6 Particle flow  $\dot{N}_o(x)$  impinging on the *zone plate* surface  $A_{zp}$  over the nozzle temperature  $T_o$  with the three different nozzle diameters of  $d_N = 3 \mu\text{m}$ ,  $d_N = 5 \mu\text{m}$  and  $d_N = 10 \mu\text{m}$  presented for the two different *zone plates* with the middle stop diameters (blocking disc) of  $d_{MS} = 20 \mu\text{m}$  and  $d_{MS} = 50 \mu\text{m}$  respectively 28
- Figure 2.7 Cosine distribution of the reflection intensities for a diffuse scattering sample, illustrating the geometrical relation for the surface area of a spherical cap. 29
- Figure 2.8  $R_{ssample}$  for varying sample-detector distances  $l$  presented for a assumed cosine distribution of the reflection. 30
- Figure 2.9 Schematic of the pumping system setup for NEMI. 37
- Figure 2.10 Detailed setup sketch for the evaluation of the ultra high vacuum part of the pumping system. 38
- Figure 2.11 principle sketch for the flow rate estimate of the nozzle 40

- Figure 2.12  $p_{SC}$ , partial source chamber pressures versus nozzle pressure  $p_o$  for the two different nozzle diameters  $d_N = 5 [\mu\text{m}]$ , and  $d_N = 10 [\mu\text{m}]$  at the two different nozzle temperatures  $T_o = 100 [\text{K}]$ , and  $T_o = 300 [\text{K}]$  respectively. 41
- Figure 2.13 Schematic for the geometrical considerations regarding the beam widening at the position of APERTURE 1 between the pumping stage chamber (PST) and the zone plate chamber (ZPC) 47
- Figure 2.14 Principle sketch of the setup for the Source Chamber prevacuum line components. 54
- Figure 2.15 Principle sketch of the setup for the pumping stage- / zone plate- / sample detector- chamber prevacuum line components. 57
- Figure 2.16 NEM1 setup sketch with the finally chosen parameters 59

Figure 3.1 Schematic illustration of the relation between the spatial intensity distribution of the virtual source and the perpendicular speed distribution of the particles passing through point  $P$ . From the perpendicular speed distribution of the particles in point  $P$  (located at the quitting surface) it is possible to find the spatial distribution of the virtual source and its source plane. After the gas particles exit the nozzle they initially propagate within a continuum flow regime symmetric around the beam axis. Since during the expansion the density of the gas declines and hence the mean free path length increases the continuum flow regime transforms continuous into a molecular flow regime. After a distance of a view nozzle diameters they reach a point from which it is possible to assume that they propagate further on purely within the molecular flow regime on straight trajectories. The area of this final transition into molecular flow is named *quitting surface*. By back tracing the particles on straight trajectories it is possible to find the location (plane) of the virtual source. Its spatial distribution can be deduced from the perpendicular speed distributions of the particles in point  $P$  following the model presented by Thomas Reisinger et al.[69, 70]. 66

Figure 4.1 Schematic for the *Fresnel zone* construction. A Spherical wave front (radius  $R$ ) which is propagating from point  $P$  is divided into a set of *Fresnel zones* by spheres centered at point  $P'$  with radii  $R' + n \cdot \lambda/2$  for  $n = 1 \rightarrow N$ . The radius of the dividing spheres is increasing with a period of  $\lambda/2$ . The *zone plate* geometry can be pictured as the projection of the originating zones on the divided spherical wavefront onto a screen when every second zone is set to be transmissive. 70

Figure 4.2 Schematic illustrating the point spread function (PSF) of a Fresnel zone plate. The relations between the longitudinal and transversal chromatic aberration are illustrated.

- Figure 4.3 SEM images of one of the NEMI *zone plates* (support chip 8, membrane 1). Top: image of the whole *zone plate* with a middle stop diameter of  $d_{MS} = 20 \mu\text{m}$  visible; middle : SEM micrograph of the same *zone plate* in higher magnification showing the outermost *Fresnel zones*; bottom: same *zone plate* in higher magnification showing the middle area *Fresnel zones* of the *zone plate*. (The circular shaped patterns overlying the top image of the whole *zone plate* are imaging artifacts) 80
- Figure 4.4 Scanning-electron micrographs showing the two different *zone plate* types utilized in the NEMI setup representing the difference in the middle stop diameter; top: outer diameter  $d_{ZP} = 192 \mu\text{m}$  *zone plate* with a middle stop diameter of  $d_{MS} = 20 \mu\text{m}$  (support chip 8, membrane 2); bottom:  $d_{ZP} = 192 \mu\text{m}$  *zone plate* with a middle stop diameter of  $d_{MS} = 50 \mu\text{m}$  (support chip 8, membrane 6). (again the in a circular wave form shaped patterns overlying both micrographs are imaging artifacts) 81
- Figure 5.1 Schematic of the working principle of a *Pitot tube* 84
- Figure 6.1 Left: principle 3D scheme of the *pinhole aperture nozzle disc (1)*, right: scheme half section of the *nozzle disc*. 89
- Figure 6.2 Left: SEM micrograph of the aperture pinhole in a  $d_N = 5 \mu\text{m}$  nozzle disc, right: SEM image of a clogged  $d_N = 5 \mu\text{m}$  nozzle disc unmounted from *Nemi*. The black stripes appearing in the image are presumably imaging artifacts due to statically charging of the dust particle during the microscopes scanning process. 90
- Figure 6.3 Left: Sketch of the *circular holding fixture (2)* for the nozzle disc, right: 3D scheme half section of the *circular holding fixture*. 90
- Figure 6.4 Left, middle: Sketch of the triangular shaped *nozzle retaining fixture (3)* for the nozzle disc, right: 3D scheme half section of the *nozzle retaining fixture*. 91

- Figure 6.5 Exploded assembly drawing of the *nozzle disc* mounting. The *nozzle disc* (1) is placed in the *circular holding fixture* (2) and sealed by a *copper gasket* (4) against the high pressure *gas tube* (5). To tighten this sealing the *circular holding fixture* gets placed within the triangular shaped *nozzle retaining fixture* (3) which again is tightened by three M3 stainless steel screws into the copper made *nozzle-cooling block* (6). The stainless steel high pressure *gas tube* (5) on the other hand is mounted by a specially vacuum proofed soldering technique directly into this copper *nozzle-cooling block* (6). 97
- Figure 6.6 Scheme of the assembled nozzle. Top left: assembled nozzle; top right, bottom left, bottom right: 3D half section scheme of the assembled nozzle. Note: the vacuum and high pressure tight sealing takes place between the *nozzle disc* (1), the *chopper gasket* (4) and the high pressure *gas tube* (5). 98
- Figure 6.7 Picture of the nozzle cooling system displaying the copper-braid connection between the copper nozzle-cooling block and the liquid nitrogen filled stainless steel tube. The two red wires are the electrical connection for a high performance heating cartridge which is inserted into the nozzle-cooling block. The thermic connection between the tube for the liquid nitrogen (LN<sub>2</sub>) and the copper braid is done by high force clamping of the braid wires onto the outer diameter of the tube. 99
- Figure 6.8 Digital images of the *Zaber* stage components. Top: vacuum compatible **TSB28-MV** linear translation stage with mounted **KT-NA08A25-SV-ENG1243** linear actuator; middle: detail picture of the actuator pin which performs the linear motion and bottom: picture of the pull back mechanism (return spring) for the stage. 100

- Figure 6.9 3D schematics of the X/Y nozzle adjustment based on two perpendicularly assembled *Zaber linear stages* (2) in combination with two *Zaber linear actuators* (1). The *nozzle setup* (3) is mounted via three *Macor spacers* (white) onto the *nozzle mounting plate* (4) which again is fixed by four M6 screws onto the *X/Y translation stage* (2). Also shown in this sketches is the high pressure helium supply *gas tube* (5) of the source. (3D CAD model *Zaber linear stages* (2) & linear actuators (1) provided by *Zaber* [87]) 101
- Figure 6.10 Photograph of the actual *Nemi* nozzle mounting showing the *Zaber stages* and linear actuators for the X/Y adjustment of the source. 102
- Figure 6.11 3D sketch of the Z-axis source movement mechanism. 103
- Figure 6.12 3D sketches of the whole nozzle (source) setup with free movement in X/Y and Z direction. 104
- Figure 6.13 Left: photograph of a skimmer for *Nemi*; middle, right: SEM micrograph of a glass tip from a skimmer similar to the ones used in *Nemi*. The SEM images were taken by Thomas Reisinger and Martin Greve. 105
- Figure 6.14 Sketches of the skimmer mounting on the CF-150 vacuum blind flange. Left: *skimmer* (gold), *skimmer fixation ring* (light-gray) *skimmer mounting ring* (dark-gray) and specially reworked *CF-150 blind flange* (green) for skimmer mount; right: 3D scheme half section to provide a better understanding for the conical shape of the components. The half section sketch also shows the VITON sealing (black) for the vacuum tight mounting of the skimmer mount flange into the source chamber. 105
- Figure 6.15 3D explosion sketch of the source chamber. Also pictured in this scheme is the connection port for the liquid nitrogen (LN<sub>2</sub>) cooling tank 106

- Figure 6.16 Sketches presenting the final skimmer and source position after mounting into the source chamber cube. For a better understanding components like the MAG W 600 turbo pumps, the 4-port cluster flange and the quick access view port are not displayed in this images. 107
- Figure 6.17 Sketch of the source chamber assembly steps. (a), (b), (c) displaying three different assemble steps chronologically arranged, (d) representing a half section sketch through the vertical middle plane of the source chamber (MAG W 600 not displayed) 108
- Figure 6.18 Schematic of the assembled source chamber. 109
- Figure 6.19 Sketches of the assembled source chamber from different view directions. 110
- Figure 6.20 Schematics of the components building up the *pumping stage chamber (PST)*. A *CF-100 gate valve* is connected with a *CF-100 tee* piece and a *CF-100 reducer cross*. The exciting aperture from the *PST* into the *ZPC* is a *CF-100 copper gasket* with a diameter 5 mm pinhole. 115
- Figure 6.21 Sketches of the *zone plate chamber CF-100 cross* showing the two *CF-100* connection flanges along the instruments beam line, the *CF-100* connection side flange for the *MAG W 300* turbo pump, the *CF-63 side connection* flange to implement the *zone plate* holding mechanism as well as the *CF-40* side flange to connect the pressure measurement gauge for the chamber. (all *CF*-connections are pictured with *CF*- copper gaskets) 116
- Figure 6.22 Sketches of the *VAB CF-100* four port distance flange connected to the *VAB* specially manufactured *CF-100 zone plate* chamber cross. Also shown in this figure is a schematic of the *MAG W 300* turbo pump and the *CF-100* copper exiting aperture. 117



- Figure 6.23 Sketch of the *zone plate* holder. The figure represents a sketch of the positioning for the *zone plate chip*. For better explanation of the principle magnified sketches of the components are shown. The *zone plate* shown in the top left part of the image is located on the *zone plate chip* (top and bottom right image). Such a chip can hold up to 9 *zone plate* patterns. It is attached to the *ZP holding plate* which is shown in bright gray in the bottom left picture. 118
- Figure 6.24 Schematic representing the assembled *zone plate holder*. The *zone plate chip* is attached onto the *ZP holding plate* which is mounted by six hexagonal socketed screws. 119
- Figure 6.25 Photographs of the *zone plate holder* especially describing the attachment process for the *zone plate chip*. This attachment is done via three fitting springs which are connected to the holder plate through hexagon socketed screws. (Fitting spring concept developed by Kurt Ansperger [83]) 119
- Figure 6.26 3D sketch (top) and photograph (bottom) of the *ZP holding plate* and the *zone plate holder* showing the milling grooves in both parts. They are necessary to ensure that the focused helium beam can pass unhindered further on into the sample chamber. The image in the bottom presents the *zone plate holder* without a mounted *zone plate chip*. 120
- Figure 6.27 Assembly sketch of the *zone plate holder* with attached *ZP holding plate*, *zone plate holder flange*, and *zone plate chip*. Also indicated is the circular spirit level as well as the grub screws fixing the rotatable part of the CF-63 flange against the fixed outer ring of the flange after the horizontal adjustment of the *ZP holding plate*. 121
- Figure 6.28 Assembly sketch of the *zone plate holder* with attached *ZP holding plate*, *zone plate holder flange*, and *zone plate chip* from a different view direction. 122
- Figure 6.29 3D sketch XYZ stage **XYZT64-50-H** from the company UHV DESIGN. (3D CAD model provided by UHV Design) 123

- Figure 6.30 Assembly sketch of the *zone plate chamber* with a mounted *zone plate holder* attached to the UHV X/Y/Z stage as well as with a mounted MAG W 300 turbo pump presented with different view directions (top, bottom). 124
- Figure 6.31 Sketch of the *zone plate holder* and the Y/X/Z zone plate adjustment stage within the zone plate chamber setup. For a better description the CF-100 *zone plate chamber cross* is faded out of the graphic. To indicate the position of the helium beam the beams center line is marked by the blue line passing through the VAB distance flange and the copper exiting pinhole aperture of the zone plate chamber. 125
- Figure 6.32 Left: Sketch of the *sample holder*; middle: schematic half section *sample holder*; right: photograph of the sample holder. The photograph also shows the eight flexible adjustable sample retaining springs attached to the sample holder with M2 socket head screws. 127
- Figure 6.33 Left: sketch of the *sample holder* with the attached *position adjustment inset*; right: the same component shown in a photograph. 128
- Figure 6.34 3D sketches of the UHV compatible high resolution xy-positioner from different view directions. The sketches show the diameter  $d = 40\text{ mm}$  aperture opening in the middle of the *piezo table*, enabling also scanning processes with the helium beam in transmission mode. 128
- Figure 6.35 Photograph of the UHV compatible high resolution xy-positioner. 129
- Figure 6.36 Left: sketch of the attachment of the *sample holder* to the *piezo table*. The sample is indicated by the blue rectangular plate placed in the middle of the sample holder; right: schematic half section sketch of the *sample holder* attached to the *piezo table* at different view directions. 131

- Figure 6.37 Schematics of the three ALIO stage components. (a): **AIO-HR4-5000E-050-XY-UHV** XY-linear stage, (b): **AIO-D8-2500E-CB-UHV** integrated linear Z-stage and (c): **AIO-40R-D-UHV** 360 degree rotary stage. (3D CAD model provided by ALIO Industries) 132
- Figure 6.38 3D sketches of the assembled XYZR stage from ALIO. (3D CAD model provided by ALIO Industries) 133
- Figure 6.39 Top: Sketches of the *sample attachment unit* from different view directions; bottom: photographs of the *sample attachment unit*. 134
- Figure 6.40 Sketches of the assembled *sample attachment unit* with the *piezo table* and the *sample holder* from different view directions. Note in the bottom left view that the *sample attachment unit* also holds a cylindrical notch to permit a undisturbed path for the helium beam line in transmission mode. 134
- Figure 6.41 3D schematic of the complete sample stage assembly consisting of the XYZR stage assembled with the *sample attachment unit*, the *piezo table* and the *sample holder* from different view directions. 135
- Figure 6.42 Sketches of the *detector nose* presented from different view directions (left, middle); right: half section sketch of the same component. 136
- Figure 6.43 Sketches of the *detector head* presented from different view directions in (a), (b) and (c); (d) represents a half section sketch from the same component. 137

- Figure 6.44 Sketches of the assembled *detector* presented without the *cold-cathode gauge*. (a), (b), (c) different view directions, (d) half section sketch. The center-line of the helium probe beam is indicated by the blue line passing through the *0-order aperture orifice*. From the sample surface reflected helium atoms enter the detector through the pinhole aperture in the *detector nose* and travel further on through the *nose* into the *detector head's* accumulation volume. The assignment for the *0-order sorting aperture* is to block out the bigger part of the *0-order* share of the helium probe beam. 141
- Figure 6.45 Sketches to show the idea for the arrangement of the *nose detector* and the mounted *sample*. The sample itself is indicated by the blue plate mounted on-top of the *sample holder* which is attached to the *piezo table*, which again is mounted onto the *sample attachment unit*. The incident helium beam is indicated by the blue line. 142
- Figure 6.46 Sketches of the *sample/detector* arrangement from different view directions. For a better understanding of the traveling path for the reflected helium atoms the *reflection detectors front part* is shown in a half section sketch. The on the sample impinging helium beam is indicated by the blue line whereas the travel path of the reflected helium atoms within the detector nose is indicated in the bottom image by the red arrow. 143
- Figure 6.47 Photographs of the *reflection detector* with the connected cooling- and heating -setup for this component (top left, right); as well as photographs of the cooling- (bottom left) and heating- (middle left) setup respectively. 144
- Figure 6.48 Photographs of the mounting panel for the LN<sub>2</sub>tank (chicken-feeder) (left, middle bottom); middle top: mounting panel with attached PTFE connection pipe; right: LN<sub>2</sub>tank (chicken-feeder) 144
- Figure 6.49 Sketch of the *reflection detector* positioning stage from VAB, presented from different view directions. (3D CAD model provided by VAB vakuum Anlagenbau GmbH) 145

- Figure 6.50 Sketch of the *extension* for the *reflection detector* mounted to the stage from different view directions (top); bottom: half section sketch of the same component. 146
- Figure 6.51 Sketch of the *reflection detector* mounted to the *extension tube*. The figure presents the *reflection detector*, the *piezo table* with mounted *sample holder* and *sample*, the *cold-cathode gauge* for the pressure measurement and the *extension tube*. For a better understanding the *extension tube* is represented in a half section sketch. The helium beam line is indicated by the blue line. 147
- Figure 6.52 Sketch describing the UHV tight mounting of the *detector extension* into the VAB X/Y/Z stage. The sealing is a CF-100 copper gasket. Note that the mounting of the *reflection detector head* has to be done after assembling the *extension tube* into the stage. 148
- Figure 6.53 Sketches of the *reflection detector mounting* from different view directions and with different magnifications. The stage will be mounted from outside on the sample chamber (see section 6.3.3). 149
- Figure 6.54 Sketches of the *reflection detector mounting* from different view directions and with different magnifications with the *reflection detector* and the *extension tube* shown in a half section sketch for better illustration. The stage is mounted from outside on the sample chamber (see section 6.3.3). 150
- Figure 6.55 Sketches from different view directions (left, middle) of the 0-order *aperture mounting setup* presented with an attached skimmer for better explanation; right: half section sketch of the same component. 151

- Figure 6.56 Sketch of the “*in line*” *transmission detector* setup, representing the *cold-cathode gauge* assembled via a CF-100/CF-40 reducer flange directly to the *sample chamber lid*. The entrance aperture for the detection system is a CF-40 copper sealing with an diameter  $d = 1$  mm orifice opening in the middle. Top left: full sketch of the assembled components; top right: half section sketch of all components; bottom left and right: half section sketch of the *sample chamber lid* and the reducer adapter as well as full sketch of the *cold-cathode gauge* and the *entrance aperture*. 151
- Figure 6.57 Sketch of the *sample chamber lid* from different view directions. It is a CF-400 blind flange with an added CF-100 connection on its bottom side which is centered in the direct beam line position. 152
- Figure 6.58 Sketches of the *sample chamber* from different view directions. 154
- Figure 6.59 Sketches of the *sample chamber* and the mounted *sample chamber lid* from different view directions. 155
- Figure 6.60 Assembly sketch of the *sample chamber* with the attached *reflection detector*, *transmission detector*, MAG W 600 turbo pump and the CF-63 connection flange for the *liquid nitrogen cooling* (LN<sub>2</sub>) of the *reflection detector* from different view directions. For better illustration, the remaining CF-blank flanges, CF-view ports and the electrical CF-feed-throughs are not displayed. 156
- Figure 6.61 Sketches of the partly assembled *sample chamber* attached to the adjacent *zone plate chamber* from different view directions. Also apparent in this figure are the MAG W 300 turbo pump for the (ZP) chamber and the UHV X/Y/Z translation stage for the zone plate adjustment. 157
- Figure 6.62 Sketch of the assembled NEMI UHV chambers, *sample chamber*, *pumping stage chamber*, *zone plate chamber*, *sample/detector chamber*. 158
- Figure 6.63 Sketch of the assembled NEMI UHV chambers, *sample chamber*, *pumping stage chamber*, *zone plate chamber*, *sample/detector chamber* from a different view direction. 159

- Figure 6.64 Sketch of the assembled NEMI UHV chambers, *sample chamber, pumping stage chamber, zone plate chamber, sample/detector chamber* from a different view direction. 160
- Figure 6.65 Sketch of the assembled NEMI UHV chambers, *sample chamber, pumping stage chamber, zone plate chamber, sample/detector chamber* from a different view direction. 161
- Figure 6.66 Sketch of the **series 784 (Clean Top II) optical table with honeycomb core** from BFI OPTILAS with the mounted ALUFLEX profile framework for holding the microscope setup in a hanging position. 162
- Figure 6.67 Sketch of the microscope NEMI setup attached to the ALUFLEX framework and the *optical table*. 163
- Figure 7.1 Screen shot image of the LABVIEW *nozzle-skimmer* adjustment program taken after performing a rectangular *raw-search* scanning process on NEMI. 166
- Figure 7.2 Screen shot image of the LABVIEW *nozzle-skimmer* adjustment program taken after performing a the circular scanning process for the fine-adjustment of the *nozzle-skimmer* position of the NEMI Source. 167
- Figure 7.3 Sketch to illustrate the *zone plate* alignment. 168
- Figure 7.4 Schematic 0-order aperture alignment. 169
- Figure 7.5 Reflection detector Z-alignment 169
- Figure 7.6 Detector stage directions for the alignment. 170
- Figure 7.7 Sketch for the illustration of the *X/Y position adjustment* of the sample holder. 171
- Figure 8.1 Sketch for the *time-of-flight* (TOF) measurement setup on the MAGIE apparatus. A chopper disc rotating with the frequency  $f$  and equipped with two trapezoidal shaped chopping slits is implemented into the neutral helium beam line to chop the beam into small beam packages. The flight time of this beam packages between chopper and ionization detector is measured and together with the given flight distance of the beam (between chopper and detector) it is possible to determine the speed distribution (*speed ratio*) of the beam. 175

- Figure 8.2 Sketch of the *chopper wheel* implemented for the *TOF* measurements. The disc is equipped with two slits of trapezoidal shape arranged  $180^\circ$  to each other. They are accounted to chop the beam. Additionally it also has two small rectangular slit openings in radial direction to the center of the disc. They deliver a trigger pulse to the *TOF* measurement electronics based on the signal of a photo-diode. All the other features present on the chopper wheel, so to say the ten elongated wide slits as well as their corresponding small rectangular shaped trigger slits, are not used for the *TOF* measurements presented here. 176
- Figure 8.3 Flight time spectrum of the *free-jet expansion* helium beam. This measurement was taken with a  $T_o = 295\text{ K}$ ,  $p_o = 81\text{ bar}$  beam at a chopper frequency of  $f = 270\text{ Hz}$  and a vertical chopper height position of  $0.835\text{ inch}$ . Particle traveling distance (chopper-detector) of  $L_{chopp-det} = 2046\text{ mm}$ . (file: TOF3297) 177
- Figure 8.4 Schematic of the chopper slit dimensions. Point *P* corresponds to the theoretical position of the tip of the trapezoidal shaped chopper slit. 183
- Figure 8.5 Evaluation curve for the position where the beam leaves the slit. This position is found where the two blue linear fit-lines cross. The measured intensities thereby are indicated by the green filled squares connected with the red dashed line. 184
- Figure 8.6 Measured *speed ratio* values *S* versus their corresponding height position on the trapezoidal chopper slit corresponding to different slit width's *w*. 185
- Figure 9.1 Principle sketch of the experimental setup for the first beam flow measurements on the NEM1 setup. 188



Figure 9.2 Source chamber pressure increases in  $p_{SC}$  &  $p_{iSC}$  versus the nozzle pressure  $p_o$ . Left: partial helium pressure increase in the high vacuum part of the source chamber ( $p_{SC}$ ) due to the RT beam (red/square curve) with the theoretical expected pressure rises additionally indicated by the red/dotted/open-squares line and for the LN<sub>2</sub> cooled beam (blue/asterisk curve) with the corresponding theoretically evaluated values in blue/dotted/open-asterisk. Right: partial helium pressure increase in the backing pump vacuum line of the source chamber ( $p_{iSC}$ ) for the RT beam (red/open-squares) and the LN<sub>2</sub> cooled beam (blue/open-asterisk). All values are background corrected as well as corrected for helium gas. 192

Figure 9.3 Pumping stage chamber pressure increases in  $p_{PST}$  &  $p_{iPST/ZPC}$  versus the nozzle pressure  $p_o$ . In both cases only the partial pressure rise due to the helium beam is shown. The left side of this figure represents the ultra high vacuum pressure characteristic for the PST chamber ( $p_{PST}$ ) whereas the right graph depicts the pressure behavior of the prevacuum line ( $p_{iPST/ZPC}$ ). RT beam measurements are depicted by red/square lines whereas the characteristics for the LN<sub>2</sub> cooled beam are shown by blue/asterisk lines. The calculated  $p_{PST}$  values for both beam temperature cases are also presented in the left figure by dotted/open-symbol lines. All values are background corrected as well as corrected for helium gas. 194

Figure 9.4 Zone plate chamber partial helium pressure increases ( $p_{ZPC}$ ) versus the nozzle pressure  $p_o$ . RT beam measurements are depicted by red/square lines whereas the characteristics for the LN<sub>2</sub> cooled beam are shown by blue/asterisk lines. The calculated  $p_{ZPC}$  values for both beam temperature cases are also presented by dotted/open-symbol lines. All values are background corrected as well as corrected for helium gas. 195

- Figure 9.5 Comparison of the “*in-line*” detector signals of a room temperature (RT) and a liquid nitrogen cooled (LN) beam. The measured detector characteristic of the RT beam is indicated by the red/square line and the corresponding calculated values are indicated by the red/open-circle-dashed line. The blue/asterisk line represents the measured values for the LN beam whereas the blue/open-pentagon-dashed curve corresponds to the calculated values for that case. 196
- Figure D.1  $J$  as a function of  $\bar{p} \cdot D$  and the various characteristic values of the different flow regimes. (Figure drawn corresponding to [60]) 241
- Figure D.2 Molecular flow through an elbow piece (right), and definition of the elbow angle  $\theta$ . 247

## LIST OF TABLES

---

- Table 1.1 Atom optical parameters and dimensions for the *neutral helium atom scattering microscope* NEMI based on the considerations in the chapters 2, 3, 4, 5 and 6.  $v_{He}$  final average He-atom velocity,  $\lambda_{He}$  mean He-beam de Broglie wavelength,  $d_{ZP}$  zone plate diameter,  $f$  zone plate focal length,  $g$  object distance (skimmer-ZP),  $b$  image distance (ZP-sample),  $M$  demagnification factor,  $d_{Sk}$  microskimmer orifice diameter,  $d_N$  nozzle diameter,  $d_{AP1}$  &  $d_{AP2}$  aperture diameter at the PST/ZPC connection and the ZPC/SDC connection and  $d_{th}$  theoretically expected focus spot diameter (limited by the chromatic aberration of the ZPs) for the two different nozzle temperatures  $T_N$ . The best expected resolution for the present setup is 380 nm. 18
- Table 2.1 Beam penetrable surface on the *zone plates*. All of them have an outer diameter of  $d_{zp} = 192 \mu\text{m}$ . 22

- Table 2.2 Final average velocity  $v_{He}$  for the two different cases of a room temperature (RT), and a liquid nitrogen cooled beam (LN) respectively. Also presented here are the required constants to calculate these values.  $\lambda$  hereby states the corresponding *de Broglie* wavelength for the helium atom beam (see section 4.3) 23
- Table 2.3 Particle density of the He-beam at the nozzle ( $n_o$ ) as well as at the ZP ( $n(x)$ ) placed at the distance  $x = L_{Nozz-ZP} = 0,945$  m from the nozzle along the beam line. The numbers are calculated for a source pressure of  $p_o = 180$  bar, and the different nozzle diameters of  $d_{N_1} = 3 \mu\text{m}$ ,  $d_{N_2} = 5 \mu\text{m}$  and  $d_{N_3} = 10 \mu\text{m}$  respectively. 24
- Table 2.4 Calculated He-particle flow  $\dot{N}_o(x)$  impacting on the ZP with a *middle-stop* diameter of  $d_{MS} = 20 \mu\text{m}$ . The corresponding penetrable zone plate surface is  $A_{zp_{MS}(20\mu\text{m})} = 2,864 \cdot 10^{-8} \text{m}^2$ , and the nozzle pressure is set to  $p_o = 180$  bar. Values for the three different nozzle diameters of  $d_{N_1} = 3 \mu\text{m}$ ,  $d_{N_2} = 5 \mu\text{m}$  and  $d_{N_3} = 10 \mu\text{m}$  are presented at the two different nozzle temperature conditions of  $T_o = 300$  K and  $T_o = 100$  K respectively. 27
- Table 2.5 Calculated He-particle flow  $\dot{N}_o(x)$  impacting on the ZP with a *middle-stop* diameter of  $d_{MS} = 50 \mu\text{m}$ . The corresponding penetrable zone plate surface is  $A_{zp_{MS}(50\mu\text{m})} = 2,699 \cdot 10^{-8} \text{m}^2$ , and the nozzle pressure is set to  $p_o = 180$  bar. Values for the three different nozzle diameters of  $d_{N_1} = 3 \mu\text{m}$ ,  $d_{N_2} = 5 \mu\text{m}$  and  $d_{N_3} = 10 \mu\text{m}$  are presented at the two different nozzle temperature conditions of  $T_o = 300$  K and  $T_o = 100$  K respectively. 27

- Table 2.6 Determined He-particle flow  $\dot{N}_R$  into the detection system following equation 2.1. For different *zone plate middle-stop* diameters  $d_{MS}$ , varying nozzle diameters of  $d_{N_1} = 3 \mu\text{m}$  and  $d_{N_2} = 5 \mu\text{m}$  and the two different nozzle temperature conditions of  $T_o = 300 \text{ K}$  and  $T_o = 100 \text{ K}$  respectively. The nozzle pressure is set to  $p_o = 180 \text{ bar}$ . The transmissivity of the ZPs is given by  $T_{ZP} = 0.08$  whereas the sample reflectivity again is varied for the two different values of  $R_{sample} = 0.1$  and  $0.8$  respectively. 32
- Table 2.7 Partial pressure increase  $p_T$  in the detector PITOT TUBE, and corresponding vacuum conductance factors, achieved with a pinhole aperture diameter of  $d_D = 1 \text{ mm}$ ,  $d_N = 5 \mu\text{m}$  and 8% ZP efficiency as well as 10% sample reflectivity.  $p_o = 180 \text{ bar}$ ,  $T_o = 300 \text{ K}$  and  $d_{MS} = 20 \mu\text{m}$ . 34
- Table 2.8 Partial pressure increase  $p_T$  in the detector PITOT TUBE, and corresponding vacuum conductance factors, achieved with a pinhole aperture diameter of  $d_D = 1 \text{ mm}$ ,  $d_N = 5 \mu\text{m}$  and 8% ZP efficiency as well as 80% sample reflectivity.  $p_o = 180 \text{ bar}$ ,  $T_o = 300 \text{ K}$  and  $d_{MS} = 20 \mu\text{m}$ . 34
- Table 2.9  $p_{SC}$ , partial source chamber pressures for different starting conditions  $d_N$  and  $T_o$ . 41
- Table 2.10  $p_{PST}(\text{diff})$  *pumping stage* pressure increase due to diffusion for different starting setup parameters:  $p_o, d_N, T_o$ , and  $d_{Sk}$  respectively. 43
- Table 2.11  $p_{ZPC}(\text{diff})$  *partial zone plate chamber* pressure increase due to diffusion from the PST chamber for different starting setup parameters:  $d, p_o, d_N, T_o$  and  $d_{Sk}$  respectively. 44
- Table 2.12  $p_{SDC}(\text{diff})$  *partial sample/detector chamber* pressure rise due to diffusion from the ZPC chamber for an aperture diameter of  $d = 5 \text{ mm}$ , with varying parameters for  $d_N$ , and  $d_{Sk}$  respectively. 45

Table 2.13	$p_{PST}$ (beam) pumping stage chamber pressure rise due to the beam for varying $d_N$ and $d_{Sk}$ respectively. 48
Table 2.14	$p_{SDC}$ (beam) sample/detector chamber pressure rise due to the beam for varying $d_N$ and $d_{Sk}$ respectively. 49
Table 2.15	$p_{PST}$ pumping stage total chamber pressure for varying $d_N$ and $d_{Sk}$ respectively. 50
Table 2.16	$p_{ZPC}$ total zone plate chamber pressure rise due to the beam and the first estimated pressure for different $d_N$ and $d_{Sk}$ respectively 50
Table 2.17	$p_{SDC}$ total sample/detector chamber pressure rise due to the beam and the first estimated pressure for varying $d_{Nozzle}$ and $d_{Skimmer}$ respectively. 51
Table 2.18	Comparison $p_{SDC}$ total sample/detector chamber pressure rise against detection pressure increase in the PITOT TUBE $p_T$ for a worst case sample reflection of 10% and a ZP middle stop diameter of $d_{MS} = 50 \mu\text{m}$ , with the starting parameters $p_o$ , $T_o$ , $d_N$ and $d_{Sk}$ . 51
Table 2.19	Final setup parameters and elements for the NEMI helium microscope system 58
Table 2.20	Final NEMI pumping setup parameters 60
Table 4.1	List presenting the number of Fresnel-rings $N_f$ for the different zone plate types fabricated for NEMI. The outer diameter of all ZPs is $d_{ZP} = 192 \mu\text{m}$ , and their first order focal length is given by $f_1 = 168.14 \text{ mm}$ . They are fabricated for two different probe beam temperatures (RT=320 K, LN=100 K) and with two different middle-stop diameters $d_{MS1} = 20 \mu\text{m}$ and $d_{MS2} = 50 \mu\text{m}$ respectively. 78
Table 4.2	Theoretically expected focal spot diameters for the two different beam temperatures of $T_o(RT) = 320 \text{ K}$ ( $S = 113.6$ , $p_o = 150 \text{ bar}$ ) and $T_o(LN) = 100 \text{ K}$ ( $S = 521.4$ , $p_o = 150 \text{ bar}$ ) and the two different skimmer diameters of $d_{Sk} = 1 \mu\text{m}$ and $d_{Sk} = 3 \mu\text{m}$ respectively. 79
Table 6.1	Detailed specifications for the KT(T) -NA08A25-SV-ENG1243 linear actuators 93

Table 6.2	Specifications ultra high vacuum compatible <b>PXY 102 CAP ID40</b> high resolution xy-positioner	130
Table 6.3	List of the implemented stages for the XYZR vacuum compatible sample stage system.	130
Table 8.1	Evaluated speed ratio numbers for a $T_o = 122.9\text{ K}$ , $p_o = 81\text{ bar}$ beam determined from the recorded TOF-spectrum for a $\Delta w = \pm 0.1\text{ mm}$ varying chopper slit width.	181
Table D.1	Basic properties of the three different flow regimes. The character $D$ is the pipe/tube diameter and $\lambda$ is the mean free path length.	239
Table D.2	Vacuum conductance values $C_m$ and $C$ for the prevacuum line at the source chamber (SC). (Figures provided by <i>VACOM Vakuum Komponenten &amp; Messtechnik GmbH</i> , product catalog)	251
Table D.3	Vacuum conductance values $C_m$ and $C$ for the prevacuum line at the PST/ZPC chamber.(Figures provided by <i>VACOM Vakuum Komponenten &amp; Messtechnik GmbH</i> , product catalog)	256
Table D.4	Vacuum conductance values $C_m$ and $C$ for the prevacuum line at the SDC & PST/ZPC chamber. (Figures provided by <i>VACOM Vakuum Komponenten &amp; Messtechnik GmbH</i> , product catalog)	257

## BIBLIOGRAPHY

---

- [1] H. Pauly. *Atom, Molecule, and Cluster Beams 1*, chapter 1, pages 105–111. Springer, 2000.
- [2] I. Estermann, R. Frisch, and O. Stern. Monochromasierung der de Broglie-Wellen von Molekularstrahlen. *Zeitschrift für Physik A Hadrons and Nuclei*, 73(5):348–365, 1932-05-21.
- [3] Arthur Kantrowitz and Jerry Grey. A high intensity source for the molecular beam. part I. theoretical. *Review of Scientific Instruments*, 22(5):328–332, may 1951.
- [4] U. Buck. *Atomic and Molecular Beam Methodes*, volume 1, chapter 18, pages 449–471. Oxford University Press, 1988.
- [5] Daniel Farias and Karl-Heinz Rieder. Atomic beam diffraction from solid surfaces. *Reports on Progress in Physics*, 61(12):1575, 1998.
- [6] D. Farias, H. Tröger, and K.H. Rieder. He-scattering studies on the adsorption of oxygen on Rh(311). *Surface Science*, 331-333, Part A(0):150 – 155, 1995.
- [7] D. Evans, V. Celli, G. Benedek, J. P. Toennies, and R. B. Doak. Resonance-enhanced atom scattering from surface phonons. *Phys. Rev. Lett.*, 50:1854–1857, Jun 1983.
- [8] Giorgio Benedek and J.Peter Toennies. Helium atom scattering spectroscopy of surface phonons: genesis and achievements. *Surface Science*, 299-300(0):587 – 611, 1994.
- [9] R. Hooke. *Micrographica, or Some physiological descriptions of minute bodies made by magnifying glasses, with observations and inquiries thereupon*. Royal Society, (1665) 1961.
- [10] Yang Leng. *Materials Characterisation: Introduction to Microscopic and Spectroscopic Methods*. John Wiley & Sons (Asia) Pte Ltd, 2008. ISBN: 978-0-470-82298-2.

- [11] G. Binnig and H. Rohrer. Scanning tunneling microscopy-from birth to adolescence. *Rev. Mod. Phys.*, 59(3):615–625, 1987.
- [12] E. Abbe. Beiträge zur Theorie des Mikroskops und der mikroskopischen Wahrnehmung. *Archiv f. mikroskop. Anat.*, 9:413–468, 1873.
- [13] J Cazaux, D Erre, D Mouze, J M Patat, S Rondot, A Sasov, P Trebbia, and A Zolfaghari. Recent developments in X-ray projection microscopy and X-ray microtomography applied to material science. *Journal de Physique* 4, 3:2099–2104, 1993.
- [14] E Pereiro-Lopez, M Howells, and S Ferrer. X-ray microscopy and biological applications. *Colloque SF 2007*, 5-8 Juni 2007.
- [15] Stefan W. Hell and Jan Wichmann. Breaking the diffraction resolution limit by stimulated emission: stimulated-emission-depletion fluorescence microscopy. *Opt. Lett.*, 19(11):780–782, Jun 1994.
- [16] Thomas A. Klar and Stefan W. Hell. Subdiffraction resolution in far-field fluorescence microscopy. *Opt. Lett.*, 24(14):954–956, Jul 1999.
- [17] Eva Rittweger, Kyu Young Han, Scott E. Irvine, Christian Eggeling, and Stefan W. Hell. STED microscopy reveals crystal colour centres with nanometric resolution. *Nat Photon*, 3(3):144–147, March 2009.
- [18] Bert Hecht, Beate Sick, Urs P. Wild, Volker Deckert, Renato Zenobi, Olivier J. F. Martin, and Dieter W. Pohl. Scanning near-field optical microscopy with aperture probes: Fundamentals and applications. *The Journal of Chemical Physics*, 112(18):7761–7774, 2000.
- [19] Heinrich G. Frey, Susanne Witt, Karin Felderer, and Reinhard Guckenberger. High-resolution imaging of single fluorescent molecules with the optical near-field of a metal tip. *Phys. Rev. Lett.*, 93:200801, Nov 2004.
- [20] C. Höppener, J.P. Siebrasse, R. Peters, U. Kubitscheck, and A. Naber. High-resolution near-field optical imaging of single nuclear pore complexes under physiological conditions. *Biophysical Journal*, 88(5):3681 – 3688, 2005.
- [21] W. Piersig. *Mikroskop und Mikroskopie- Ein wichtiger Helfer auf vielen Gebieten*. GRIN Verlag, 2009.



- [22] M. Knoll and E. Ruska. Beitrag zur geometrischen Elektronenoptik. ii. *Annalen der Physik*, 404(6):641–661, 1932.
- [23] M. Knoll and E. Ruska. Das Elektronenmikroskop. *Zeitschrift für Physik A Hadrons and Nuclei*, 78:318–339, 1932. 10.1007/BF01342199.
- [24] L. de Broglie. -. *Ann. de Physique*, 3 (22):–, 1925.
- [25] J Goldstein, D E Newbury, P Echlin, D C Joy, C E Lyman, E Lifshin, L Sawyer, and J R Michael. *Scanning Electron Microscopy and X-Ray Microanalyses*. Springer Science-Buisness Media, LLC, 3 edition, 2003. ISBN: 978-0-306-47292-3.
- [26] Edith Stabentheiner, Armin Zankel, and Peter Pölt. Environmental scanning electron microscopy (ESEM)-a versatile tool in studying plants. *Protoplasma*, 246:89–99, 2010. 10.1007/s00709-010-0155-3.
- [27] L Reimer and H Kohl. *Transmission Electron Microscopy*. Springer Science-Buisness Media, LLC, 5 edition, 2008. ISBN: 978-0-387-40093-8.
- [28] Rolf Erni, Marta D. Rossell, Christian Kisielowski, and Ulrich Dahmen. Atomic-resolution imaging with a sub-50-pm electron probe. *Phys. Rev. Lett.*, 102:096101, Mar 2009.
- [29] M. T. Postek and A. E. Vladar. Helium ion microscopy and its application to nanotechnology and nanometrology. *Scanning*, 30(6):457–462, 2008.
- [30] L. Scipioni, L. A. Stern, J. Notte, S. Sijbransij, and B. Griffin. Helium ion microscope. *Advanced Materials & Processes*, pages 27–30, June 2008.
- [31] G. Binnig, H. Rohrer, Ch. Gerber, and E. Weibel. Surface studies by scanning tunneling microscopy. *Phys. Rev. Lett.*, 49:57–61, Jul 1982.
- [32] G. Binnig, C. F. Quate, and Ch. Gerber. Atomic force microscope. *Phys. Rev. Lett.*, 56:930–933, Mar 1986.
- [33] Clemens Möller, Mike Allen, Virgil Elings, Andreas Engel, and Daniel J. Müller. Tapping-mode atomic force microscopy produces faithful high-resolution images of protein surfaces. *Biophysical Journal*, 77(2):1150 – 1158, 1999.

- [34] M. Koch, S. Rehbein, G. Schmahl, T. Reisinger, G. Bracco, W. E. Ernst, and B. Holst. Imaging with neutral atoms—a new matter-wave microscope. *Journal of Microscopy*, 229(1):1–5, 2008.
- [35] S. Jochim, M. Bartenstein, A. Altmeyer, G. Hendl, S. Riedl, C. Chin, J. Hecker Denschlag, and R. Grimm. Bose-Einstein condensation of molecules. *Science*, 302(5653):2101–2103, 2003.
- [36] M. D. Barrett, J. A. Sauer, and M. S. Chapman. All-optical formation of an atomic Bose-Einstein condensate. *Phys. Rev. Lett.*, 87:010404, Jun 2001.
- [37] Bodil Holst and William Allison. An atom-focusing mirror. *Nature*, 390(6657):244–244, November 1997.
- [38] A. E. Weeks. *Si(111) Atom-Optical Mirrors for Scanning Helium Microscopy*. PhD thesis, University of Cambridge, 2007.
- [39] K. Fladischer, H. Reingruber, T. Reisinger, V. Mayrhofer, W. E. Ernst, A. E. Ross, D. A. MacLaren, W. Allison, D. Litwin, J. Galas, S. Sitarek, P. Nieto, D. Barredo, D. Fariás, R. Miranda, B. Surma, A. Miros, B Piatkowski, E. Søndergård, and B. Holst. An ellipsoidal mirror for focusing neutral atomic and molecular beams. *New Journal of Physics*, 12(3):033018, 2010.
- [40] D. Barredo, F. Calleja, P. Nieto, J. J. Hinarejos, G. Laurent, A. L. V. de Parga, D. Fariás, and R. Miranda. A quantum-stabilized mirror for atoms. *Advanced Materials*, 20(18):3492–3497, 2008.
- [41] D. Barredo, G. Laurent, F. Calleja, P. Nieto, J. J. Hinarejos, A. L. Vázquez de Parga, D. Fariás, and R. Miranda. A high-reflectivity atom-focusing mirror stable at room temperature. *Applied Physics Letters*, 96(8):081901, 2010.
- [42] P. Sutter, M. Minniti, P. Albrecht, D. Fariás, R. Miranda, and E. Sutter. A high-reflectivity, ambient-stable graphene mirror for neutral atomic and molecular beams. *Applied Physics Letters*, 99(21):211907, 2011.
- [43] A. Politano, B. Borca, M. Minniti, J. J. Hinarejos, A. L. Vázquez de Parga, D. Fariás, and R. Miranda. Helium reflectivity and Debye temperature of graphene grown epitaxially on Ru(0001). *Phys. Rev. B*, 84:035450, Jul 2011.

- [44] T. Reisinger and B. Holst. Neutral atom and molecule focusing using a Fresnel zone plate. *J. Vac. Sci. Technol. B*, 26(6):2374–2379, Nov/Dez 2008.
- [45] H. Christian Schewe, Bum Suk Zhao, Gerard Meijer, and Wieland Schöllkopf. Focusing a helium atom beam using a quantum-reflection mirror. *New Journal of Physics*, 11(11):113030, 2009.
- [46] O. Carnal, M. Sigel, T. Sleator, H. Takuma, and J. Mlynek. Imaging and focusing of atoms by a Fresnel zone plate. *Phys. Rev. Lett.*, 67:3231–3234, Dec 1991.
- [47] O. Carnal and J. Mlynek. Young’s double-slit experiment with atoms: A simple atom interferometer. *Phys. Rev. Lett.*, 66:2689–2692, May 1991.
- [48] David W. Keith, Christopher R. Ekstrom, Quentin A. Turchette, and David E. Pritchard. An interferometer for atoms. *Phys. Rev. Lett.*, 66:2693–2696, May 1991.
- [49] R. B. Doak, R. E. Grisenti, S. Rehbein, G. Schmahl, J. P. Toennies, and Ch. Wöll. Towards realization of an atomic de Broglie microscope: Helium atom focusing using Fresnel zone plates. *Phys. Rev. Lett.*, 83:4229–4232, Nov 1999.
- [50] S. Rehbein, R.B. Doak, R.E. Grisenti, G. Schmahl, J.P. Toennies, and Ch. Wöll. Nanostructuring of zone plates for helium atom beam focusing. *Microelectronic Engineering*, 53(1-4):685 – 688, 2000.
- [51] Stefan Rehbein. *Entwicklung von freitragenden nanostrukturierten Zonenplatten zur Fokussierung und Monochromatisierung thermischer Helium-Atomstrahlen*. PhD thesis, Georg-August Universität zu Göttingen, Mathematische-Naturwissenschaftliche Fakultät, 2001.
- [52] Philip Witham and Erik Sanchez. A simple approach to neutral atom microscopy. *Review of Scientific Instruments*, 82(10):103705, 2011.
- [53] J. Braun, P. K. Day, J. P. Toennies, G. Witte, and E. Neher. Micrometer-sized nozzles and skimmers for the production of supersonic He atom beams. *Review of Scientific Instruments*, 68(8):3001–3009, 1997.

- [54] Martin Greve. Testing nano-structured fresnel zoneplates for neutral helium microscopy on a molecular-beam ultra-high-vacuum apparatus. Master's thesis, University of Bergen, Norway, June 2010.
- [55] D. Bassi. *Atomic and Molecular Beam Methodes*, volume 1, chapter 6-8, pages 153–192. Oxford University Press, 1988.
- [56] U. Hefter and K. Bergmann. *Atomic and Molecular Beam Methodes*, volume 1, chapter 9, pages 193–253. Oxford University Press, 1988.
- [57] M. Zen. *Atomic and Molecular Beam Methodes*, volume 1, chapter 10, pages 254–273. Oxford University Press, 1988.
- [58] B. Samelin. Neu-und Weiterentwicklung von Elektronenstoßionisations-detektoren. Master's thesis, Max Planck Institute for Dynamics and Self-Organization, Göttingen, 1993.
- [59] D.R. Miller. *Atomic and Molecular Beam Methodes*, volume 1, chapter 2, pages 14–53. Oxford University Press, 1988.
- [60] A. Roth. *Vacuum Technology*. North-Holland, third, updated and anlarged edition edition, 1990.
- [61] W. Jitschin. *Wutz Handbuch Vakuumtechnik*, volume 8, chapter Chapter 3. Vieweg & Sohn Verlag, 2004.
- [62] W. Jitschin. *Wutz Handbuch Vakuumtechnik*, volume 8, chapter Chapter 4. Vieweg & Sohn Verlag, 2004.
- [63] M. D. Morse. *Atomic, Molecular, and optical Physics, Atoms and Molecules*, volume 29B, chapter 2, pages 21–47. Academic Press, Inc., 1996.
- [64] Alan G. Michette. *Optical Systems for Soft X Rays*. Plenum Press, New York, 1968.
- [65] T. Reisinger, S. Eder, M.M. Greve, H.I. Smith, and B. Holst. Free-standing silicon-nitride zoneplates for neutral-helium microscopy. *Microelectronic Engineering*, 87:1011–1014, 2010.
- [66] A. A. Maradudin, I. Simonsen, T. A. Leskova, and E. R. Mèndez. Design of one-dimensional Lambertian diffusers of light. *Waves in Random Media*, 11(4):529–533, 2001.

- [67] S. Leutwyler M. Kappes. *Atomic and Molecular Beam Methodes*, volume 1. Oxford University Press, 1988.
- [68] H.C.W. Beijerinck and N.F. Verster. Absolute intensities and perpendicular temperatures of supersonic beams of polyatomic gases. *Physica B+C*, 111(2-3):327 – 352, 1981.
- [69] T. Reisinger, M.M. Greve, S. Eder, G. Bracco, and B. Holst. Virtual source size of a supersonic-expansion deuterium beam. *submitted to Phys. Rev. A*.
- [70] Thomas Reisinger. *Free-standing, axially-symmetric diffraction gratings for neutral matter-waves: experiments and fabrication*. PhD thesis, UNiversity of Bergen Department of Physics and Technology, August 2011. ISBN 978-82-308-1833-6.
- [71] H. Pauly. *Atom, Molecule, and Cluster Beams 1*, chapter 3.5, pages 105–111. Springer, 2000.
- [72] E. Hecht. *Optics*, volume 4. Addison Wesley, 2002.
- [73] R. E. Grisenti, W. Schöllkopf, J. P. Toennies, G. C. Hegerfeldt, T. Köhler, and M. Stoll. Determination of the bond length and binding energy of the helium dimer by diffraction from a transmission grating. *Phys. Rev. Lett.*, 85:2284–2287, Sep 2000.
- [74] Gerhard C. Hegerfeldt and Thorsten Köhler. Atomic versus molecular diffraction: Influence of breakups and finite size. *Phys. Rev. A*, 57:2021–2029, Mar 1998.
- [75] Gerhard C. Hegerfeldt and Thorsten Köhler. Deviations from classical optics in matter diffraction and determination of the size of weakly bound molecules. *Phys. Rev. A*, 61:023606, Jan 2000.
- [76] R. E. Grisenti, W. Schöllkopf, J. P. Toennies, G. C. Hegerfeldt, and T. Köhler. Determination of atom-surface van der Waals potentials from transmission-grating diffraction intensities. *Phys. Rev. Lett.*, 83:1755–1758, Aug 1999.
- [77] Yuxin Wang, Wenbing Yun, and Chris Jacobsen. Achromatic Fresnel optics for wideband extreme-ultraviolet and X-ray imaging. *Nature*, 424(6944):50–53, July 2003.

- [78] J. Daniel, J.R. Stigliani, R. Mittra, and R.G. Semoni. Resolving power of a zone plate. *J. Opt. Soc. Am.*, 57(5):610–611, May 1967.
- [79] Thomas Reisinger, Gianangelo Bracco, Stefan Rehbein, Günter Schmahl, Wolfgang E. Ernst, and Bodil Holst. Direct images of the virtual source in a supersonic expansion. *The Journal of Physical Chemistry A*, 111(49):12620–12628, 2007. PMID: 17985855.
- [80] Stefan Wilfert. *Grundlagenuntersuchungen zur Entwicklung eines langzeit-stabilen Kaltkathoden-Ionisationsmanometer vom inversen Magnetron-Typ*. PhD thesis, Otto von Guericke Universität Magdeburg, 2006.
- [81] K. Jousten. *Wutz Handbuch Vakuumtechnik*, volume 8, chapter 12. Vieweg & Sohn Verlag, 2004.
- [82] Parametric Technology Corporation (PTC). Pro engineer wildfire 5.0.
- [83] Kurt Ansperger. Kurt Ansperger Konstruktion, Entwicklung und Bau von Prototypen.
- [84] Plano. PLANO GmbH.
- [85] HS-Heizelemente. Heinz Stegmeier GmbH.
- [86] Eurotherm. Eurotherm Deutschland GmbH.
- [87] Zaber. Zaber Technologies Inc.
- [88] J.L. Rae and R.A. Levis. *Fabrication of Patch Pipets*, chapter 4, pages 53–78. John Wiley & Sons, Inc., 2001.
- [89] R.D. Purves. The mechanics of pulling a glass micropipette. *Biophysical Journal*, 29(3):523 – 529, 1980.
- [90] VACOM. Vakuum Komponenten & Messtechnik GmbH, Germany.
- [91] Pfeiffer. Pfeiffer Vacuum GmbH, Germany.
- [92] VAB. Vakuum-Anlagenbau GmbH, Germany.
- [93] UHV Design. UHV Design Ltd.
- [94] Pjezo Jena. pjezosystem jena GmbH.

- [95] ALIO. Alio Industries.
- [96] LASER 2000. Laser 2000 GmbH.
- [97] BFI Optilas. BFi OPTiLAS international S.A.S.
- [98] J. P Toennies and Klaus Winkelmann. Theoretical studies of highly expanded free jets: Influence of quantum effects and a realistic intermolecular potential. *The Journal of Chemical Physics*, 66(9):3965–3979, 1977.
- [99] L. Pedemonte, G. Bracco, and R. Tatarek. Theoretical and experimental study of the free-jet expansions. *Phys. Rev. A*, 59:3084–3087, Apr 1999.
- [100] L. Pedemonte and G. Bracco. Study of the flow properties to test the dimer potentials. *The Journal of Chemical Physics*, 119(3):1433–1441, 2003.
- [101] D. J. Auerbach. *Atomic and Molecular Beam Methodes*, volume 1. Oxford University Press, 1988.
- [102] H. Pauly. *Atom, Molecule, and Cluster Beams 2*, volume 2, chapter 3.2, pages 156–171. Springer, 2000.
- [103] J.P. Toennies and K. Winkelmann. Theoretical studies of highly expanded free jets: Influence of quantum effects and a realistic intermolecular potential. *The Journal of Chemical Physics*, 66(9):3965–3979, May 1977.
- [104] J. L. Luneng. Low-energy surface vibration measurements on the alpha-quartz (0001) surface. Master's thesis, University of Bergen, Norway, March 2011.











